

# Effects of De-icing and Anti-icing Chemicals on the Durability of Reinforcing Steel in Concrete

by

Matthew James Hunt

A thesis

presented to the University of Waterloo

in fulfillment of the

thesis requirement for the degree of

Master of Applied Science

in

Mechanical Engineering

Waterloo, Ontario, Canada, 2013

© Matthew James Hunt 2013

I hereby declare that I am the sole author of this thesis. This is a true copy of the thesis, including any required final revisions, as accepted by my examiners.

I understand that my thesis may be made electronically available to the public.

## Abstract

Concrete is strong in compression; however, it is quite fragile in tension. To overcome this flaw, concrete is frequently reinforced with bars typically made of low grade, low carbon steel. The environment inside of concrete is favorable for steel; unfortunately when passive steel is exposed to chlorides, active corrosion can initiate, resulting in damage to the structure.

One source of chloride contamination is through anti-icing agents which are used to inhibit the formation of ice on roadways, ensuring safe driving conditions. This represents a serious concern from both the cost associated with rehabilitation (Canadian infrastructure deficit in 2003 was \$125 billion [1]) and as a safety concern to the public. In Canada, 5 million tonnes of road salts are used each year [2], of which Ontario uses 500 to 600 thousand tonnes [3].

As a result, the Ministry of Transportation Ontario (MTO) has requested a study of four frequently used anti-icing agents: 25.5% NaCl, 31.5% MgCl<sub>2</sub>, 37.9% CaCl<sub>2</sub> and 32.6% multi Cl<sup>-</sup> (12% NaCl, 4% MgCl<sub>2</sub> and 16% CaCl<sub>2</sub>). The objective of the study is two-fold, the first is comparing the effects of the solutions on steel embedded in concrete (high pH environment) and the second is to compare the effects of the anti-icing agents to a variety of construction steels in atmospheric conditions (neutral pH).

Macro-cell and micro-cell corrosion in concrete were tested using both modified ASTM G109 prisms and concrete beams with 6 embedded black steel bars. Unfortunately, these tests proved inconclusive; all of the steel remained passive. This was a result of casting a high quality concrete in laboratory conditions which ultimately lead to minimal diffusion of the anti-icing solutions. Therefore, it is recommended that for short term corrosion testing (<2 years), poor quality concrete or cement paste should be used.

Micro-cell testing in synthetic concrete pore solution contaminated with the anti-icing solutions was conducted in order to obtain results in the period of the M.A.Sc. program and to directly observe the corrosion. The initial concentration of Cl<sup>-</sup> in each solution was 0.00% Cl<sup>-</sup>; this was incrementally increased by 0.005% Cl<sup>-</sup>/week. Potentiostatic linear polarization to resistance measurements and pH measurements were used to monitor the corrosion on a weekly basis. The results of this test showed that MgCl<sub>2</sub> has the most detrimental effects due to the drop in pH (from 13.5 to 9.1) caused by Mg

replacing Ca in  $\text{Ca}(\text{OH})_2$  to form the less soluble  $\text{Mg}(\text{OH})_2$ . The transition from passive to active corrosion initiated at 0.7, 0.4-0.9, 0.6 and 0.6%  $\text{Cl}^-$  for NaCl,  $\text{MgCl}_2$ ,  $\text{CaCl}_2$  and multi  $\text{Cl}^-$ , respectively. The active corrosion current densities were  $11\text{mA}/\text{m}^2$  for NaCl,  $\text{CaCl}_2$  and multi  $\text{Cl}^-$ , whereas  $\text{MgCl}_2$  had active corrosion rates of  $\sim 100\text{mA}/\text{m}^2$ . One bar exposed to  $\text{CaCl}_2$  showed corrosion rates as high as  $600\text{mA}/\text{m}^2$ . This was a result of crevice corrosion between the shrink fitting and the rebar. Once the expansive corrosion products broke through the shrink fitting and ample supply of oxygen became available, allowing the corrosion rates to spike dramatically.

The following steels were tested directly in the diluted solution in a cyclic corrosion chamber: stainless steels: 304L, 316LM, 2101, 2205, 2304, XM28; corrosion resistant steel reinforcing bars (rebar): galvanized rebar, guard rail (galvanized plate steel) and MMFX; carbon steels: black steel rebar, box girder, drain, weathering steel. The reinforcing bars were virgin steels whereas the remaining steels were components from the field. The testing regime followed SAE J2334 using the anti-icing solutions diluted to 3% by wt.  $\text{Cl}^-$  as the immersion liquid. Unfortunately, the multi  $\text{Cl}^-$  solution was not tested due to time constraints. The mass change per unit area was measured every five cycles.

All stainless steels exposed to all anti-icing solutions exhibited similar changes in mass per unit area, less than  $10\text{g}/\text{m}^2$ . All plain carbon steels including weathering steel exhibited mass changes per unit area of more than  $1000\text{g}/\text{m}^2$  with some variability between the various anti-icing solutions and steel types, although the black steel rebar typically outperformed the other carbon steels. The corrosion products of MMFX were non-adherent, resulting in inconclusive results.

The galvanized layer on the guard rail, which had been exposed to the environment in service, proved to be more protective than the fresh zinc coating on the galvanized rebar. When exposed to the  $\text{MgCl}_2$  solution, the mass change of both new and used galvanized steels was comparable to that found in the stainless steels. When exposed to NaCl solutions, the galvanized guard rail also exhibited this trend, whereas the new galvanic coating did not, suggesting that with exposure to the atmosphere a galvanic coating will protect the steel against NaCl. In all cases galvanized steel exposed to  $\text{CaCl}_2$  solutions exhibited mass changes per unit area of less than  $100\text{g}/\text{m}^2$  this is considered moderate, as this value is one order of magnitude higher than the stainless steels and one order of magnitude lower than the carbon steels exposed to the same test.

It is recommended that galvanic coatings be utilized in areas heavily exposed to anti-icing solutions. The weathering steel offers no advantages over carbon steels when directly exposed to anti-icing solutions. Furthermore, in areas with high amounts of exposed galvanized steel,  $\text{CaCl}_2$  should be avoided.

Between the four solutions tested, NaCl solutions are recommended as the anti-icing agents that, overall, causes the least amount of damage to both the reinforcing steel in concrete and to exposed metallic components. NaCl is followed by multi  $\text{Cl}^-$  and  $\text{CaCl}_2$ . Even though  $\text{MgCl}_2$  causes less damage when directly exposed to carbon steels and galvanized steels than  $\text{CaCl}_2$ , it is much easier to repair external components than internal components. Therefore,  $\text{MgCl}_2$  is not recommended.

## **Acknowledgments**

I would like to thank Dr. Carolyn Hansson, my supervisor, who is the sole reason for my pursuit of an M.A.Sc. Degree. The assistance and opportunities she has afforded me are immeasurable and I will be forever grateful to her. I would like to thank the lab group: Tim Bandura, James Cameron, Cecilia Hou, Ali Shabbir, and Colin Van Niejenhuis. I would like to especially point out the assistance provided by Dr. Amir Poursaei for allowing me the use of his ACMP program. Without it, I would have written a dissertation on data collection rather than corrosion. I would like to thank Bradley Bergsma and Dr. Shazma Jaffer for answering all of my unrelenting questions. And finally from “Team Corrosion”, Mark Cremasco, who was a source of inspiration and madness in the lab.

My appreciation and thanks goes to the lab technicians who assisted in creating concrete specimens, repairing perpetually faulty lab equipment, training and assisting in the use of lab equipment and ensuring my safety in the labs: Ann Allen, Dr. Yuquan Ding, Mark Griffet, Douglas Hirst, Richard Morrison, Terry Ridgway, Norval Wilhelm.

This project would not have been possible without the assistance of The Ministry of Transportation Ontario (MTO) for supplying the financial support and materials for this project. In addition to the MTO, Holcim Canada, Algoma, Valbruna, Otukompu, Talley, Cascade Steel and Harris Rebar Ltd. supplied materials for this project. Special thanks to Dr. Laura Mammoliti for providing the concrete mix design and assisting in the details about casting.

I would also like to thank Dr. Adrian Gerlich and Dr. Scott Walbridge for their time and valuable input as my thesis reviewers.

Finally, I would like to thank my Mother and Father who stand behind me no matter how many degrees I decide to chase. I would like to thank Mary Bland, the Engineering Society Manager who has been my mom-away-from-home and great friend for my entire university career. And last but not least, my partner Melissa Mesenbrink, whose patience and kindness knows no bounds as she inspires me to do all that I do.

# Table of Contents

Author’s Declaration.....	ii
Abstract.....	iii
Acknowledgments .....	vi
List of Figures .....	xii
List of Tables .....	xxiii
List of Abbreviations .....	xxvi
List of Equations.....	xxvii
Chapter 1 Introduction .....	1
1.1 Background of the Problem.....	1
1.2 Statement of the Problem.....	3
1.3 Objective.....	3
1.4 Importance of Study.....	4
1.5 Scope of the Study.....	4
1.6 Thesis Structure .....	5
Chapter 2 Background and Literature Review .....	6
2.1 Effects of Chlorides on the Corrosion of Steel Reinforcement and Concrete.....	6
2.1.1 Salt Chemistry .....	9
2.1.2 Chloride Content of Cement Pore Solution.....	11
2.1.3 Effects of Salt on Steel in Concrete .....	12
2.1.4 Effects of Salt on Concrete Durability .....	13
2.1.5 Diffusion of Salt in Concrete.....	17
2.1.6 Effects of Salt on pH .....	18
2.2 Electrochemical Corrosion.....	20

2.2.1	Macro-cell Corrosion .....	23
2.2.2	Micro-cell Corrosion .....	23
2.2.3	Review of Electrochemical Measurement Techniques .....	29
2.3	Corrosion Resistant Steels Outside of Concrete.....	30
2.3.1	Stainless Steel.....	31
2.3.2	Galvanized Steel .....	32
2.3.3	Other Forms of Reinforcement and Comparison.....	34
2.3.4	Weathering Steel.....	35
2.3.4.1	Applications.....	36
2.3.4.2	Corrosion Resistance.....	36
Chapter 3	Experimental Procedure .....	39
3.1	Research Design .....	39
3.2	Macro-cell Testing: ASTM G109 Testing.....	40
3.3	Micro-cell Testing .....	45
3.3.1	Beams with Ponding Well .....	49
3.3.2	Synthetic Pore solution Testing.....	52
3.4	Cyclic Corrosion Chamber (SAE J2334 Immersion Testing) .....	55
3.4.1	Test Set Up .....	55
3.4.2	Specimen Preparation .....	57
3.4.3	Deviation from the Test Schedule .....	58
3.5	Materials.....	59
3.5.1	Salt Solution .....	59
3.5.2	Concrete .....	59
3.5.2.1	Casting.....	60
3.5.2.2	Air Content.....	62

3.5.2.3	Twenty Eight Day Compressive Strength .....	62
3.5.3	Metal Composition .....	63
3.5.3.1	Steel Specifications .....	63
3.5.3.2	Scanning Electron Microscope, Energy-Dispersive X-ray Spectroscopy and Energy Dispersive X-Ray Fluorescence .....	68
Chapter 4	Experimental Results and Discussion .....	69
4.1	Materials Tested .....	69
4.1.1	Salt Solution .....	69
4.1.2	Concrete .....	71
4.1.3	Metals' Compositions .....	71
4.1.3.1	X-Ray Fluorescence Results .....	72
4.1.3.2	Scanning Electron Microscopy and Energy-Dispersive X-ray Spectroscopy Results .....	74
4.2	Macro-cell Results: ASTM G109 .....	80
4.2.1	Corrosion Potential Measurements .....	82
4.2.2	Macro-Cell Corrosion Current Density .....	83
4.2.3	Micro-cell Corrosion of the Top and Bottom Bars of the ASTM G109 Specimens .....	85
4.3	Micro-cell Results: Beams with Ponding Well .....	90
4.3.1	Concrete Resistance .....	91
4.3.2	Corrosion Potential Measurements .....	93
4.3.3	Micro-cell Corrosion Current Density .....	95
4.4	Micro-cell Results: Synthetic Pore Solution .....	96
4.4.1	Corrosion Potential Measurements .....	98
4.4.2	Micro-cell Corrosion Current Density .....	100
4.4.3	Cyclic Polarization .....	102
4.4.4	Reinforcing Steel Autopsy .....	106

4.4.4.1	Surface Cleaning and Pickling .....	107
4.4.4.2	Scanning Electron Microscopy of the Black Steel Surface After Exposure to Chloride Contaminated Synthetic Pore Solution .....	110
4.5	Cyclic Corrosion Chamber Testing: SAE J2334-Immersion Testing .....	111
4.5.1	Comparison between Steel Types.....	111
4.5.2	Comparison between Anti-Icing Solution Type.....	114
4.5.2.1	Stainless Steels Exposed to Various Anti-Icing Solutions.....	114
4.5.2.2	Carbon Steels and Weathering Steel Exposed directly to Various Anti-Icing Solutions .	118
4.5.2.3	Galvanized Steels and MMFX Exposed to Various Anti-Icing Solutions.....	123
Chapter 5	Summary and Conclusions .....	128
5.1	Steel Embedded in Concrete .....	128
5.2	Macro-cell Corrosion: ASTM G109 .....	128
5.3	Micro-cell Corrosion: Synthetic Pore Solution .....	129
5.4	Cyclic Corrosion Chamber Tests .....	130
Chapter 6	Recommendations .....	132
6.1	Testing .....	132
6.1.1	Concrete .....	132
6.1.2	ASTM G109.....	132
6.1.3	Beams with Ponding Well .....	133
6.1.4	Synthetic Pore Solution .....	133
6.1.5	Cyclic Corrosion Chamber .....	133
6.2	Anti-Icing Solutions.....	134
6.3	Steel Selection When Exposed Directly to the Solution.....	135
References...	.....	136
Appendix A: Electrochemical Analysis .....	.....	144

A-1 Galvanostatic Pulse Technique.....	148
A-2 Potentiostatic Technique .....	149
A-3 Steady State Testing .....	151
A-4 Cyclic Polarization.....	153
A-4.1 Linear Region ( $\sim\pm 20$ mV).....	153
A-4.2 Log-Linear Region ( $\sim\pm 200$ mV) .....	156
Appendix B: Casting and Concrete .....	163
B-1 Determining Saturated Surface Dry Conditions .....	165
B-2 Casts .....	168
B-3 Concrete Properties.....	174
Appendix C: Experimental Methods.....	175
C-1 Inductively Coupled Plasma Optical Emission Spectroscopy and Ion Beam Chromatography: Tests Used to Determine Anti-Icing Solution Composition.....	175
C-2 X-Ray Fluorescence.....	175
Appendix D: Experimental Results.....	177
D-1 Macro-cell Results: ASTM G109 .....	177
D-1.1 Corrosion Potential Measurements .....	177
D-1.2 Galvanic Corrosion Current Density .....	180
D-2 Micro-cell Results: Beams with Ponding Well .....	182
D-3 Micro-cell Results: Synthetic Pore Solution .....	185
D-4 Cyclic Corrosion Chamber Testing: SAE J2334-Immersion Testing .....	187

## List of Figures

Figure 1-1: Damage on the Gardiner Expressway, corrosion products from the steel expand and cause the concrete to delaminate and crack. The results are falling concrete that pose a threat do motorists driving underneath the expressway [8].....	3
Figure 2-1: Potential (SHE) vs. pH diagram of iron [11].....	7
Figure 2-2: Specific volume of the corrosion products from iron [12].....	9
Figure 2-3: Liquidus lines of NaCl, CaCl <sub>2</sub> and MgCl <sub>2</sub> [13] [14].....	10
Figure 2-4: Ice melting capacity of deicers measured at -5°C for reagent grade chlorides, chloride-based (CB), CMA, and ag-based (AB) deicers. Deicers not listed as reagent grade are commercially available produces. The salt/sand blend is 10% salt by weight [15]......	11
Figure 2-5: Relation between chloride content in concrete and cement to pore solutions [17].....	12
Figure 2-6: Surface of specimens, 130 weeks after exposure to different salt solutions [20].....	16
Figure 2-7: Chloride penetration into concrete from one direction measured after 2, 19 and 59 weeks soaking by weight of cementitious materials [13].....	17
Figure 2-8: The variation in the molar solubility of magnesium hydroxide as a function of pH (in the absence of species other than magnesium and hydroxyl) [32].....	19
Figure 2-9: Schematic of (a) micro-cell corrosion and (b) macro-cell corrosion [6].....	21
Figure 2-10: Comparison between the macro-cell and micro-cell corrosion current densities for the steel in OPC and HPC specimens when the top bars are disconnected from the bottom bars [24].....	22
Figure 2-11: Comparison between macro- and micro-cell corrosion current densities [20].....	22
Figure 2-12: Configuration of micro-cell activity before and after forming a macro-cell by connecting to a passive metallic zone. Only in deaerated media does the galvanic current equate to the corrosion intensity in macro-cell activity [34].....	23

Figure 2-13: Randles Circuit,  $R_s$  represents the resistance of the concrete (or solution),  $C$  represents the double layer capacitance,  $R_p$  represents the polarization resistance, and  $W$  represents the specific electrochemical element of diffusion also known as a Warburg element [36]. ..... 24

Figure 2-14: Double layer capacitor [37] ..... 25

Figure 2-15: The polarization resistance is the slope of the polarization curve (I-E) around the corrosion potential (when I changes the polarity from negative to positive) [34]..... 26

Figure 2-16: Ranges of  $I_{corr}$  values registered in the laboratory after numerous tests in many different conditions [34] ..... 28

Figure 2-17: Decrease of bar diameter/bar cross-section with time as a function of  $I_{corr}$  values (propagation period). Based on the time to reach a certain cross-section loss, for corrosion levels are established: negligible, low, moderate and high [34]. ..... 28

Figure 2-18: A typical bridge deck highlighting critical areas on a bridge deck typically exposed to higher amounts of de-icing salts. These areas are good candidates where alternate reinforcement could be utilized such as stainless, galvanized, fiber reinforced polymer, or other alternatives [50]. ... 32

Figure 2-19: Potential (SHE) vs. pH diagram of zinc [11] ..... 33

Figure 2-20: Zinc rich corner of the binary Fe-Zn phase diagram [55] ..... 34

Figure 2-21: Effects of copper and other alloying elements on the long-term atmospheric corrosion resistance of steel in [60] adopted from [61]..... 37

Figure 2-22: Surface oxides of (a) carbon steel and (b) weathering steel [63] ..... 37

Figure 3-1: Schematic of ASTM G109 specimen, (a) and (b) are from the ASTM G109 standard [68], (c) is the modified ASTM G109 with a cast-in ponding well ..... 41

Figure 3-2: (a) black steel bar sample prior to testing, (b) black steel bar sample coated with shrink wrap containing adhesive exposed to 1M HCl with shrink wrap and (c) with the shrink wrap removed ..... 42

Figure 3-3: Schematic of macro-cell corrosion, modified diagram of Carolyn Hansson [6] ..... 46

Figure 3-4: Theoretic galvanostatic pulse response ..... 47

Figure 3-5: Theoretic potentiostatic linear polarization to resistance response, the applied potential (blue) is the potential difference from  $E_{corr}$ . Note:  $R_T$  in this schematic is the total resistance, i.e. the cathodic scan's concrete resistance and polarization resistance as well as the anodic scan's concrete resistance and polarization resistance. .... 48

Figure 3-6: Beam schematic (Note: not to scale) ..... 50

Figure 3-7: Replica bridge deck beams with cast in ponding well test set up ..... 52

Figure 3-8: Pore solution (a) specimen, (b) bars in solution, (c) top of specimen wired and ready for testing ..... 53

Figure 3-9: SAE J2334 test cycle [72] ..... 55

Figure 3-10: ASCOTT (a) reservoir and (b) corrosion chamber ..... 56

Figure 3-11: Corrosion chamber specimen holder [58] ..... 56

Figure 3-12: Steel rebar specimens prior to testing in the corrosion chamber ..... 57

Figure 3-13: Plate steel specimens prior to testing in the corrosion chamber ..... 58

Figure 3-14: Casting pictures (a) formwork of a set of ASTM G109s, (b) close up of inside an ASTM G109 showing the three rebar and the ponding-well, note that the specimens are cast inverted, (c) the formwork on top of the vibration table ready for concrete and (d) 12 cast ASTM G109 Specimens ..... 61

Figure 3-15: Vertical air pressure chamber use for determining the total air content of concrete using the air method ..... 62

Figure 3-16: As-received materials (a and b) are the two box girder sections (a) is the thicker web section sample and (b) is the thinner top flange section sample. (c) is a drain. (d) is weathering steel obtained from Algoma Steel, it was originally virgin steel but left outside, it was exposed to the

elements; unlike the other specimens it had not been exposed to anti-icing solutions. (e) is the galvanized guard rail, all samples were taken from the web of the guard rail which had the most intact coating. .... 67

Figure 4-1: SEM image of galvanized reinforcing steel (a) overview of the cross section (b), (c) and (d) right are three other areas where composition and depth measurements were taken. Location (d) is where composition measurements across the Zn-Fe boundary were made. .... 75

Figure 4-2: SEM image of a guard rail sample (a) overview of the cross section (b) left, (c) top and (d) right are three other areas where composition and depth measurements were taken. Location (b) is where composition measurements across the Zn-Fe boundary were made. .... 76

Figure 4-3: High magnification micrograph of the left side zinc coating of the guard rail ..... 79

Figure 4-4: Twenty indoor ASTM G109 specimens ..... 81

Figure 4-5: Fifteen outdoor ASTM G109 specimens ..... 82

Figure 4-6: Average corrosion potential measurements against SCE of ASTM G109 specimens (a) indoor specimens with resistor connected, (b) indoor specimens with resistor disconnected, (c) outdoor specimens with resistor connected and (d) outdoor specimens with resistor disconnected. \*Note all values above  $-200 \text{ mV}_{\text{SCE}}$  in the 90% no corrosion region according to ASTM G1 ..... 83

Figure 4-7: Average macro-cell corrosion current density measurements of indoor specimens. Note  $1 \mu\text{A}/\text{m}^2 = 0.1 \text{ nA}/\text{cm}^2 \approx 1 \text{ nm}/\text{year}$  ..... 84

Figure 4-8: Average macro-cell corrosion current density measurements of outdoor specimens. Note  $100 \mu\text{A}/\text{m}^2 = 10 \text{ nA}/\text{cm}^2 \approx 135 \text{ nm}/\text{year}$  ..... 85

Figure 4-9: Average concrete resistance measurements of 4 and 3 bars respectively for indoor and outdoor ASTM G109 specimens including error bars of one standard deviation, the spread of the outdoor water-exposed specimens was significantly higher than the other specimens and the standard deviation of the top and bottom bars are  $16410 \Omega$  and  $16501 \Omega$  respectively ..... 87

Figure 4-10: Average corrosion potential measurements  $\pm$ one standard deviation of 4 and 3 bars respectively for indoor and outdoor ASTM G109 specimens tested using the galvanostatic pulse technique..... 88

Figure 4-11: Average corrosion current density measurements of 4 and 3 bars respectively for indoor and outdoor ASTM G109 specimens including error bars of one standard deviation. Note  $1 \text{ mA/m}^2 = 100 \text{ nA/cm}^2 \approx 1 \text{ }\mu\text{m/year}$  ..... 89

Figure 4-12: Micro-cell versus macro-cell corrosion current density measurements of ASTM G109 specimens. Note: that both the ordinate and abscissa axis are plotted on a log scale; the black line has a slope of one. Note  $1 \text{ }\mu\text{A/m}^2 = 0.1 \text{ nA/cm}^2 \approx 1 \text{ }\mu\text{m/year}$  ..... 90

Figure 4-13: Sample beam ponded with  $\text{CaCl}_2$  solution and disconnected from electrochemical measuring equipment ..... 91

Figure 4-14: Average of six resistance measurements between the counter electrode (Ti mesh) and reinforcing steel specimens against time ..... 92

Figure 4-15: Average of six black steel bar’s corrosion potential measurements against time..... 94

Figure 4-16: Crystallization of NaCl solution due to relative humidity formation of NaCl stalactite (Left) ..... 94

Figure 4-17: Effects of NaCl leaching around and being absorbed via capillary suction through the bottom of the beam causing corrosion ..... 95

Figure 4-18: Average of six black steel bar’s corrosion current density measurements against time Note:  $100 \text{ }\mu\text{A/m}^2 = 10 \text{ nA/cm}^2 \approx 135 \text{ nm/year}$  ..... 96

Figure 4-19: Set up of micro-cell corrosion test in synthetic pore solution ..... 97

Figure 4-20: Temperature and pH of pore solution vs.  $\text{Cl}^-$  concentration..... 98

Figure 4-21: Average corrosion potential measurements of 5 bars in pore solution exposed to various concentrations of anti-icing solutions. According to ASTM C876 potentials above the upper limit

(purple line) represents where there is a 90% chance of stability, the potentials below the lower limit (red line) represent where there is a 90% chance of corrosion. In between these two lines the probability of corrosion is uncertain. .... 99

Figure 4-22: Bars exposed to various chlorides with a concentration 0.70% Cl<sup>-</sup> taken in a glove box in a nitrogen environment..... 100

Figure 4-23: Average corrosion current density measurements of 5 bars in pore solution exposed to various concentrations of anti-icing solutions. Note  $1E-2A/m^2 = 1 \mu A/cm^2 \approx 12 \mu m/year$  and  $1E-10 mA/m^2 = 1 \mu A/cm^2 \approx 13 \mu m/year$ ..... 101

Figure 4-24: Black steel exposed to CaCl<sub>2</sub> showing higher corrosion rates than the other bars exposed to CaCl<sub>2</sub> at 2.75% Cl<sup>-</sup>. Note the large corrosion product that has amassed along the rib ..... 102

Figure 4-25: Cyclic polarization results of a single bar from each solution at a chloride concentration of 2.75% Cl<sup>-</sup>. The scan rate used was 0.01mV/s. Note<sup>1</sup> that the abscissa axis is plotted on a logarithmic scale. Note<sup>2</sup>  $1 A/m^2 = 100 \mu A/cm^2 \approx 1 mm/year$  ..... 104

Figure 4-26: Cyclic polarization results of a two bars exposed to NaCl solution at a chloride concentration of 2.75% Cl<sup>-</sup>. The scan rate used was 0.01mV/s. Note<sup>1</sup> that the abscissa axis is plotted on a logarithmic scale. Note<sup>2</sup>  $1 A/m^2 = 100 \mu A/cm^2 \approx 1 mm/year$  ..... 105

Figure 4-27: Black Steel exposed to 2.75%Cl<sup>-</sup> by weight using (a) NaCl, (b) MgCl<sub>2</sub>, (c) CaCl<sub>2</sub> and (d) Multi Cl<sup>-</sup> after cyclic polarization testing from the open circuit potential to 300 mV<sub>SCE</sub> to 900 mV<sub>SCE</sub> and back to the open circuit potential..... 106

Figure 4-28: Black steel bars exposed to 2.75%Cl<sup>-</sup> by weight using (a) NaCl, (b) MgCl<sub>2</sub>, (c) CaCl<sub>2</sub> and (d) multi Cl<sup>-</sup> ..... 107

Figure 4-29: Black steel bars exposed to 2.75%Cl<sup>-</sup> by weight using (a) NaCl, (b) MgCl<sub>2</sub>, (c) CaCl<sub>2</sub> and (d) multi Cl<sup>-</sup> the bars have also spent several days outside of the pore solution in a desecrator with air at ambient temperature and pressure. .... 108

Figure 4-30: Black steel bars exposed to 2.75%Cl<sup>-</sup> by weight of (a) NaCl, (b) MgCl<sub>2</sub>, (c) CaCl<sub>2</sub> and (d) Multi Cl<sup>-</sup>. The bars have also spent several days outside of the pore solution in a desiccator with air at ambient temperature and pressure and have been pickled according to ASTM G1. .... 109

Figure 4-31: Black steel exposed to 2.75%Cl<sup>-</sup> by weight using (a) NaCl, (b) MgCl<sub>2</sub>, (c) CaCl<sub>2</sub> and (d) multi Cl<sup>-</sup>. .... 110

Figure 4-32: Average mass change per unit area vs. SAE J2234 cycles (in days) exposed to NaCl anti-icing solution. Note: the ordinate axis is logarithmic. .... 113

Figure 4-33: Average mass change per unit area vs. SAE J2234 cycles (in days) exposed to MgCl<sub>2</sub> anti-icing solution. Note: the ordinate axis is logarithmic. .... 113

Figure 4-34: Average mass change per unit area vs. SAE J2234 cycles (in days) exposed to CaCl<sub>2</sub> anti-icing solution. Note: the ordinate axis is logarithmic. .... 114

Figure 4-35: 304L specimen (a) prior to testing and exposed to 50 cycles of (b) NaCl, (c) MgCl<sub>2</sub> and (d) CaCl<sub>2</sub>..... 115

Figure 4-36: 304L average mass change per unit area vs. SAE J2234 cycles (in days) exposed to various anti-icing solutions..... 115

Figure 4-37: 316LN average mass change per unit area vs. SAE J2234 cycles (in days) exposed to various anti-icing solutions..... 115

Figure 4-38: 316LN specimen (a) prior to testing and exposed to 50 cycles of (b) NaCl, (c) MgCl<sub>2</sub> and (d) CaCl<sub>2</sub>..... 116

Figure 4-39: 2101 specimen (a) prior to testing and exposed to 50 cycles of (b) NaCl, (c) MgCl<sub>2</sub> and (d) CaCl<sub>2</sub>..... 116

Figure 4-40: 2101 average mass change per unit area vs. SAE J2234 cycles (in days) exposed to various anti-icing solutions..... 116

Figure 4-41: 2205 average mass change per unit area vs. SAE J2234 cycles (in days) exposed to various anti-icing solutions.....	116
Figure 4-42: 2205 specimen (a) prior to testing and exposed to 50 cycles of (b) NaCl, (c) MgCl <sub>2</sub> and (d) CaCl <sub>2</sub> .....	117
Figure 4-43: 2304 specimen (a) prior to testing and exposed to 50 cycles of (b) NaCl, (c) MgCl <sub>2</sub> and (d) CaCl <sub>2</sub> .....	117
Figure 4-44: 2304 average mass change per unit area vs. SAE J2234 cycles (in days) exposed to various anti-icing solutions.....	117
Figure 4-45: XM28 average mass change per unit area vs. SAE J2234 cycles (in days) exposed to various anti-icing solutions.....	117
Figure 4-46: XM28 specimen (a) prior to testing and exposed to 50 cycles of (b) NaCl, (c) MgCl <sub>2</sub> and (d) CaCl <sub>2</sub> .....	118
Figure 4-47: Black steel specimen (a) prior to testing and exposed to 50 cycles of (b) NaCl, (c) MgCl <sub>2</sub> and (d) CaCl <sub>2</sub> .....	119
Figure 4-48: Black steel average mass change per unit area vs. SAE J2234 cycles (in days) exposed to various anti-icing solutions .....	119
Figure 4-49: Box girder average mass change per unit area vs. SAE J2234 cycles (in days) exposed to various anti-icing solutions .....	119
Figure 4-50: Box girder specimen (a) prior to testing and exposed to 50 cycles of (b) NaCl, (c) MgCl <sub>2</sub> and (d) CaCl <sub>2</sub> .....	120
Figure 4-51: Drain specimen (a) prior to testing and exposed to 50 cycles of (b) NaCl, (c) MgCl <sub>2</sub> and (d) CaCl <sub>2</sub> .....	121
Figure 4-52: Drain average mass change per unit area vs. SAE J2234 cycles (in days) exposed to various anti-icing solutions.....	122

Figure 4-53: Weathering steel average mass change per unit area vs. SAE J2234 cycles (in days) exposed to various anti-icing solutions .....	122
Figure 4-54: Weathering steel specimen (a) prior to testing and exposed to 50 cycles of (b) NaCl, (c) MgCl <sub>2</sub> and (d) CaCl <sub>2</sub> .....	123
Figure 4-55: Galvanized rebar specimen (a) prior to testing and exposed to 50 cycles of (b) NaCl, (c) MgCl <sub>2</sub> and (d) CaCl <sub>2</sub> .....	124
Figure 4-56: Galvanized rebar average mass change per unit area vs. SAE J2234 cycles (in days) exposed to various anti-icing solutions .....	125
Figure 4-57: Guard rail (galvanized plate) average mass change per unit area vs. SAE J2234 cycles (in days) exposed to various anti-icing solutions.....	125
Figure 4-58: Guard rail specimen (a) prior to testing and exposed to 50 cycles of (b) NaCl, (c) MgCl <sub>2</sub> and (d) CaCl <sub>2</sub> .....	126
Figure 4-59: MMFX specimen (a) prior to testing and exposed to 50 cycles of (b) NaCl, (c) MgCl <sub>2</sub> and (d) CaCl <sub>2</sub> .....	127
Figure 4-60: MMFX average mass change per unit area vs. SAE J2234 cycles (in days) exposed to various anti-icing solutions .....	127
Figure A-1: Randles circuit.....	144
Figure A-2: Randles circuit excluding the diffusional element, for analysis.....	145
Figure A-3: Simplified Randles circuit at steady-state .....	151
Figure A-4: Example relationship between current and potential. The anodic curve shows the decomposition (oxidation) of hydrogen gas and the formation (reduction) of hydrogen ions to hydrogen gas [60] .....	157
Figure A-5: Mixed potential of zinc dissolving in an acid [60]. .....	159

Figure A-6: (a) The theoretic cathodic and anodic curves of a metal dissolving reducing hydrogen ions to hydrogen gas and (b) showing the resulting measured potential from the theoretic curves [60]... 160

Figure B-1: Various states of aggregates used in concrete [85] ..... 165

Figure C-1: Schematic diagram showing the internal components of a hand-held XRF[93] (left) and the principles of XRF [94] (right) ..... 176

Figure D-1: Individual corrosion potential measurements of indoor specimens exposed to various anti-icing solution mixed potentials (left) and anodic potentials (right) ..... 179

Figure D-2: Individual corrosion potential measurements of outdoor specimens exposed to various anti-icing solution mixed potentials (left) and anodic potentials (right)..... 180

Figure D-3: Individual corrosion current density measurements of indoor specimens exposed to various anti-icing solution ..... 181

Figure D-4: Individual corrosion current density measurements of outdoor specimens exposed to various anti-icing solution ..... 182

Figure D-5: Concrete resistance measurements of concrete between individual bars and Ti mesh counter electrode in the ponding well of concrete exposed to various anti-icing solutions against time ..... 183

Figure D-6: Corrosion potential measurements of individual bars in concrete exposed to various anti-icing solutions against time ..... 184

Figure D-7: Corrosion current density measurements of individual bars in concrete exposed to various anti-icing solutions against time, note that the ordinate axis is logarithmic ..... 185

Figure D-8: Corrosion potential measurements of individual bars in pore solution exposed to varying concentrations of anti-icing solution. Note that the ordinate axis scale varies for each solution..... 186

Figure D-9: Corrosion current density measurements of individual bars in pore solution exposed to varying concentrations of anti-icing solution. Note that the ordinate axis scale is logarithmic. .... 187

Figure D-10: Individual specimens exposed to NaCl solution vs. SAE J2334 cycles. Note that the ordinate axis for each plot varies in order to show the detail of the individual specimens. ....189

Figure D-11: Individual specimens exposed to MgCl<sub>2</sub> solution vs. SAE J2334 cycles. Note that the ordinate axis for each plot varies in order to show the detail of the individual specimens. ....192

Figure D-12: Individual specimens exposed to CaCl<sub>2</sub> solution vs. SAE J2334 cycles. Note that the ordinate axis for each plot varies in order to show the detail of the individual specimens. ....194

## List of Tables

Table 1-1: Solution salt and chloride concentration [9] .....	4
Table 2-1: Cathodic half-cell reactions .....	8
Table 2-2: Synthetic pore solution composition [16] .....	11
Table 2-3: Constituents of proprietary salt tested by McDonald and Perenchio [19] .....	15
Table 2-4: Chloride diffusion coefficients for different salts [26].....	18
Table 2-5: Gecor6 and 3LP interpretation guidelines [43] [44] compiled by Otieno [42] .....	29
Table 2-6: Fe-Zn phase compositions [55].....	34
Table 2-7: Comparison of corrosion-resistant reinforcing materials [46] .....	35
Table 3-1: ASTM G109 sample configuration .....	43
Table 3-2: Chemical cleaning procedures for removal of corrosion products .....	55
Table 3-3: Concrete mix design (per m <sup>3</sup> ) .....	60
Table 3-4: Casting batches.....	61
Table 3-5: Deformed bar designation numbers and associated requirements CSA G30.18-09 [76] .....	64
Table 3-6: Chemical composition limits for analysis of finished bars CSA G30.18-09 [76] .....	64
Table 3-7: Chemical requirements (heat analysis) of ASTM weathering steel [77] [78] .....	65
Table 3-8: Chemical composition of weathering steels, wt.%, CSA 40-21 [79] .....	65
Table 3-9: Metals tested in the corrosion chamber .....	66
Table 3-10: Materials and corresponding test methods used for characterization.....	68
Table 4-1: Salt solution composition in mg/L [9].....	69

Table 4-2: Bulk salt and chloride concentration .....	70
Table 4-3: Solution eutectic point, concentration and solution freezing point .....	71
Table 4-4: Concrete average 28-day strength .....	71
Table 4-5: Composition of stainless steels according to the mill certificate provided by steel suppliers and weathering steel by analysis.....	72
Table 4-6: Major alloying elements by wt. % of materials tested determined using XRF.....	73
Table 4-7: Zinc thickness measurements of the galvanized rebar and guard Rail .....	77
Table 4-8: Composition of the zinc coating .....	77
Table 4-9: Composition across the zinc–iron interface .....	78
Table 4-10: Chemical composition of the substrate steel of the galvanized rebar and guard rail.....	79
Table 4-11: EDS Analysis of the various regions found in the zinc layer of the guard rail .....	80
Table 4-12: EDS Analysis of white region on the outside edge of the zinc coating.....	80
Table 4-13: Summary of Cyclic Polarization Results (Approximate values) .....	103
Table B-1: Requirements for C, F, N A, and S classes of exposure [84] .....	164
Table B-2: Specimen size calculations .....	169
Table B-3: Cast 1 constituents for micro-cell beams .....	171
Table B-4: Cast 2 constituents for 15 G109s.....	172
Table B-5: Cast 3 constituents for 10 G109s.....	172
Table B-6: Cast 3 constituents for 10 G109s.....	173
Table B-7: Air content and slump .....	174

Table B-8: Twenty eight day concrete strength.....174

## List of Abbreviations

Abbreviation	Name
ACMP	Automatic Corrosion Monitoring Program
ASTM	American Society for Testing and Materials
CE	Counter electrode
CP	Cyclic polarization
C-S-H	Calcium-silicate-hydrate
CSE	Copper-copper sulfate electrode
EDS	Energy-dispersive X-ray spectroscopy
EIS	Electrochemical impedance spectroscopy
EN	Electrochemical noise
GD	Galvanodynamic
GP	Galvanostatic Pulse
HPC	High performance concrete
HSLA Steel	High strength low alloy steel
KCL	Kirchhoff's current law
KVL	Kirchhoff's voltage law
LPR	Linear polarization to resistance
MOE	Manganese-manganese dioxide electrode
M-S-H	Magnesium-silicate-hydrate
MTO	Ministry of Transportation Ontario
PD	Poentiodynamic
OPC	Ordinary portland cement
PS	Potentiostatic
RE	Reference electrode
Rebar	Reinforcing bars
SCE	Saturated calomel electrode
SHE	Standard hydrogen electrode
SSD	Saturated surface dry
SEM	Scanning electron microscope
w/c	Water to cement (ratio)
w/cm	Water to cementitious materials (ratio)
WE	Working electrode (typically the specimen)
XRF	X-ray fluorescence

## List of Equations

2-1.....	8
2-2.....	8
2-3.....	8
2-4.....	8
2-5[34][40].....	26
2-6[34][40].....	26
2-7[34][40].....	26
2-8.....	27
2-9[34][40][41].....	27
3-1.....	44
3-2.....	44
3-3.....	45
3-4.....	45
3-5.....	54
3-6.....	54
3-7.....	54
3-8.....	54
3-9.....	54
A-1.....	146

A-2.....	146
A-3.....	146
A-4.....	146
A-5.....	146
A-6.....	147
A-7.....	147
A-8.....	148
A-9.....	148
A-10.....	148
A-11.....	148
A-12.....	148
A-13.....	148
A-14.....	149
A-15.....	149
A-16.....	149
A-17.....	149
A-18.....	149
A-19.....	149
A-20.....	150

A-21.....	150
A-22.....	150
A-23.....	150
A-24.....	150
A-25.....	150
A-26.....	151
A-27.....	151
A-28.....	151
A-29.....	153
A-30.....	153
A-31.....	153
A-32.....	153
A-33.....	153
A-34.....	153
A-35.....	154
A-36.....	154
A-37.....	155
A-38.....	155
A-39.....	155

A-40.....	155
A-41.....	155
A-42.....	155
A-43.....	156
A-44.....	156
A-45 [60] .....	157
A-46 [60] .....	157
A-47 [60] .....	157
A-48 [60] .....	158
A-49.....	158
A-50.....	158
A-51.....	158
A-52.....	158
A-53 [60] .....	159
A-54.....	160
A-55 [60] .....	161
A-56 [60] .....	161
A-57.....	161
A-58.....	161

A-59[83].....	161
A-60.....	162
A-61.....	162
A-62.....	162
B-1.....	165
B-2.....	165
B-3.....	165
B-4.....	165
B-5.....	166
B-6.....	166
B-7.....	166
B-8.....	166
B-9.....	166
B-10.....	166
B-11.....	166
B-12.....	167
B-13.....	168
B-14.....	168
B-15.....	168

## **Chapter 1 Introduction**

This chapter discusses the background on purpose of the project. Details are provided about the purpose of anti-icing solutions, the associated costs of Canada's degrading infrastructure. Furthermore, there is a need to choose more appropriate anti-icing solutions to provide safe roads for motorists and minimize the damage to the existing infrastructure (specifically concrete reinforced structures).

### **1.1 Background of the Problem**

Concrete is the most widely used material; the only substance used more is water, which is one of the primary ingredients in concrete. The consumption of concrete by weight is 10 times that of steel- over one ton of concrete is produced for every human being [4]. Concrete on its own does not supply sufficient strength in tension to meet many of the structural applications. To overcome this problem, reinforcement bars (rebar), typically carbon steel (known in the field as black steel) is required to provide the tensile strength not available through concrete alone. Furthermore, in some applications where corrosion of black steel is considered problematic, alternatives such as stainless steel, galvanized steel, fiber reinforced polymers and other corrosion resistant materials have been utilized.

In addition to reinforcement in the concrete, weathering steel is used to create the box girders of many bridges and overpasses supporting the reinforced concrete deck. Both the reinforcing steel and weathering steel are considered passive in their respective working environments, resulting in corrosion rates that are negligible. However, when this environment is altered, corrosion can become a significant problem.

The principal concern is corrosion due to the presence of chlorides. Chlorides are typically introduced onto the structure from the proximity of marine environments in coastal regions and as anti- or de-icing agents on roads in colder climates. The focus of this thesis is on the latter.

In areas such as Canada, the temperature will frequently dip below the freezing point of water. This causes a risk to drivers as the pressure between the ice surface and the vehicle tire is sufficient to cause regelation. The water from this process acts as a lubricant and greatly reduces the traction between the tires and the remaining ice, resulting in unsafe driving conditions. Furthermore, "slush" from the ice and snow can fill the tread of the tire which can further reduce the surface area of the tire in contact with the road. To combat this issue road salts are used to help prevent the formation of

ice. The salts form a solution with the water causing a drop in the freezing point. This allows for a higher contact area between the tire and road, allowing for safer driving conditions.

On average 5 million tonnes of road salts are used each year in Canada [2]. Of those 5 million tonnes per year, Ontario uses 500 to 600 thousand tonnes [3]. One method used to distribute the salts is by spraying a salt solution on the roads. The brine also acts as a mild adhesive for rock salt and sand which can further improve road safety. The Province of Ontario currently uses four brines (CaCl<sub>2</sub>, NaCl, MgCl<sub>2</sub>, and Multi-chloride brine). Which salt is used is dependent on the availability of the solution and the geographic location of where the solution is being applied. In addition to salt spray used as an anti-icing agent, CaCl<sub>2</sub> solutions are also used in the summer months as a dust suppressor on un-paved roadways.

In terms of infrastructure, corrosion of reinforcing steel in concrete is a primary concern. Steel in concrete is normally protected due to the alkaline nature of the concrete pore solution, which allows the formation of a passive film [5]. When chlorides are present, the passive film breaks down and causes the reinforcing steel to actively corrode, which is a much more rapid process than passive corrosion.

The impact of corrosion on the load carrying capabilities of the steel is less of a concern than the damage the corrosion products induce on the surrounding concrete. The corrosion products of steel are expansive (between 2-3.5 times the size of the original steel [6] [7] and will build up pressure with time. This eventually causes de-lamination, cracking, and spalling as shown below in Figure 1-1. This results in chunks of concrete falling off the structure which represents a safety concern to motorists and a cost to the public in terms of rehabilitation. Similarly, weathering steel attacked by chlorides fail to produce an adhesive passive film (which typically inhibits continued corrosion). Instead the corrosion products can form thick layers which lose their adhesion to the steel and can eventually detach and fall. Once again this represents both a safety concern to motorists and a cost due to rehabilitation.



**Figure 1-1: Damage on the Gardiner Expressway, corrosion products from the steel expand and cause the concrete to delaminate and crack. The results are falling concrete that pose a threat do motorists driving underneath the expressway [8].**

## **1.2 Statement of the Problem**

The Ministry of Transportation Ontario (MTO) has requested an investigation be carried out to determine the relative effects of four different de-icing solutions ( $\text{CaCl}_2$ ,  $\text{NaCl}$ ,  $\text{MgCl}_2$ , and Multi-chloride brine) on reinforcing steel in concrete, weathering steel exposed to the atmosphere, and concrete exposed to the atmosphere. The focus of this thesis is on the effects on the reinforcing steel and weathering steel.

## **1.3 Objective**

The objective of this report is to quantitatively determine the impact of different de-icing agents on reinforcing steel and various other corrosion resistant steels. The salt and chloride concentration of the anti-icing solutions being investigated are shown below in Table 1-1, the full analysis can be found in Chapter 4 Experimental Results and Discussion. It is the aim of this report to categorize the solutions according to the severity and onset of damage to the various steels.

**Table 1-1: Solution salt and chloride concentration [9]**

<b>Primary Solution Constituent</b>	<b>% Salt (by mass)</b>	<b>% Chloride (by mass)</b>
<i>NaCl</i>	25.5	15.7
<i>MgCl<sub>2</sub></i>	31.51	23.3
<i>CaCl<sub>2</sub></i>	37.9	24.5
<i>Multi-Chloride</i>	32.554	21.1

## **1.4 Importance of Study**

In North America degradation due to corrosion costs over \$300 billion per year [10] with the costs to Canada estimated to be \$125 billion in 2003 [1]. Of this approximately one third of this cost could be prevented or avoided with the appropriate measures taken [10]. The results of this study will aid the Ministry of Transportation Ontario in determining the best choice of anti-icing agents to use on highway overpasses and bridges. This will allow the bridge a longer service life and help devise appropriate maintenance plans and schedules for these structures.

## **1.5 Scope of the Study**

This study has utilized electrochemical methods to determine the corrosion rates of the reinforcing steel in concrete. This has been done on both the macro-cell level utilizing the ASTM G109 test and at the micro-cell level observing steel embedded in concrete and submerged in synthetic pore solution. Black steel, stainless steel and a variety of other corrosion resistant steels have been tested in a corrosion chamber using SAE J2334 immersion test.

The results of this study are comparative in nature and should not be considered absolute when attempting to predict the life expectancy of a bridge component. The aim was to categorize which solutions do the most and least amount of damage and by what factor. Furthermore, the corrosion chamber has provided a glimpse at which grades of stainless steels and corrosion resistance steels provide the best resistance when exposed directly to the salt solutions and what differences (if any) are there between the various steels.

## **1.6 Thesis Structure**

This thesis is organized in the following manner. Chapter 2 Background and Literature Review, is a literature review on studies completed in the field of corrosion of weathering steel and reinforcing steel. Chapter 2 also contains the theoretic premise of corrosion and the chemistry involved. Chapter 3 Experimental Procedure covers the testing methods implemented in detecting corrosion of the reinforcing steel and weathering steel as well as the methods used to determine the corrosion products. Chapter 4 Experimental Results and Discussion analyzes and interprets the results gathered during experimental testing and summarize the data collected. Chapter 5 is the summary and conclusions drawn from the results collected in Chapter 4. Chapter 6 Recommendations outlines lessons learned from the current research including ways in which to improve upon it; as well as, recommendations for future research in the corrosion of reinforcing steel and weathering steel.

## **Chapter 2 Background and Literature Review**

This chapter provides an overview of similar research completed in the field of corrosion and concrete degradation as a result of anti-icing solutions and anti-icing salts. It is important to note that any effects on the concrete will also directly impact the performance of the embedded reinforcement.

### **2.1 Effects of Chlorides on the Corrosion of Steel Reinforcement and Concrete**

Steel, like many metals, does not occur naturally and is typically found as an oxide or bound with other elements to form a variety of other compounds. When iron ore is processed into steel it naturally wants to corrode and revert back to its lower energy states. Luckily, as mentioned in Chapter 1, steel in concrete forms a naturally passive film that reduces the rates of corrosion to a negligible level. This is a result of the high pH environment (typically pH 12.6-13.8) found in concrete. From the E-pH diagram in Figure 2-1, shown in volts vs. a standard hydrogen electrode (SHE), it can be seen that at pH levels above 9 the steel can form a passive film. This film is not formed instantaneously and will take time, about a week [6], to form as the cement reacts and the concrete cures. Unfortunately, the passive film will become unstable and breakdown in the presence of Cl<sup>-</sup> ions or with a drop in pH. If the concentration of Cl<sup>-</sup> and/or the drop in pH is significant enough, the corrosion mechanism will transform from passive to active corrosion. Material loss due to active corrosion is several orders of magnitude higher than passive corrosion, from about 0.1-1.0 μm/year to several mm/year for passive and active corrosion, respectively [6].

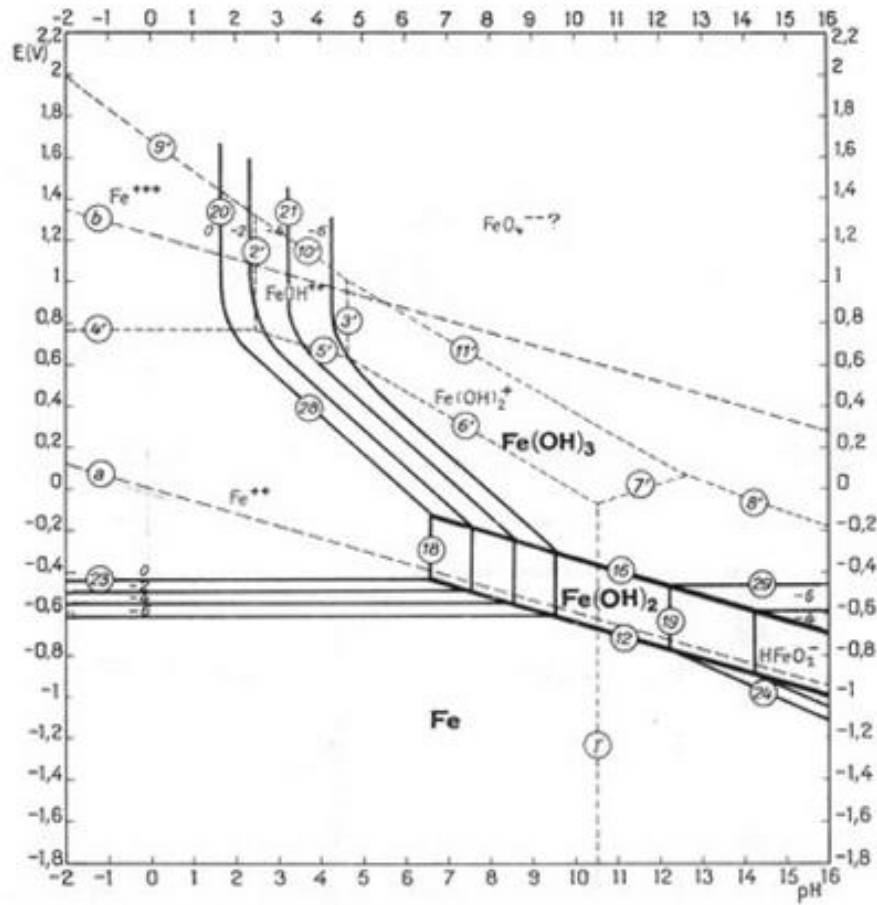


Figure 2-1: Potential (SHE) vs. pH diagram of iron [11]

Once corrosion initiates, electrons are “freed” from the metal. These electrons cannot remain unbound and will flow from the anode to the cathode. This results in a localized corrosion cell. There are four primary cathodic reactions that can occur during the oxidation of a metal, shown below in Table 2-1. Concrete is quite basic and the typical reaction is the reduction of dissolved oxygen, equation 2-3.

**Table 2-1: Cathodic half-cell reactions**

pH	Region of E-pH diagram in Figure 2-1	Cathodic reaction	
<7 (acid)	Between a and b line (water stability)	$O_2 + 4H^+ + 4e^- \rightarrow 2H_2O$	<b>2-1</b>
	Below the a line (hydrogen gas stability)	$2H^+ + 2e^- \rightarrow H_2$	<b>2-2</b>
>7 (base)	Between a and b line (water stability)	$O_2 + 2H_2O + 4e^- \rightarrow 4(OH)^-$	<b>2-3</b>
	Below the a line (hydrogen gas stability)	$2H_2O + 2e^- \rightarrow H_2 + 2(OH)^-$	<b>2-4</b>

Note: above the b line is the oxygen stability region. Cathodic half-cell reactions do exist here; however, these typically do not occur naturally and will not be considered in this thesis.

The exact mechanism of  $Cl^-$  attack is not fully understood. However, two prominent theories exist. The first is that the  $Cl^-$  ions react with the passive film and become incorporated into the compound. This results in a reduction in resistance and allows the steel to react more freely. This occurs locally and will generate an area that is more anodic than the surrounding. This potential difference will act as the driving force and perpetuate the localized corrosion. The second is that the  $Cl^-$  reacts with the steel in place of the  $OH^-$  ions and forms a soluble compound rather than a passive film whilst also not allowing the formation of a passive film. This compound then dissolves once it has been removed from the steel's surface. The previously bound  $Cl^-$  ion is now free to continue reacting with the remaining steel [6].

Once the iron ions are removed from the steel, they are free to react with the surrounding environment (typically  $OH^-$  ions and dissolved oxygen) to form a variety of compounds. All of these compounds are expansive as illustrated in Figure 2-2. Jaffer [7] found the largest steel corrosion product found in concrete when exposed to chlorides is ferric hydroxide,  $Fe(OH)_3$ , that has a specific volume four times larger than iron. As these corrosion products form, they exert an expansive force on the concrete. This is what damages concrete structures; the concrete delaminates and de-bonds from the bars. The resulting cracks help aid the ingress of the chloride species, oxygen and acidic carbon dioxide making corrosion self perpetuating.

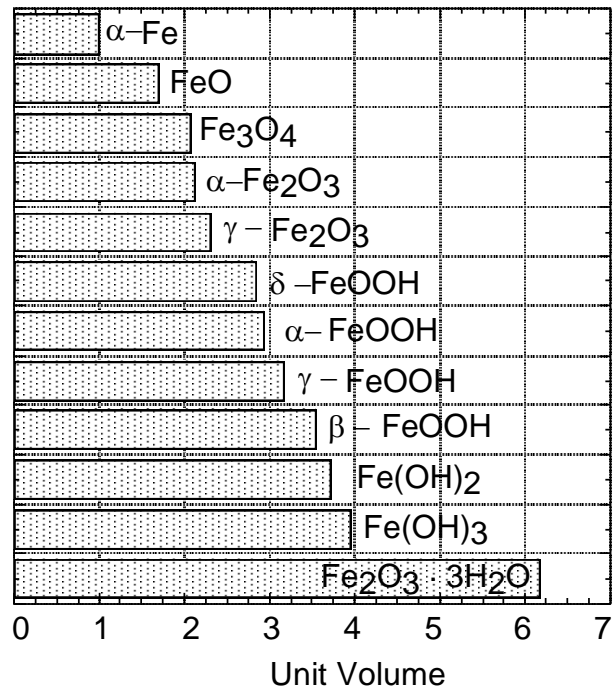
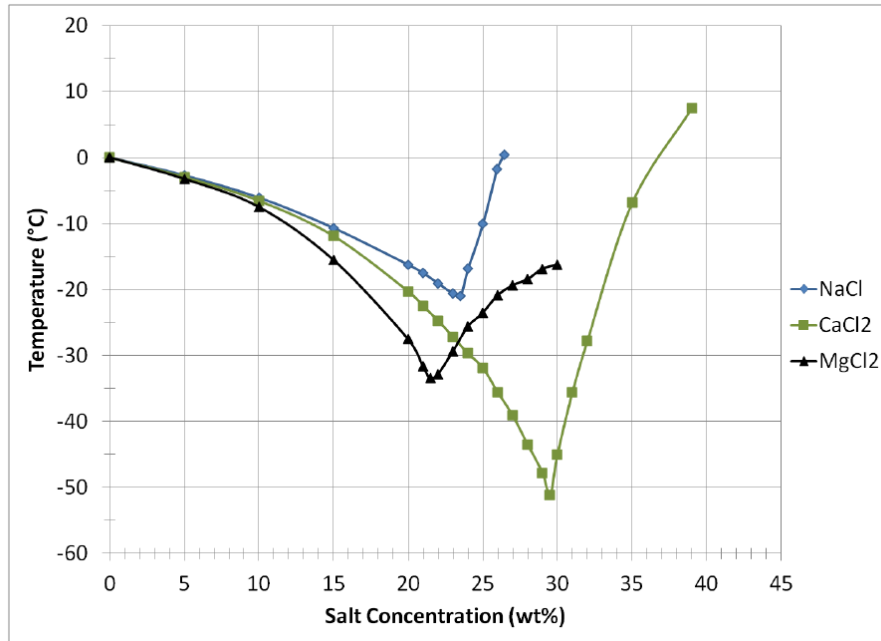


Figure 2-2: Specific volume of the corrosion products from iron [12]

### 2.1.1 Salt Chemistry

Although this research focuses on the effects of the various anti-icing salts, their effectiveness as anti-icing agents should not go without mention. One such property is the snow melting ability of each anti-icing salt. Below in Figure 2-3 the phase diagrams around the eutectic point for all of the salt solutions is shown. It is clear that CaCl<sub>2</sub>, with a eutectic temperature around -51°C has the potential for melting ice to much lower temperatures than MgCl<sub>2</sub> and NaCl with a eutectic temperature of -34°C and -21°C, respectively. At a glance one would expect CaCl<sub>2</sub> to be the obvious choice for anti-icing; however, at temperatures well below zero, the traction between vehicle tires and ice is sufficient for driving. Furthermore, phase diagrams only reveal the thermodynamic equilibrium phases at each temperature and provide no information about the kinetics of the reaction. Likewise, if a eutectic mixture of NaCl were used in an environment where the temperature dipped below -21°C, ice could form. This ice would likely not provide adequate traction that may have been present had the melting point not been suppressed by the application of the NaCl.



**Figure 2-3: Liquidus lines of NaCl, CaCl<sub>2</sub> and MgCl<sub>2</sub> [13] [14]**

With regards to the kinetics of salts melting ice, Fay et al. [15] completed research comparing a wide variety of anti-icing media and were primarily focused on comparing salt based de-icers with acetates, formates and other agricultural based products. Figure 2-4 below shows the results of Fay et al. of the various anti-icing agents' ability to melt snow at 5°C. From this it is apparent that CaCl<sub>2</sub> and MgCl<sub>2</sub> are the best choice for rapidly melting ice, where NaCl is more capable of melting larger amounts of ice over longer durations. It is important to note that these are solid salt crystals and that the MgCl<sub>2</sub> solution performed the worst in terms of its ability to melt ice. However, Fay et al. [15] pointed out that the MgCl<sub>2</sub> solution was excellent at preventing the formation of ice. Overall their report showed that, in terms of damage to infrastructure and negative environmental impact, chloride based anti-icing agents performed least favourably.

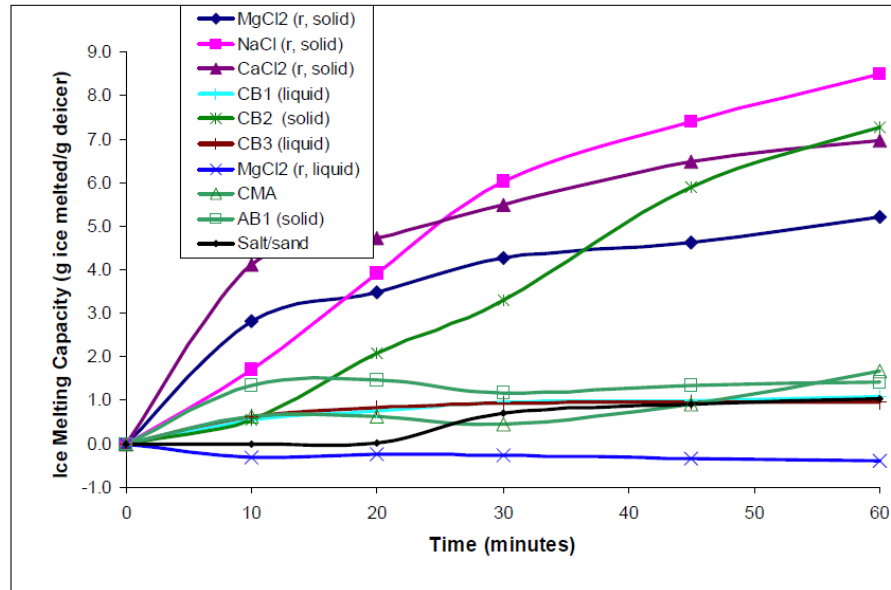


Figure 2-4: Ice melting capacity of de-icers measured at -5°C for reagent grade chlorides, chloride-based (CB), CMA, and ag-based (AB) de-icers. De-icers not listed as reagent grade are commercially available produces. The salt/sand blend is 10% salt by weight [15].

### 2.1.2 Chloride Content of Cement Pore Solution

Synthetic pore solution is chemically equivalent to the environment found inside of concrete there are a few advantage using synthetic pore solution over concrete in corrosion testing: (i) much more control over the chemistry is afforded in synthetic pore solution than in concrete, (ii) it is possible to visually inspect the bars through the life of the test and (iii) there is no waiting time for diffusion in synthetic pore as it can be mixed. There are some disadvantages as well, such as the lack of crevices, the possible reaction that may occur with aggregates, and relating the results gathered from synthetic pore solution testing to field data. Several recipes for mixture design have been proposed, the mixture used in this thesis is that proposed by Marcotte shown in Table 2-2.

Table 2-2: Synthetic pore solution composition [16]

Compound	Quantity [g]
Na(OH)	12.8
K(OH)	44.9
CaSO <sub>4</sub> •2H <sub>2</sub> O	1.38
Ca(OH) <sub>2</sub> *	5.71
H <sub>2</sub> O	2430

\*Note: Excess amount

To relate the chloride content in pore solution to chloride content in concrete and cement paste Anders and Bergsma [17] cast cement paste samples with different NaCl contents and expressed and analyzed the pore solution; the results are shown in Figure 2-5.

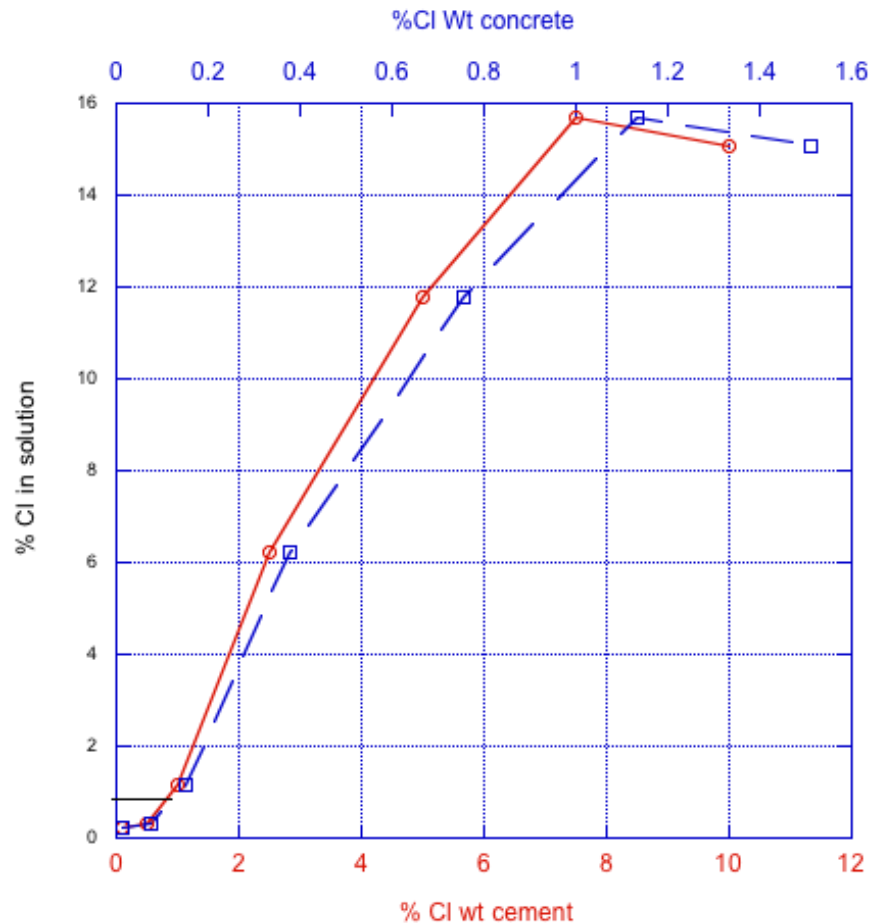


Figure 2-5: Relation between chloride content in concrete and cement to pore solutions [17]

### 2.1.3 Effects of Salt on Steel in Concrete

As mentioned previously, the ability of carbon steel to form a protective passive layer in concrete makes it an excellent candidate for concrete reinforcement. However, in the presence of chlorides or if the pH of the concrete drops, the bars are no longer capable of forming that protective film. When comparing different anti-icing agents the primary concern is with how the cations (a) influence the ability of the  $\text{Cl}^-$  ions to penetrate the concrete and (b) affect the pH and conductivity of the concrete.

The former is a combination of diffusion rates and of the interaction and damage they cause with the surrounding concrete. If the damage to the concrete is significant and/or the chemistry of the cement and pore solution is modified, so too will the diffusion rates. Furthermore, if the damage is severe enough to cause significant cracking the diffusional driving force can be replaced by capillary action which is much more rapid. Hansson et al. [18] found that “neither the  $\text{Cl}^-$  content alone nor the  $\text{Cl}^-$  content of the pore solution alone can be used as a measure of the corrosion rate...[which] is controlled by other factors, such as resistivity, porosity, pH and availability of oxygen”.

The pH and conductivity of the concrete is dependent on how the cation interacts with the surrounding cement. Typically the salts will not drop the pH below the region where it is impossible to form a passive layer; however, at lower pH levels it is more difficult for the steel to form a passive film [11]. This combined with the presence of  $\text{Cl}^-$  all but guarantees the onset of corrosion.

#### ***2.1.4 Effects of Salt on Concrete Durability***

It is well established that concrete is affected by de-icing agents by a variety of mechanisms including concrete strength, scaling, aggregate attack, etc. Attempts at tabulating the severity of damage induced in concrete by these salts has been extensively researched [13] [19]- [20] with the results being somewhat agreed upon. Furthermore, the mechanism of degradation is not fully agreed upon and ranges from the formation of complex salts to the replacement and leaching of  $\text{Ca}(\text{OH})_2$  in the cement paste. This section reviews some of the studies and their findings with regards to the degradation of OPC-based concretes.

Cremasco [13] conducted a study comparing the effects of the same anti-icing agents described in Table 1-1 on the mechanical properties of concrete. He used the same anti-icing solutions and concrete mix-design as used in the present study. Concrete prisms were exposed to 400 freezing and thawing cycles ranging from  $-18^\circ\text{C}$  to  $4^\circ\text{C}$ . The prisms were divided into five groups. Each group was exposed to the solutions at 1/3 concentration and a control group (exposed to water). He found that the prisms exposed to  $\text{CaCl}_2$ , multi  $\text{Cl}^-$  and  $\text{NaCl}$  had worst damage as a result of scaling than the prisms exposed to water. The  $\text{MgCl}_2$  causing less damage than the other anti-icing agents from the freeze thaw tests correlates with the findings of McDonald and Perenchio [19]. It should be noted that, during Cremasco’s tests, all of the solutions with the exception of  $\text{MgCl}_2$  solidified. He speculated the

reason for this was due to the impurities found in the solution or that exposure time to the low temperatures was not sufficient enough to allow the solidification transformation.

Lee et al. [21] completed a similar study examined concrete exposed to wet/dry and freeze/thaw cycles exposed to NaCl, CaCl<sub>2</sub>, MgCl<sub>2</sub>, calcium magnesium acetate (CMA) of 5 different Ca/Mg ratios, Ca-acetate and Mg-acetate. Cores from existing Iowa structures were cut to 3 cm x 1.5 cm x 1.5 cm blocks. The wet/dry cycles consisted of repeated cycles of exposing the concrete to the solution at 58°C for 132 hrs, air drying at 58°C for 24 hrs and cooled to 25°C. The freeze thaw cycles included exposing the concrete to the solution at 58°C for 132 hrs, air drying at 25°C, further cooled to -4°C and held for 24 hrs, air warmed to 25°C after which the specimens are returned to the solution and the cycles repeated. Lee et al. found that the solutions containing Mg caused severe damage to the concrete paste by forming brucite (Mg(OH)<sub>2</sub>) and non-cementitious magnesium silicate hydrate (M-S-H) and that NaCl was the least damaging to the cement paste and aggregates. This test may have proven to be somewhat biased for CaCl<sub>2</sub> as Chatterji [22] found that deterioration of concrete by CaCl<sub>2</sub> was primarily due to the formation of complex salts, that do not form at temperatures greater than 40°C. This suggests that during the warm exposure cycles of 58°C, the complex salts that induce damage on concrete would not form until the cooling cycles leaving more opportunity for the Mg containing solutions to cause more damage.

CaCl<sub>2</sub> is known to attack and crack concrete [23] [24], which in turn results in the bars being exposed to the solution in shorter periods of time. Chatterji found that the actual mechanism of attack below 20°C is due to the formation of complex salts containing CaCl<sub>2</sub>, Ca(OH)<sub>2</sub> and/or CaCO<sub>3</sub> at concentrations of CaCl<sub>2</sub> of 15% or higher [22] which is well below the 38% used as an anti-icing in Ontario. Chatterji exposed anhydrous and partly hydrated powders of Portland cement in various concentrations of CaCl<sub>2</sub> and at 40°C, 20°C and 5°C [22]. Chatterji also found that the presence of CaCl<sub>2</sub> leaches out Ca(OH)<sub>2</sub> at all temperatures [22]. This could result in the decrease in pH of the concrete, which like the MgCl<sub>2</sub> solution would result in the degradation of the bar's passive film.

McDonald and Perenchio [19] found in a test exposing three concrete mixes to 4% salt solutions created using the following salts: (i) 80% rock salt, 20% CaCl<sub>2</sub>; (ii) 100% rock salt; (iii) a proprietary salt (composition shown below in Table 2-3); (iv) 69% rock salt, 30% KCl, 1% CaCl<sub>2</sub> and (v) 50% rock salt, 50% KCl. The specimens included direct exposure via a ponding well and underwent 100 freezing and

thawing cycles. They found that the solution made using the proprietary salt caused the least amount of damage for 2 of the 3 concrete mixes. McDonald and Perenchio suspected that the reason for this could be attributed to the presence of Mg [19]. The reverse relationship was found when high strength concrete was exposed to the proprietary salt solution. It is important to note that the proprietary salt is composed mainly of chloride and sodium and in comparison to the solutions used in this study; the levels of magnesium are quite low even when compared to the multi-chloride solution which contained about 39 g/l  $Mg^{2+}$  ( $\approx 3.9\%$  wet basis).

**Table 2-3: Constituents of proprietary salt tested by McDonald and Perenchio [19]**

Constituent	Percent by weight on dry basis
Sodium	34.09
Chloride	53.97
Potassium	0.02
Magnesium	1.38
Calcium	0.30
Sulfate	1.07

Another part of Cremasco's [13] study included five beams with embedded strain gauges and a cast-in ponding well. Again he exposed the beams to the four salt solutions and one control and measured the resulting strain over time. He found that the  $MgCl_2$ ,  $CaCl_2$  and multi solutions caused the most strain in the specimens when compared with the NaCl and the water exposed specimens. This correlates well with his freeze/thaw data with the exception of the  $MgCl_2$  solution.

Darwin et al. [25] tested the effects of distilled water, air, various concentrations of NaCl,  $CaCl_2$ ,  $MgCl_2$  and CMA solutions on the modulus of elasticity of concrete. The concrete was exposed to weekly wetting and drying cycles of concentrations ranging from 6.04 molal ion concentration, equivalent in ion concentration to a 15% solution of NaCl, or a 1.06 molal ion concentration, equivalent in ion concentration to a 3% solution of NaCl, for periods of up to 95 weeks. They found that NaCl in low and

high concentration showed a relatively small effect on the concrete although a greater effect being observed at higher concentrations.  $\text{CaCl}_2$  had a low impact at low concentrations but a significant impact at higher concentrations.  $\text{MgCl}_2$  and CMA caused measureable damage at low concentrations and like  $\text{CaCl}_2$  caused considerable damage at higher concentrations.

Poursaee et al. [20] compared the effects of  $\text{NaCl}$ ,  $\text{MgCl}_2$  and  $\text{CaCl}_2$  in solution by observing the macro- and micro-cell corrosion of embedded steel in OPC mortar. They varied the concentration between 3 to 30% and found extensive damage to the concrete exposed to  $\text{CaCl}_2$ , less damage to the concrete exposed to  $\text{MgCl}_2$  and little to no damage to concrete exposed to  $\text{NaCl}$ , as shown below in Figure 2-6. The damage observed in the  $\text{CaCl}_2$  specimens is also the likely cause of the high macro-cell corrosion rates Figure 2-11. This damage would allow the ions to enter the concrete directly. Furthermore, they found that the corrosion rates from  $\text{NaCl}$  and  $\text{MgCl}_2$  at low concentrations were comparable but once the concentrations were increased, the micro-cell corrosion of the specimens exposed to  $\text{MgCl}_2$  increased significantly.

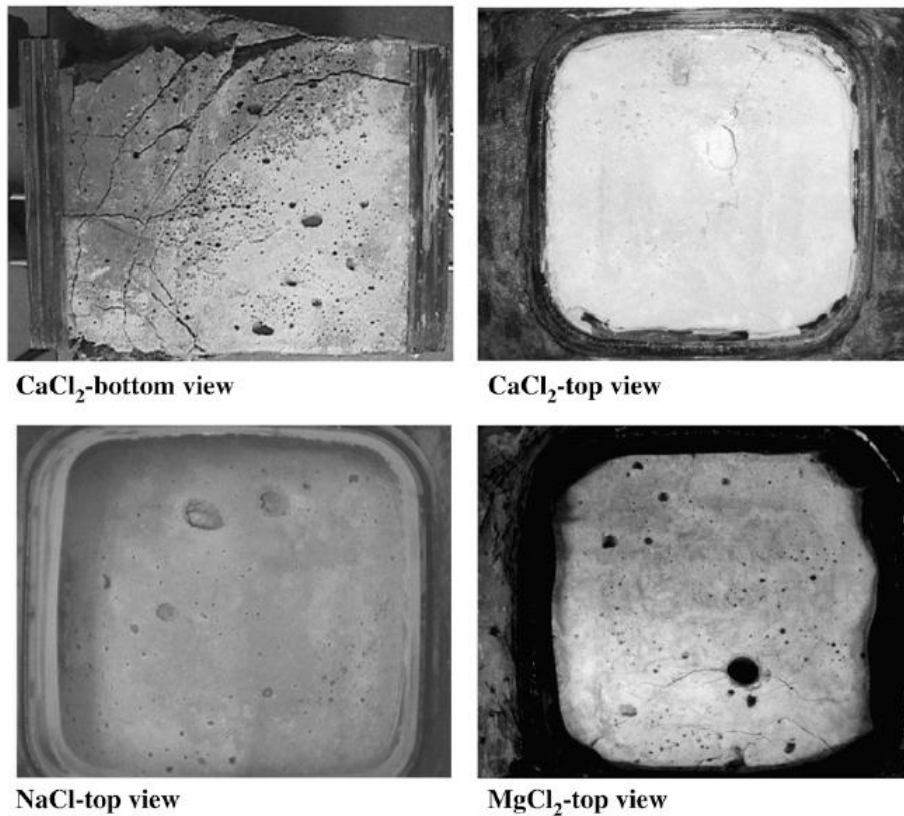


**Figure 2-6: Surface of specimens, 130 weeks after exposure to different salt solutions [20]**

### 2.1.5 Diffusion of Salt in Concrete

Cremasco [13] also conducted testing of diffusion of the various salts into the concrete. He found that NaCl had the fastest initial diffusion when compared to the other salts. However, at longer times exposed to the CaCl<sub>2</sub>, MgCl<sub>2</sub> and multi solutions had higher concentration than that exposed to the NaCl solution. This is shown below in Figure 2-7. Cremasco suggest that initially the NaCl solution could cause more damage than the other solutions to the concrete and reinforcing steel but in the long-run would be surpassed by the other anti-icing solutions. The vertical concrete cover required for reinforcing steel according to CSA S6-06 Section 8.11.2.2 Table 8.5 is 40 mm, this is four times greater than the depth measured by Cremasco. This would likely result in the bar being exposed to the multi chloride mixture first as it has the highest concentration at 10 mm and 59 weeks exposure.

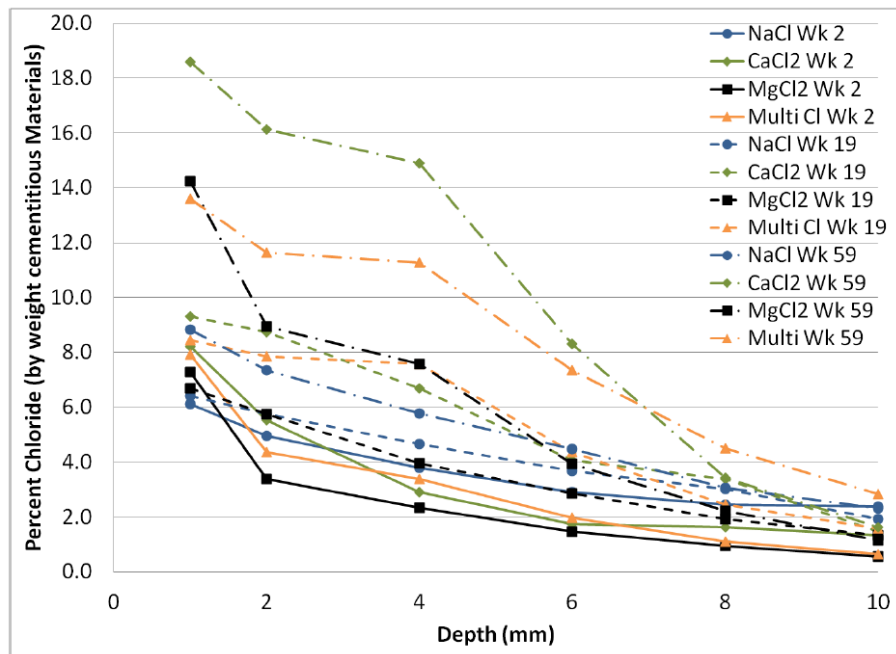


**Figure 2-7: Chloride penetration into concrete from one direction measured after 2, 19 and 59 weeks soaking by weight of cementitious materials [13]**

Mussato et al. [26] report similar findings for diffusion coefficients of the various salts in OPC mortar, slag blended cement mortar and OPC paste shown in Table 2-4. It is interesting to note that the difference between the diffusion coefficients in slag blended cement is significantly lower than the other cements tested, which would give explanation as to why Cremasco's data, also on slag concrete, showed very little variation between the different solutions. Furthermore, a field study of chloride diffusion showed that diffusion rates were twice as high in areas where both MgCl<sub>2</sub> and NaCl were

used compared to areas where only NaCl was used. A study by Kondo [27] agrees with Mussato and Cremasco’s findings, suggesting MgCl<sub>2</sub> has the highest diffusion rates, CaCl<sub>2</sub> less so, and the lowest for NaCl. Combining this information with Cremasco’s findings suggests that the combined effects of the various anti-icing solutions have a significant impact on diffusion rates and thus potentially an effect on onset times of active corrosion.

**Table 2-4: Chloride diffusion coefficients for different salts [26]**

Salt Type	Effective Diffusion Coefficient (m <sup>2</sup> /s) x 10 <sup>-12</sup>		
	OPC Mortar	Slag Blended Cement Mortar	OPC Paste
NaCl	9.1	1.4	6.6
CaCl <sub>2</sub>	22.9	1.5	9.9
MgCl <sub>2</sub>	29.0	1.8	20.8

Hansson et al. [18] found that CaCl<sub>2</sub> created a more open pore structure in the concrete, whereas NaCl and KCl also increased the pore structure but to a lesser extent. This would explain the higher diffusion rates found in CaCl<sub>2</sub> when compared to NaCl. It can also be speculated that, as the MgCl<sub>2</sub> reacts with the calcium-silicate-hydrate (C-S-H) and Ca(OH)<sub>2</sub> and produces M-S-H, Mg(OH)<sub>2</sub> and CaCl<sub>2</sub>, a similar mechanism would occur, which explains the more severe diffusion observed in MgCl<sub>2</sub>.

On the other hand, Poursaee et al. [20] found MgCl<sub>2</sub> can form brucite, solid Mg(OH)<sub>2</sub>. Brucite has the ability to block the pores on the concrete surface, which inhibits further ingress of the MgCl<sub>2</sub> and thus Cl<sup>-</sup> species. As a result, there is a subsequent reduction in corrosion rates of the steel.

### **2.1.6 Effects of Salt on pH**

It has been found that both MgCl<sub>2</sub> and CaCl<sub>2</sub> can lower the pH of concrete pore solution whereas NaCl can raise the pH [28]. This combined with the diffusion rates suggests that steel corrosion will likely occur first when exposed to MgCl<sub>2</sub> and CaCl<sub>2</sub>. The explanation for the drop in pH is explained by the chemical reactions between the concrete and the salt. The Mg in MgCl<sub>2</sub> replaces the Ca in the C-S-H and in Ca(OH)<sub>2</sub> to form M-S-H and Mg(OH)<sub>2</sub> respectively [29] [30]. The pH of saturated Mg(OH)<sub>2</sub> (pH≈9.5) is significantly lower than Ca(OH)<sub>2</sub> (pH≈12.7). Furthermore, M-S-H is not cementitious and will reduce the strength of the concrete and eventually result in cracking [23] [30]. Similarly the CaCl<sub>2</sub> also reduces the pH of concrete, though this is not as severely as in the case with MgCl<sub>2</sub> and the addition of NaCl or KCl resulted in an increase in pH [18]. The decrease in pH due to CaCl<sub>2</sub> exposure

and the increase in pH due to NaCl exposure were also observed by Xu et al. [31]. This is a result of NaCl reacting with the  $\text{Ca(OH)}_2$  to form  $\text{Na(OH)}$ .  $\text{Na(OH)}$  has a much higher solubility than  $\text{Ca(OH)}_2$  and as a result a higher pH. The reverse reaction is true with the addition of  $\text{CaCl}_2$  [18].

Effects of  $\text{Mg}^{+2}$  ion solubility and pH found by Brown and Doerr [32] are shown in Figure 2-8. The relations between pH and  $\text{Mg}^{+2}$  solubility was found to be that as the pH decreases, the solubility and diffusivity of  $\text{Mg}^{+2}$  into the concrete increases. This would result in the pH near the bar dropping which reduces the steels ability to form a passive film. In addition to this, the solubility of  $\text{Mg}^{+2}$  increases allowing high concentrations of the now unbound  $\text{Cl}^-$  ions to attack the steel and break down the already compromised passive film.

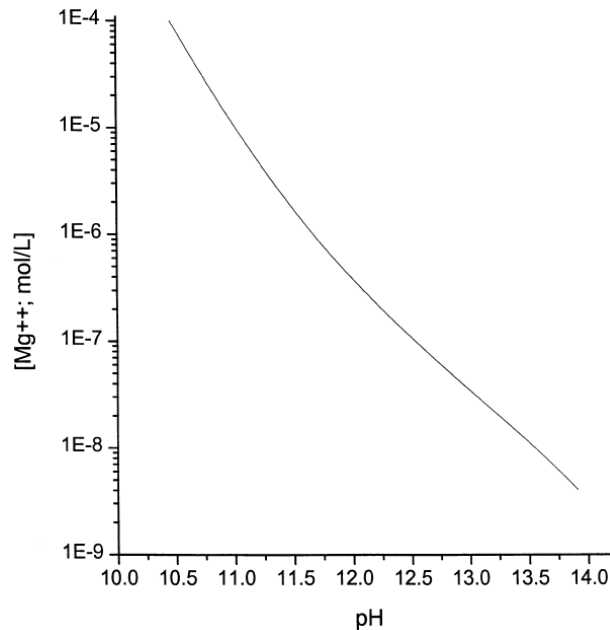


**Figure 2-8: The variation in the molar solubility of magnesium hydroxide as a function of pH (in the absence of species other than magnesium and hydroxyl) [32].**

A study from Levelton Engineering Ltd. by Mussato et al. [26] suggested that the higher diffusion rates associated with  $\text{MgCl}_2$  would result in reduced [active] corrosion initiation times; also the  $\text{MgCl}_2$  would react with the cement resulting in damage to the concrete. Although they mentioned that data in this field are limited, they concluded that the use of  $\text{MgCl}_2$ , when compared to NaCl, would reduce the life expectancy of a structure by 10-20 years. It is also suggested that the use of NaCl as a pre-wetting agent in milder climates experienced in BC would be sufficient while colder climates  $\text{MgCl}_2$  would be more effective and at significantly colder climates the use of sand would be more appropriate.

## 2.2 Electrochemical Corrosion

The corrosion cell that is occurring at the surface of the reinforcing steel can occur in two primary fashions: macro-cell and micro-cell corrosion. In the first instance a macro-cell is essentially a galvanic corrosion cell. In galvanic corrosion three criterion must be met (i) a potential difference between two dissimilar metals, (ii) physically connected for the flow of electrons and (iii) an electrolytic medium for the flow of ions.

As chlorides migrate through the surface of the concrete, the top layer of reinforcing steel is attacked and the passive film breaks down. Once this occurs, the potential of the top reinforcing steel adjusts and becomes more anodic while the lower layer's potential remains the same. This is analogous to the two dissimilar metals found in galvanic corrosion. This change in potential creates a driving force for both the  $\text{OH}^-$  ions to migrate through the concrete and for the electrons to travel through the electrical connections (vertical rebar, tie wires, expansion joints, etc.). This ultimately results in macro-cell corrosion, Figure 2-9 (a).

Micro-cell corrosion, on the other hand, is a result of local geometry and initiation points for the breakdown of the passive film on the same bar shown schematically in Figure 2-9 (b). This type of corrosion is typically higher than macro-cell corrosion as both  $\text{OH}^-$  ions and electrons have far less distance to travel and fewer obstacles to overcome.

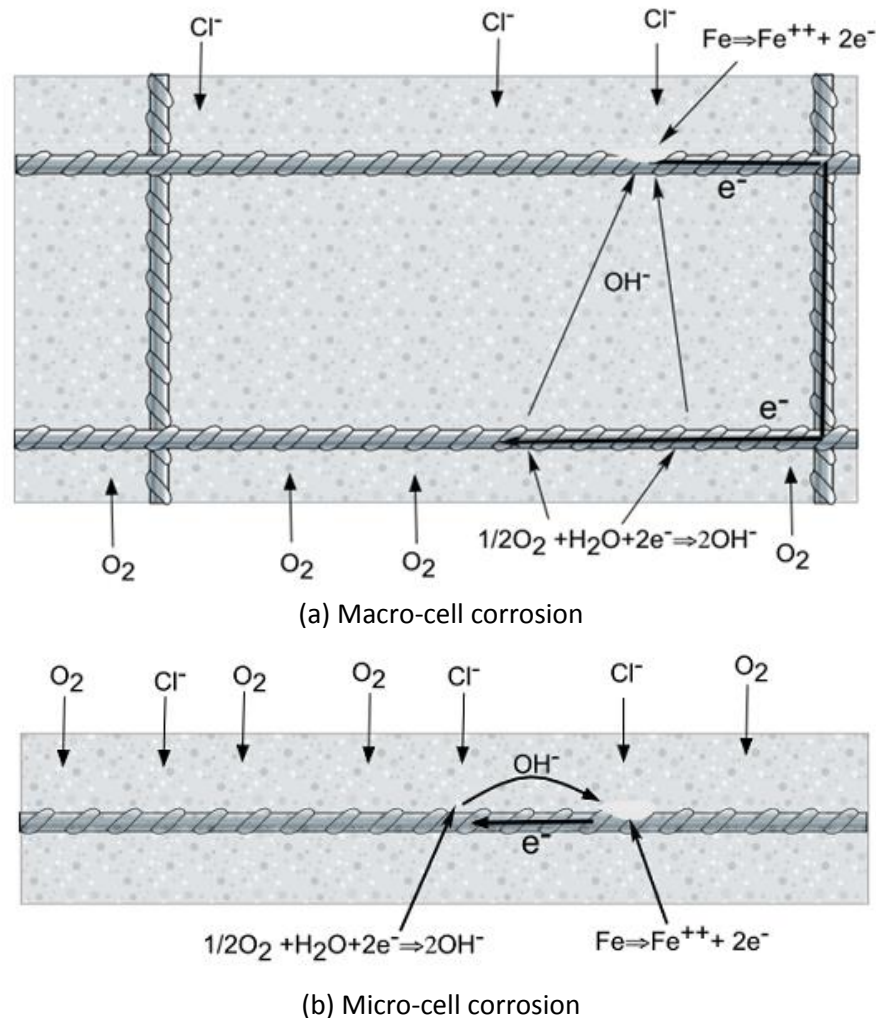


**Figure 2-9: Schematic of (a) micro-cell corrosion and (b) macro-cell corrosion [6]**

Typically, micro-cell corrosion is considered the primary mechanism of corrosion of reinforcing steel but this does vary depending on the environment present. Work completed by Hansson et al. [24] found that between ordinary Portland cement (OPC), high performance concrete (HPC) with slag and or fly ash, the HPC had significantly lower macro-cell corrosion due HPC resistance to ionic flow. These tests incorporated the ASTM G109 “Standard Test Method for Determining Effects of Chemical Admixtures on Corrosion of Embedded Steel Reinforcement in Concrete Exposed to Chloride Environments” as described in Chapter 3 Experimental Procedure. It was found that the micro-cell corrosion was always higher than the macro-cell corrosion, with the smallest difference between measurements observed in the OPC specimens shown in Figure 2-10. Although micro-cell corrosion does dominate, macro-cell corrosion can still be a significant contributor to the overall corrosion of

reinforcing steel in concrete as some of the values (especially those in OPC) begin to approach a ratio of unity between macro- and micro-cell corrosion.

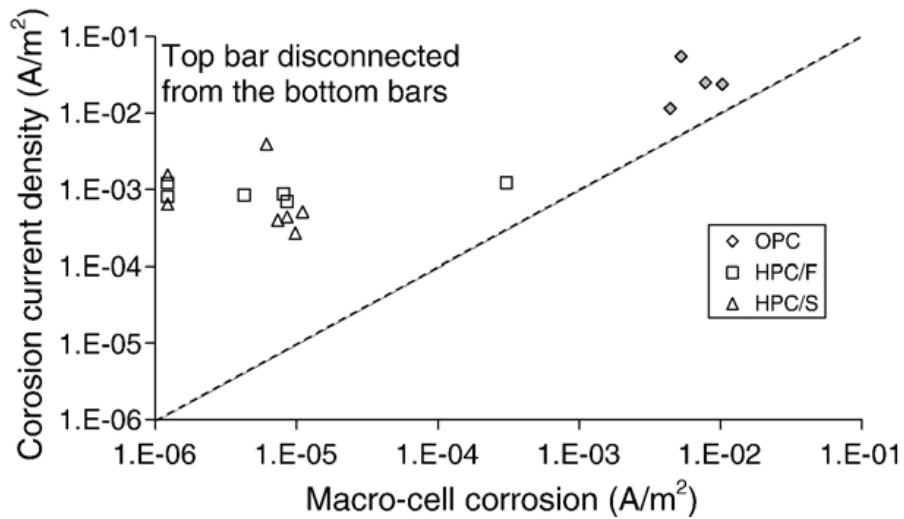


**Figure 2-10: Comparison between the macro-cell and micro-cell corrosion current densities for the steel in OPC and HPC specimens when the top bars are disconnected from the bottom bars [24]**

A similar trend was found when comparing NaCl, MgCl<sub>2</sub> and CaCl<sub>2</sub> in mortar by Poursaei et al. as shown below in Figure 2-11. Note in this figure the abscissa and ordinate axis have switch from the previous figure, Figure 2-10. This figure does show several points with significantly higher macro-cell corrosion current densities.

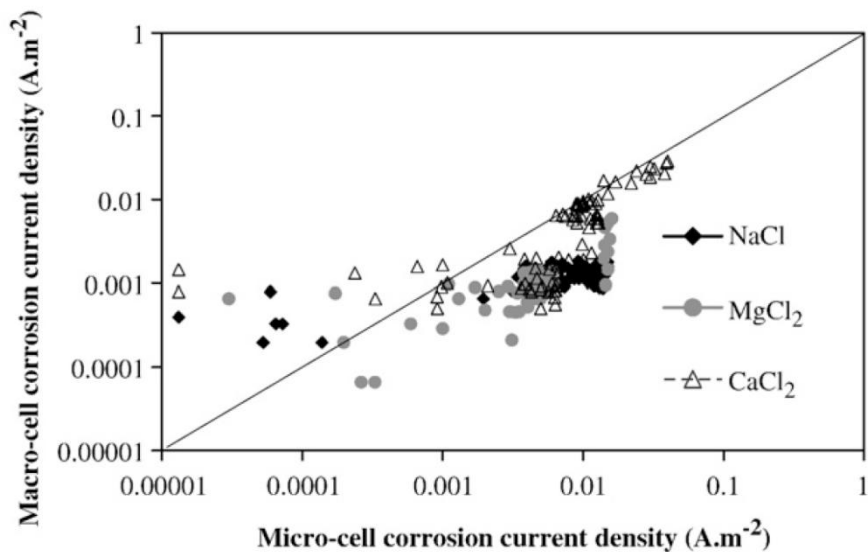


**Figure 2-11: Comparison between macro- and micro-cell corrosion current densities [20]**

### 2.2.1 Macro-cell Corrosion

Andrade et al. states that the galvanic current is not a perfect measurement of determining corrosion because, without a deaerated environment, the anode can still form micro-cells shown in Figure 2-12. Although the reduction of oxygen and water to  $\text{OH}^-$  will be slowed or eliminated in deaerated concrete, it is still possible for active corrosion to occur by the reduction of water to hydrogen gas and  $\text{OH}^-$  [33]. Therefore, micro-cell corrosion will always be a factor and should not be neglected.

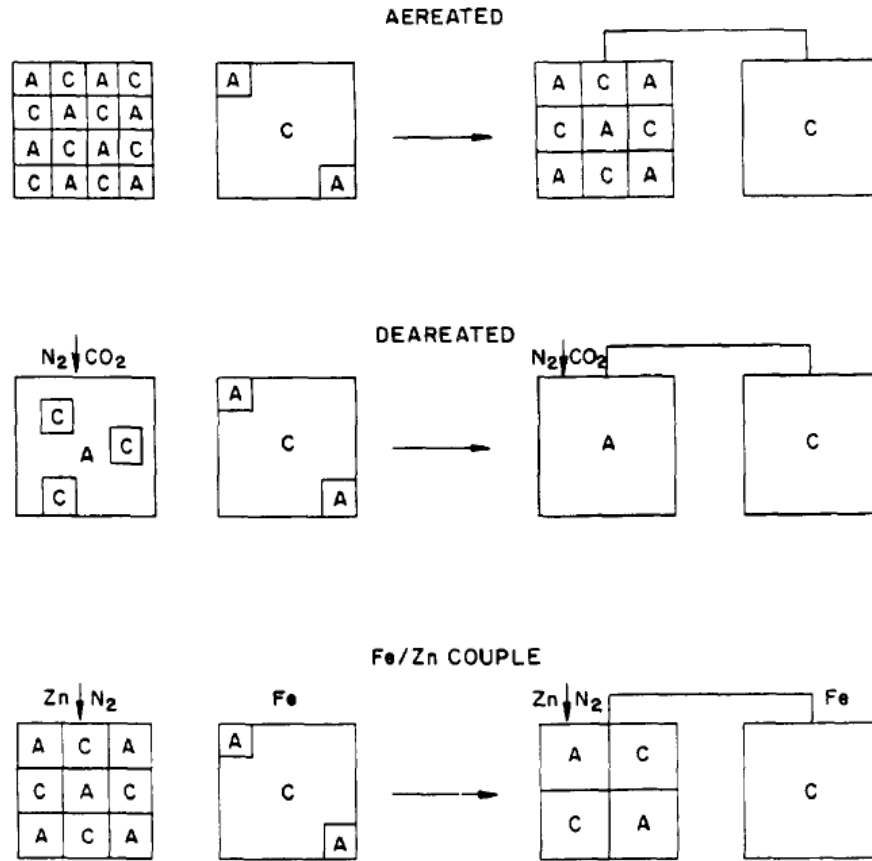
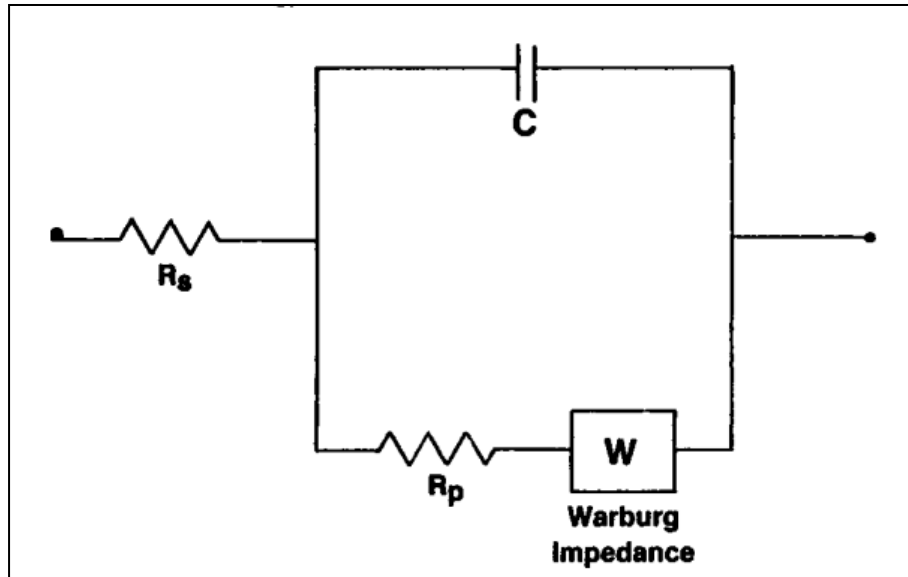


Figure 2-12: Configuration of micro-cell activity before and after forming a macro-cell by connecting to a passive metallic zone. Only in deaerated media does the galvanic current equate to the corrosion intensity in macro-cell activity [34]

### 2.2.2 Micro-cell Corrosion

The corrosion reaction can be modeled by an electrical circuit. Typically, the circuit used to emulate steel in concrete is the Randles circuit [35] as shown below in Figure 2-13.



**Figure 2-13: Randles Circuit,  $R_s$  represents the resistance of the concrete (or solution),  $C$  represents the double layer capacitance,  $R_p$  represents the polarization resistance, and  $W$  represents the specific electrochemical element of diffusion also known as a Warburg element [36].**

The resistance  $R_s$  is dependent on the medium the measurements are being taken across and the distance the electrons have to travel. For example, when testing reinforcing steel in pore solution the  $R_s$  is negligible as the synthetic pore solution is highly conductive. On the other hand, the resistance in a specimen of concrete is about four orders of magnitude higher and varies depending on the temperature and relative humidity.

The double layer capacitance occurs at the surface of any charged solid immersed in a solution of polar molecules. In the example shown below in Figure 2-14 the negatively charged surface attracts the positively charged hydrogen atoms of a water molecule. The two layers represent the two plates of a capacitor.

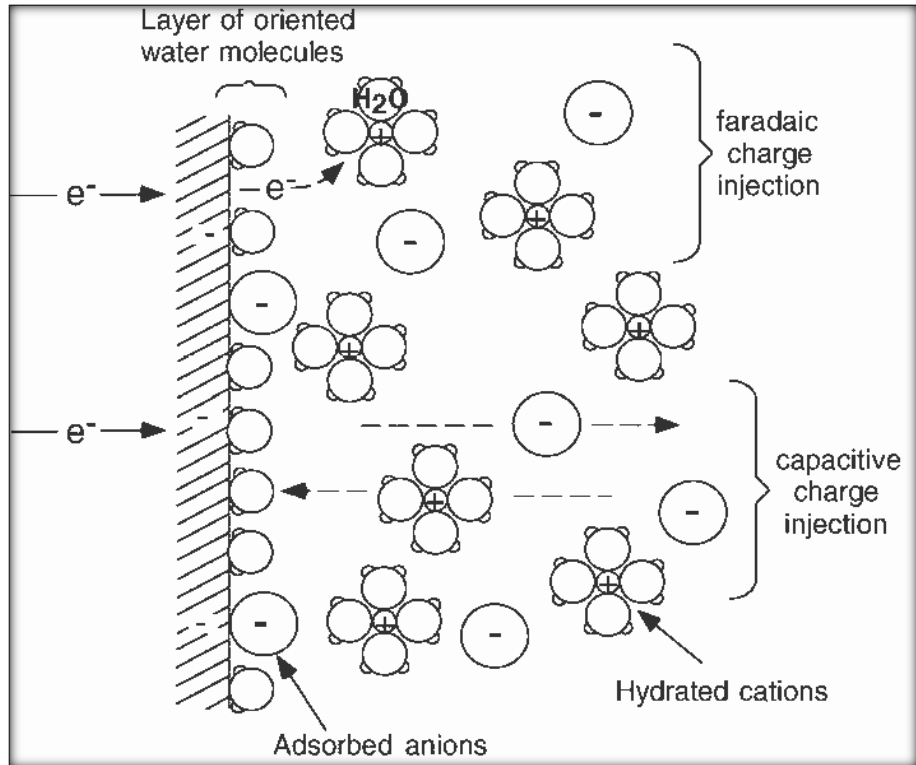


**Figure 2-14: Double layer capacitor [37]**

The Warburg impedance element,  $W$ , is used when the diffusion of atoms can limit the rate of reaction. For example, in concrete the corroding steel needs to remove iron ions away from its surface as well as have those ions react with water. The diffusion of the iron ions away from the surface and the diffusion of oxygen from the atmosphere into the concrete can limit the rate of the reaction. The Warburg impedance is frequently omitted from analysis.

The polarization resistance,  $R_p$ , is the atoms resistance to ionization. That is to say, in order for an atom to become an ion a certain amount of energy is required to strip electrons from the atom. The amount of energy is proportional to  $R_p$  which ultimately dictates the speed at which electrochemical corrosion can occur. This value will vary with both material and environment.

Stern and Geary [38] determined that at potentials close to the  $E_{corr}$  value, the relationship between  $I$  and  $E$  were linear which resulted in equation 2-5 and is represented schematically in Figure 2-15. Furthermore, Stern determined that the polarization resistance was related to  $I_{corr}$  by a constant,  $B$ , which varied between 13 and 52 mV. For steel in concrete it was found that 26 mV was used for the active state and 52 mV was used for the passive state [38]-[39] [34]. This is derived in 0 section A-4.2.

$$R_p = \left( \frac{\Delta E}{\Delta I} \right)_{\Delta E \rightarrow 0} \quad 2-5[34][40]$$

$$B = \frac{\beta_a \beta_c}{2.303(\beta_a + \beta_c)} \quad 2-6[34][40]$$

$$I_{corr} = \frac{B}{R_p} \quad 2-7[34][40]$$

Where:

$R_p$  is the polarization resistance,

$\Delta E$  is the potential difference from  $E_{corr}$ ,

$\Delta I$  is the change in current,

$\beta_a$  and  $\beta_c$  are the anodic and cathodic tafel slopes, respectively,

$B$  is the Stern-Geary constant and

$I_{corr}$  is the corrosion current.

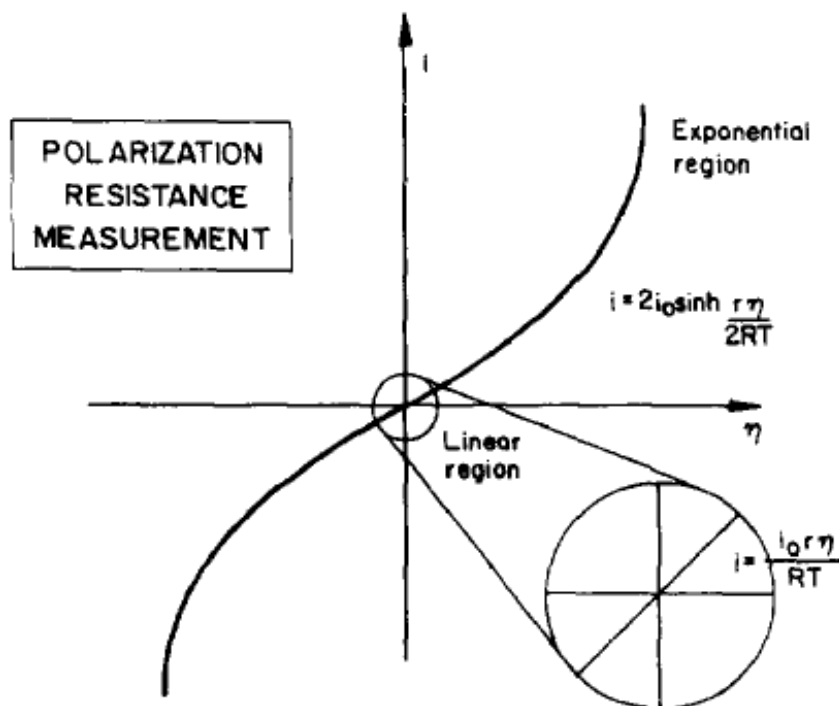


**Figure 2-15: The polarization resistance is the slope of the polarization curve (I-E) around the corrosion potential (when I changes the polarity from negative to positive) [34]**

It can be shown that the transient response of a potentiostatic (PS) linear polarization to resistance (LPR) test, the resulting curve for a single capacitor resistor pair results in equation 2-8 (full derivation shown in Appendix A: Electrochemical Analysis). From this equation it is quite apparent that the time constant for potential controlled tests are significantly more complex than the time constant for the GP test. This is further complicated when additional parallel capacitor-resistor elements are

introduced. For this reason, only the steady state values of the LPR are used with scan rates over 30s in length, see Chapter 3 Experimental Procedure for details.

$$\frac{I_0}{\Delta E_{applied}} = \frac{1}{(R_p + R_c)} + \left( \frac{R_p}{R_c(R_p + R_c)} \right) e^{\left( \frac{-(R_p + R_c)t}{C_{dl}R_pR_c} \right)} \quad \mathbf{2-8}$$

Specifically for GP technique Andrade and Alonso [34], Newton [40] and Law [41] report the transient relationship to be that shown in equation 2-9 which is further discussed in Appendix A: Electrochemical Analysis. Newton [40] and Law [41] also suggests several other models including multiple time constants (multiple resistor-capacitor circuits in parallel) as part of the model.

$$\frac{\Delta E}{\Delta I} = R_p \left( 1 - e^{\frac{-t}{R_p C_{dl}}} \right) + R_e \quad \mathbf{2-9[34][40][41]}$$

Andrade [34] goes on to report the various values for  $i_{corr}$  and their meaning towards corrosion of steel in concrete as shown in Figure 2-16 and Figure 2-17 determined using the Gecor6 field testing instrument. When compared to the values compiled by Otieno [42] in Table 2-5, the values of passivity are comparable but the rates for active corrosion are up to two orders of magnitude higher for than Andrade's values.

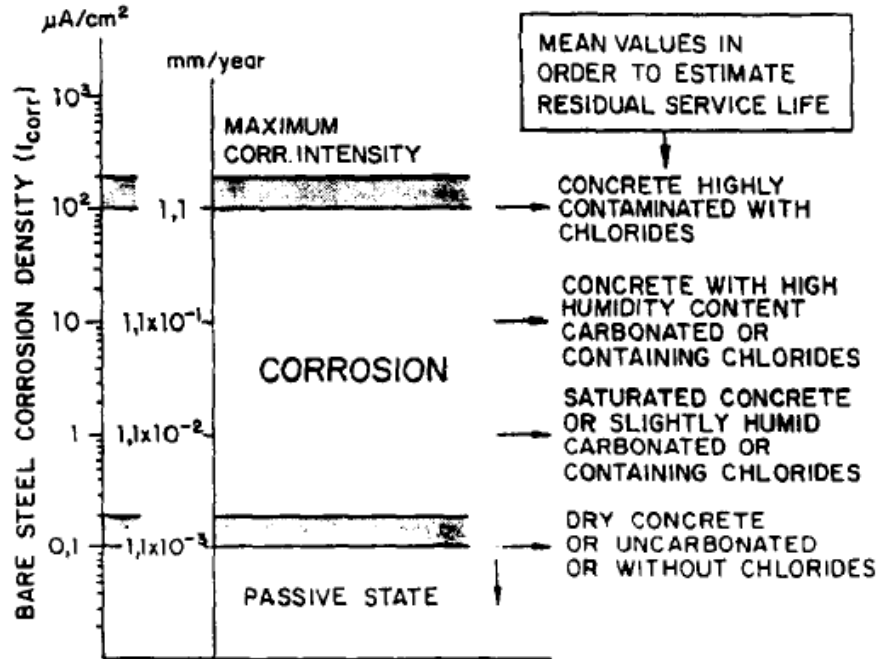


Figure 2-16: Ranges of  $I_{corr}$  values registered in the laboratory after numerous tests in many different conditions [34]

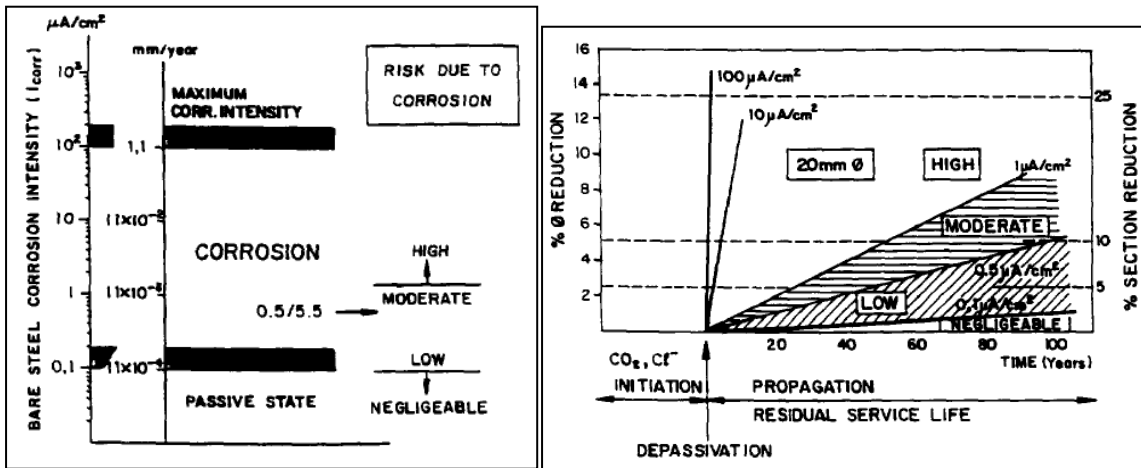


Figure 2-17: Decrease of bar diameter/bar cross-section with time as a function of  $I_{corr}$  values (propagation period). Based on the time to reach a certain cross-section loss, for corrosion levels are established: negligible, low, moderate and high [34].

**Table 2-5: Gecor6 and 3LP interpretation guidelines [43] [44] compiled by Otieno [42]**

$i_{\text{corr}}$ ( $\mu\text{A}/\text{cm}^2$ )	Gecor (corrosion state)	$i_{\text{corr}}$ ( $\mu\text{A}/\text{cm}^2$ )	3LP (expected damage)
<0.1	Passive	<0.2	No damage expected
0.1–0.5	Low corrosion	0.2–1.1	Damage expected in 10–15 years
0.5–1.0	Moderate	1.1–11	Damage expected in 2–10 years
>1.0	High corrosion	>11	Damage expected in <2 years

Note: left  $i_{\text{corr}}$  values correspond to Gecor guidelines and right  $i_{\text{corr}}$  values correspond to 3LP guidelines

### **2.2.3 Review of Electrochemical Measurement Techniques**

Several techniques are available to measure micro-cell corrosion, most of which revolve around determining the polarization resistance. These methods include, but are not limited to: potentiostatic (PS) (LPR), potentiodynamic (PD) LPR, PD cyclic polarization (CP), galvanostatic pulse (GP) LPR, galvanodynamic (GD) LPR, GD CP, electrochemical impedance spectroscopy (EIS), electrochemical noise, resistivity measurements and corrosion potential ( $E_{\text{corr}}$ ) measurements. The latter two cannot be used to determine  $R_p$ .

Potentiodynamic and galvanodynamic cyclic polarization apply a potential or current respectively that is increasing or decreasing at a constant rate. These tests have several major benefits in that they provide a large amount of information about the specimen being tested. However, the major limitations include damaging and altering the surface species of the sample. Tests can also be quite time consuming as scans rates need to be sufficiently low to ensure the system is not shocked and the changes can be properly recorded. Furthermore, scans need to cover several hundred millivolts and several decades of current, making the test take upwards of two days.

Galvanodynamic LPR and potentiodynamic LPR are similar to their cyclic polarization counter-parts but do not cover the large range of potentials and currents. The potentials and currents applied were the relationship between potential and current remain linear. The major advantage of this method is the number of data points used to determine the total resistance of the system has increase and is therefore more robust then the transient techniques (shown below). The major disadvantages are the difficulties associated with determining the concrete resistance and the longer times required for testing compared to transient techniques.

Electrochemical impedance spectroscopy applies a sinusoidal potential with an amplitude between 10-20 mV and a variety of frequencies from 1 Hz-20 kHz [34]. These tests can show the response of the system including a direct measurement of the polarization resistance and the double layer capacitor. The major short coming of this system is that steel in concrete can also be controlled by diffusion, which introduces another element in the electrical system. This can result in complex curves that are difficult to analyze.

Electrochemical noise applies very small voltages (micro volts) from the corrosion potential and records the resulting current. This technique requires very sensitive equipment and the relationship between electrochemical noise and  $I_{corr}$  values is still considered uncertain [34].

Galvanostatic pulse LPR and potentiostatic LPR are among the most widely used. The steady state results can help determine  $R_p$ . The resistance of the concrete can also be corrected for using IR compensation techniques. Using the transient response, many of the properties found using EIS can be determined with the use of curve fitting. Esmailpoursaee [45] found that the LPR technique provided the most accurate results for determining values of  $i_{corr}$  where EIS and GP techniques are most suitable for determining  $R_c$ . Law [41] somewhat disagrees with this assessment finding that LPR measurements are somewhat lower than the GP measurements. This was about 2.5 times lower for active corrosion which is considered reasonable but concludes that for actively corroding steel there may be time constants present when time intervals of less than 30 s are used which can result in significant errors when using the LPR method.

## **2.3 Corrosion Resistant Steels Outside of Concrete**

One of the other concerns of the MTO is corrosion with regards to exposed steel. Initially the scope of this testing was to expose weathering steel and plain carbon steel directly to the salt solutions using SAE J2334 immersion testing. However, the size of the chamber was sufficiently large to incorporate more specimens. As a result, a variety of stainless steel grades, galvanized steel and black steel were also included in the test. This section outlines the materials tested and discusses their associated advantages, disadvantages and typical use.

### ***2.3.1 Stainless Steel***

A significantly more robust option for reinforcement is stainless steel. In the atmosphere stainless steel forms a protective passive coating of  $\text{Cr}_2\text{O}_3$ . In high pH environments (like those found in concrete) the mechanisms of corrosion protection are not well understood, but it is known to provide a significant improvement over black steel (Grades 304 and 316 are 800 to 1500 times more corrosion resistant than regular black steel [46]) several studies are underway to help determine the corrosion resistant mechanisms of stainless steel in concrete in Canada, Italy, Spain and the United States of America. One such study conducted by Bergsma and Hansson consisted of exposing various grades of stainless steels to synthetic pore solution (a solution chemically equivalent to that in concrete) and utilized Raman spectroscopy to determine the passive films. It was found that at potentials more anodic than -100 mV vs. a Saturated Calomel Electrode (SCE) the air-formed  $\text{Cr}_2\text{O}_3$  is not stable and instead  $\text{CrO}_3$  and mixed spinels form. Furthermore, stainless steels with Mn exhibited Raman peaks associated with manganese spinels suggesting that it is not chromium based compounds protecting the steel [47].

The obvious disadvantage to stainless steel is the higher cost, being up to five times that of black steel [6]. This is due to the large amount of alloying elements required to provide the higher corrosion resistance. The conventional stainless steels, UNS31653 and UNS32205 contain significant amounts of both Ni and Mo. More recently, development of lower cost alloys replaces some of the Ni and Mo with lower cost Mn [47]. Long term studies of these stainless steels in concrete and the effects of their exposure to chlorides are being conducted in a number of research labs [47]. It is predicted that these steels will outperform black steel and will fulfill the requirements of the current building code to provide the 75 year life expectancy of bridge construction [48][49] [6].

In addition to lowering the price of stainless steels by using less costly alloying elements, further construction savings can be made by strategic placement of stainless. Utilizing stainless steels in locations where corrosion is considered critical rather than using stainless in the entire structure. These areas include marine environments and on key locations exposed to anti-icing solutions, road salts, etc. as shown below in Figure 2-18 [50].

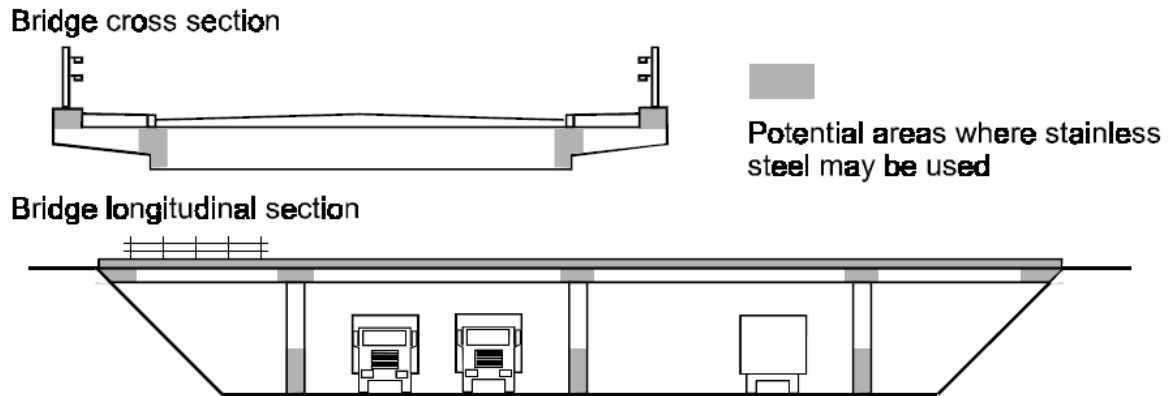


**Figure 2-18: A typical bridge deck highlighting critical areas on a bridge deck typically exposed to higher amounts of de-icing salts. These areas are good candidates where alternate reinforcement could be utilized such as stainless, galvanized, fiber reinforced polymer, or other alternatives [50].**

### ***2.3.2 Galvanized Steel***

Galvanized steel can protect steel in two manners (i) it provides a boundary between the steel and the  $\text{Cl}^-$  and can withstand 2.5 to 10 times the amount of  $\text{Cl}^-$  when compared with steel[51] [46][6]. In addition to zinc's lower susceptibility to  $\text{Cl}^-$  it is also capable of remaining passive at lower pH levels (closer to a pH of 6) as shown in Figure 2-19. Furthermore, if the surface of the steel is damaged, the zinc is anodic to the steel and will act as a sacrificial anode and corrode more rapidly while the steel's corrosion rates will slow drastically [46][6].

Though not investigated in this thesis, zinc in concrete is also known to be unstable at the higher pH levels (above a pH of 10). However, the zinc will react with the calcium in the calcium hydroxide to form a protective film of calcium hydroxyzincate and once the concrete hardens, the corrosion rates will drop significantly [52][53]. Due to zinc's ability to protect the steel in both alkaline environments and in neutral solutions it is ideal for protecting steel both inside and out of concrete.

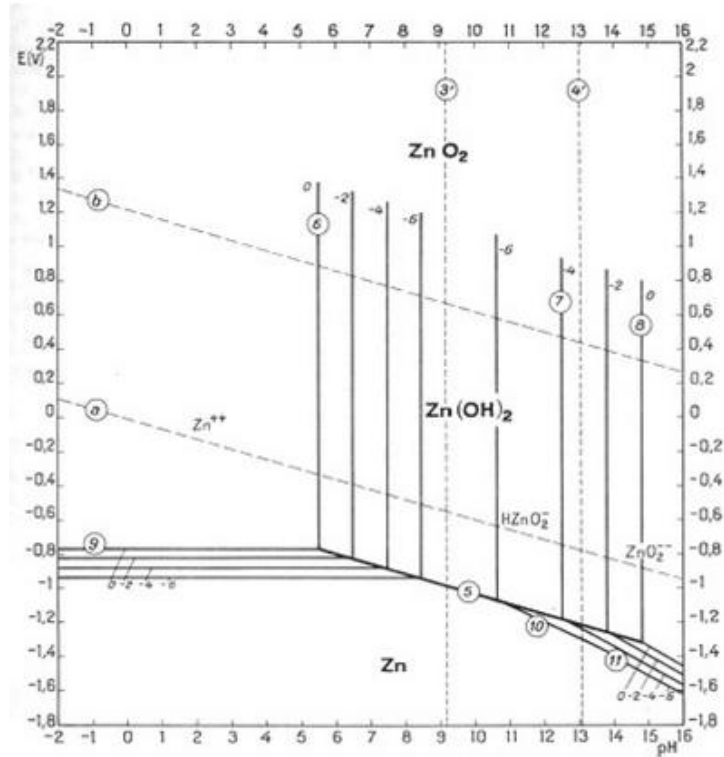


Figure 2-19: Potential (SHE) vs. pH diagram of zinc [11]

During the processing of galvanizing steel, specifically flame spray and hot-dip galvanizing, the steel substrate will diffuse into the zinc layer. The zinc-rich corner of the Fe-Zn phase diagram and the corresponding phase compositions are shown below in Figure 2-20 and Table 2-6, respectively. In atmospheric conditions with chloride contamination the presence of Fe-Zn intermetallic have been found to protect the underlying steel [54]; however, in concrete the opposite trend has been found [52].

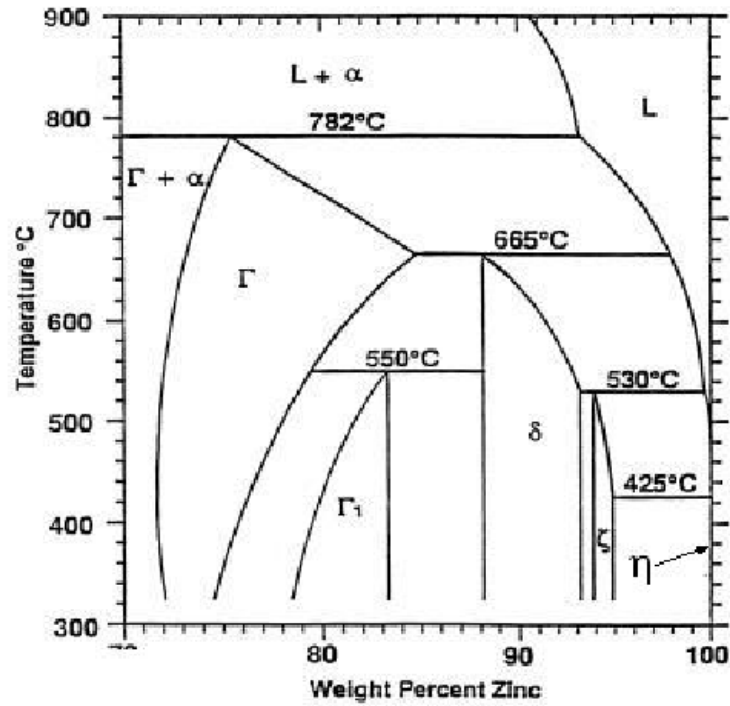


Figure 2-20: Zinc rich corner of the binary Fe-Zn phase diagram [55]

Table 2-6: Fe-Zn phase compositions [55]

Phases	Formula	% Iron
αFe	Fe(Zn)	96.1
γ	FeZn <sub>3</sub>	23.5-28.0
γ <sub>1</sub>	Fe <sub>20</sub> Zn <sub>80</sub>	17.0-19.5
δ	Fe <sub>10</sub> Zn <sub>90</sub>	7.0-11.5
ζ	Fe <sub>5</sub> Zn <sub>95</sub>	5.0-6.0
η	Zn(Fe)	0.03

### 2.3.3 Other Forms of Reinforcement and Comparison

There are several other available options of reinforcement available, the most common being fibre reinforced polymers, epoxy coated rebar and corrosion resistant bars. With the exception of MMFX, these types of reinforcement are outside the scope of this thesis but should not go without mention. Both polymers and epoxy are generally not affected by chlorides; however, there are limitations to their use. These options are compared below by Basham in Table 2-7.

**Table 2-7: Comparison of corrosion-resistant reinforcing materials [46]**

Type of rebar	Times more corrosion resistant than black rebar	Scratch and chip resistance	Bending	Cutting	Welding	Chloride threshold	Cost, \$/lb <sup>1</sup>
Epoxy-coated ■ Damage level 0.5% ■ Damage level 0.004%	150 to 1,175 69 to 1,762	Easily damaged, requiring field repairs	Allowed but can damage epoxy coating	Allowed; coating of cut end required	Allowed; coating of weld required	Same as black rebar Very high	0.32
Galvanized (zinc-coated)	38	Very tough; hard to damage	Allowed but may weaken coating	Allowed; coating of cut end required	Allowed; coating of weld required	4 to 10 times higher than black steel	0.50
GFRP	Won't corrode	Fairly tough; difficult to damage	Field bends not allowed	Allowed; sealing of cut end may be required	Nonweldable	Immune to chloride attack	3.00 to 4.00 <sup>2</sup>
Solid stainless steel	800 to 1,500	Not an issue	Allowed	Allowed	Allowed; special welding procedures apply	15 to 24 times higher than black rebar	1.60
Stainless-steel-clad	Same as solid stainless-steel rebar	Very tough; nearly impossible to damage	Allowed	Allowed; coating of cut end may be required	Allowed; special welding procedures apply	Same as solid stainless-steel rebar <sup>3</sup>	0.60

MMFX is an available alloy that provides a cost and corrosion resistance combination between black steel and stainless steel. The lower cost is attributed to the lower amount of alloying elements; it is considered a low carbon, low chromium microcomposite steel (ASTM A615 Grade 75). The corrosion initiation times of this alloy have been found to be 2 times that of black steel [56]. It must be noted that the test completed on this steel in this thesis were comparing the steel's resistance to corrosion with direct exposure to the various de-icing salts and not embedded in concrete.

### **2.3.4 Weathering Steel**

Weathering steel has been used in many structural applications as it is a high-strength, low-alloy steel that provides significantly higher corrosion resistance when exposed to atmospheric conditions than regular carbon steels[57] [58]. This is due to the nature of the corrosion products of the weathering

steel. These products form a protective coating and adhere well to the body of the steel, whereas the corrosion products of plain carbon steel do not adhere well and flake off.

#### **2.3.4.1 Applications**

In the environment under normal conditions weathering steel does not require protective coatings for extending its service life. Structural carbon steel requires coatings or other protective measures to ensure they do not corrode. These coatings eventually degrade and re-application is required. Weather steel does not require this form of protections which greatly reduces the costs of maintenance as it does not need to be initially treated or retreated. Because of weathering steel's ability to withstand corrosion it is frequently a candidate for highway structures. Currently weathering steel is and has been used in Europe, Japan, and North America for over half a century [59][58].

#### **2.3.4.2 Corrosion Resistance**

One of the primary alloying elements of weathering steel is copper which is typically added to alloy steels for increased corrosion protection [10]. In addition to copper, some high strength low alloying steels (HSLA) have small amounts of chromium, nickel, and silicon at (0.2 to 1.2%). The addition of these alloying elements allow the formation of a tenacious oxide film that will protect the surface of the exposed metal if normal wetting and drying cycles are permitted [60]. As shown below in Figure 2-21, copper gives significant corrosion resistance to carbon steel; however, it is the combination of copper and other alloying elements that enhance weathering steels corrosion resistance [57]. On the other hand, when exposed to chlorides the nature of the corrosion products change and large pieces have been seen to become loose and cause damage [58].

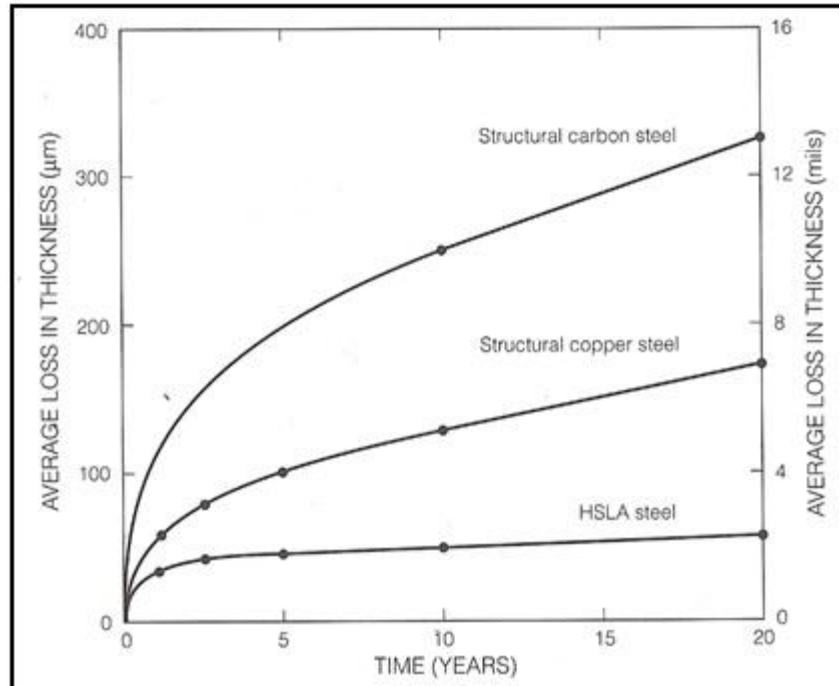


**Figure 2-21: Effects of copper and other alloying elements on the long-term atmospheric corrosion resistance of steel in [60] adopted from [61]**

Alloying elements contribute to a more compact corrosion product that adheres well to the surface of the steel, Figure 2-22. Coburn and Kim [62] found that when weathering steel was exposed to water the steel must be allowed to dry in order to develop iron oxides and/or sulfates to form the protective coating that seals the metal from the corrosive environment. If this is not possible and the weathering steel remains wetted it will corrode at rates similar to carbon steels.

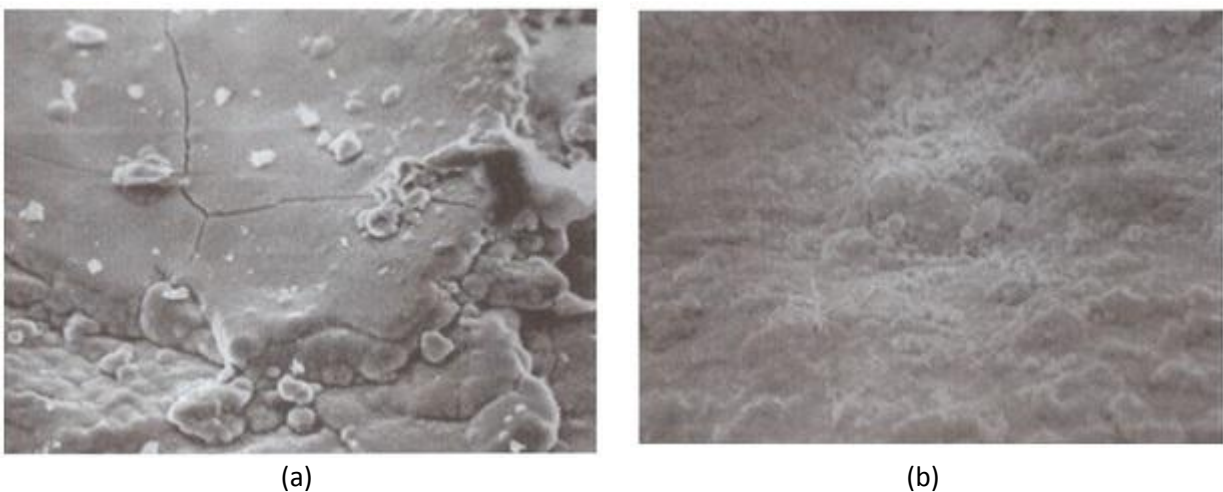


**Figure 2-22: Surface oxides of (a) carbon steel and (b) weathering steel [63]**

The effectiveness of the corrosion resistance provided by weathering steel can be greatly reduced if water is allowed to pool on the surface of the metal. This can occur if proper drainage of water is not designed in, in the ground where ground water is present and in crevices frequently created by bolts and rivets in the structure [64]. To accommodate for this, minimum spacing for bolts [65] has been derived as well as specifications for caulking or other sealants [62] for large overlapping joints.

Although weathering steel has shown greater resistance to corrosion than structural carbon steels, there are still documented cases of corrosion occurring in structures at higher than expected rates. On highway bridges and overpasses this is represents a significant problem for two reasons. The first is the thinning of the steel which compromises the structural integrity of the bridge and the second is pieces of corrosion products falling onto the road that pose a threat to the passing traffic [66] [58].

As mentioned pooling water and galvanic coupling can induce excessive corrosion in weathering steel but they are also susceptible to attack by chlorides. Hara et al. [67] found accelerated corrosion induced by chlorides was a result of rust growing by the chloride ions; this rust has micro-pores in its structure which form around the chloride ions. They went on to find that even residual chloride ions remaining on the steel in the summer from the winter applications of the salt greatly accelerated the corrosion of the weathering steel by increasing the rust particle size [67].

## Chapter 3 Experimental Procedure

This chapter outlines the research methods used and describes what each test intends to prove. The tests can be divided into two major categories: (i) steel reinforcement exposed to anti-icing solutions in a high pH environment either in concrete or synthetic concrete pore solution and (ii) various grades of steel reinforcement and structural steels exposed to anti-icing solution in a neutral pH environment. The former is discussed in Sections 3.2 and 3.3; the latter is discussed in Section 3.4. The research design and materials are discussed in Sections 3.1 and 3.5, respectively.

### 3.1 Research Design

For black reinforcing steel (rebar), three tests were chosen: macro-cell corrosion in concrete prisms following ASTM G109, micro-cell corrosion in concrete beams, and micro-cell corrosion in synthetic pore solution. The ASTM G109 test represents layers of a bridge deck where the top mat is exposed to anti-icing solutions whereas the bottom mat is in chloride-free concrete. Macro-cell corrosion is typically slower than micro-cell corrosion [20] but it is an important mechanism that can have severely detrimental effects once active corrosion is initiated. The micro-cell beams, with a cast-in ponding well, are concrete beams containing six reinforcing bars each and exposed to the anti-icing solution in the ponding well. For the third test, reinforcing bars are submerged directly in synthetic pore solution containing the salt solution at specified concentrations. This test was conducted both to guarantee results in the time frame of the project and to allow for direct visual inspection of the corrosion.

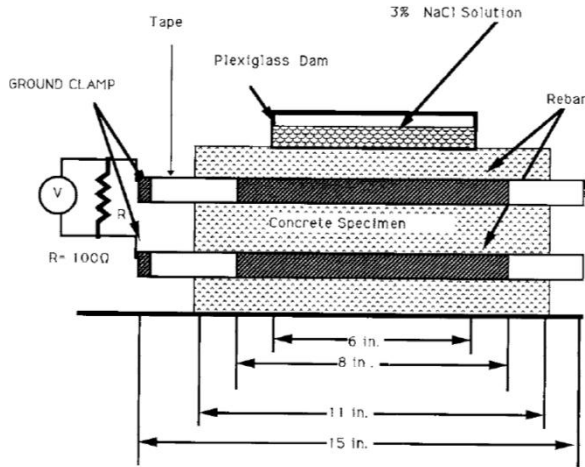
The final set of testing includes a variety of construction materials, including different stainless reinforcing steels, weathering steel, black steel rebar, plain carbon steel and galvanized steel. All of these materials are placed inside a corrosion chamber which runs on a 24 hour cycle according to the SAE J2334 test standard. This includes direct exposure to diluted anti-icing solutions. Though these conditions are not the same as those found in concrete, this test provides a comparative glimpse of which of these steels can resist direct exposure and which of the anti-icing solutions induces the most damage. Furthermore, if cracks initiate in concrete and the concrete begins to delaminate from the reinforcing steel, the anti-icing solution will penetrate through the macro cracks and the reinforcing steel will be exposed directly to the anti-icing solution. Weathering steel, galvanized steel, and plain carbon steel are frequently used as I beams and box girders, which are directly exposed to anti-icing solution.

### 3.2 Macro-cell Testing: ASTM G109 Testing

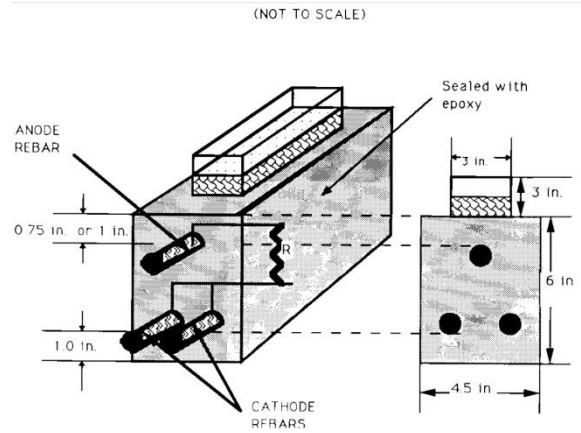
The ASTM G109 test is used to emulate the effects of layered rebar which are commonly found on bridge decks and overpasses. Three bars are cast into a prism, one bar is located near the top and two are located near the bottom; all bars are parallel as shown in Figure 3-1 (a). The top of the prism is typically fastened with a container to act as a ponding well where the solution is contained. In this test, the ponding well was cast-in rather than fastened afterwards. Typically ASTM G109 is used to test the effects of chemical admixtures to the concrete on corrosion of embedded steel reinforcement exposed to chloride environments and specifies the solution used in the ponding well as 3 parts sodium chloride to 97 parts water by mass [68]. However, the objective of this project was to determine the comparative effects of the four anti-icing agents on steel reinforcement in concrete, thus, the full-strength (i.e. non-diluted) anti-icing solutions were used in place of the 3% sodium chloride solution and the concrete mix design remained constant.

In this case, the top bar is the first bar exposed to chlorides, as the anti-icing agent will diffuse through the ponding well located at the surface. The passive film of the top bar will break down as a result of exposure to chlorides, making this bar more anodic. The bottom bars, in chloride<sup>-</sup> free concrete, remain at the same electrochemical potential and are thus more cathodic to the top bar. These two bars are connected with an external wire providing little to no resistance. The anodic bar is connected via a 100  $\Omega$  resistor to the cathodic bars, which can be thought of as the ends of the bridge deck being connected by stirrups and expansion joints. This completes the circuit for a macro-cell corrosion to occur between the top and bottom bars. A schematic of the ASTM G109 is shown in Figure 3-1.

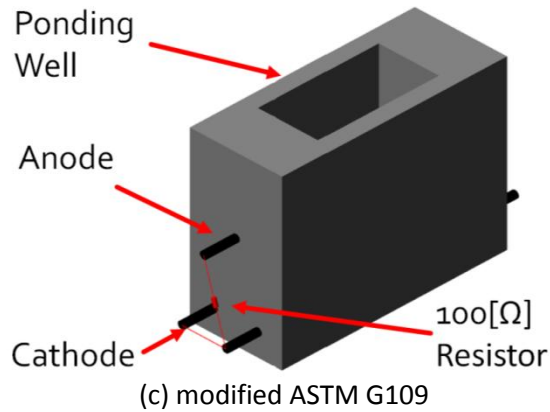
The reason for using two cathodic bars is to ensure the cathodic reaction is not the limiting factor during macro-cell corrosion. The cathodic bars accept the excess electrons from the top bar and provide a constant supply of OH<sup>-</sup> ions, as described in section 2.2 Electrochemical Corrosion. Furthermore, the test follows a four week cycle of two weeks wet and two weeks dry. This is intended to replicate the inconsistent environment of precipitation and application of anti-icing salts. The wetting and drying also encourage the ingress of the salt solution by allowing capillary absorption as well as diffusion.



(a) ASTM G109 side view



(b) ASTM G109 front view



(c) modified ASTM G109

**Figure 3-1: Schematic of ASTM G109 specimen, (a) and (b) are from the ASTM G109 standard [68], (c) is the modified ASTM G109 with a cast-in ponding well**

The bars used in this test were cut to a length of 360mm and no additional surface treatments were performed on the bars, i.e. they were used as-received which is typical of the practices on a construction site. The bars themselves were drilled and tapped at one end and fastened with a stainless steel bolt and two stainless steel nuts for electrical lead connections. The ends of the bars were then sealed with a heat shrink tubing containing an inside coating of glue ensuring 200 mm of bar steel was exposed. A quick tested was completed to ensure a tight seal between the tubing and the bar as follows. A small bar sample was sealed at one end with the shrink wrap and the entire bar was exposed to 1 M HCl. The bar was removed after about 5 minutes of exposure. The shrink wrap was removed and the results are shown below in Figure 3-2.

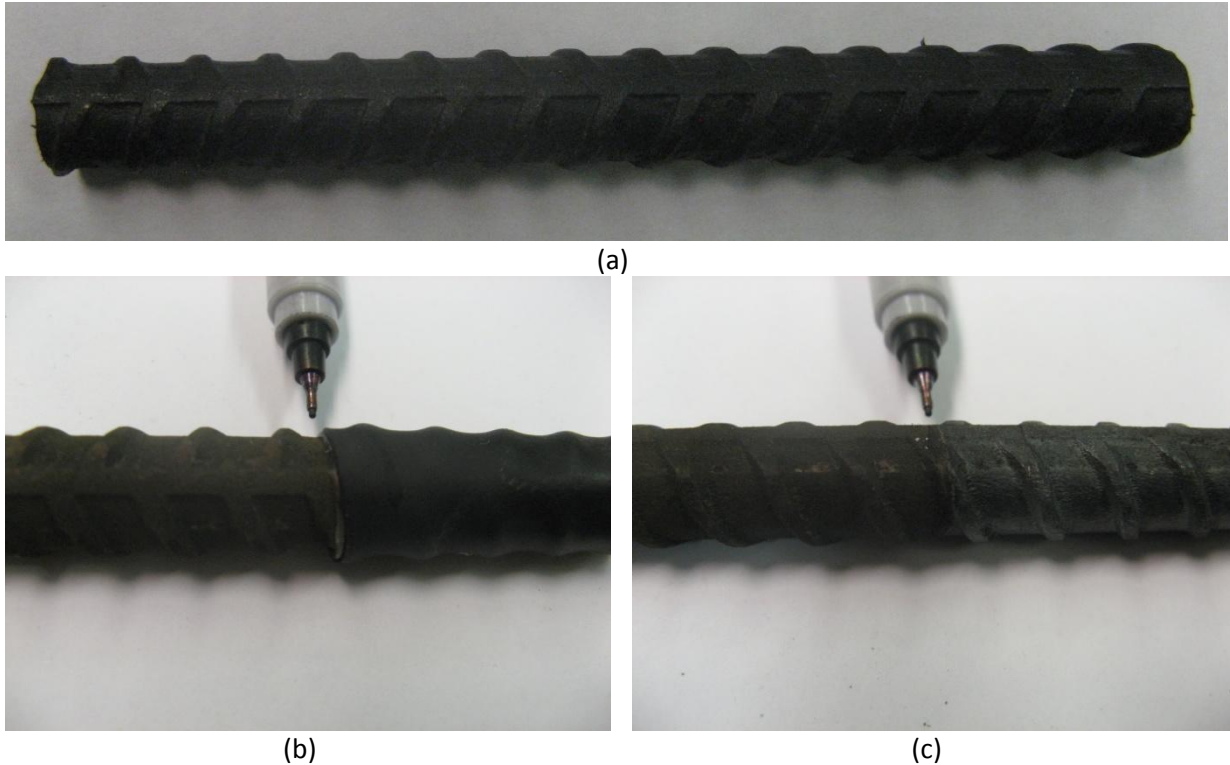


**Figure 3-2: (a) black steel bar sample prior to testing, (b) black steel bar sample coated with shrink wrap containing adhesive exposed to 1M HCl with shrink wrap and (c) with the shrink wrap removed**

The shrink wrap with adhesive appeared to provide an adequate seal and was used on the bars for ASTM G109 testing, micro-cell corrosion in concrete and micro-cell corrosion in pore solution. Electroplaters tape (recommended by ASTM G109) was not used as the glue from the shrink wrap provided a sufficient seal; furthermore, the standard specifies that the shrink wrap encase the electroplater's tape, which would result in an unwanted crevice.

In total, 35 ASTM G109 specimens were cast and connected to a data acquisition system, each with its own unique channel; this is summarized below in Table 3-1. All specimens were exposed to the same curing conditions; however, not all samples came from the same concrete batch (see section 3.5.2.1 Casting for details). Fifteen specimens were placed outside and exposed to the elements. These specimens did not experience wet/dry cycles and, instead, were continually exposed to the solution. This resulted in variations of concentration as precipitation and evaporation diluted and concentrated the solution, respectively. At no point were the solutions allowed to dry completely, although, on

occasion, salt crystals would form in the bottom of the ponding well and had to be periodically removed to unblock the pores.

Three ASTM G109 samples were cast for each solution, including the control sample which was exposed only to potable water, for outdoor exposure. The remaining 20 specimens were divided into five groups, one for each solution plus a control that remained indoors and followed the specified wet dry cycles. The ponding wells were all covered with duct tape to limit the amount of evaporation that would occur. When taking corrosion potential ( $E_{corr}$ ) measurements during the dry cycle, water was added to the ponding well. There were two reasons for this: the first is that a solution or damp sponge is required to make an electrical connection between the reference electrode and the black steel, the second was to dissolve the salt crystals that formed at the bottom of the ponding due to the evaporation of the remaining solution. This water was removed after all the  $E_{corr}$  measurements were complete.

**Table 3-1: ASTM G109 sample configuration**

Location	Solution in ponding well	Number of specimens	Channels
laboratory	H <sub>2</sub> O	4	101-104
	NaCl	4	117-120
	MgCl <sub>2</sub>	4	113-116
	CaCl <sub>2</sub>	4	105-108
	Multi	4	109-112
Exposed to the elements (outdoor)	H <sub>2</sub> O	3	121-123
	NaCl	3	133-135
	MgCl <sub>2</sub>	3	130-131
	CaCl <sub>2</sub>	3	124-126
	Multi	3	127-129

The primary deviations from the standard include: (i) creating a cast-in ponding well rather than attaching a plastic ponding well after the concrete had cured, (ii) exposing the specimen to various salt solutions to compare their effects instead of exposing the specimen to the standard 3% NaCl to test the effects of rust inhibitors and (iii) the specimen's width was increased from 115 mm to 155 mm (4.5 in to 6.1 in). The reason for increasing the width of the ASTM G109 specimen was to increase the thickness of the ponding well walls. The walls were initially 20 mm (0.79 in) as specified by ASTM

G109, less than double the size of the coarse aggregate, and were increased to 40 mm (1.57 in) to allow consolidation.

Further alterations were made to the testing schedule. The standard recommends macro-cell and  $E_{corr}$  measurements to be collected every month - this was altered to weekly for the macro-cell test and every two weeks for the  $E_{corr}$  measurements. In addition to completing  $E_{corr}$  measurements with the top and bottom bars connected with the 100  $\Omega$  resistor, measurements were also taken when the bars were disconnected. This was done to show the difference between the mixed potential and anodic potential. Both values are reported in Chapter 4.

The  $E_{corr}$  potential measurements were taken manually using a high impedance multimeter and a saturated calomel reference electrode (SCE). The resistors were wired away from the samples on 25-pin connector boards to enable easy connections and disconnections to the resistors. Thus it was possible to easily monitor the  $E_{corr}$  potential with the bars connected and disconnected.

Wired in parallel to the resistors, a Keithley™ Model 2700 DMM, Data Acquisition in conjunction with ExcelINX™, a Microsoft™ Excel add-on was used to measure the potential difference across the 100  $\Omega$  resistor. The system was set up in such a way that when measuring the potential, the software would average 100 readings over a short period of time (less than a minute). This value represents a “snap-shot” of the potential and not the average over the week. This was the reported value used to complete further calculations. In addition to the automated system, the wiring was checked periodically to ensure that a resistance of  $100 \pm 5 \Omega$  was maintained between the top and bottom bars, no short circuits were present, and to cross reference the readings with those measured using the Keithley™.

To determine the corrosion current density of the macro-cell, a combination of Ohm’s law and Faraday’s law was used. Ohm’s law, as shown in equation 3-1, is used to determine the corroding current which is divided by the exposed area of the top bar to give the corrosion current density.

$$I_{corr} = \frac{\Delta E}{R} \tag{3-1}$$

$$i_{corr} = \frac{I_{corr}}{A_a} = \frac{\Delta E}{A_a R} \tag{3-2}$$

Where:

$i_{corr}$  is the corrosion current in A,  
 $i_{corr}$  is the corrosion current density in A/m<sup>2</sup>,  
 $\Delta E$  is the potential difference between the anode and the cathode in V,  
 $A_a$  is the corroding area of the top bar in m<sup>2</sup> and  
 $R$  is the resistance between the top and bottom bars, in this case the 100  $\Omega$  resistors.

The mass loss per unit exposed area can be obtained from the corrosion current densities using Faraday's law.

$$\bar{m} = \frac{i_{corr} t M}{F z} \quad 3-3$$

Equation 3-3 can be converted to depth loss due to corrosion by dividing by density.

$$\Delta r = \frac{\bar{m}}{\rho} = \frac{i_{corr} t M}{\rho F z} \quad 3-4$$

Where:

$\bar{m}$  is the mass loss per unit area in g/m<sup>2</sup>,  
 $\rho$  is the density of the material in kg/m<sup>3</sup>,  
 $t$  is the elapsed time in s,  
 $M$  is the molar mass in g/mol,  
 $F$  is Faraday's constant 96 485 C/mol and  
 $z$  is the valance number of the ion.

### 3.3 Micro-cell Testing

The aim of these tests is to determine the micro-cell corrosion of black steel when exposed to the various anti-icing solutions. This differs from macro-cell corrosion in that the corrosion happens locally on a single bar with various areas of the bar acting as the anode and the cathode providing all the necessary elements for corrosion. This is represented schematically below in Figure 3-3. Note that this figure is not to scale and that the micro-cell would be much smaller in size, typically with a local crack or cavity containing pore solution contaminated with salt. The pore solution will then act as the medium for the OH<sup>-</sup> ions to pass through.

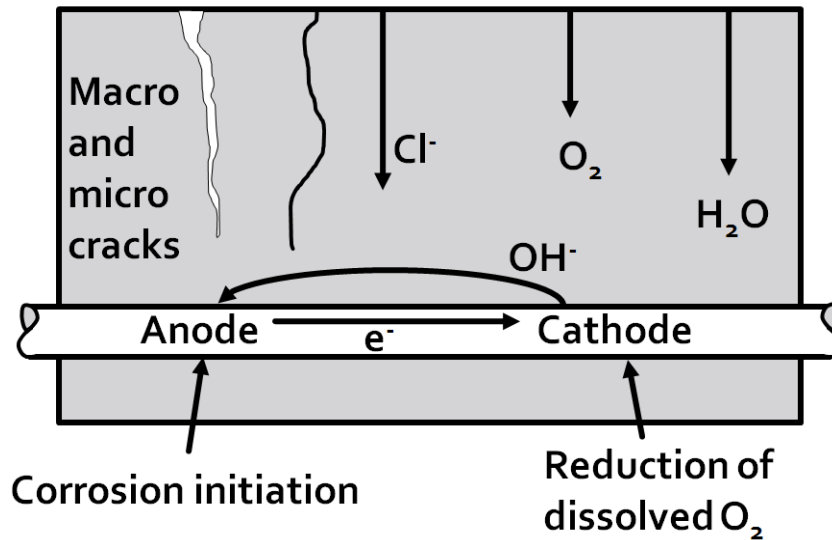


**Figure 3-3: Schematic of macro-cell corrosion, modified diagram of Carolyn Hansson [6]**

Multiple electrochemical tests were utilized to determine the corrosion rates of the bars. The principal behind these methods is described in Appendix A: Electrochemical Analysis. The two primary methods used were: galvanostatic pulse (GP) and potentiostatic linear polarization to resistance (LPR). To compensate for the resistance of the concrete, the transient response was used and analyzed. This provides the detail required to determine potential drops due to concrete resistance. An attempt was made at utilizing PowerSuites™ IR compensation but this provided faulty results and unreadable scans. Ansuji [69] found that potential drifts resulting from IR drops of reinforcing steel in concrete can be complex and result in erroneous results.

The GP method is used to determine the resistance of the concrete; it was omitted from the pore solution test as the resistance of the solution is negligible. This method can be used to determine the polarization resistance ( $R_p$ ). The GP test used applied  $10 \mu\text{A}$  for 10 s. An example of a theoretical GP scan is shown below in Figure 3-4. The first point is the open circuit potential,  $E_{\text{corr}}$ . The initial potential spike is a result of the concrete resistance and represents the “IR drop”. The gradual increase in potential represents the charging of the double layer capacitor ( $C_{\text{dl}}$ ). This changes the branch of the circuit from a closed circuit to an open circuit. This forces the iron ions to lose electrons and polarize (representing the polarization resistance). During an experimental test, a passive specimen may not achieve steady-state because the  $E_{\text{corr}}$  potential of the specimen can drift with the test, which is why this method was not utilized to determine  $R_p$ . This drift occurs because the passive layer is either being

depleted or enhanced for cathodic and anodic scans, as oxygen is expelled or consumed from the surface of the material the potential will drift. In the case of active corrosion, iron ions are either being deposited or stripped from bare metal for cathodic and anodic scans, respectively. As the concentration of iron ions in the surrounding solution changes, so will the potential; however, this happens at a much slower rate than with passive material, which is why the potential drift during testing is less likely to occur in actively corroding specimens in the span of the test.

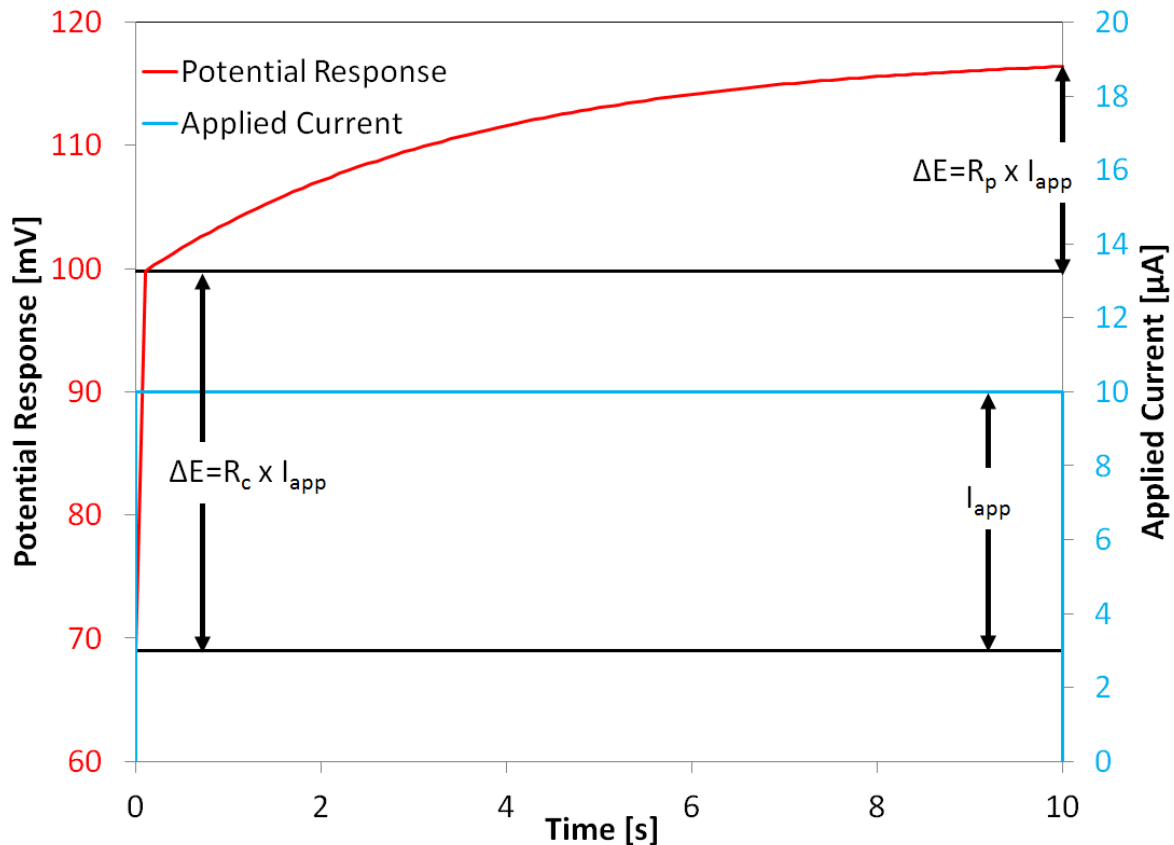


**Figure 3-4: Theoretic galvanostatic pulse response**

To determine the polarization resistance, the PS LPR technique was utilized. This technique applies a constant potential away from the equilibrium potential. Two scans are used to determine both the anodic and cathodic steady state response. The concrete resistance can also be determined using this method but was not used in these tests. The applied potential needs to be in the region that results in a linear response [38] typically taken in concrete to be  $\pm 20$  to  $\pm 30$  mV but up to 100 mV have been used [34]. For this test a potential step of  $\pm 20$  mV was chosen. To ensure that the steady state response was achieved, each scan was held for 150 s. A schematic diagram of an LPR scan is shown

below in Figure 3-5. Different values of  $R_c$ ,  $R_p$  and  $C_{dl}$  (defined in Figure 2-13 pg 24) were used to generate both scans, as a typical test would result in slightly different values for the anodic and cathodic scan. As expected, the LPR scan has similar traits to the GP scan. The initial current spike is a result of the concrete resistance and occurs as soon as the potential is applied (i.e. the instrument turned on).

The gradual decrease in current represents charging of the double layer capacitor ( $C_{dl}$ ) and that branch of the circuit in Figure 2-13 becomes an open circuit, forcing the iron ions to polarize and lose or gain electrons for the anodic and cathodic scan, respectively (representing the polarization resistance).

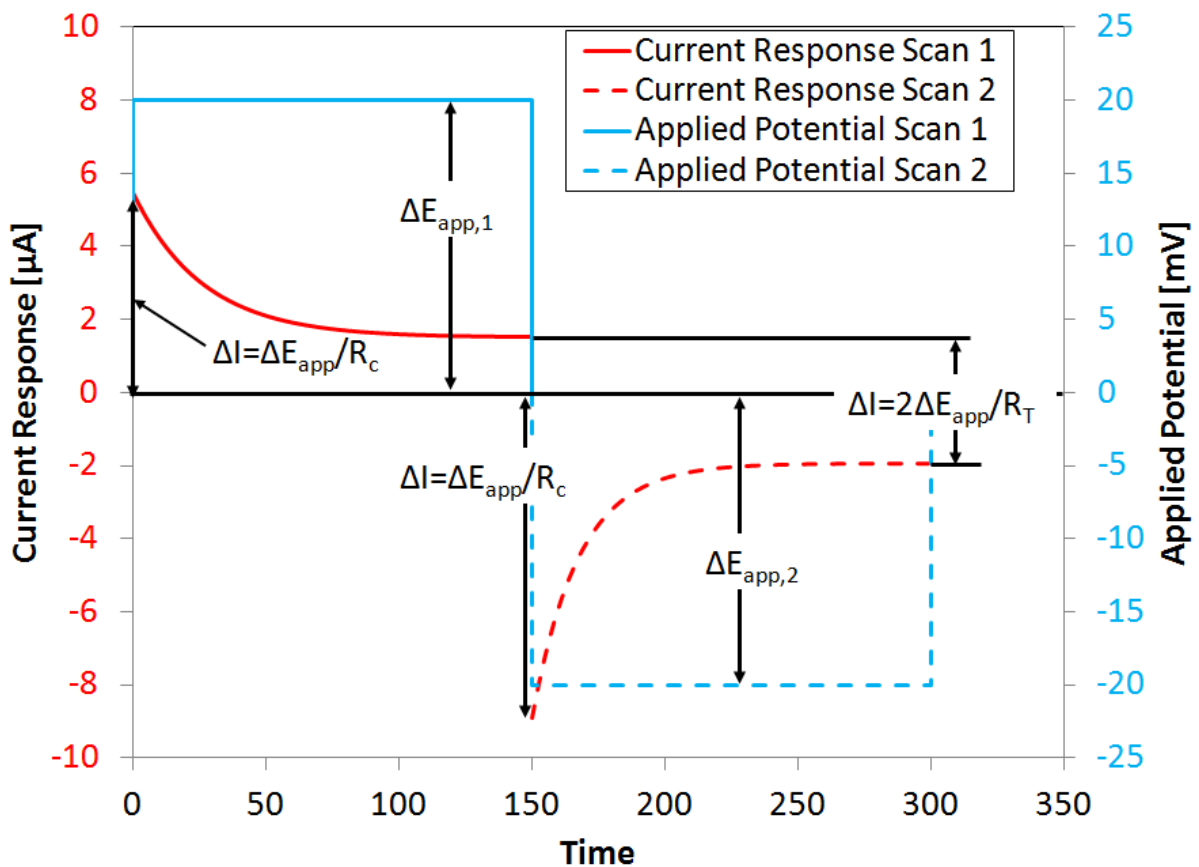


**Figure 3-5: Theoretic potentiostatic linear polarization to resistance response, the applied potential (blue) is the potential difference from  $E_{corr}$ . Note:  $R_T$  in this schematic is the total resistance, i.e. the cathodic scan's concrete resistance and polarization resistance as well as the anodic scan's concrete resistance and polarization resistance.**

The final method used was potentiodynamic cyclic polarization (CP). This method applies a constant potential sweep at a constant scan rate and the range of potentials is much larger than the techniques

discussed above (typically several hundred millivolts). The major advantage of this test is the amount of detail it provides about the system; the major disadvantage is its potentially destructive nature, which is why it will only be utilized on specimens upon completion of their testing cycle. A sufficiently low scan rate will be applied to avoid both shocking the system and to ensure it has time to reach equilibrium at all potentials. For this project, a scan rate of 0.01 mV/s was used. Furthermore, the scans started and ended at the open circuit potential which allowed the observation of any changes to the corrosion potential and corrosion current densities.

### ***3.3.1 Beams with Ponding Well***

The beams with a cast-in ponding well are designed with the intention of replicating the top layer of bars on a bridge deck. The bars were cut and prepared based on the ASTM G109 test standard. This was done and to make the comparison of macro-cell to micro-cell corrosion easier. For the full details of how the sizes were determined see Appendix B: section B-2 Casts. A schematic diagram of a beam is shown in Figure 3-6.

NOTE1: ALL DIMENSIONS IN MM  
 NOTE2: THE PONDING WELL IS  
 CENTERED IN THE BEAM  
 NOTE3: NOT TO SCALE

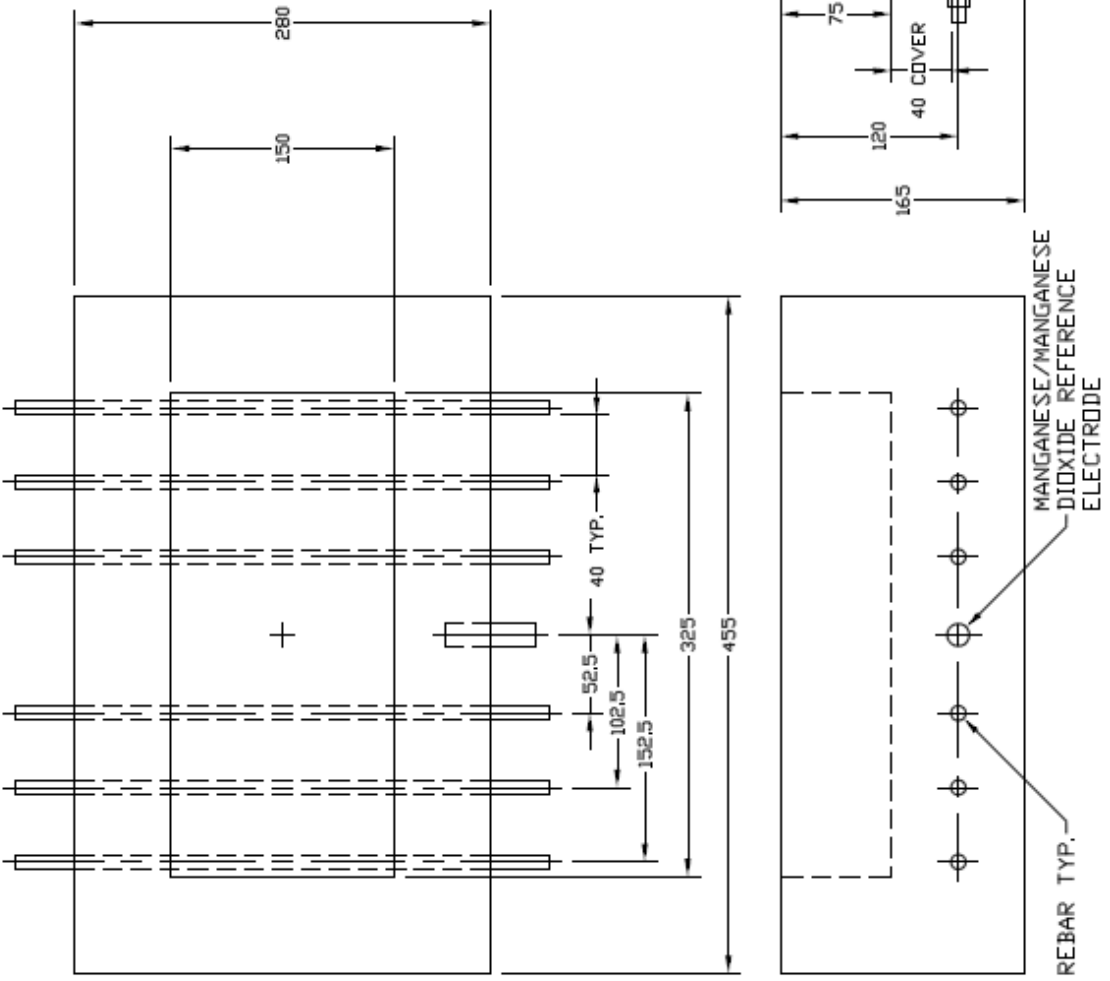
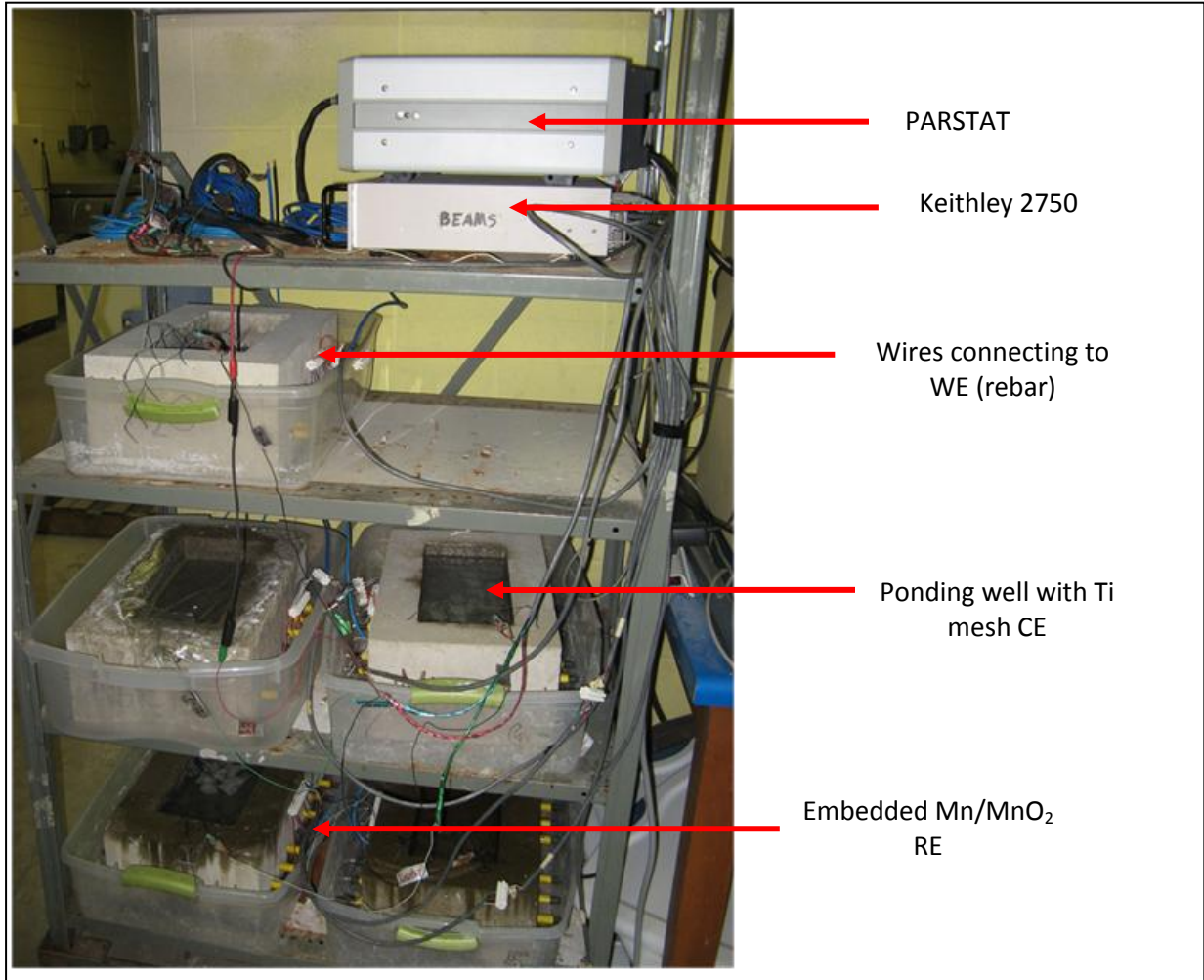


Figure 3-6: Beam schematic (Note: not to scale)

Five beams were cast: one for each anti-icing solution and a control that is exposed to potable water. As shown in Figure 3-6, there are six bars in each beam and one cast-in manganese/manganese dioxide reference electrode (MOE) which was developed for good stability in chloride-free concrete but can show deviations in long-term (~10 year) chloride contaminated concrete [69]. The reference electrode in the water-exposed specimen began to malfunction early during testing and was replaced by an SCE positioned in the ponding well during testing. The counter electrode was a mixed metal oxide activated titanium mesh that was placed in the bottom of the ponding well.

The ponding wells were continuously wet for 350 days. After January 23, 2013 the beams followed the wet/dry cycles of two weeks wet followed by two weeks dry. During testing in the intermittent dry week, it was noted that salt crystals had precipitated at the bottom of the well, preventing good electrical contact between the electrodes and the concrete. Therefore, the ponding well was temporarily filled with potable water (similar to the ASTM G109) to provide the necessary electrical connection and to dissolve any salt crystals that had formed due to the evaporation of remaining solution. After completing the weekly test the water was removed and the beams were allowed to continue drying.

The specimens were wired through the Keithley™ Model 2750 DMM, Data Acquisition which was used to control the channels. A Princeton Applied Research™ PARSTAT® 2263 potentiostat/ galvanostat/ FRA using PowerSuite™ software was used to run the various electrochemical tests. The Automatic Corrosion Monitoring Program ACMP [70], written in Labview™ 6.0 was used to communicate between the instruments and control switching the channels. Periodically, the results obtained in this way were cross referenced with tests completed using only the PARSTAT and PowerSuite™ to ensure there were no electrical connection issues. The set up of the test is shown below in Figure 3-7.



**Figure 3-7: Replica bridge deck beams with cast in ponding well test set up**

**3.3.2 Synthetic Pore solution Testing**

The synthetic pore, as defined in Table 2-2, solution was used to test micro-cell corrosion in a controlled environment where the pH and chloride content could be closely monitored and controlled respectively. This was to understand the effects of the cations in the solution as well as to determine the chloride threshold for the steel in each solution. This was used in conjunction with research preformed in parallel on the diffusion rate of these chlorides in concrete [13].

In total, five pore solution cells were created, one for each salt solution and one control specimen in salt-free pore solution. Each cell contained five bars which were prepared in a similar fashion to the ASTM G109 and beam black steel. The only variation was that the bars were 120 mm in length with an

exposed length of 50 mm and a stainless steel shim was added to suspend the bar from the top of the cell, this is shown below in Figure 3-8 (a). The bars were suspended by the shim in plastic containers that held the pore solution. A central hole was cut in the center of the container lid that would act as the port for a SCE as well as a small hole to connect to the titanium mesh counter electrode, shown in Figure 3-8 (b) and (c). Initially the mesh was only a small central wire. Later it was suspected that the surface area of the counter electrode was not sufficient and it was replaced with a larger portion of mesh that surrounded the perimeter of the container no differences in test results were observed after this change. Every week, prior to adding the anti-icing solution, each specimen was tested using the PS LPR test method. This was done in exactly the same fashion as for the beams; the details can be found in Section 3.3.1 Beams with Ponding Well.

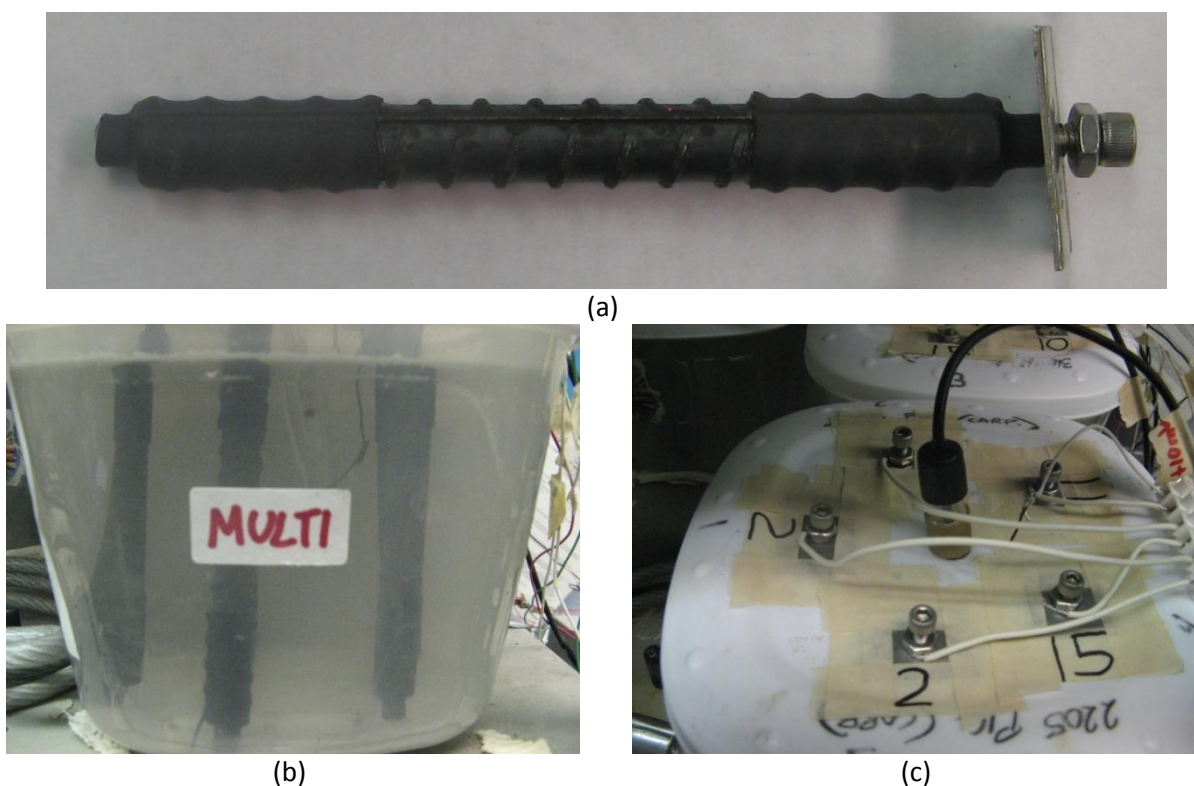


**Figure 3-8: Pore solution (a) specimen, (b) bars in solution, (c) top of specimen wired and ready for testing**

Anti-icing solution was added to the synthetic pore solution by incrementally increasing the total chloride content by 0.05 wt. %  $\text{Cl}^-$  ions per week. Equation 3-5 denotes the wt. %  $\text{Cl}^-$  ions at any given time using the subscripts "i" to denote the current concentration and "i+1" to denote the future concentration.

$$w_{i+1} = \frac{m_{Cl,tot}}{m_{tot}} \quad 3-5$$

$$m_{Cl,tot} = m_{Cl,in} + m_{Cl} - m_{Cl,out} = V_{in} * C + R_i * m_i - V_{out} * \rho_{soln} * w_i \quad 3-6$$

$$m_{tot} = m_{in} + m_i - m_{out} = V_{in} * \rho_{soln,cl} + m_i - V_{out} * \rho_{soln} \quad 3-7$$

Where:

w is the wt. % Cl ions,

m is mass,

V is volume of solution (using subscripts "in" to denote chloride solution being added, and "out" to denote total solution being removed),

C is the concentration of Cl<sup>-</sup> ions in the salt solution, and

ρ is density.

The density of the salt solutions and the pore solution are about 1% higher than the density of water. For simplicity, the density of water was substituted for the density of pore solution and salt solutions. Substituting equation 3-6 and 3-7 into 3-5 yields equation 3-8, which can be rearranged to determine the volume of new solution to be added to achieve the desired wt.% Cl<sup>-</sup> ions as shown in equation 3-9.

$$w_{i+1} = \frac{V_{in} * C + w_i * m_i - V_{out} * \rho * w_i}{V_{in} * \rho + m_i - V_{out} * \rho} \quad 3-8$$

$$w_{i+1} * V_{in} * \rho + w_{i+1} * m_i - w_{i+1} * V_{out} * \rho = V_{in} * C + w_i * m_i - V_{out} * \rho * w_i$$

$$V_{in} * C - w_{i+1} * V_{in} * \rho = w_{i+1} * m_i - w_{i+1} * V_{out} * \rho - w_i * m_i + V_{out} * \rho * w_i$$

$$V_{in} * (C - w_{i+1} * \rho) = m_i * (w_{i+1} - w_i) + V_{out} * \rho * (w_i - w_{i+1})$$

$$V_{in} = \frac{m_i * (w_{i+1} - w_i) - V_{out} * \rho * (w_{i+1} - w_i)}{(C - w_{i+1} * \rho)}$$

$$V_{in} = \frac{(m_i - V_{out} * \rho) * (w_{i+1} - w_i)}{(C - w_{i+1} * \rho)} \quad 3-9$$

One specimen from each cell was autopsied for visual inspection. This included photographic documentation prior to and post pickling. The pickling solution used is designated by ASTM G1 Annex A1. Chemical Cleaning Procedures [71] and given in Table 3-2.

**Table 3-2: Chemical cleaning procedures for removal of corrosion products**

Solution	Time	Temperature	Remarks
1000mL hydrochloric acid (HCl, sp gr 1.19) 20g antimony trioxide (Sb <sub>2</sub> O <sub>3</sub> ) 50g stannous chloride (SnCl <sub>2</sub> )	1 to 25 min	20 to 25°C	Solution should be vigorously stirred or specimen should be brushed. Longer times may be required in certain instances.

### 3.4 Cyclic Corrosion Chamber (SAE J2334 Immersion Testing)

The purpose of the cyclic corrosion testing was twofold. The first was to compare the effects of each of the four anti-icing agents on the steels under atmospheric conditions and exposed directly to salt. The second was to compare the various steels' corrosion resistance to the anti-icing agents. Each solution was diluted to 3 wt.% Cl<sup>-</sup> ions by mass using de-ionized water.

#### 3.4.1 Test Set Up

Damgaard [58] found that the SAE J2334 test in the laboratory could replicate the damage to weathering steel observed in the field. The test was originally design for automotive components and follows a 24 h test regime shown below in Figure 3-9.

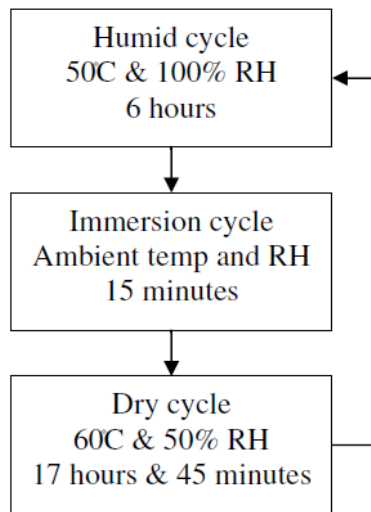


**Figure 3-9: SAE J2334 test cycle [72]**

The specimens were photographed and weighed every 5 cycles for a total of 50 cycles per salt solution. The solution's pH and conductivity were monitored using a Geotech<sup>TM</sup> Multi 350i pH/ISE/DO conductivity measuring instrument. The test regimen was imposed by placing the specimens in an

Ascott Cyclic Corrosion Test Chamber (model CC450). The system has two components, each with a 450 L capacity: a corrosion chamber and a solution reservoir shown in Figure 3-10.



(a) (b)  
**Figure 3-10: ASCOTT (a) reservoir and (b) corrosion chamber**

The Ascott system is programmable through a touch screen, and automatically adjusts the temperature, humidity of the chamber and immersion of the specimens. Its capacity for automatic operation means that it could operate continuously.

Test racks for the specimens were cut from black ABS plastic tubing. Figure 3-11 shows a diagram of the test rack (dimensions are in mm). The specimens were identified by different coloured nail polish. Furthermore, the specimens were placed in order inside the corrosion chamber. This was done to aid in keeping track of the specimens in the event the nail polish indicator was removed. Each time the specimens were weighed, they were replaced in a different location, shifting the specimens back one row each test to limit the amount of bias introduced by any variations in temperature and/or relative humidity in the chamber. Furthermore, the specimens were inverted to ensure the surface facing upwards altered with each five day cycle.

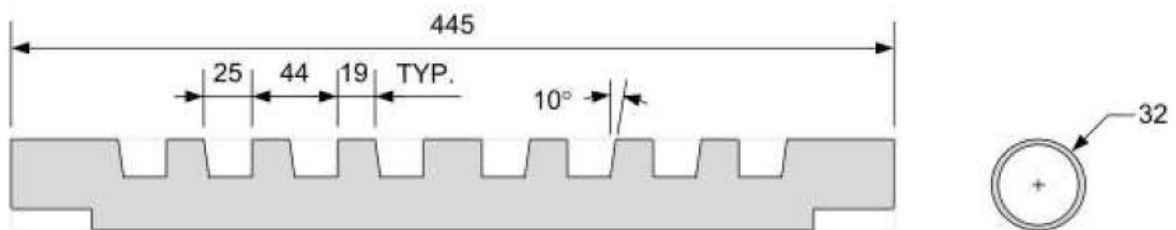


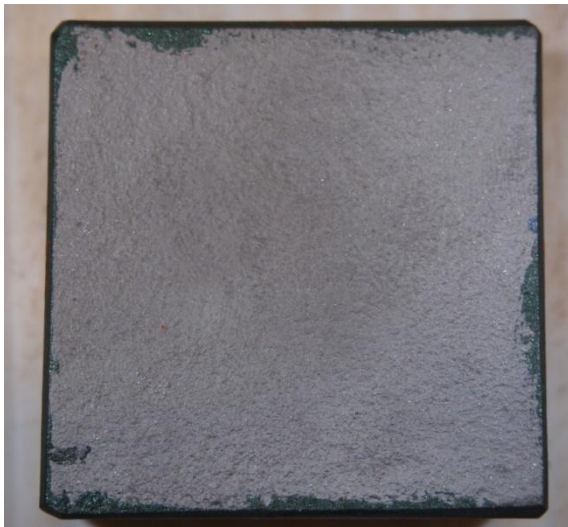
**Figure 3-11: Corrosion chamber specimen holder [58]**

### 3.4.2 Specimen Preparation

As mentioned, the black and stainless steel rebar specimens were cut to 110 mm lengths and had their ends coated in nail polish of a colour specific to each grade. The plate specimens were cut into 50 mm x 50 mm. With the exception of the guard rail, all plate specimens had their surface sandblasted to remove any paint present and to expose fresh metal. The guard rail was galvanized and sandblasting would have removed the zinc coating. Finally, all of the ends of the plate specimens were coated in nail polish. This reason for this was three fold: (i) was to eliminate variation in exposed surface area between plate specimens due to the variation in specimen thickness, (ii) the paint was also used to identify the different specimen type and specimen number and (iii) to remove any end effects from the cutting process, particularly for the guard rail which would obviously not have the zinc coating on the cut surfaces. Samples of each specimen are shown below in Figure 3-12 and Figure 3-13.



Figure 3-12: Steel rebar specimens prior to testing in the corrosion chamber



box girder



drain



guard rail



weathering steel

**Figure 3-13: Plate steel specimens prior to testing in the corrosion chamber**

### ***3.4.3 Deviation from the Test Schedule***

Unfortunately during testing two of the components, discussed in more detail below, failed during testing. Both failures resulting in the ASCOTT alarm system being activated and causing some downtime during which the specimens were exposed to the room temperature and humidity at about 23°C and 37% respectively. This may have resulted in a slight biased of mass gain during the time exposed to these conditions. However, this bias would be so small making it difficult if not impossible to measure. Furthermore, the bias would be overshadowed by the effects of the highly aggressive testing regime.

During the  $\text{CaCl}_2$  testing, the machine was interrupted five times as the reservoir was hitting the overflow switch, resulting in approximately 5-7 days of exposure to ambient conditions. The cause of this was the small reservoir in the corrosion chamber. This reservoir was not properly draining between the immersion cycle and the humid cycle – which also meant the solution, had to be adjusted to maintain the proper  $\text{Cl}^-$  concentration. The small reservoir contains the heating elements of the chamber, which need to be continually submerged to avoid damage. Under normal operation the reservoir pumps this fluid out prior to pumping in solution from the reservoir. To solve this problem an intermittent dry stage (which includes an automatic pump-out incorporated into its process) was added.

The second problem occurred during the  $\text{MgCl}_2$  testing: the ball valve controlling the air intake began to fail. This caused two shorter interruptions and two longer interruptions when the component failed. This resulted in approximately 2 weeks of exposure to ambient conditions before the ball valve was cleaned and serviced.

### **3.5 Materials**

This section provides an overview of the testing methods utilized to classify the materials and to create the specimens.

#### ***3.5.1 Salt Solution***

The salt solutions were specified by the MTO and provided by various anti-icing contractors throughout Ontario. In addition to acting as anti-icing agents, the  $\text{CaCl}_2$  solution is also used as a dust suppressor during the summer months. The compositions of the various salt solutions were determined by Activation Labs Ltd. using inductively coupled plasma optical emission spectroscopy (ICP-OES) and ion beam chromatography (IC).

#### ***3.5.2 Concrete***

The mix design of the concrete used for testing was specified by the MTO as a standard bridge deck mix and is shown below in Table 3-3. Furthermore, the amount of water was corrected such that the aggregates were in the saturated surface dry (SSD) condition. The method of determining SSD conditions and the specifics of each cast can be found in Appendix B: Casting and Concrete.

**Table 3-3: Concrete mix design (per m<sup>3</sup>)**

<b>Constituent</b>	<b>Value</b>	<b>Unit</b>
<b><i>Gravel (12.7mm, 0.5in)</i></b>	1045	kg
<b><i>Sand</i></b>	705	kg
<b><i>Cement (GU Typ1)</i></b>	297	kg
<b><i>Slag</i></b>	98	kg
<b><i>Water</i></b>	155	l
<b><i>Euclid air extra<sup>TM</sup></i></b>	237	ml
<b><i>Euclid water reducer<sup>TM</sup></i></b>	800	ml
<b><i>Glenium 7700<sup>TM</sup></i> <b><i>(superplasticizer)*</i></b></b>	386-2896	ml

\*130-975ml/100kg cement as recommended by the manufacturer

### **3.5.2.1 Casting**

The casting procedures used ASTM C192/C192M-07 [73] as guidelines but were not followed strictly. The concrete mixer used was a PMSA turbine pan mixer. Due to the volume limitations of the turbine pan mixer, four batches of concrete were cast. The micro-cell beams were cast first and the ASTM G109 samples were cast in three batches (see Table 3-4). A portion of one of these batches is shown below in Figure 3-14. The G109 samples were divided into two batches of 10 indoor specimens for a total of 20 samples and one batch of 15 samples for outdoor exposure. The nature of this testing is to compare the effects of the various anti-icing agents to one another; therefore, to minimize potential biases present from the two batches of concrete used to create the indoor specimens, two samples from each batch were exposed to each anti-icing solution and to potable water for a total of four samples per solution. Each of the batches was consolidated using a vibration table shown in Figure 3-14 (c). Each batch had sufficient concrete to test for total air concentration, slump and 28 day compressive strength. The results of these tests can be seen in Appendix B: Casting and Concrete.

Table 3-4: Casting batches

Specimen	Location	Total samples	Batch	Number of samples in batch	Description
<i>Micro-cell Beam</i>	<i>Laboratory</i>	5	1	5	1 NaCl, 1 MgCl <sub>2</sub> , 1 CaCl <sub>2</sub> , 1 Multi, 1 H <sub>2</sub> O
<i>G109</i>	<i>Outdoors</i>	15	2	15	3 NaCl, 3 MgCl <sub>2</sub> , 3 CaCl <sub>2</sub> , 3 Multi, 3 H <sub>2</sub> O
	<i>Laboratory</i>	20	3	10	2 NaCl, 2 MgCl <sub>2</sub> , 2 CaCl <sub>2</sub> , 2 Multi, 2 H <sub>2</sub> O
			4	10	2 NaCl, 2 MgCl <sub>2</sub> , 2 CaCl <sub>2</sub> , 2 Multi, 2 H <sub>2</sub> O



(a)



(b)



(c)



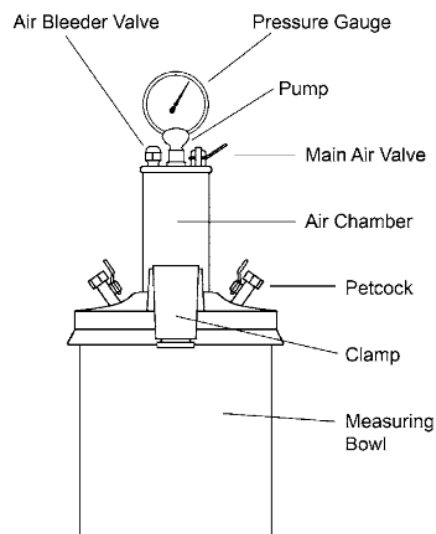
(d)

Figure 3-14: Casting pictures (a) formwork of a set of ASTM G109s, (b) close up of inside an ASTM G109 showing the three rebar and the ponding-well, note that the specimens are cast inverted, (c) the formwork on top of the vibration table ready for concrete and (d) 12 cast ASTM G109 Specimens

All concrete specimens were cured under wet burlap and vapour barrier for two days then demoulded and stored in a humidity chamber for 26 days. The ends of the 28 day strength compression testing cylinders were ground flat and parallel prior to being placed in the humidity room.

### 3.5.2.2 Air Content

In colder climates where temperatures drops below zero degrees, liquid water in the concrete can expand and crack the concrete; to avoid this, concrete must have a sufficient amount of space to allow the ice to expand. To achieve this, an air entraining agent is added to the mix to produce large numbers of minute air voids. However, the concrete cannot have too many voids or large voids as this will have a detrimental impact on its strength and durability. The test to determine air content was ASTM C231/C231M – 10 Standard Test Method for Air Content of Freshly Mixed Concrete by the Pressure Method. A schematic of the air chamber is shown below in Figure 3-15.



**Figure 3-15: Vertical air pressure chamber use for determining the total air content of concrete using the air method**

### 3.5.2.3 Twenty Eight Day Compressive Strength

One of the most important qualities of concrete is its compressive strength. This is no different for corrosion research as it (a) gives a comparison between the concrete in the lab and similar concrete in the field and (b) gives an idea of the soundness of the concrete. This information must be used carefully as typical cast cylinders for compressive strength testing are roughly 10% stronger than strength measurements of cylinders created from cores for up to 91 days [74]. The concrete for this

project was created and cured following ASTM C873/C873M – 10 Standard Test Method for Compressive Strength of Concrete Cylinders Cast in Place in Cylindrical Molds [74] and ASTM C39/C39M – 12a Standard Test Method for Compressive Strength of Cylindrical Concrete Specimens [75].

### **3.5.3 Metal Composition**

This section deals with the metals tested and the various testing methods used to determine some of the material composition. The information from the mill certificate is used when provided; in the cases where no mill certificate was available, x-ray fluorescence (XRF) analysis, scanning electron microscope (SEM) and energy-dispersive x-ray spectroscopy (EDS) have been utilized to determine coatings and major alloying elements. It is important to note that none of these methods can determine lighter elements such as carbon.

#### **3.5.3.1 Steel Specifications**

The reinforcing steel used in the G109, micro-cell beams and pore solution was 10M, 400W reinforcing steel, i.e., approximately 10 mm diameter, 400 MPa, black, weldable reinforcing steel. The chemical composition of this steel is designated by CSA G30.18-09 Carbon steel bars for concrete reinforcement and is shown below in Table 3-6.

For all surface area calculations for ribbed rebar, the equivalent diameter of a circle with the area of a bar cross section, taking into account the ribs, was used, namely 11.3 mm (0.445 in) for the 10M black steel. The stainless steels used in the cyclic corrosion chamber testing were 15M and 20M. The same method described above was used for calculating the surface area of each bar. A complete list of equivalent diameters is shown below in Table 3-5.

**Table 3-5: Deformed bar designation numbers and associated requirements CSA G30.18-09 [76]**

Designation number*	Nominal dimensions†			Mass (weight) per unit length, kg/m	Deformation requirements, mm		
	Cross-sectional area, mm <sup>2</sup>	Diameter, mm	Perimeter, mm		Maximum average spacing	Minimum average height	Maximum gap chord of 12.5% of nominal perimeter
10	100	11.3	35.5	0.785	7.9	0.45	4.4
15	200	16.0	50.1	1.570	11.2	0.72	6.3
20	300	19.5	61.3	2.355	13.6	0.98	7.7
25	500	25.2	79.2	3.925	17.6	1.26	9.9
30	700	29.9	93.9	5.495	20.9	1.48	11.7
35	1000	35.7	112.2	7.850	25.0	1.79	14.0
45	1500	43.7	137.3	11.775	30.6	2.20	17.2
55	2500	56.4	177.2	19.625	39.4	2.55	22.2

\*Designation numbers are based on the nominal diameter of the bars in millimetres.

†The nominal dimensions of a deformed bar are equivalent to those of a plain round having the same mass per unit length as the deformed bar.

**Table 3-6: Chemical composition limits for analysis of finished bars CSA G30.18-09 [76]**

Element	Maximum, %	
	Grades 400R and 500R	Grades 400W and 500W
Carbon	—	0.33
Manganese	—	1.65
Phosphorus	0.06	0.043
Sulphur	—	0.053
Silicon	—	0.55

There are two primary designations given by ASTM for weathering steels. The first is ASTM A242 (“COR-TEN A”) and the newer ASTM A588 (“COR-TEN B”). The chemical composition of these two primary weathering steels is shown below in Table 3-7. For the Canadian standard of weathering steel CSA G40-21 is used. The compositions of these steels are shown in Table 3-8.

**Table 3-7: Chemical requirements (heat analysis) of ASTM weathering steel [77] [78]**

Element	A242 Type 1	A588 Grade A	A588 Grade B	A588 Grade C	A588 Grade K
<b>Carbon<sup>1</sup></b>	0.15 (max)	0.19 (max)	0.20 (max)	0.15 (max)	0.17 (max)
<b>Manganese<sup>1</sup></b>	1.00 (max)	0.80-1.25	0.75-1.35	0.80-1.35	0.50-1.20
<b>Phosphorus</b>	0.15 (max)	0.04 (max)	0.04 (max)	0.04 (max)	0.04 (max)
<b>Sulfur</b>	0.05 (max)	0.05 (max)	0.05 (max)	0.05 (max)	0.05 (max)
<b>Silicon</b>	...	0.30-0.65	0.15-0.50	0.15-0.40	0.25-0.50
<b>Nickel</b>	...	0.40 (max)	0.50 (max)	0.25-0.50	0.40 (max)
<b>Chromium</b>	...	0.40-0.65	0.40-0.70	0.30-0.50	0.40-0.70
<b>Molybdenum</b>	...	...	...	...	0.10 (max)
<b>Copper</b>	0.20 (min)	0.25-0.40	0.20-0.40	0.20-0.50	0.30-0.50
<b>Vanadium</b>	...	0.02-0.10	0.01-0.10	0.01-0.10	...
<b>Columbium</b>	...	...	...	...	0.005-0.05 <sup>2</sup>

Note: Where “...” appears in this table, there is no requirement specified

Note 1: For each reduction of 0.01 percentage point below the specified maximum for carbon, an increase of 0.06 percentage point above the specified maximum for manganese is permitted, up to a maximum of 1.50%

Note 2: For plates under ½ in. 13 [mm] in thickness, the minimum columbium is waived.

**Table 3-8: Chemical composition of weathering steels, wt.%, CSA 40-21 [79]**

Element	350R	350A	350AT
C	0.16 max	0.20 max	0.20 max
Mn	0.75 max	0.75-1.35	0.75-1.35
P	0.05-0.15	0.03 max	0.03 max
S	0.04 max	0.04 max	0.04 max
Si	0.75 max	0.15-0.50	0.15-0.50
Cr	0.30-1.25	0.70 max	0.70 max
Ni	0.90 max	0.90 max	0.90 max
Cu	0.20-0.60	0.20-0.60	0.20-0.60

A variety of steels, shown below in Table 3-9, were tested in the corrosion chamber. All sharp edges were ground smooth and the cut surfaces (i.e. outside faces) were coated in nail polish of different colours. This was done to protect the steel from any deformities incurred during cutting, protect the uncoated surface in the case of coatings and to identify the various bars. Not all of the material was virgin; this is indicated in the table. All of the box-girder specimens are from the same box girder;

however, the samples were from different sections which accounts for the variation in thickness. The reason for the variability in the number of samples is due to the amount of material available and the limitations imposed by the size of the corrosion chamber.

**Table 3-9: Metals tested in the corrosion chamber**

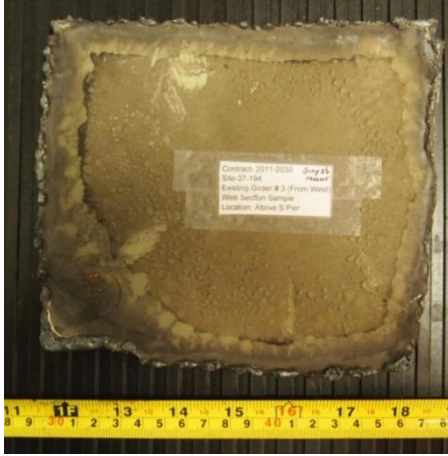
<b>Material/Name*</b>	<b>Number of Samples</b>	<b>Virgin Material</b>	<b>Length [mm]</b>	<b>Width [mm]</b>	<b>Bar designation</b>	<b>Thickness/ Diameter [mm]</b>	<b>Exposed Surface Area [mm<sup>2</sup>]</b>
<i>UNS30403/304L</i>	5	Yes	110		20M	19.5	6,739
<i>UNS31653/316LN</i>	5	Yes	110		15M	16.0	5,529
<i>UNS32101/2101</i>	5	Yes	110		15M	16.0	5,529
<i>UNS32205/2205</i>	5	Yes	110		15M	16.0	5,529
<i>UNS32304/2304</i>	5	Yes	110		15M	16.0	5,529
<i>XM28</i>	5	Yes	110		15M	16.0	5,529
<i>MMFX</i>	5	Yes	110		15M	16.0	5,529
<i>Galvanized Rebar**</i>	5	Yes	110		15M	16.0	5,529
<i>Guard Rail***</i>	3	No	50	50	N/A	13.3	5,000
<i>Black Steel Rebar</i>	5	Yes	110		10M	11.3	3,905
<i>Box Girder A</i>	2	No	50	50	N/A	19.5	5,000
<i>Box Girder B</i>	1	No	50	50	N/A	10.5	5,000
<i>Drain</i>	6	No	50	50	N/A	8.1	5,000
<i>Weathering Steel</i>	5	No	50	50	N/A	16.1	5,000

\* Where applicable the material will be referred to by its common name and not the UNS numerical designation

\*\* Hot-dip galvanized 15M rebar

\*\*\* galvanized

The as-received condition of the non-virgin steels can be seen below in Figure 3-16. The original edges of the as-received samples were cut using a torch, leaving them heat treated and, for this reason, the edges were removed. All of these samples were cut to size using a band saw with coolant to avoid overheating and possible heat treatment. Lastly, all plate samples with the exception of the guard rail were sand blasted to expose fresh metal.



(a) Box girder A



(b) Box girder B



(c) Drain



(d) Weathering steel



(e) Guard Rail

**Figure 3-16: As-received materials (a and b) are the two box girder sections (a) is the thicker web section sample and (b) is the thinner top flange section sample. (c) is a drain. (d) is weathering steel obtained from Algoma Steel, it was originally virgin steel but left outside, it was exposed to the elements; unlike the other specimens it had not been exposed to anti-icing solutions. (e) is the galvanized guard rail, all samples were taken from the web of the guard rail which had the most intact coating.**

### 3.5.3.2 Scanning Electron Microscope, Energy-Dispersive X-ray Spectroscopy and Energy Dispersive X-Ray Fluorescence

The SEM and EDS were used to determine the coating thickness, inter diffusion of the coating and steel substrate, the chemical composition of the coating and substrate metal and finally to analyze the surface of the black reinforcing steel exposed to synthetic pore solution and anti-icing solutions. XRF was used to determine the major alloying elements of steels where no mill certificate was provided. The steels that were tested are outlined below in Table 3-10.

**Table 3-10: Materials and corresponding test methods used for characterization**

<b>Material Analyzed</b>	<b>Methods Used</b>	<b>Purpose</b>
<b>304L</b>	XRF	composition
<b>Black steel-mill scale</b>	XRF	composition
<b>Black steel-sand blasted</b>	XRF	composition
<b>Black steel tested in synthetic pore solution contaminated with anti-icing solution</b>	SEM	Observe corroded surface morphology
<b>Box Girder</b>	XRF	composition
<b>Drain</b>	XRF	composition
<b>Galvanized rebar</b>	XRF/SEM/EDS	composition surface and substrate/coating thickness/composition surface and substrate
<b>Guard rail</b>	XRF/SEM/EDS	composition surface and substrate/coating thickness/composition surface and substrate
<b>Weathering steel</b>	XRF	composition

## Chapter 4 Experimental Results and Discussion

This chapter provides the results obtain from the testing outlined in Chapter 3 Experimental Procedure. The section are divided by test type and are: 4.1 Materials Tested, 4.2 Macro-cell Results: ASTM G109, 4.3 Micro-cell Results: Beams with Ponding Well, 4.4 Micro-cell Results: Synthetic Pore Solution and 4.5 Cyclic Corrosion Chamber Testing: SAE J2334-Immersion Testing.

### 4.1 Materials Tested

This section outlines the results of the various tests used to determine the chemical and physical attributes of the materials tested in all tests. This includes the anti-icing solution composition, the metals composition, properties of the concrete, and coating thicknesses, in addition to the results of the various tests carried out. In many cases, average data for the replicate specimens are presented here while those for individual specimens are shown in Appendix D: Experimental Results.

#### 4.1.1 Salt Solution

The compositions of the four salt solutions were determined by Activation Labs Ltd. and are shown below in Table 4-1. Constituents with less than 30mg/L have been omitted from Table 4-1 these include: Ba, Al, K, Mg, Mn, Si, Ag, As, Be, Bi, Ca, Cd, Ce, Co, Cr, Fe, Cu, Li, Mo, Na, Ni, P, Pb, Sb, S, Se, Sn, Sr, Te, Ti, Tl, U, V, W, Y, Zn, F, Cl, NO<sub>2</sub> (as N), Br, NO<sub>3</sub> (as N), PO<sub>4</sub> (as P) and SO<sub>4</sub>.

**Table 4-1: Salt solution composition in mg/L [9]**

Analyte symbol	K	Mg	Ca	Fe	Na	S	Sr	Cl	Br	SO <sub>4</sub>
<b>NaCl</b>	172	157	1,840	< 1	98 000	1030	26.6	157 000	< 50	2 970
<b>MgCl<sub>2</sub></b>	1 640	82 100	98.6	4.34	1 650	539	4.22	233 000	3 730	1 470
<b>CaCl<sub>2</sub></b>	7500	< 10	134 000	1.14	4 490	< 100	2 450	245 000	3 140	83.4
<b>Multi Cl</b>	5 990	9 940	58 500	3.57	46 100	< 100	1 110	211 000	2 640	125

The type and amount of impurities are a result of the other minerals found from where the solutions are mined and processed. The multi Cl<sup>-</sup> is mined directly in Ontario and requires minimal processing prior to being used on the road whereas the other solutions require additional processing to achieve the required concentrations, making the multi-chloride a more favourable option [80]. This also can give insight to where the solutions came from. For example, both the CaCl<sub>2</sub> and the multi Cl<sup>-</sup> brines

contain higher concentrations of strontium and potassium; lower concentrations of sulphate and sulphur; moderate to higher amounts of bromine. This suggests that these two products either came from the same or similar mine or that higher levels of strontium naturally accompany  $\text{CaCl}_2$ .

Although the  $\text{MgCl}_2$  and  $\text{NaCl}$  solutions have some similarities: (both containing higher concentrations of  $\text{SO}_4$  and low concentrations of strontium) they differ in bromine and potassium concentrations. Even though the amounts of  $\text{SO}_4$  are higher in the  $\text{MgCl}_2$  and  $\text{NaCl}$ , the  $\text{NaCl}$  concentrations are about double that of the  $\text{MgCl}_2$ .

The composition of the primary salt and chloride concentration are shown below in Table 4-2.  $\text{NaCl}$  has the lowest salt concentration (26%) and the lowest stoichiometric ratio between  $\text{Na}^+$  and  $\text{Cl}^-$  at one to one. Whereas  $\text{MgCl}_2$  and  $\text{CaCl}_2$  have higher salt concentrations (32% and 38% respectively) and higher stoichiometric ratio with both salts having a two to one ratio of  $\text{Mg}^{+2}$  and  $\text{Ca}^{+2}$  to  $\text{Cl}^-$ . The multi-chloride solution primarily consists of  $\text{CaCl}_2$  and  $\text{NaCl}$  with trace amounts of  $\text{MgCl}_2$  and has an intermediate concentration of 32% which is why the  $\text{Cl}^-$  concentration is higher than the  $\text{NaCl}$  but lower than the  $\text{MgCl}_2$  and  $\text{CaCl}_2$  counterparts. Finally, all solutions contain  $\text{K}$  which is likely present in the form of  $\text{KCl}$  with the  $\text{NaCl}$  solution having the lowest concentration.

**Table 4-2: Bulk salt and chloride concentration**

Solution name (primary constituent)	Per cent of constituent			
	$\text{NaCl}$	$\text{MgCl}_2$	$\text{CaCl}_2$	Total $\text{Cl}^-$
<i><b>NaCl</b></i>	25	1	0	16
<i><b>MgCl<sub>2</sub></b></i>	0	32	0	23
<i><b>CaCl<sub>2</sub></b></i>	1	0	37	25
<i><b>Multi Cl</b></i>	12	4	16	21

It is important to note that all of the solutions' concentrations are high (considering ocean water is frequently assumed to be about 5%  $\text{NaCl}$ ). The solution concentration is higher than that required to prevent ice formation, as the solution will be diluted with time from precipitation.

What is surprising is that these solutions are so concentrated that they are beyond the eutectic point of the solution, as can be shown below in Table 4-3. It is also important to note that the  $\text{MgCl}_2$  and  $\text{CaCl}_2$  solutions have eutectic freezing points significantly lower than  $\text{NaCl}$  at  $-33.9^\circ\text{C}$  and  $-51.0^\circ\text{C}$

respectively. At these low temperatures the ice is sufficiently cold that it will not regelate and poses little risk to motorists.

**Table 4-3: Solution eutectic point, concentration and solution freezing point**

Solution	Eutectic Point		Actual		
	Salt concentration [wt.%]	Liquidus temperature [°C]	Salt concentration [wt.%]	Cl <sup>-</sup> concentration [wt.%]	Liquidus temperature [°C]
<i>NaCl</i>	23.3	-21.1	25.5	15.7	-6
<i>MgCl<sub>2</sub></i>	21.7	-33.9	31.5	23.3	-16
<i>CaCl<sub>2</sub></i>	29.8	-51.0	37.9	24.5	-4
<i>Multi</i>	N/A	N/A	32.6	21.1	N/A

### 4.1.2 Concrete

The compression tests were completed using an ELE International compression tester; the loading rate was maintained between 0.15 and 0.35 MPa/s during loading prior to rapid yielding where no adjustments were made as per ASTM C39 [75]. The average strength of each batch is presented below in Table 4-4.

**Table 4-4: Concrete average 28-day strength**

Batch	Average Strength	
	MPa	psi
1	43	6280
2	58	8380
3	54	7800
4	51	7450

### 4.1.3 Metals' Compositions

The compositions of the stainless steels (not including 304L) obtained from the mill certificate, used in the cyclic corrosion chamber tested are shown below in Table 4-5. It is important to note the increased manganese in XM28 and 2101 both of which have lower nickel and molybdenum than their traditional counterparts, 316LN and 2205, respectively, making them less costly alloys. MMFX is not considered a true stainless due to its low chromium and nickel contents; this also makes it significantly cheaper than traditional stainless steels.

Also shown in Table 4-5 is the composition of the weathering steel. The weathering steel was analyzed by Bodycote Testing Group of Burlington, Ontario for Damgaard [58]. The results were obtained following ASTM D1-1976 M and ASTM E-1019. From this analysis, the steel would be considered 350A or 350AT according to CSA G40.21-04. Alternatively, the steel could be classified as an ASTM A588 Grad B or A588 Grade C.

**Table 4-5: Composition of stainless steels according to the mill certificate provided by steel suppliers and weathering steel by analysis**

Material	C	Mn	P	S	Si	Ni	Cr	Mo	N
<b>316LN</b>	0.025	1.17	0.031	0.028	0.66	10.54	18.00	2.03	0.14
<b>2101</b>	0.022	4.810	0.024	0.001	0.700	1.510	21.430	0.180	0.211
<b>2205</b>	0.023	1.46	0.030	0.001	0.59	4.95	22.71	3.03	0.14
<b>2304</b>	0.018	1.61	0.032	0.0010	0.43	4.05	22.44	0.19	0.136
<b>MMFX</b>	0.09	0.65	0.009	0.009	0.26	0.09	9.83	0.01	0.021
<b>XM28</b>	0.05	12.12	0.022	0.001	0.5	0.7	17.2	0.2	0.31
<b>Weathering steel</b>	0.06	1.16	0.011	0.006	0.40	0.29	0.49	0.01	

**Table 4-5: Composition of stainless steels according to the mill certificate continued**

Material	Co	Cu	V	Sn	B	Al	Ca	Nb
<b>316LN</b>								
<b>2101</b>		0.245						
<b>2205</b>								
<b>2304</b>	0.08	0.38						
<b>MMFX</b>		0.14	0.025	0.020				
<b>XM28</b>	0.1	0.1			0.002			
<b>Weathering steel</b>		0.24	0.053			0.03	<0.005	<0.005

#### 4.1.3.1 X-Ray Fluorescence Results

X-ray fluorescence analysis was used to determine some of the major alloying elements in the materials supplied without a mill certificate. The major limitation of the technique was the inability to detect the lighter elements, such as carbon and nitrogen. The results of the XRF analyses are shown below in Table 4-6 below.

From this analysis, the weathering steel could be classified as an ASTM A242 Type 1, A588 Grade A or A588 Grade B (see Table 3-7) but does not meet any of the CSA specifications for weathering steel (see Table 3-8). The guard rail interior, box girder and drain do not meet any of the specifications and are likely a plain carbon steel. The black steel rebar shows slightly higher than expected levels of sulphur and silicon to be classified as weldable steel (see Table 3-6) with almost double the amount of maximum allowable silicon in the mill scale. The phosphorus levels are low enough to meet specifications to be black steel.

The exterior of the guard rail shows about 9% less zinc and 7% more iron than the galvanized rebar. This is likely due to the guard rail being a field sample. Some of the zinc will have been consumed during the service life of the component by either dissolving and forming new compounds in the surroundings or forming a passive film of  $Zn(OH)_2$  depending on the environment. It is also possible that the material was galvanized.

**Table 4-6: Major alloying elements by wt. % of materials tested determined using XRF**

<b>Material</b>	<b>Fe</b>	<b>Zn</b>	<b>Ni</b>	<b>Cr</b>	<b>Al</b>	<b>Mo</b>	<b>Cu</b>	<b>Mn</b>	<b>Si</b>
<i><b>Black steel rebar-mill scale</b></i>	95.806	0.165	<LOD	0.108	<LOD	0.008	0.95	1.178	1.092
<i><b>Black steel rebar-sandblasted</b></i>	94.08	0.012	<LOD	0.064	3.048	0.007	0.74	1.154	0.696
<i><b>Guard rail (galvanized)-exterior</b></i>	7.823	85.328	<LOD	0.026	1.176	<LOD	0.071	<LOD	2.76
<i><b>Guard rail (galvanized)-interior</b></i>	98.014	0.202	0.099	0.149	<LOD	0.018	0.184	0.376	0.442
<i><b>Drain</b></i>	93.404	0.018	<LOD	0.064	4.959	0.01	0.161	0.481	0.678
<i><b>Weathering steel</b></i>	92.472	0.016	0.273	0.572	3.857	0.009	0.403	1.148	1.044
<i><b>Box girder</b></i>	91.277	1.302	<LOD	0.035	4.525	0.006	0.114	1.158	1.375
<i><b>Galvanized rebar-interior</b></i>	75.433	5.713	0.103	0.118	15.475	0.022	0.314	0.93	1.599
<i><b>Galvanized rebar-exterior</b></i>	0.988	94.019	0.109	0.151	2.715	<LOD	0.041	0.016	1.557
<i><b>304L</b></i>	69.067	0.021	8.515	17.81	<LOD	0.491	0.696	1.343	1.228

Note: Areas marked with “<LOD” are below levels of detection

**Table 4-6: Major alloying elements by wt. % of materials tested determined using XRF continued**

<b>Material</b>	<b>Nb</b>	<b>Zr</b>	<b>Pb</b>	<b>W</b>	<b>Co</b>	<b>Sn</b>	<b>V</b>	<b>Ti</b>	<b>S</b>	<b>P</b>
<i>Black steel rebar-mill scale</i>	<LOD	<LOD	<LOD	<LOD	<LOD	0.011	0.055	0.006	0.159	<LOD
<i>Black steel rebar-sandblasted</i>	<LOD	<LOD	<LOD	<LOD	<LOD	0.01	0.038	0.028	0.05	<LOD
<i>Guard rail (galvanized)-exterior</i>	<LOD	<LOD	1.459	1.149	<LOD	<LOD	<LOD	0.048	<LOD	0.132
<i>Guard rail (galvanized)-interior</i>	<LOD	<LOD	<LOD	<LOD	<LOD	0.022	<LOD	<LOD	0.106	<LOD
<i>Drain</i>	0.027	<LOD	<LOD	<LOD	<LOD	0.011	0.007	0.067	0.037	0.02
<i>Weathering steel</i>	<LOD	<LOD	<LOD	<LOD	<LOD	<LOD	0.089	0.037	0.053	<LOD
<i>Box girder</i>	<LOD	<LOD	<LOD	<LOD	<LOD	0.014	<LOD	0.053	0.053	<LOD
<i>Galvanized rebar-interior</i>	<LOD	0.003	<LOD	<LOD	<LOD	0.012	0.008	<LOD	0.189	0.065
<i>Galvanized rebar-exterior</i>	<LOD	<LOD	0.239	<LOD	0.028	0.079	<LOD	0.012	<LOD	<LOD
<b>304L</b>	0.022	<LOD	<LOD	<LOD	0.244	0.02	0.102	<LOD	0.079	<LOD

Note: Areas marked with “<LOD” are below levels of detection

**4.1.3.2 Scanning Electron Microscopy and Energy-Dispersive X-ray Spectroscopy Results**

Scanning electron microscopy and energy dispersive x-ray spectroscopy were used to analyze the cross-section of the galvanized rebar, galvanized guard rail and the surface of the black steel rebar used in the synthetic pore solution testing, which will be discussed in Section 4.4.4.2.

Samples of the galvanized rebar and guard rail were sectioned and polished with a final polishing step using a 0.05 µm suspended alumina powder. An SEM image of each is shown in Figure 4-1 and Figure 4-2, respectively. The macrographs in Figure 4-1 (a) and Figure 4-2 (a) show an overview of each component. The thickness and composition of the zinc coating were taken at three locations on the cross section extending approximately over 1/3 the circumference/length of the specimen, Figure 4-1 (b), (c), (d) and Figure 4-2 (b), (c), (d). In addition to these measurements, the composition of the substrates was measured and the composition across the Zn-Fe interface was measured, shown in Figure 4-1 (d) and Figure 4-2 (b) for the galvanized rebar and guard rail respectively. The two bands observed in Figure 4-1 (b) were both scanned and the composition of the inner band was found to be

the  $\zeta$  phase (95.25% Zn-4.75%Fe). As such, the thickness measurements were made from the boundary between the inner band and the steel and the outside edge.

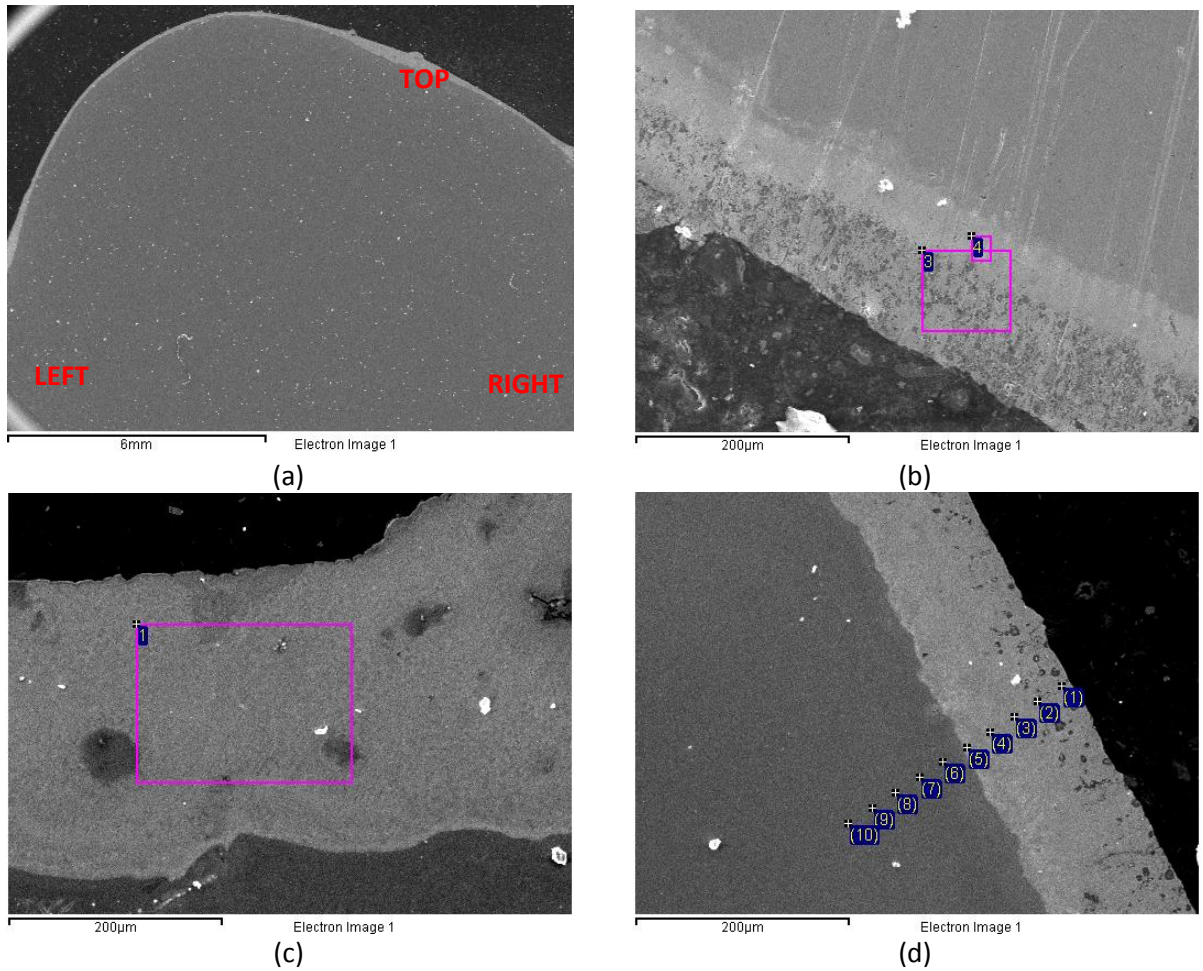


**Figure 4-1: SEM image of galvanized reinforcing steel (a) overview of the cross section (b), (c) and (d) right are three other areas where composition and depth measurements were taken. Location (d) is where composition measurements across the Zn-Fe boundary were made.**

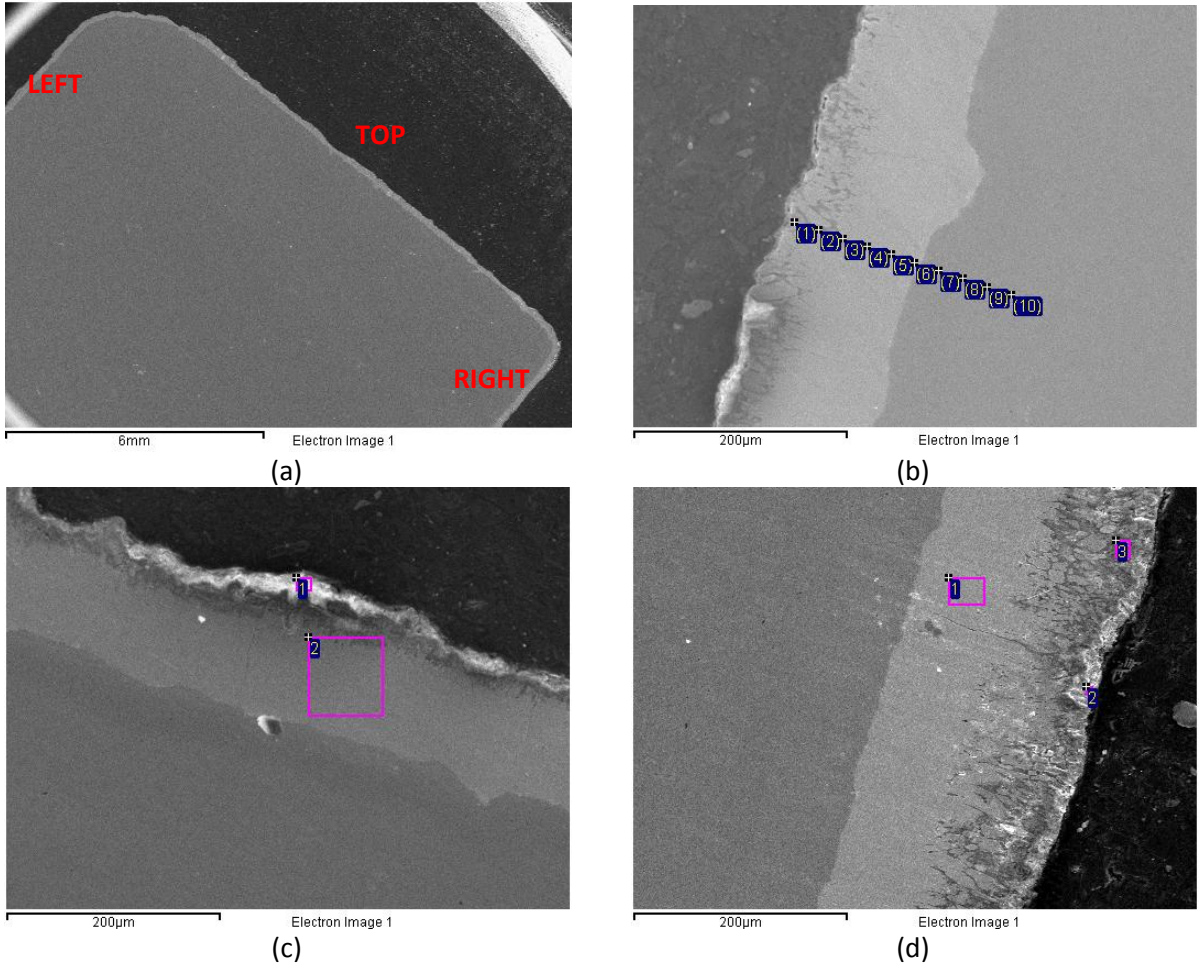


**Figure 4-2: SEM image of a guard rail sample (a) overview of the cross section (b) left,(c) top and (d) right are three other areas were composition and depth measurements were taken. Location (b) is where composition measurements across the Zn-Fe boundary were made.**

The thickness measurements of the zinc coatings are shown below in Table 4-7. On average, the zinc layer of the guard rail is 15% less than that of the galvanized rebar. Because the guard rail was taken from the field, it is not possible to determine the original thickness of the zinc layer.

**Table 4-7: Zinc thickness measurements of the galvanized rebar and guard Rail**

Location Figure 4-1 (a) and Figure 4-2 (a)	Thickness [ $\mu\text{m}$ ]	
	Galvanized Rebar	Guard Rail
Left	138	118
	113	147
	149	141
Top	285	113
	251	112
	275	117
Right	107	207
	126	199
	127	185
<b>Average</b>	<b>175</b>	<b>149</b>
<b>Standard deviation</b>	<b>73</b>	<b>39</b>

The composition of the zinc coating was determined using EDS. The results are shown below in Table 4-8. The amount of zinc in the guard rail's galvanic coating is slightly less than that of the galvanized rebar's coating as expected. The guard rail is both used and, as mentioned, has a thinner zinc coating. The galvanic coating of the guard rail and rebar would be primarily composed of the intermetallic  $\delta$  phase ( $\text{Fe}_{10}\text{Zn}_{90}$ ) and  $\zeta$  phase ( $\text{Fe}_5\text{Zn}_{95}$ ), respectively.

**Table 4-8: Composition of the zinc coating**

Location Figure 4-1 (a) and Figure 4-2 (a)	Galvanized rebar		Galvanized guard rail	
	Zn	Fe	Zn	Fe
<b>Top</b>	100.0	0.0	91.1	8.9
<b>Right</b>	97.9	2.1	92.1	7.9
<b>Left</b>	98.2	1.8	94.3	5.7
<b>Average</b>	<b>98.7</b>	<b>1.3</b>	<b>92.5</b>	<b>7.5</b>

The line composition was taken to determine the amount of diffusion between the zinc and substrate as shown in Table 4-9. Once again the results were not surprising as the diffusion of iron into the zinc layer of the guard rail was higher than the galvanized rebar, which may be attributed to its older age and thinner zinc coating or it may be galvanized. In the rebar the galvanized layer was found to contain diffused magnesium from the substrate. The surface of the rebar consisted primarily of the

zinc rich  $\eta$  phase whereas the surface of the guard rail was a mixture of the zinc rich  $\eta$  phase and the intermetallic  $\zeta$  ( $\text{Fe}_5\text{Zn}_{95}$ ) phase. It should be noted that these variations are not exact because the volumes of material sampled by EDS would overlap to some degree.

**Table 4-9: Composition across the zinc–iron interface**

Location*	Galvanized rebar				Guard rail		
	Mn	Fe	Zn	Probable phase(s)	Fe	Zn	Probable phase(s)
<b>1</b>	0.0	0.0	100.0	$\eta$	1.1	98.9	$\eta+\zeta$
<b>2</b>	0.0	1.4	98.7	$\eta+\zeta$	2.6	97.4	$\eta+\zeta$
<b>3</b>	0.0	2.6	97.4	$\eta+\zeta$	8.7	91.3	$\delta$
<b>4</b>	0.0	7.5	92.5	$\delta$	6.2	93.8	$\zeta+\delta$
<b>5</b>	0.1	9.0	90.9	$\delta$	11.8	88.2	$\delta+\Gamma_1$
<b>6</b>	1.4	97.4	1.1	$\alpha\text{Fe}$	10.3	89.8	$\delta$
<b>7</b>	1.0	98.4	0.6	$\alpha\text{Fe}$	99.9	0.1	$\alpha\text{Fe}$
<b>8</b>	0.5	99.5	0.0	$\alpha\text{Fe}$	100.0	0.0	$\alpha\text{Fe}$
<b>9</b>	0.8	99.2	0.0	$\alpha\text{Fe}$	98.6	1.4	$\alpha\text{Fe}$
<b>10</b>	2.7	97.3	0.0	$\alpha\text{Fe}$	98.5	1.5	$\alpha\text{Fe}$

\* The location is shown in the corresponding figures, it does not correspond to a distance

Note: the zinc-iron interface in both samples is between location 5 and 6 for the galvanized rebar and between 6 and 7 for the guard rail

The compositions of the substrate steel of both samples are shown below in Table 4-10. The major difference is the larger amount of alloying elements in the guard rail. This also explains why it appears as though a larger amount of zinc diffused into the base metal from Table 4-9. However, from the EDS measurements taken at the centre of the base metal, it is apparent that zinc is an alloying (or contaminant) element in the guard rail steel.

**Table 4-10: Chemical composition of the substrate steel of the galvanized rebar and guard rail**

Element	Galvanized rebar	Guard rail
<i>Cr</i>	0.0	0.3
<i>Cu</i>	0.0	1.2
<i>Fe</i>	97.3	95.5
<i>Mn</i>	2.4	0.6
<i>Ni</i>	0.0	0.5
<i>S</i>	0.0	0.3
<i>Si</i>	0.4	0.2
<i>Zn</i>	0.0	1.4

One attribute that was apparent on the guard rail was the various regions in the zinc coating. Upon closer inspection there are three distinct regions or phases. On the outer edge, there is a white layer as shown in Figure 4-2 (c) and (d) above. Deeper into the zinc coating but still near the surface a second layer intermingled with the primary layer is visible. This is shown below in Figure 4-3 highlighted by region one and two.

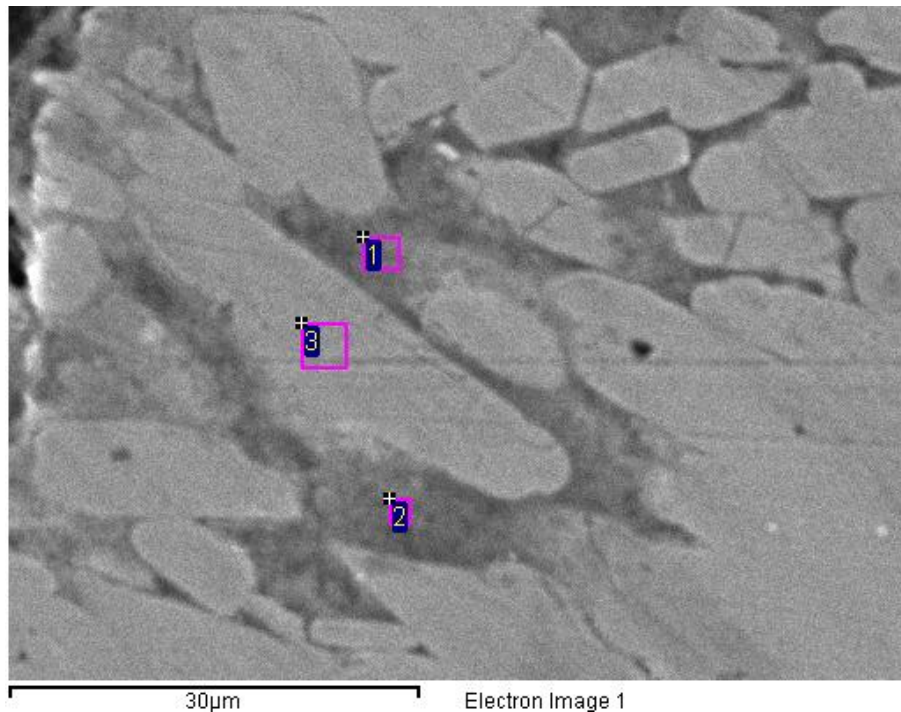


**Figure 4-3: High magnification micrograph of the left side zinc coating of the guard rail**

The EDS analysis of these regions is shown below in Table 4-11. The galvanized region is the bulk of the galvanized layer and consists primarily of zinc it also has low amounts of magnesium, calcium and chlorine. However, there is still a significant amount of sodium. The reason for this is still unclear. In all regions the amount of magnesium and calcium is low with higher amounts of sodium and chlorine. This suggests the guard rail was exposed to anti-icing solution in service.

**Table 4-11: EDS Analysis of the various regions found in the zinc layer of the guard rail**

colour	Location Figure 4-2 (a)	Na	Mg	Ca	Cl	Zn	Fe
<i>dark</i>	<i>left</i>	17.1	0.0	0.0	21.8	60.3	0.8
	<i>left</i>	9.3	0.5	0.7	22.7	66.8	0.2
	<i>right</i>	10.4	0.4	0.6	11.5	62.6	14.5
	<b>Average</b>	<b>12.3</b>	<b>0.3</b>	<b>0.4</b>	<b>18.6</b>	<b>63.2</b>	<b>5.2</b>
<i>Galvanized region</i>	<i>left</i>	7.1	0.0	0.0	1.1	84.9	6.8
	<i>right</i>	15.3	0.0	0.0	0.0	78.0	6.7
	<b>Average</b>	<b>11.2</b>	<b>0.0</b>	<b>0.0</b>	<b>0.6</b>	<b>81.5</b>	<b>6.8</b>
<i>light</i>	<i>right</i>	<b>12.8</b>	<b>0.0</b>	<b>0.2</b>	<b>18.6</b>	<b>62.6</b>	<b>5.7</b>

An EDS analysis was also completed showing amounts of oxygen in the lighter region. It is important to note that the ability for EDS to quantify the oxygen content is unreliable and these measurements should only be considered qualitatively. No oxygen was found in the galvanized region. The high amounts of oxygen in the “light” layer suggest it may be zinc hydroxide or possibly a complex salt due to the high presence of chlorine.

**Table 4-12: EDS Analysis of white region on the outside edge of the zinc coating**

Location Figure 4-2 (a)	O	Cl	Fe	Zn
<i>top</i>	24.6	10.7	16.1	48.6
<i>right</i>	17.8	10.3	13.4	58.5
<b>Average</b>	<b>21.2</b>	<b>10.5</b>	<b>14.8</b>	<b>53.5</b>

## 4.2 Macro-cell Results: ASTM G109

The following section discusses the results of the ASTM G109 tests of black steel embedded in concrete and exposed to anti-icing agents. The indoor and outdoor specimens are shown below in Figure 4-4 and Figure 4-5 respectively. All measurements reported here are the averages of all black

steel rebar exposed to similar conditions, i.e. indoor or outdoor and anti-icing solution. There are a total of four and three specimens for each anti-icing solution for indoor and outdoor conditions, respectively. The individual measurements are reported in Appendix D: section D-1 Macro-cell Results: ASTM G109.



**Figure 4-4: Twenty indoor ASTM G109 specimens**



Figure 4-5: Fifteen outdoor ASTM G109 specimens

#### 4.2.1 Corrosion Potential Measurements

Corrosion potential measurements were taken every two weeks, once with the top and bottom bars connected, resulting in a mixed potential and once with the bars disconnected labeled “anodic” potentials. The results are shown in Figure 4-6. The reason for the sinusoidal appearance of the plots is a result of taking measurements during both the wet and dry cycles with the dry cycles having more positive corrosion potential measurements than the wet cycles. All of the indoor bars appear to be passive which accounts for the small variability between the mixed potentials and the “anodic” potential. If active corrosion were to initiate, it would be expected that the mixed potential would be more cathodic than that of the top bar taken when it is disconnected from the bottom bars.

With regards to the outdoor specimens, some of the potentials appear to have dropped to a region that suggests corrosion may initiate. But again the difference between the mixed and “anodic” potential is very low suggesting that the all the bars are still passive. Lastly, the gap in the outdoor

specimen corrosion potential measurements is a result of the solution freezing. This occurred during a snow storm which drastically diluted the solutions as well as providing adequately low temperatures.

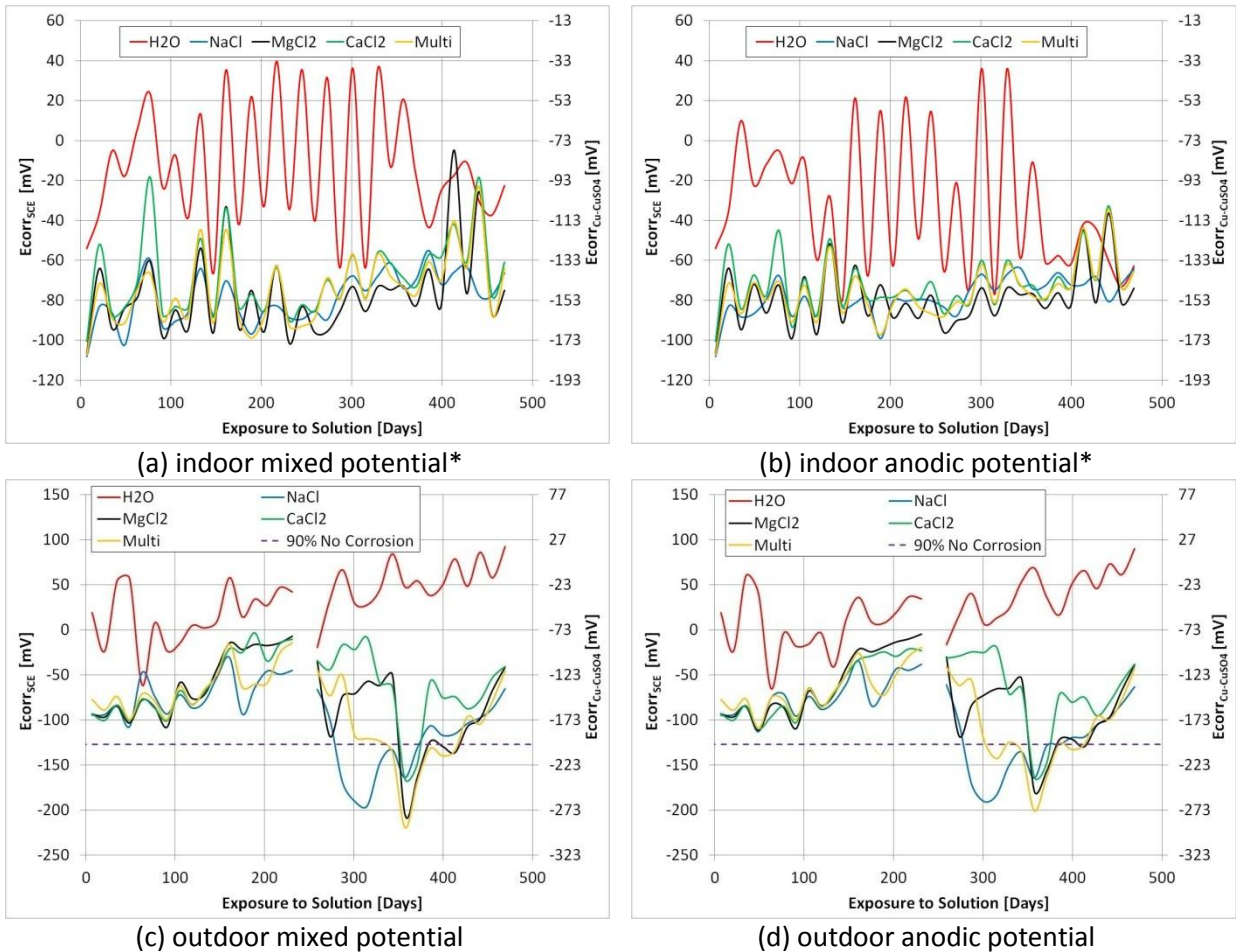


**Figure 4-6: Average corrosion potential measurements against SCE of ASTM G109 specimens (a) indoor specimens with resistor connected, (b) indoor specimens with resistor disconnected, (c) outdoor specimens with resistor connected and (d) outdoor specimens with resistor disconnected.\*Note all values above  $-200 \text{ mV}_{\text{SCE}}$  in the 90% no corrosion region according to ASTM G1**

#### 4.2.2 Macro-Cell Corrosion Current Density

Macro-cell corrosion current density measurements of ASTM G109 specimens were taken weekly and the results are displayed below in Figure 4-7 and Figure 4-8 for indoor and outdoor specimens respectively. In all cases the corrosion current density is low and in the passive region. In fact, the variation in measurements is likely due to environmental factors such as electrical noise, temperature and relative humidity. The outdoor specimens display this trend during the summer months with the

increase in corrosion current density (both in the positive and negative direction) with current densities that are still considered passive. Though the current densities measured in the outdoor specimens are two orders of magnitude higher than the corrosion current densities measured on the indoor specimens they are still passive with less than half a micrometer of depth loss per year. One possible reason for this is the length and location of the wires. The indoor specimens are within about 2 m from the data acquisition system inside a concrete room. On the other hand, the outdoor specimens have wires that travel from the same room as the indoor specimen through the engineering materials building to the outside (about 10 m), leaving them significantly more exposed to electrochemical noise. The results to-date do not show current densities high enough to be considered active corrosion and variations are attributed to be the result of electrical noise.

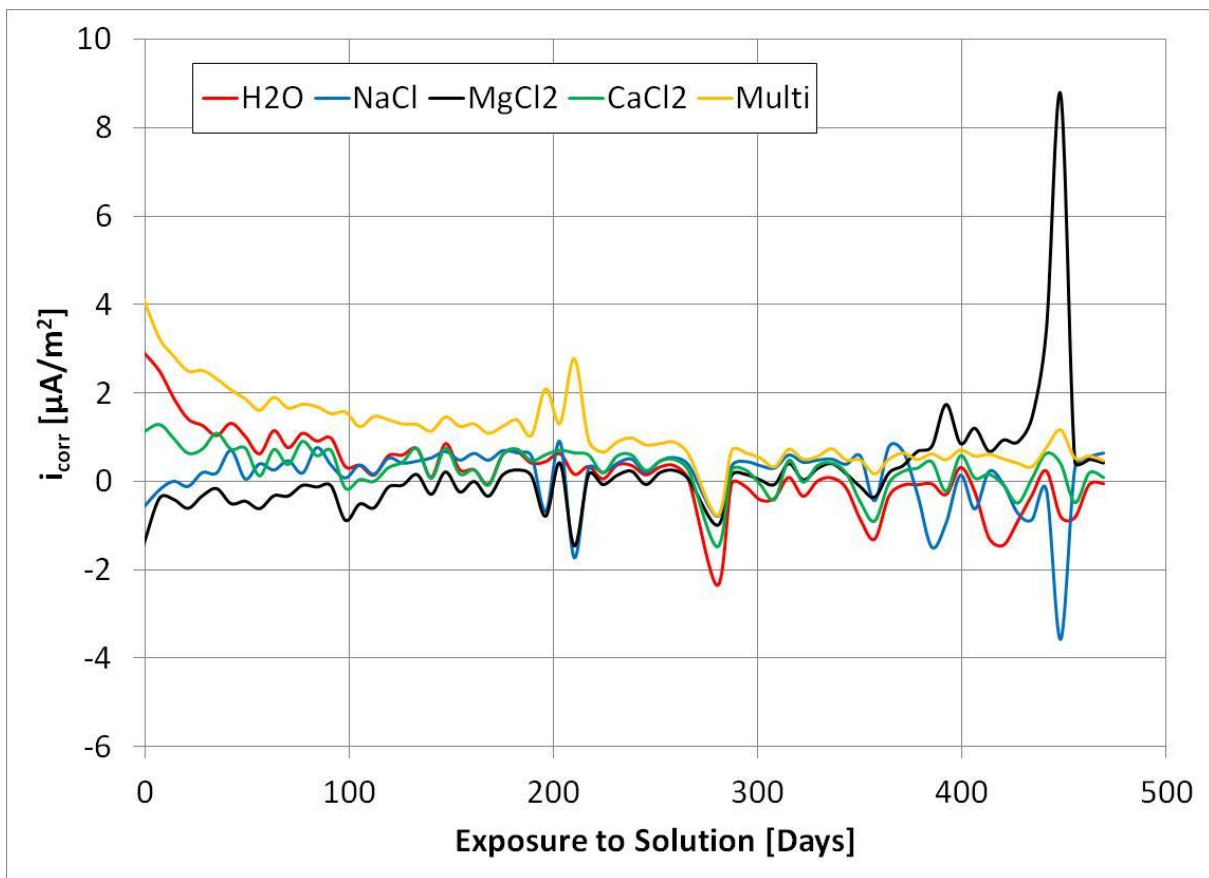


Figure 4-7: Average macro-cell corrosion current density measurements of indoor specimens. Note  $1 \mu\text{A}/\text{m}^2 = 0.1 \text{ nA}/\text{cm}^2 \approx 1 \text{ nm}/\text{year}$

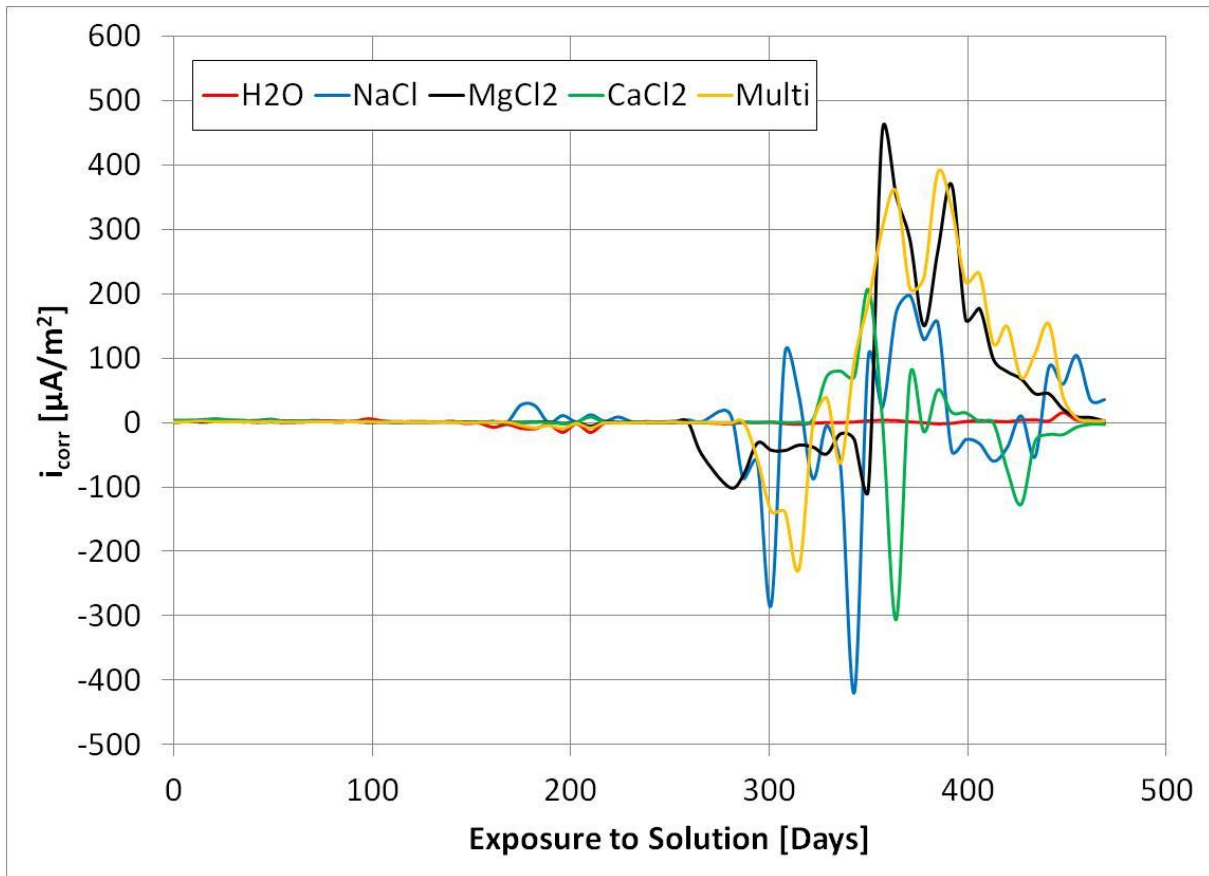


Figure 4-8: Average macro-cell corrosion current density measurements of outdoor specimens.  
 Note  $100\mu\text{A}/\text{m}^2 = 10 \text{ nA}/\text{cm}^2 \approx 135 \text{ nm}/\text{year}$

### 4.2.3 Micro-cell Corrosion of the Top and Bottom Bars of the ASTM G109

#### Specimens

Galvanostatic pulse and potentiostatic LPR tests were completed in order to compare the micro-cell corrosion with the typically measured macro-cell corrosion. The test parameters used for these tests were the same as those outlined in section 3.3.1. The exception to this was that the GP tests were held for 30 s instead of 10 s. The counter and reference electrode were both placed in the ponding well with solution. The tests measurements were made on the dates of 2013-May-22, 2013-May-22 and 2013-June-10 which correspond to 372, 385 and 404 days of exposure, respectively. The data, shown in Figure 4-9, Figure 4-10 and Figure 4-11, are the averages of the bars exposed to the particular environment and solution. Furthermore, the top bars were disconnected from the bottom bars, i.e. all measurements for the top bar represent only the top bar and measurements of the

bottom bars are mixed measurements of both bottom bars as they are still connected electrically with a wire.

The resistance of the concrete is measured between the counter electrode and the working electrode, i.e. the bar(s) being tested, the results are shown in Figure 4-9. The bottom bar of all specimens exhibited higher resistances than the top counterpart. This was a result of the greater layer of concrete between the bars and the counter electrode. The outdoor water-exposed specimens showed significantly higher resistances than the other specimens (more than a factor of two) but the difference between the top and bottom bars was actually quite low in comparison to the other specimens. Anti-icing solutions in the concrete are expected to decrease the electrical resistance of the pore solution. Therefore the similar resistance of the indoor specimens exposed to the salts to that exposed to water suggests that the anti-icing solutions are diffusing slowly. On the other hand, if the solutions were to diffuse through the top layer of concrete in the water-exposed specimen, the small difference in resistance between the top bar and bottom bars suggest that the ionic flow between the bars would be easier and, therefore, allow the initiation of macro-cell corrosion. Furthermore, the specimens outside had become diluted due to precipitation, and during the winter allowed the specimens to freeze. The freezing and thawing cycles would have induced damage to the concrete. This would have opened existing cracks and/or created new cracks. These new cracks would allow the diffusion of more salt solution and increased the conductivity.

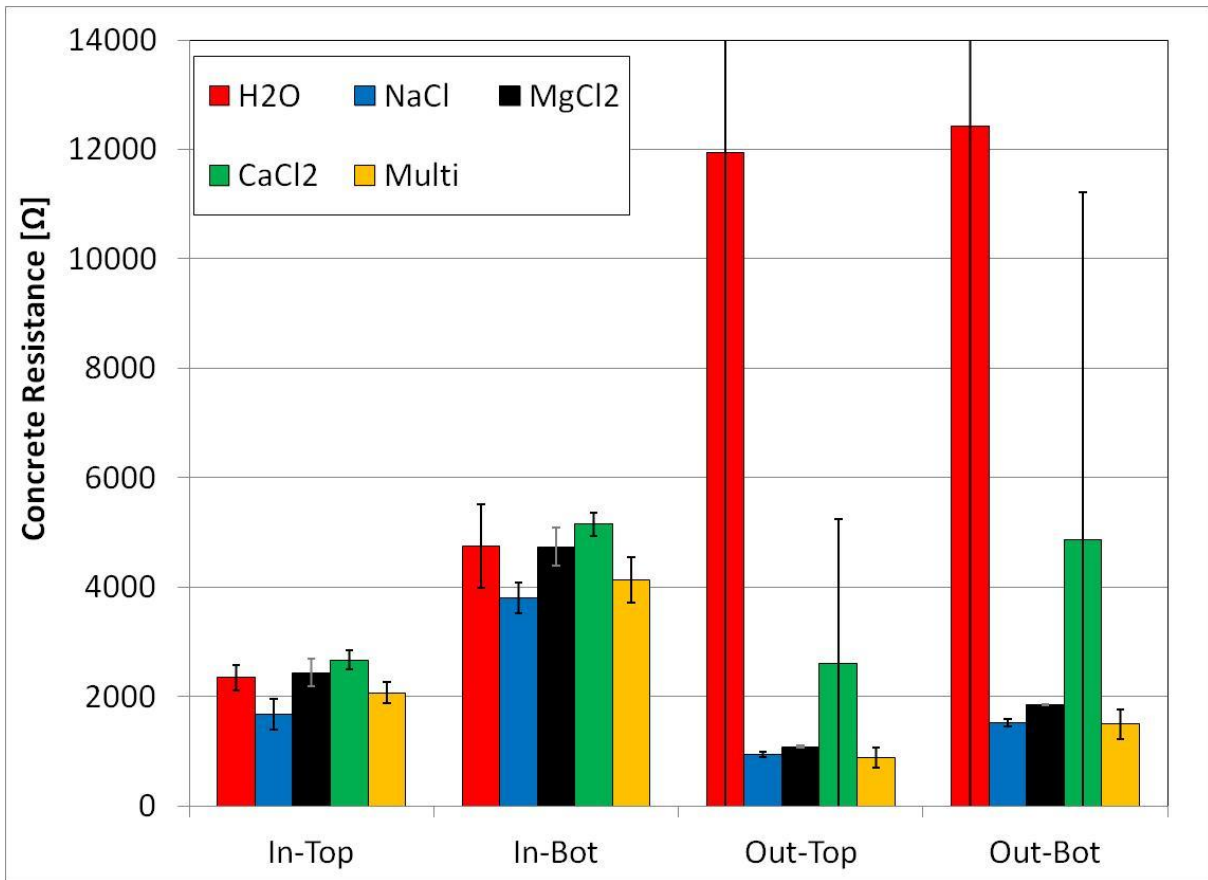


**Figure 4-9: Average concrete resistance measurements of 4 and 3 bars respectively for indoor and outdoor ASTM G109 specimens including error bars of one standard deviation, the spread of the outdoor water-exposed specimens was significantly higher than the other specimens and the standard deviation of the top and bottom bars are 16410  $\Omega$  and 16501  $\Omega$  respectively.**

The corrosion potential measurements of plus/minus two standard deviations ( $\sigma$ ) from the average corrosion potential of both the top and bottom bars are shown below in Figure 4-10. The data for all bars, except the outdoor specimens exposed to multi  $\text{Cl}^-$  solutions show potentials more positive than  $-127 \text{ mV}_{\text{SCE}}$  ( $-200 \text{ mV}_{\text{CSE}}$ ) which, according to ASTM C876, implies there is a 90% probability of no corrosion. The outdoor specimens exposed to multi  $\text{Cl}^-$  solutions have potentials in the region where the probability of corrosion is uncertain. All of the outdoor specimens did have at least one bar that was in the region where corrosion may be present, while the indoor specimens were all in the region of 90% probability of no corrosion region.

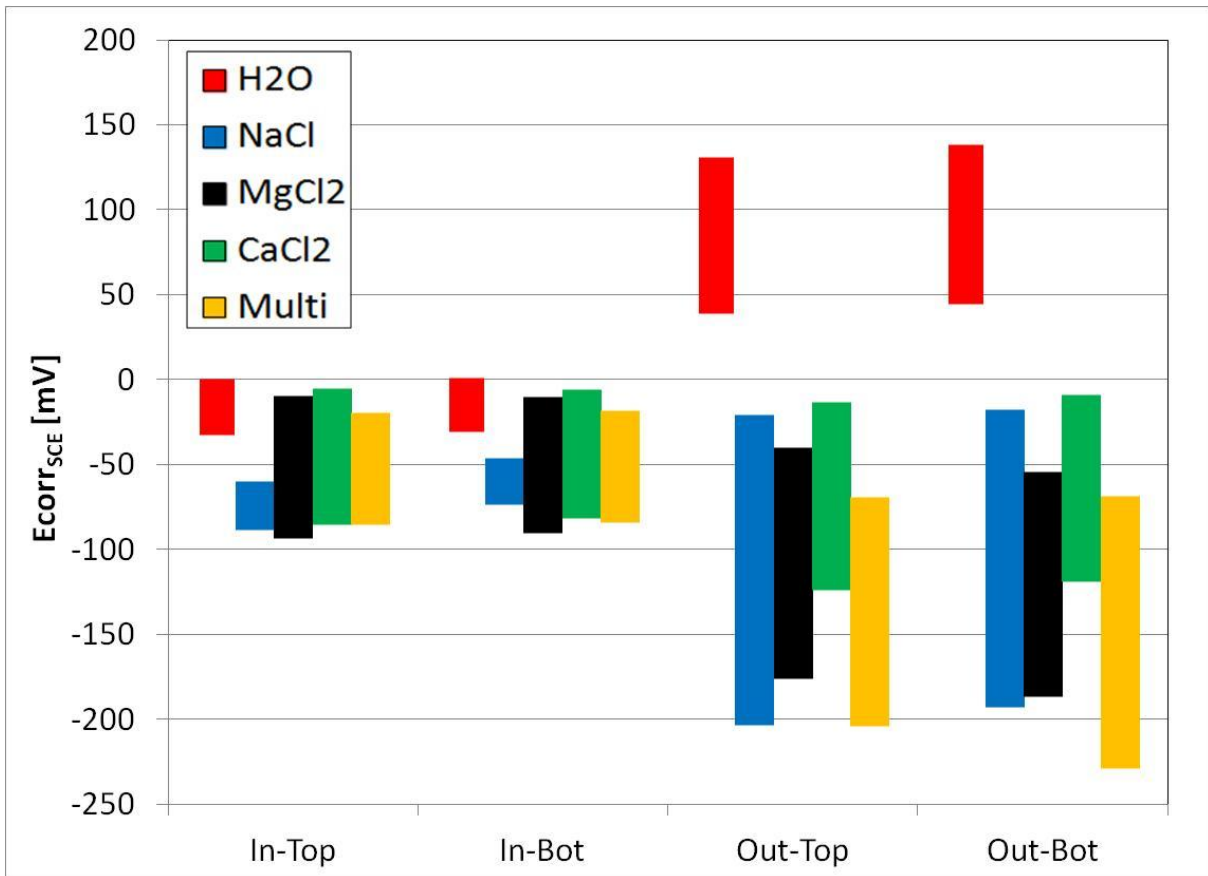


**Figure 4-10: Average corrosion potential measurements  $\pm$  one standard deviation of 4 and 3 bars respectively for indoor and outdoor ASTM G109 specimens tested using the galvanostatic pulse technique**

The micro-cell corrosion measurements in Figure 4-11 are all in the region of milliamps per square metre which is equivalent to  $\sim 1 \mu\text{m}/\text{year}$  and generally regarded as passive. The indoor top bars are all corroding more than the bottom bars. This may be attributed to the ingress of chlorides reducing the effectiveness of the passive film of the top bars. However, the water-exposed specimen also shows this trend. This could be attributed to the greater availability of oxygen, however due to the small values for corrosion and significant overlap of values between the top and bottom bars, no definite correlation can be drawn. The only conclusions that can be drawn are that all bars are passive and the outdoor bars experience mildly higher corrosion rates with a higher spread in data.

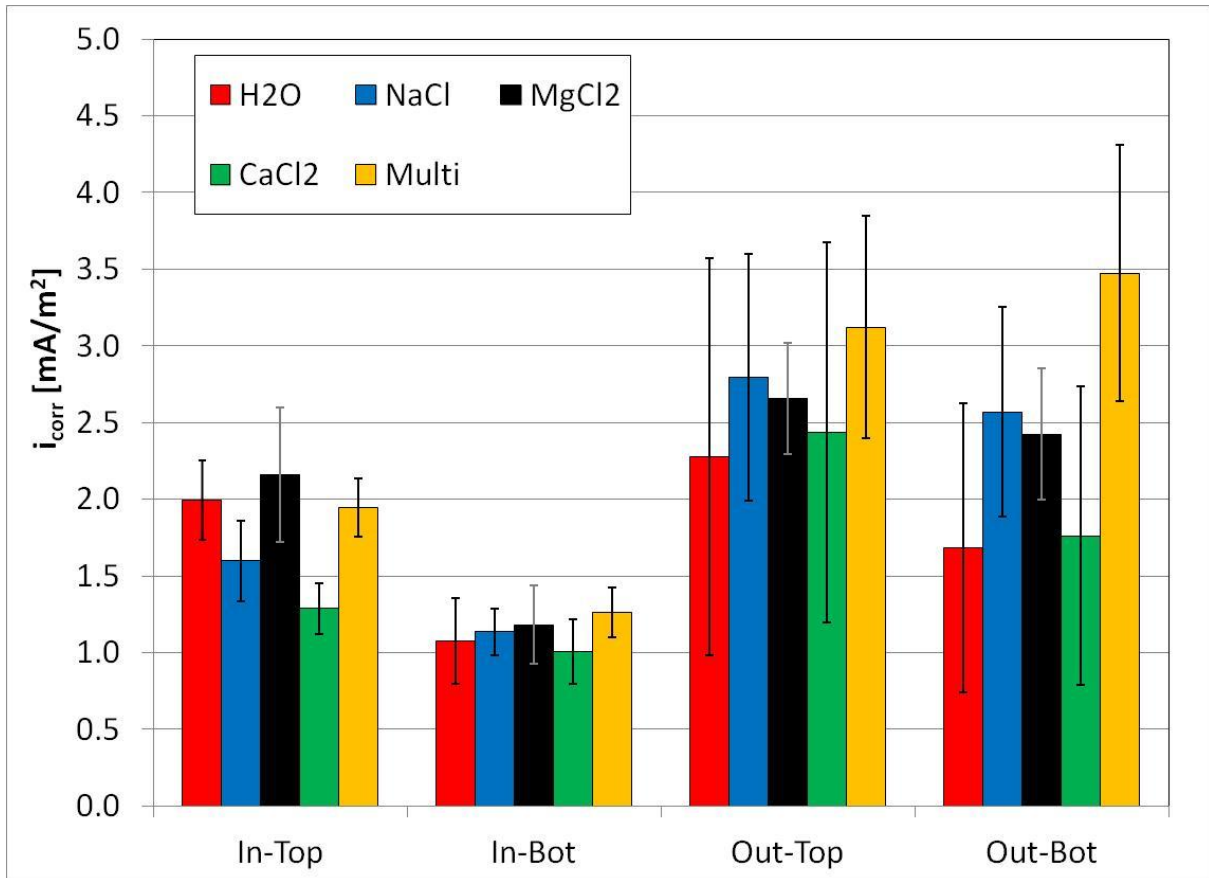


**Figure 4-11: Average corrosion current density measurements of 4 and 3 bars respectively for indoor and outdoor ASTM G109 specimens including error bars of one standard deviation. Note  $1 \text{ mA/m}^2 = 100 \text{ nA/cm}^2 \approx 1 \text{ } \mu\text{m/year}$**

In addition to the typical corrosion measurements, a comparison was made between micro- and macro- corrosion. The comparison of these two forms of corrosion is shown in Figure 4-12. It is important to note that both axes are plotted on a log scale and that the black line indicates a slope of one, i.e. any points above this line represent areas dominated by micro-cell corrosion and any points below this line represent areas dominated by macro-cell corrosion. In all cases the micro-cell corrosion dominated the macro-cell corrosion, in most cases by three orders of magnitude. A few of the outdoor specimens showed some trend towards unity between micro-cell and macro-cell corrosion, but for the most part there is still an order of magnitude difference between the two types of corrosion. It is also important to note that all of these measurements would be considered passive, with the highest measurements being  $4.6 \text{ mA/m}^2$  which is approximately  $5.3 \text{ } \mu\text{m/year}$  of depth loss. It is also interesting to note the spread of the two types of data. The micro-cell corrosion varies by less than two orders of magnitude while macro-cell corrosion covers more than four orders of magnitude.

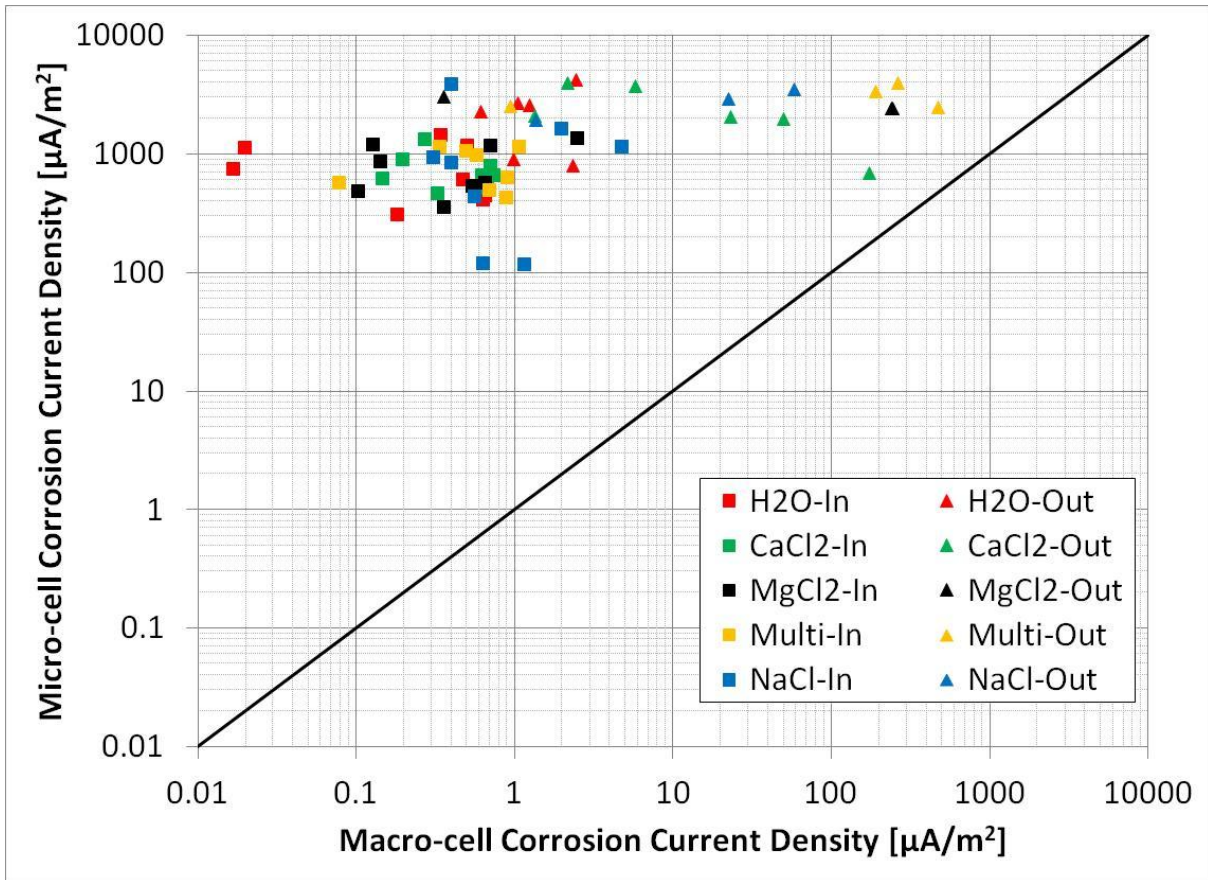
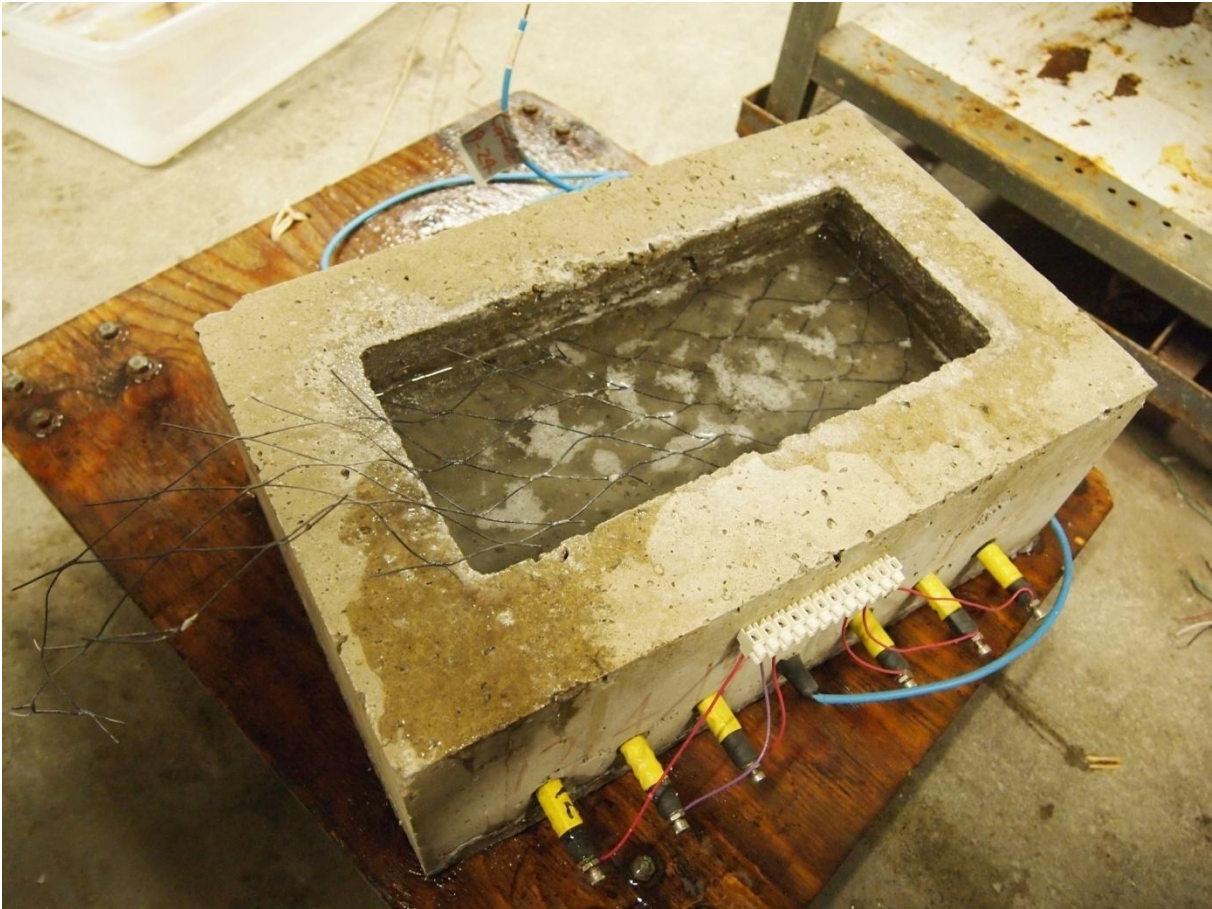


Figure 4-12: Micro-cell versus macro-cell corrosion current density measurements of ASTM G109 specimens. Note: that both the ordinate and abscissa axis are plotted on a log scale; the black line has a slope of one. Note  $1 \mu\text{A}/\text{m}^2 = 0.1 \text{ nA}/\text{cm}^2 \approx 1 \mu\text{m}/\text{year}$

### 4.3 Micro-cell Results: Beams with Ponding Well

The following section discusses the results of the micro-cell beam tests shown in Figure 4-13. Using the test data, it was possible to determine the concrete resistance ( $R_c$ ), corrosion potential ( $E_{corr}$ ) and the corrosion current density ( $i_{corr}$ ). All of the measurements displayed in this section are the averages of six black steel rebar in each beam (i.e. the average of all specimens exposed to the same anti-icing solution). The results gathered from the individual bars can be found in Appendix D: Section D-2.



**Figure 4-13: Sample beam ponded with  $\text{CaCl}_2$  solution and disconnected from electrochemical measuring equipment**

### ***4.3.1 Concrete Resistance***

The resistance of the concrete between the reinforcing steel and the surface of the concrete exposed to chlorides helps determine the quality and the state of the concrete. Furthermore, this value is needed to determine the polarization resistance from potentiostatic LPR tests (as discussed in Chapter 3 Experimental Procedure). The resistance was determined for each bar using the galvanostatic pulse (GP) technique. The results for bars exposed to the same chlorides have been averaged for each data point and the results are shown in Figure 4-14 below.

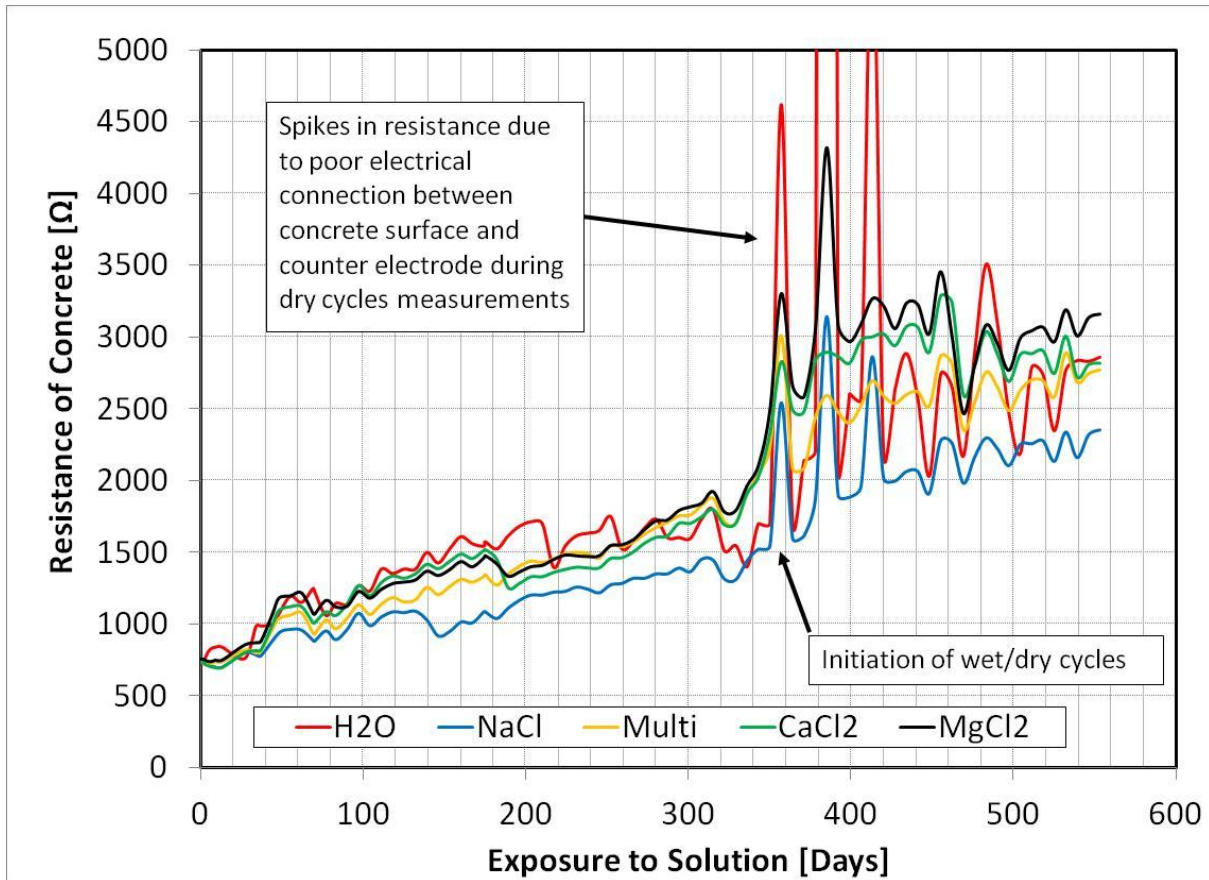


**Figure 4-14: Average of six resistance measurements between the counter electrode (Ti mesh) and reinforcing steel specimens against time**

The reason for the drastic change at about the 360 day mark is that this is when the exposure of anti-icing solution was changed from continuous to cyclic. The high peaks represent measurements taken during the midst of a dry cycle, whereas, the low points represent the midst of a wet cycle. This is expected as the amount of electrolytic material available for electrons to travel is decreased in dry concrete. Furthermore, the points with extremely high resistance are a result of the surface being too dry when testing during dry cycles, adding to the contact resistance between the interface of the counter electrode and the concrete. The future measurements do not show this tendency as the amount of pre-wetting of the concrete was increased.

The gradual increase of resistance of all specimens is a result of the concrete maturing. As the concrete cures and hardens, the amount of available electrolytic paths decreases resulting in the increase in concrete resistance. The possible reason for the higher resistance of specimens exposed to the MgCl<sub>2</sub> solution compared to the other solutions is the formation of brucite (Mg(OH)<sub>2</sub>) at the

surface. However, the difference between the reference sample and  $MgCl_2$  is only about 5% which is not significant when the spread of the data and variation in concrete is considered.

Other than the cycling of resistance with the wet and dry cycles, there is no significant change in the concrete resistance. This suggests that there are currently no observable effects of the salts on the concrete and no cracks (corrosion induced or otherwise) have formed.

### ***4.3.2 Corrosion Potential Measurements***

The corrosion potential measurements thus far have all been in the range designated by ASTM C876 as 90% probability of no corrosion, with the exception of the specimens exposed to NaCl solution as shown in Figure 4-15. Due to NaCl's properties of saturation and relative humidity, at about 20-25°C NaCl will maintain the relative humidity at its surface of about 74% [81]. If the relative humidity of the surrounding air is less than this, water evaporates and NaCl will begin to crystallize out of the solution. This resulted in a large amount of NaCl leaching out over the edge of the ponding well and onto the outside of the bars as shown in Figure 4-16. Furthermore, the solution seeped underneath the beam and began to be absorbed into the beam through the bottom, resulting in two bars showing signs of active corrosion, shown in Figure 4-17.

To remedy this problem, all of the beams were removed and disconnected from the measuring equipment and cleaned with a pressure washer. The beams were then returned, raised on PVC pipe that acted as 2.5 cm (~1 in) legs and placed inside plastic containers. Furthermore, the ponding wells were never fully filled and the NaCl specimen was covered with cellophane to limit evaporation. Once the beams were cleaned and replaced, the two NaCl specimens that showed signs of corrosion subsequently repassivated with time. It is interesting to note the steel has the ability to self heal with time provided the continual ingress of  $Cl^-$  is halted.

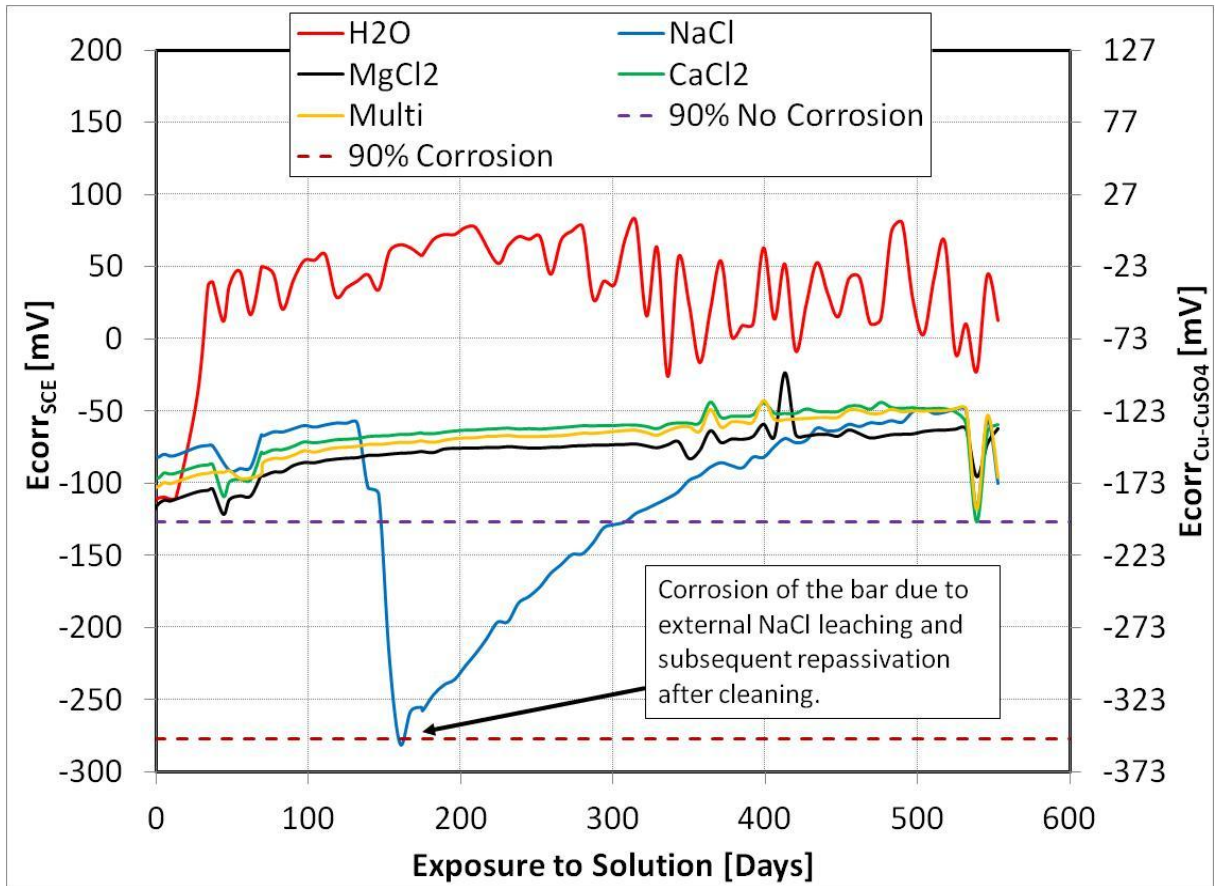
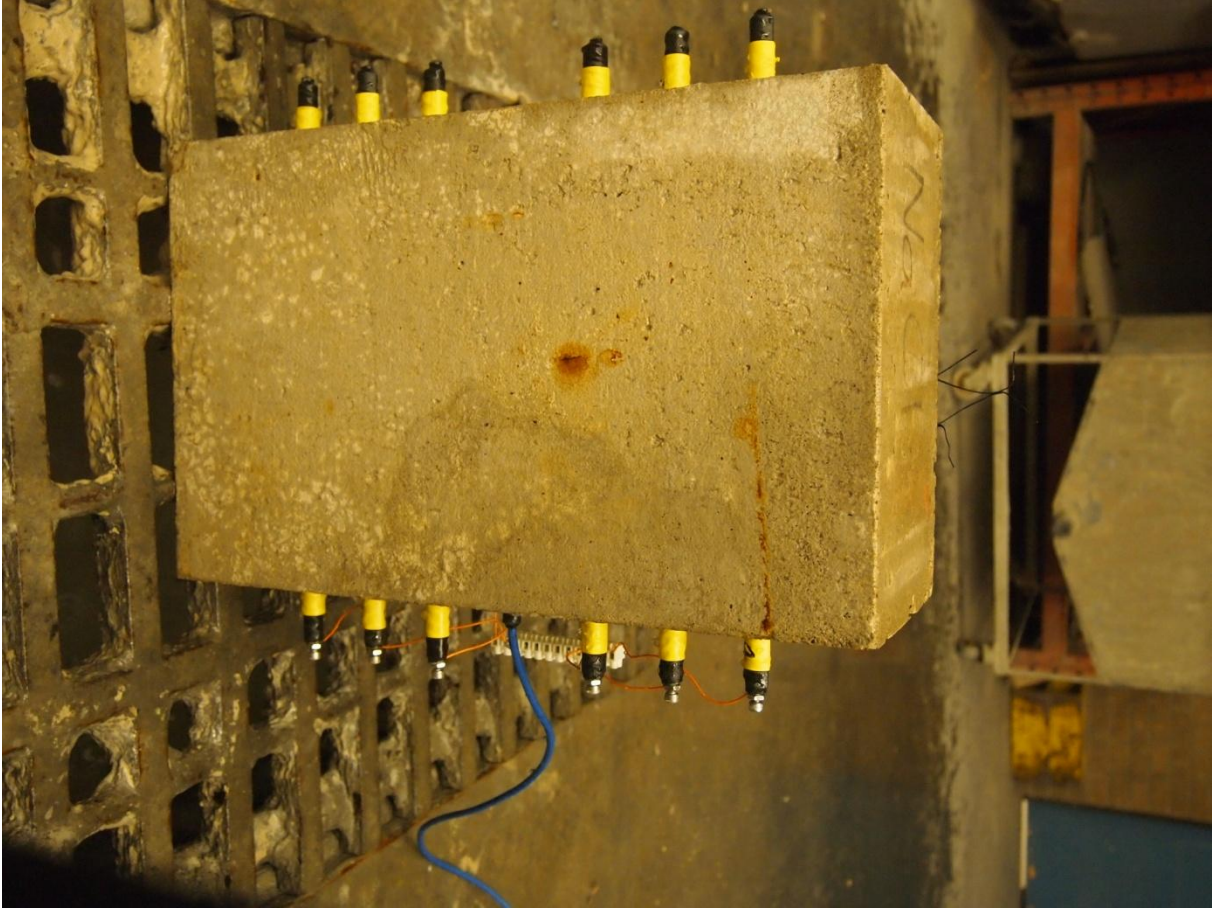


Figure 4-15: Average of six black steel bar's corrosion potential measurements against time



Figure 4-16: Crystallization of NaCl solution due to relative humidity formation of NaCl stalactite (Left)



**Figure 4-17: Effects of NaCl leaching around and being absorbed via capillary suction through the bottom of the beam causing corrosion**

### ***4.3.3 Micro-cell Corrosion Current Density***

The corrosion current densities shown in Figure 4-18 are all in the passive region. Even the spike caused by the leaching of NaCl crystals is low and passive. This suggests that the corrosion products observed in Figure 4-17 are actually rust from the metal shelf that the beams were initially sitting on and not from the internal bars. Furthermore, all corrosion current density values are still decreasing, possibly due to the concrete resistance increasing, suggesting that the passive film is still developing albeit very little.

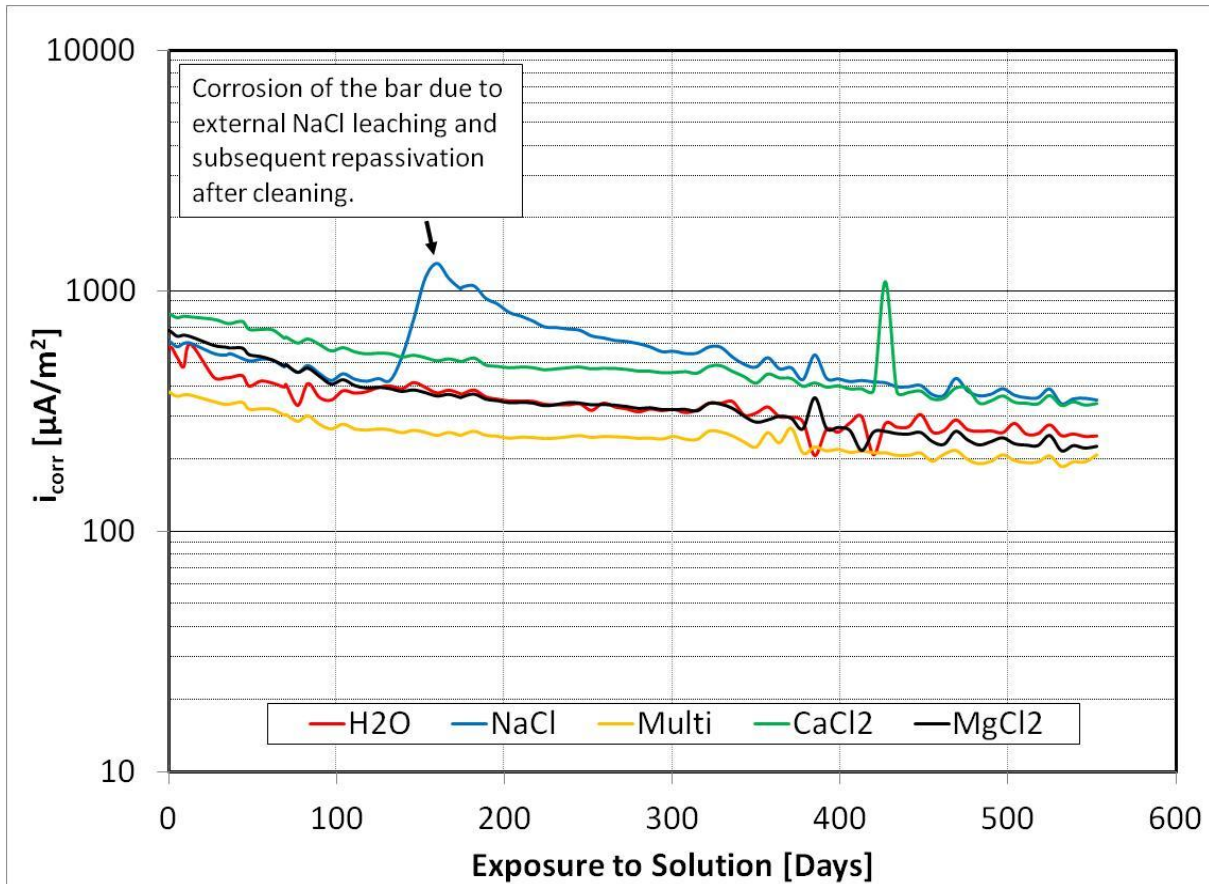


**Figure 4-18: Average of six black steel bar's corrosion current density measurements against time**  
**Note:  $100 \mu\text{A}/\text{m}^2 = 10 \text{ nA}/\text{cm}^2 \approx 135 \text{ nm}/\text{year}$**

#### 4.4 Micro-cell Results: Synthetic Pore Solution

The following section discusses the results of the micro-cell pore solution test, using the four cells shown in Figure 4-19. From the test data, it was possible to determine the corrosion potential ( $E_{corr}$ ) and the corrosion current density ( $i_{corr}$ ). Because the testing was completed in solution, there was no need to test for solution resistance as it was negligible. The data points in this section are the averages of the five black steel bars in each cell (i.e. the average of all specimens immersed in the same anti-icing solution of increasing chloride content). The results gathered from the individual bars can be found in Appendix D: section D-3 Micro-cell Results: Synthetic Pore Solution.

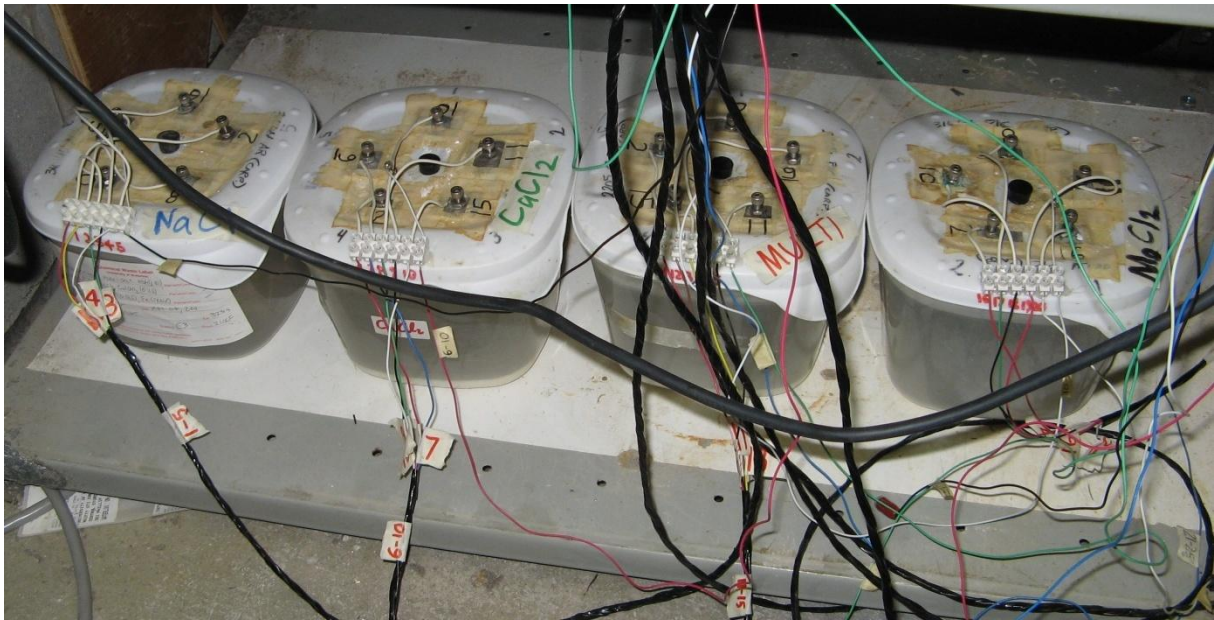


**Figure 4-19: Set up of micro-cell corrosion test in synthetic pore solution**

In addition to electrochemical measurements, the pH and temperature of the pore solution were monitored as a function of  $\text{Cl}^-$  content and are shown in Figure 4-20. The pH of the solution contaminated with NaCl was maintained at about 13. The solution containing  $\text{CaCl}_2$  showed a slight decrease closer to a pH of 12.5. This can be attributed to the calcium exchanging with the potassium and sodium in the potassium hydroxide and sodium hydroxide to form calcium hydroxide, which has a pH of 12.6. The solution with the multi  $\text{Cl}^-$  follows the same trend as that with  $\text{CaCl}_2$  with a slightly smaller decrease in pH. This is due to the fact that the multi  $\text{Cl}^-$  is composed primarily of  $\text{CaCl}_2$  and NaCl. The solution containing  $\text{MgCl}_2$  showed a significant drop in pH from 13.5 to 9.1. This decrease begins to occur at 0.90%  $\text{Cl}^-$  and levels out between 1.90% and 2.00%  $\text{Cl}^-$ . This is due to the replacement of calcium in the calcium hydroxide with the magnesium from the magnesium chloride [18], the pH 9.1 being the saturation pH for  $\text{Mg}(\text{OH})_2$  in this solution. This results in the steel having difficulty maintaining its passive film and thus becoming more susceptible to active corrosion.

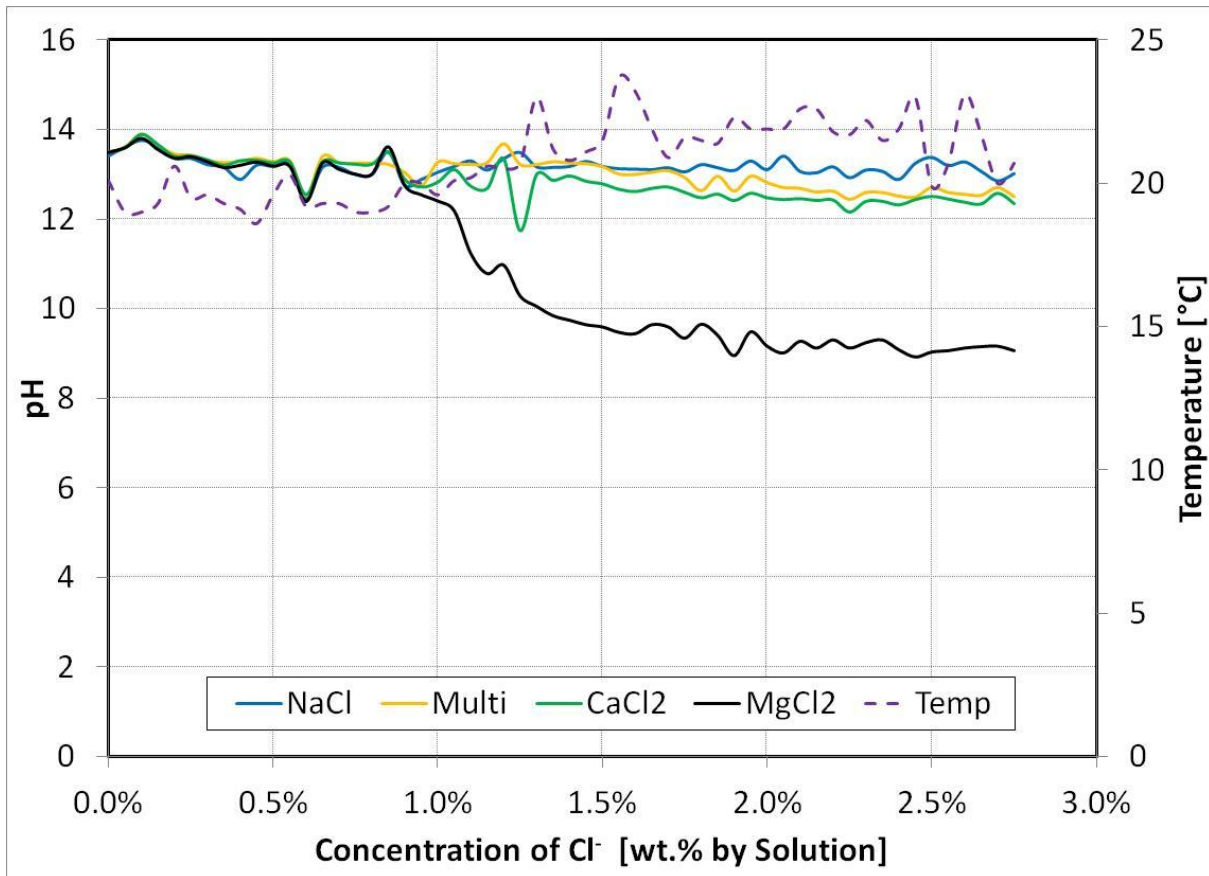
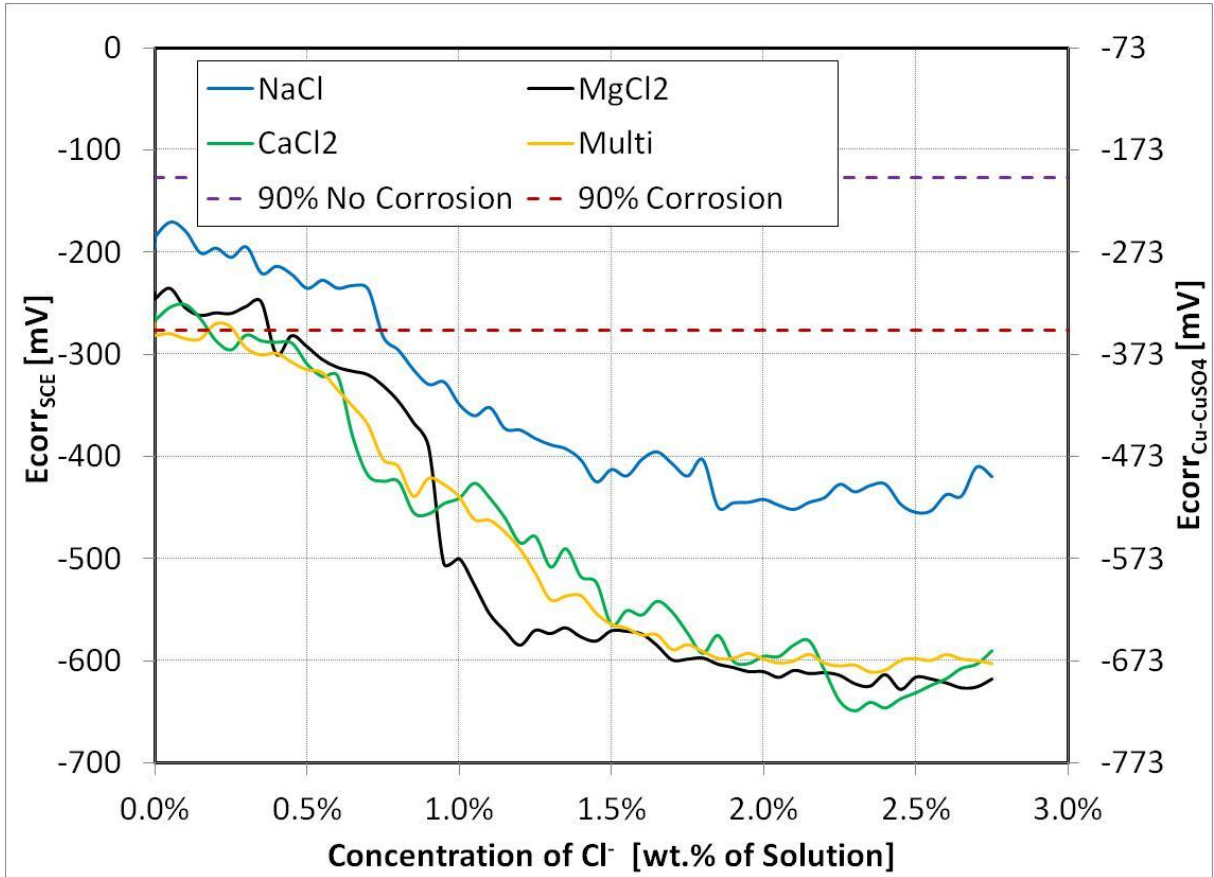


Figure 4-20: Temperature and pH of pore solution vs. Cl<sup>-</sup> concentration

#### 4.4.1 Corrosion Potential Measurements

Figure 4-21 shows the average corrosion potentials of the bars exposed to increasing amounts of an anti-icing solution. All of these measurements begin within the region of uncertainty according to ASTM C876 (i.e. between  $-127 \text{ mV}_{\text{SCE}}$  and  $-277 \text{ mV}_{\text{SCE}}$ ). The reasons these measurements are lower than those found in the concrete is due to the voltage drop across the concrete cover, which is negligible in the pore solution tests, making the ASTM standard somewhat unreliable for black steel in pore solution. Photographs of the bars taken after exposure to 0.70% Cl<sup>-</sup> are shown in Figure 4-22. Little to no corrosion is present on samples exposed to NaCl; only some of the bars show corrosion in the CaCl<sub>2</sub> and Multi Cl<sup>-</sup> solutions, most bars exposed to MgCl<sub>2</sub> show slightly more signs of corrosion.



**Figure 4-21: Average corrosion potential measurements of 5 bars in pore solution exposed to various concentrations of anti-icing solutions. According to ASTM C876 potentials above the upper limit (purple line) represents where there is a 90% chance of stability, the potentials below the lower limit (red line) represent where there is a 90% chance of corrosion. In between these two lines the probability of corrosion is uncertain.**



(a) NaCl



(b) MgCl<sub>2</sub>



(c) CaCl<sub>2</sub>



(d) Multi Cl<sup>-</sup>

**Figure 4-22: Bars exposed to various chlorides with a concentration 0.70% Cl<sup>-</sup> taken in a glove box in a nitrogen environment**

#### ***4.4.2 Micro-cell Corrosion Current Density***

Figure 4-23 shows the average corrosion current density measurements as a function of chloride content. These data are clearer indicators of the onset of active corrosion, which begins first with bars exposed to MgCl<sub>2</sub> solution at about 0.35%-0.40% Cl<sup>-</sup>. The following increase from around 10 mA/m<sup>2</sup> to 100mA/m<sup>2</sup> correlates to the drop in pH from 13.5 to 9.1 shown in Figure 4-20. Both sets of bars exposed to the Multi Cl<sup>-</sup> and CaCl<sub>2</sub> solution transitioned from passive to active corrosion around 0.60%-0.65% Cl<sup>-</sup>. The spike observed in the bars exposed to CaCl<sub>2</sub> at 1.7% Cl<sup>-</sup> is the result of a single bar corroding very rapidly (Figure 4-24). It is speculated that multiple areas of the bar began to corrode

actively and after a time some of these areas become protected from further rapid corrosion by voluminous corrosion products resulting in lowering the measurable corrosion current density. The remaining bars exhibited corrosion current density rates similar to those found in the NaCl and Multi Cl<sup>-</sup> exposed bars. Finally the bars exposed to NaCl transitioned from passive to active corrosion at about 0.70%-0.80% Cl<sup>-</sup>.

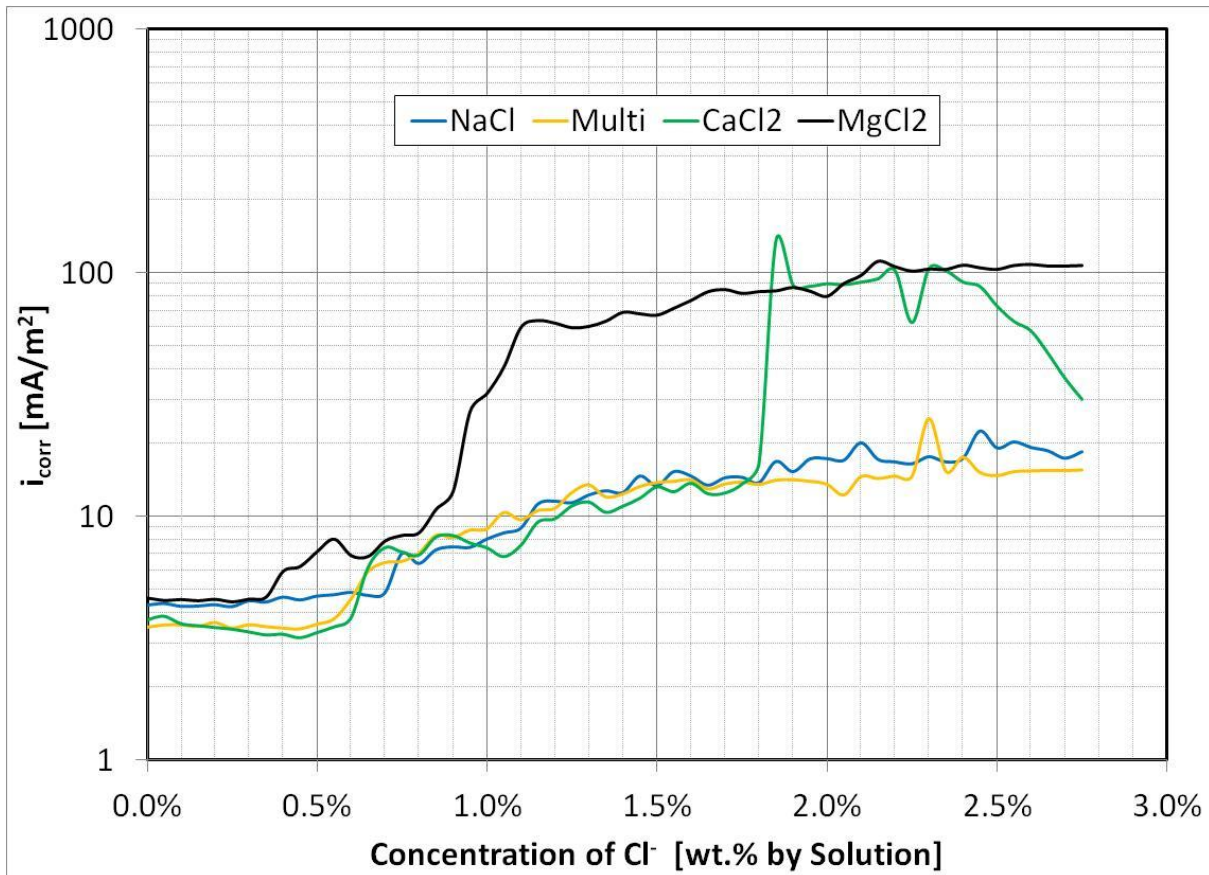
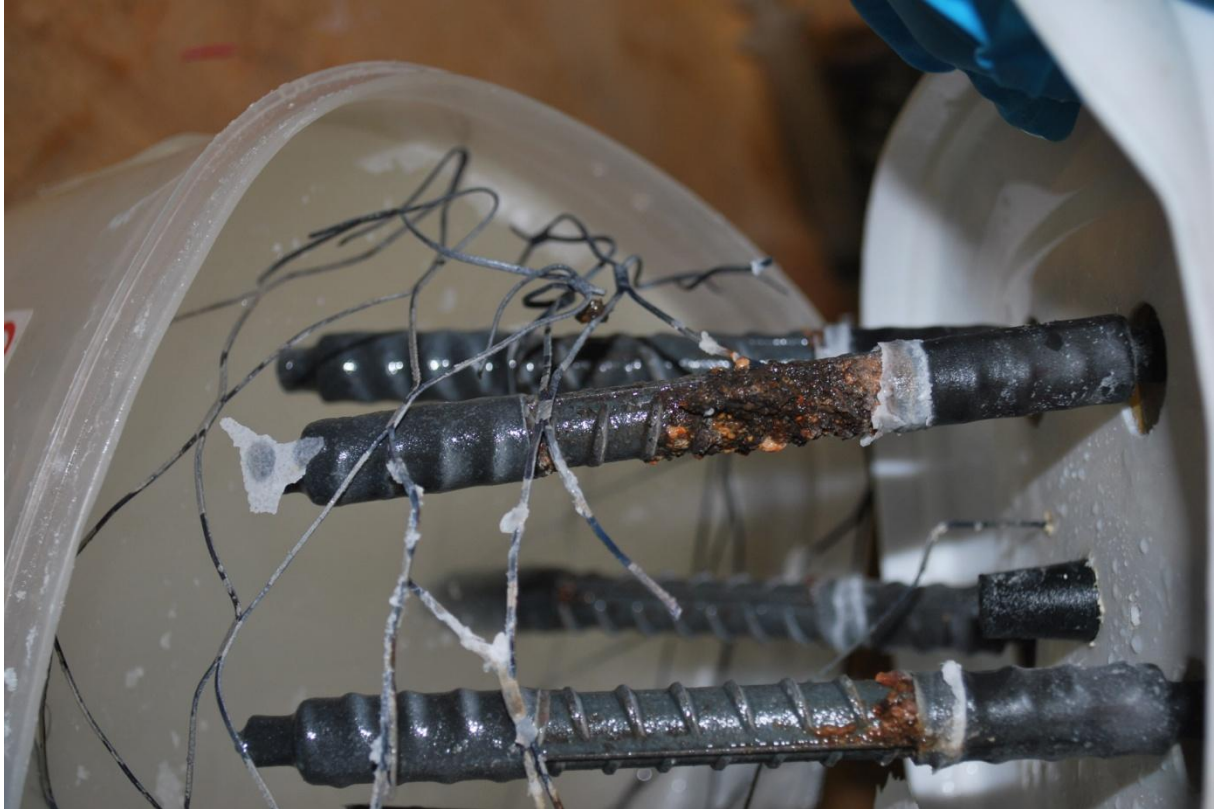


Figure 4-23: Average corrosion current density measurements of 5 bars in pore solution exposed to various concentrations of anti-icing solutions. Note  $1\text{E-}2\text{A/m}^2 = 1\ \mu\text{A/cm}^2 \approx 12\ \mu\text{m/year}$  and  $1\text{E-}10\ \text{mA/m}^2 = 1\ \mu\text{A/cm}^2 \approx 13\ \mu\text{m/year}$



**Figure 4-24: Black steel exposed to  $\text{CaCl}_2$  showing higher corrosion rates than the other bars exposed to  $\text{CaCl}_2$  at 2.75%  $\text{Cl}^-$ . Note the large corrosion product that has amassed along the rib**

#### **4.4.3 Cyclic Polarization**

One bar from each cell was tested using potentiodynamic cyclic polarization (CP) exposed to 2.75%  $\text{Cl}^-$ . The bar from each test cell was chosen based on how close its corrosion current density was to the average of all the bars in that particular cell. A scan rate of 0.01mV/s was used with the scan beginning at  $E_{\text{corr}}$ , increasing to 300 mV<sub>SCE</sub>, and decreasing to -900 mV<sub>SCE</sub>. The results are shown below in Figure 4-25 and summarized in Table 4-13. The contaminant free bar was a bar exposed only to synthetic pore solution; in its passive state the equilibrium potential was significantly higher than the other bars, and the current density was about an order of magnitude lower than the bars exposed to anti-icing solutions.

The black steel exposed to NaCl had the most anodic corrosion potential and lowest corrosion current density of the bars exposed to anti-icing solution. However, after the test was completed the bar's new equilibrium position was significantly lower and had a higher corrosion current density. This trait was also observed in the bar exposed to the multi  $\text{Cl}^-$  solution. This suggest that  $\text{Na}^+$  ions cause the

bars to maintain the higher corrosion rates after they experiences high levels of corrosion more than do the other salt solutions.

Pitting potentials were observed on the bars exposed to NaCl, CaCl<sub>2</sub>, and multi Cl<sup>-</sup> at -168 mV, -256 mV and -300 mV respectively. The bar exposed to NaCl also exhibited what appeared to be a second rapid increase in current density at 0 mV, which is similar to the bar exposed to CaCl<sub>2</sub>. No pitting potential was observed in the bar exposed to the MgCl<sub>2</sub> solution, which was actively corroding at the open circuit potential. This is likely a result of the NaCl<sub>2</sub>, CaCl<sub>2</sub> and multi Cl<sup>-</sup> undergoing crevice corrosion near the seams of the shrink wrap and the mill scale being preferentially corded. After the mill scale is consumed and the crevices are blocked by corrosion products, smaller pits begin to form on the surface of the bar, hence the observable pitting potentials occurring during active corrosion of the bars exposed to those three salts.

The E<sub>corr</sub> values of the bar exposed to MgCl<sub>2</sub>, CaCl<sub>2</sub> and multi Cl<sup>-</sup> were all comparable around -600 mV<sub>SCE</sub>. The bars in NaCl had E<sub>corr</sub> values significantly more positive at -386 mV<sub>SCE</sub>. Values for i<sub>corr</sub> using the CP scan were estimated using visual extrapolating of the anodic portion of the curve. These values proved to be quite conservative when compared with values of i<sub>corr</sub> obtained from potentiostatic LPR tests. Nevertheless, the trends observed in both methods were the same. The bars exposed to NaCl, CaCl<sub>2</sub> and multi Cl<sup>-</sup> showed higher i<sub>corr</sub> values and lower E<sub>corr</sub> values on the return scan. The bar exposed to MgCl<sub>2</sub> also exhibited this trend, but to a much lesser extent.

**Table 4-13: Summary of Cyclic Polarization Results (Approximate values)**

Anti-icing solution	Equilibrium				Pitting potential [mV <sub>SCE</sub> ]	Maximum corrosion current density [A/m <sup>2</sup> ]
	Determined using CP		Determined using LPR			
	E <sub>corr</sub> [mV <sub>SCE</sub> ]	i <sub>corr</sub> [A/m <sup>2</sup> ]	E <sub>corr</sub> [mV <sub>SCE</sub> ]	i <sub>corr</sub> [A/m <sup>2</sup> ]		
<b>NaCl</b>	-386	0.007	-387	0.016	-168	69
<b>MgCl<sub>2</sub></b>	-617	0.070	-634	0.083	N/A	283
<b>CaCl<sub>2</sub></b>	-629	0.010	-631	0.017	-256	42
<b>Multi Cl<sup>-</sup></b>	-592	0.003	-608	0.010	-300	218
<b>Contaminant Free</b>	-201	0.001	N/A	N/A	N/A	0.02

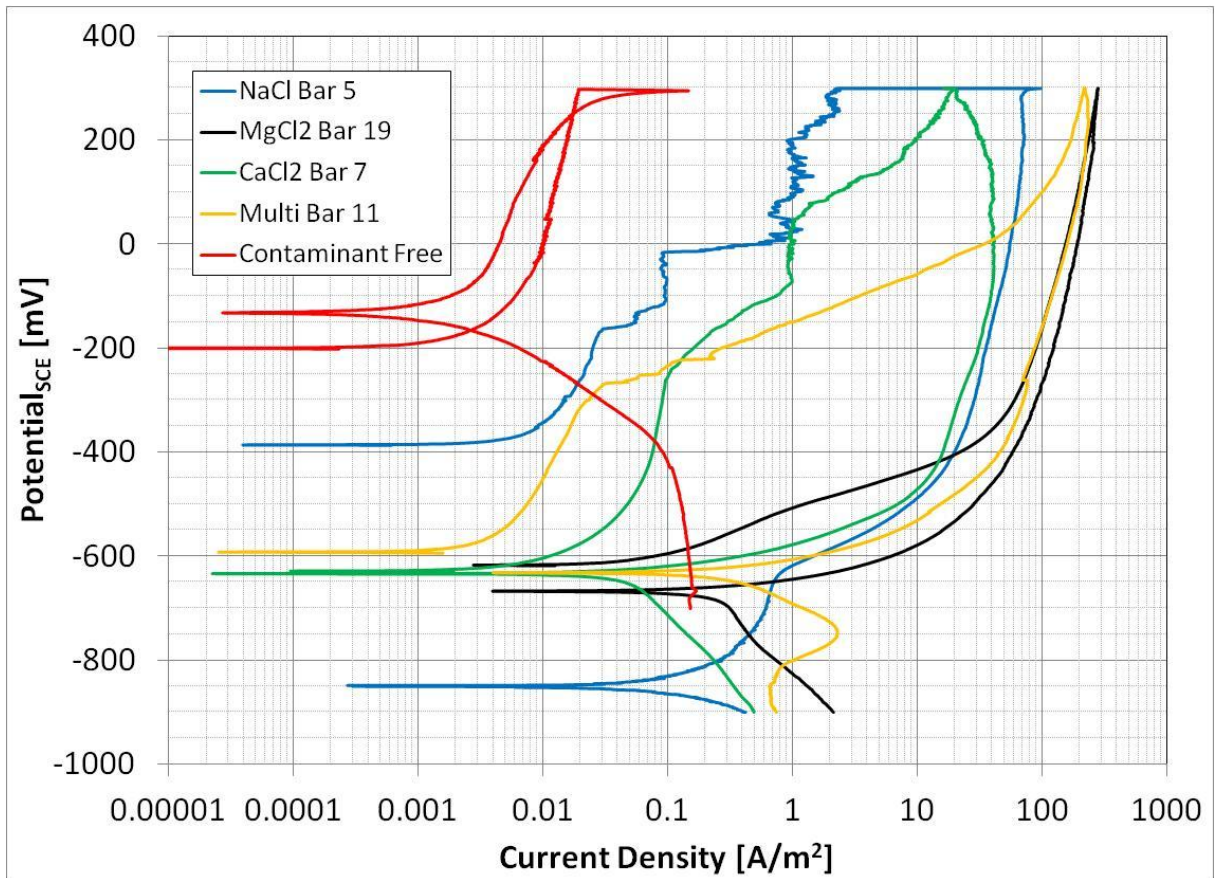


**Figure 4-25: Cyclic polarization results of a single bar from each solution at a chloride concentration of 2.75%  $\text{Cl}^-$ . The scan rate used was 0.01mV/s. Note<sup>1</sup> that the abscissa axis is plotted on a logarithmic scale. Note<sup>2</sup>  $1 \text{ A/m}^2 = 100 \mu\text{A/cm}^2 \approx 1 \text{ mm/year}$**

An additional potentiodynamic CP scan was conducted on a second bar exposed to the NaCl solution; it is shown with the previous CP scan of “bar 5”, which was also exposed to the NaCl solution, in Figure 4-26. Bar 4 (exposed to NaCl) shows no “pitting potential” and appears to be actively corroding, similar to the bar exposed to  $\text{MgCl}_2$ ; however, the corrosion current of the bar exposed to NaCl is significantly lower (over an order of magnitude) than the bar exposed to  $\text{MgCl}_2$ .

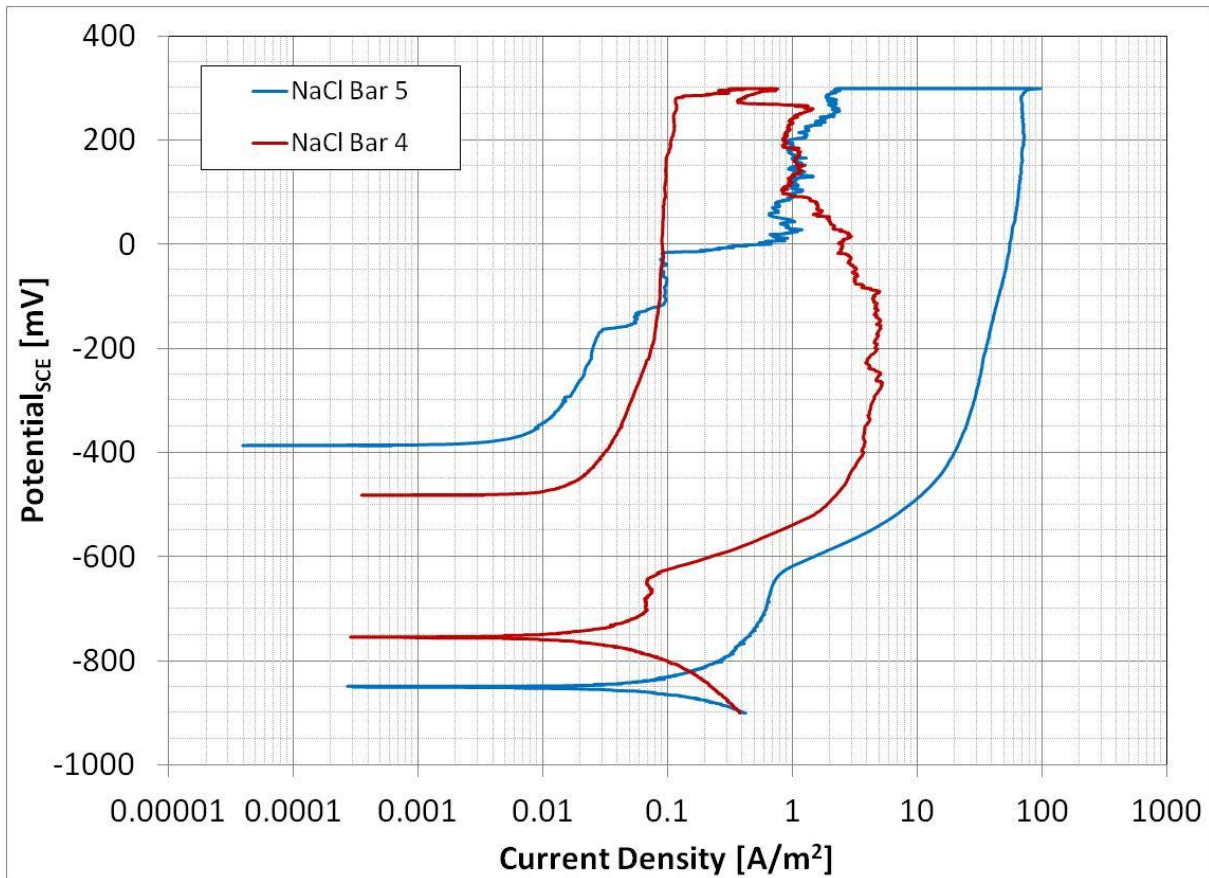


**Figure 4-26: Cyclic polarization results of a two bars exposed to NaCl solution at a chloride concentration of 2.75% Cl<sup>-</sup>. The scan rate used was 0.01mV/s. Note<sup>1</sup> that the abscissa axis is plotted on a logarithmic scale. Note<sup>2</sup> 1 A/m<sup>2</sup>= 100 μA/cm<sup>2</sup>≈ 1 mm/year**

After completing the CP tests, the bars were photographed as can be seen in Figure 4-27. The bar exposed to NaCl in Figure 4-27 (a), appeared to show the treelike structure, growing from specific areas that are likely pits. The bars exposed to the other anti-icing solutions showed more general corrosion shown in Figure 4-27 (b), (c) and (d). It is also interesting to note that the counter electrode used in the MgCl<sub>2</sub> solution was uniformly coated in what appears to be corrosion products, Figure 4-27 (b).

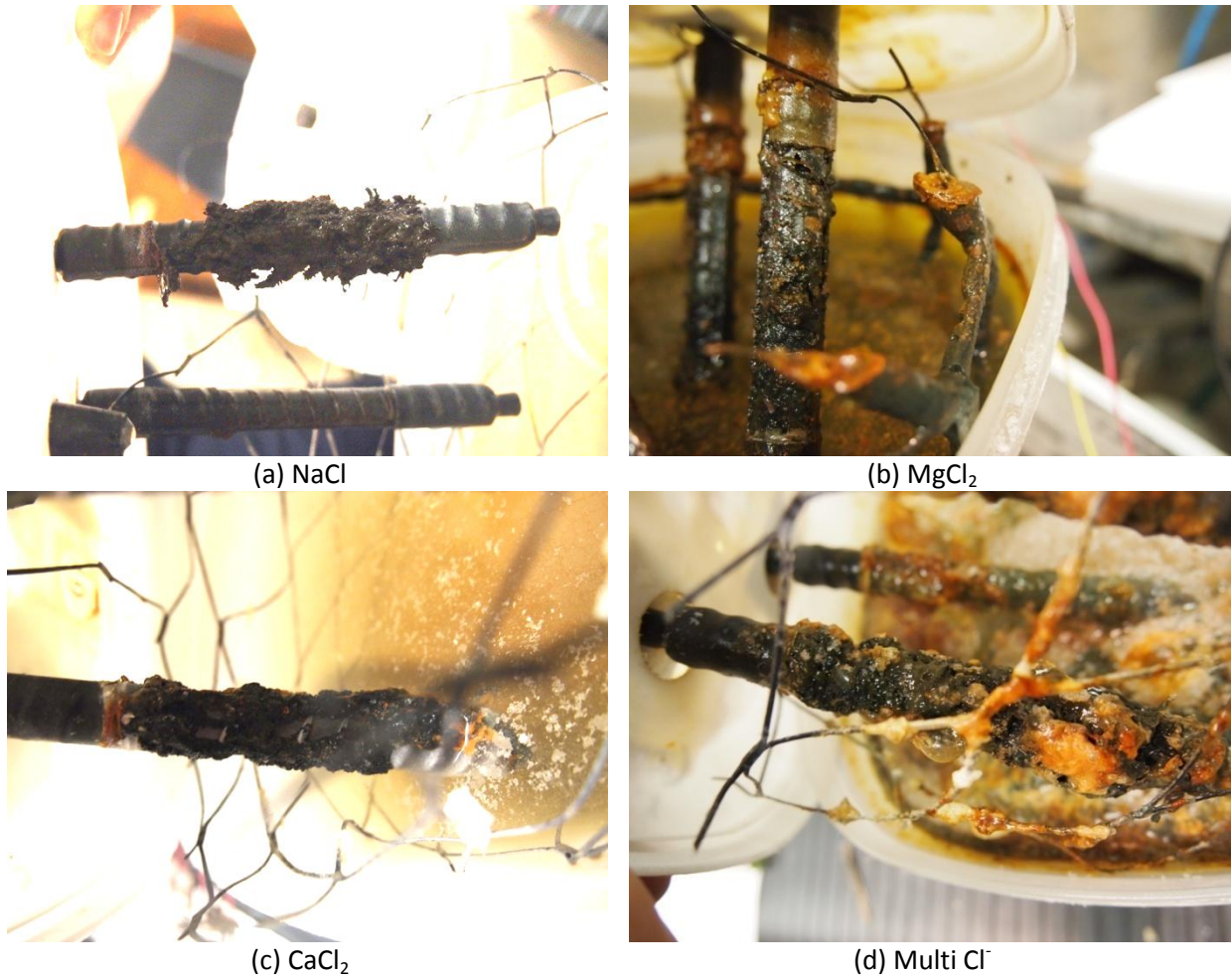


**Figure 4-27: Black Steel exposed to 2.75%Cl<sup>-</sup> by weight using (a) NaCl, (b) MgCl<sub>2</sub>, (c) CaCl<sub>2</sub> and (d) Multi Cl<sup>-</sup> after cyclic polarization testing from the open circuit potential to 300 mV<sub>SCE</sub> to 900 mV<sub>SCE</sub> and back to the open circuit potential.**

#### ***4.4.4 Reinforcing Steel Autopsy***

Initially all cells were opened and photographed as depicted in Figure 4-28. From this it is clear that the corrosion observed on specimens exposed to MgCl<sub>2</sub> show significantly more corrosion products and the specimens exposed to NaCl show significantly less corrosion products with the specimens exposed to CaCl<sub>2</sub> and the multi Cl<sup>-</sup> falling in between the other two.

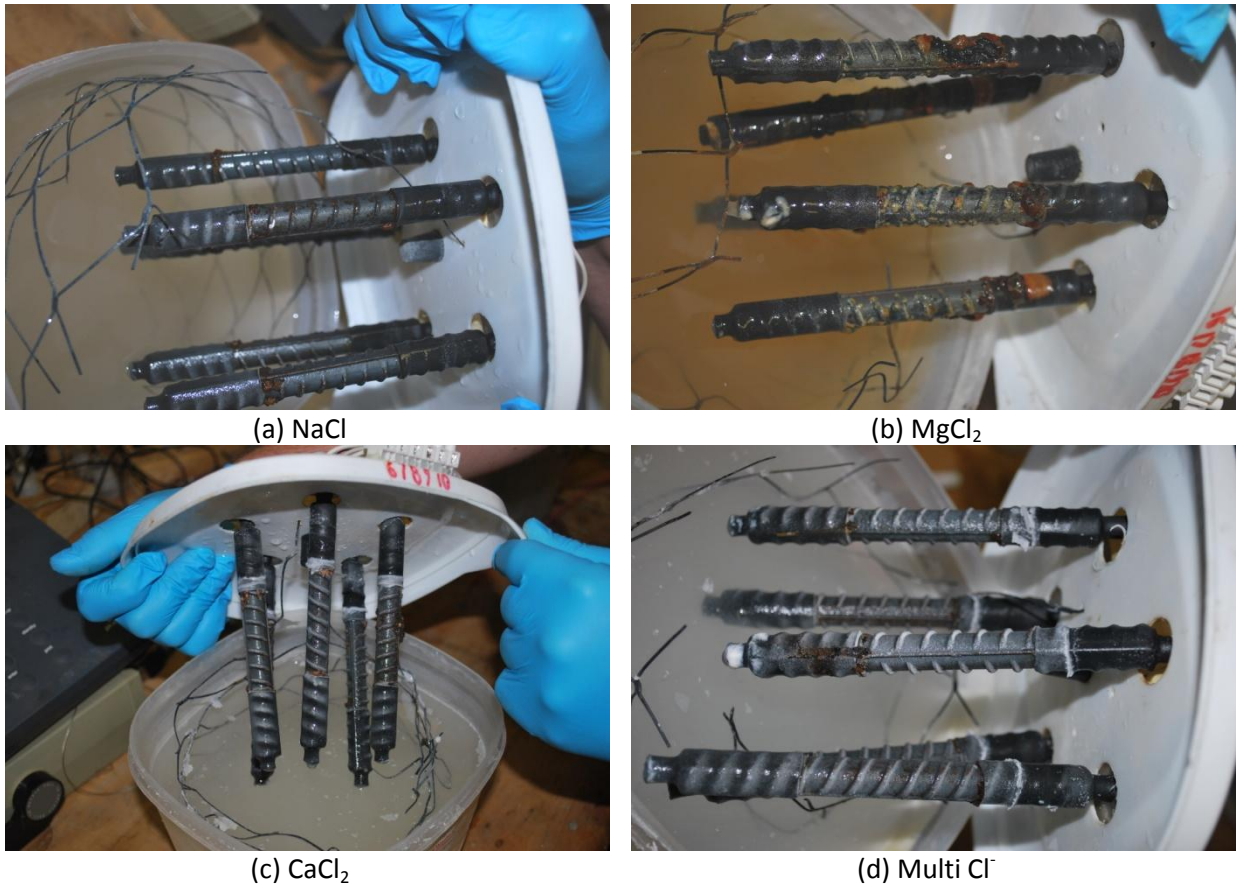


**Figure 4-28: Black steel bars exposed to 2.75%Cl<sup>-</sup> by weight using (a) NaCl, (b) MgCl<sub>2</sub>, (c) CaCl<sub>2</sub> and (d) multi Cl<sup>-</sup>.**

#### 4.4.4.1 Surface Cleaning and Pickling

One bar from each cell was then removed for further visual inspection. The bars were disconnected from the cell and the shrink wrap with glue was removed. The nuts and bolts depicted in the figure were reattached after being disconnected from the cell to keep track of the bars. From the photographs in Figure 4-29, it is quite apparent that the shrink wrap and glue did not suffice at protecting the bars. This was observed in all cases and, due to both the bar ribbing and concrete's heterogeneous nature; crevices are always prevalent making the comparison between bars still relevant.

The major differences between the bars are observed between that exposed to NaCl and the others. It shows relatively uniform corrosion primarily underneath the shrink wrap. The bar exposed to MgCl<sub>2</sub> shows more corrosion products that are dispersed and primarily located on the exposed surface of the bar and not covered by shrink wrap. The bar exposed to CaCl<sub>2</sub> is more heavily corroded than that

exposed to NaCl, especially the surface covered by shrink wrap; also the corrosion products look smaller and more dispersed than the clusters found on the bar exposed to MgCl<sub>2</sub>. The bar exposed to the multi Cl<sup>-</sup> shows similar corrosion products where the shrink wrap was covering but across its surface a white “powdery” substance was observed. It is unclear whether this is a corrosion products or a salt that has crystallized on the surface of the bar.



(a) NaCl Bar 1



(b) MgCl<sub>2</sub>



(c) CaCl<sub>2</sub>



(d) Multi Cl<sup>-</sup>

**Figure 4-29: Black steel bars exposed to 2.75%Cl<sup>-</sup> by weight using (a) NaCl, (b) MgCl<sub>2</sub>, (c) CaCl<sub>2</sub> and (d) multi Cl<sup>-</sup> the bars have also spent several days outside of the pore solution in a desecrator with air at ambient temperature and pressure.**

After pickling, the bars were cleaned, dried and photographed using a scanner. To achieve a scan of the full circumference of the bar, the bars were rolled across the scanner at the approximately the same speed of the charge-coupled device (component of scanner that captures the image). The purpose of this was to create an approximate 2D image of the 3D surface of the bars as displayed in

Figure 4-30. Almost all of the visible damage to all bars show randomly distributed large shallow pits over the entire area of the bar, regardless of solution exposure. Furthermore, the mill scale appears to be preferentially corroding when compared to the steel substrate. Some narrower and deeper pits were visible, but the pits were not nearly as severe as anticipated.



(a) NaCl Bar 1



(b)  $\text{MgCl}_2$



(c)  $\text{CaCl}_2$



(d) multi  $\text{Cl}^-$

**Figure 4-30: Black steel bars exposed to 2.75% $\text{Cl}^-$  by weight of (a) NaCl, (b)  $\text{MgCl}_2$ , (c)  $\text{CaCl}_2$  and (d) Multi  $\text{Cl}^-$ . The bars have also spent several days outside of the pore solution in a desiccator with air at ambient temperature and pressure and have been pickled according to ASTM G1.**

#### 4.4.4.2 Scanning Electron Microscopy of the Black Steel Surface After Exposure to Chloride Contaminated Synthetic Pore Solution

A portion of each pickled specimen was sectioned and the exposed surface was analyzed using SEM and EDS. The SEM images in Figure 4-31 show that there are very few pits in the any of the specimens and those that are present are so broad and shallow that it is more akin to general corrosion than pitting. This is quite unusual as the typical for of corrosion in a material with a passive film is pitting and is possibly a result of the mill scale reacting with the solution or breaking down as the corrosion products underneath expand and push the mill scale off the bar.

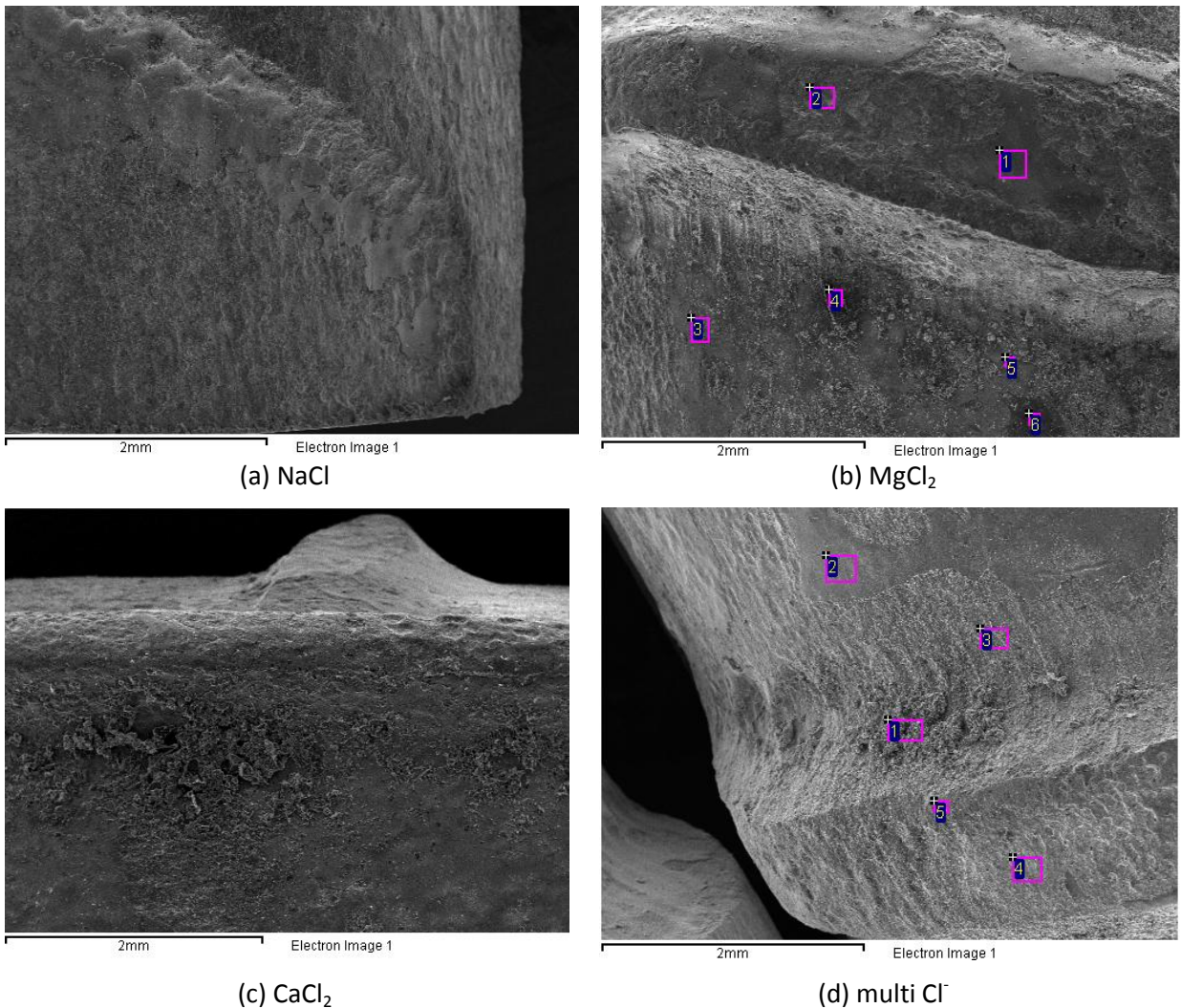


Figure 4-31: Black steel exposed to 2.75%Cl<sup>-</sup> by weight using (a) NaCl, (b) MgCl<sub>2</sub>, (c) CaCl<sub>2</sub> and (d) multi Cl<sup>-</sup>.

## 4.5 Cyclic Corrosion Chamber Testing: SAE J2334-Immersion Testing

The following sections present and discuss the results of the cyclic corrosion testing of various steels used in highway structures and exposed directly to diluted anti-icing solutions as well as some stainless steels and corrosion resistant rebar alloys. It is emphasized that the various grade of stainless steels, the galvanized rebar, the black steel rebar and the MMFX rebar are intended for use as concrete reinforcement and that this test was completed in atmospheric conditions. Nevertheless, this study represents a comparison between the steel types when exposed to the same anti-icing solution and a comparison of the effects of the different salts on these steels.

### 4.5.1 Comparison between Steel Types

The mass change per unit area is plotted on a log scale; for this reason, the absolute value of mass change was used. It is important to note, that the mass changes measured in most cases were positive. This is a result of the metal reacting with the available oxygen in the surrounding atmosphere, creating various oxides. The corrosion products then bond, albeit poorly, to the surface of the steel. Efforts were made to ensure minimal mass loss occurred; however, this was not always possible. In particular, the corrosion products of MMFX were “flaky” and de-bonded easily, which will be discussed in further detail below. The actual values are in section 4.5.2 Comparison between Anti-Icing Solution Type. Due to time constraints the effects of the multi  $\text{Cl}^-$  solution were not included in this thesis.

Figure 4-32, Figure 4-33 and Figure 4-34 show the average mass change per unit area of all steels exposed to  $\text{NaCl}$ ,  $\text{MgCl}_2$  and  $\text{CaCl}_2$  respectively. All of the stainless steel rebar grades exposed to all solutions showed small amounts of variability and showed no signs of increasing or decreasing in mass change with respect to time. Their mass change remained below  $10 \text{ g/m}^2$  for  $\text{NaCl}$  and  $\text{CaCl}_2$  and only slightly above that in some cases for specimens exposed to  $\text{MgCl}_2$ . Overall, there were no major differences in behaviour of the stainless steels.

The “flaky” non-adherent corrosion product on the MMFX made the results highly variable and not a good representation of mass change per unit area. This can be seen in the individual measurements in Appendix D: Section D-4 Cyclic Corrosion Chamber Testing: SAE J2334-Immersion Testing.

The galvanized steel rebar performed in between the stainless and the plain carbon steels and weathering steels but varied between the various anti-icing agents are discussed below in section 4.5.2 Comparison between Anti-Icing Solution Type. The “used” galvanized guard rail generally performed better than the “new” galvanized rebar. This was expected under atmospheric conditions as the surface of the “used” galvanized steel, containing 1.06 wt.% Fe, consisted of intermetallic  $\zeta$  ( $\text{Fe}_5\text{Zn}_{95}$ ) phase which is desirable for atmospheric protection against corrosion [54]. On the other hand, the “new” galvanized steel showed no Fe and consisted of  $\eta$  ( $\text{Zn}(\text{Fe})$ ) phase at the surface. If the galvanized steels were embedded in concrete the opposite would be true [52].

The remaining steels including the weathering steel performed poorly, having mass gains of  $>1000 \text{ g/m}^2$  in all anti-icing solutions. This suggests that weathering steel, even when exposed to wet/dry cycles, will not form a protective adherent coating when contaminated with chlorides irrespective, of the source. When exposed to any of the salt solutions, the box girder performed the poorest with the highest mass change per unit area. On the other hand, the weldable black steel rebar performed the best in all solutions when compared to the other carbon steels and to the weathering steel. This is less apparent for specimens exposed to the NaCl solution. The corrosion products of the black steel rebar adhered well to the surface and did not “flake off”. This may be attributed to the cylindrical geometry of the specimen because many of the observed cracks that formed on the flat steel plates occurred along the edges. Furthermore the black steel rebar still had its mill scale intact, which may have offered additional protection.

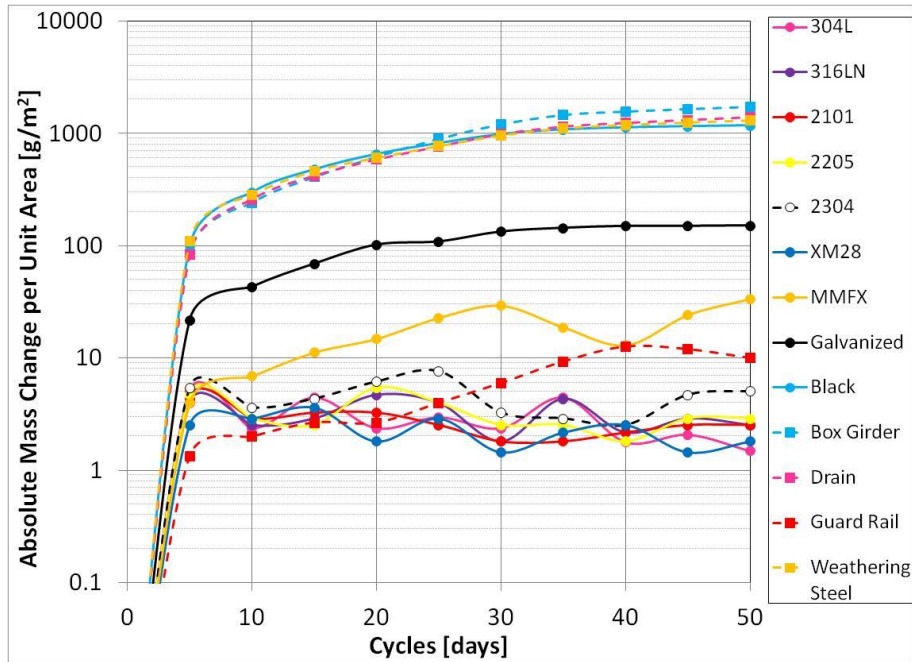


Figure 4-32: Average mass change per unit area vs. SAE J2234 cycles (in days) exposed to NaCl anti-icing solution. Note: the ordinate axis is logarithmic.

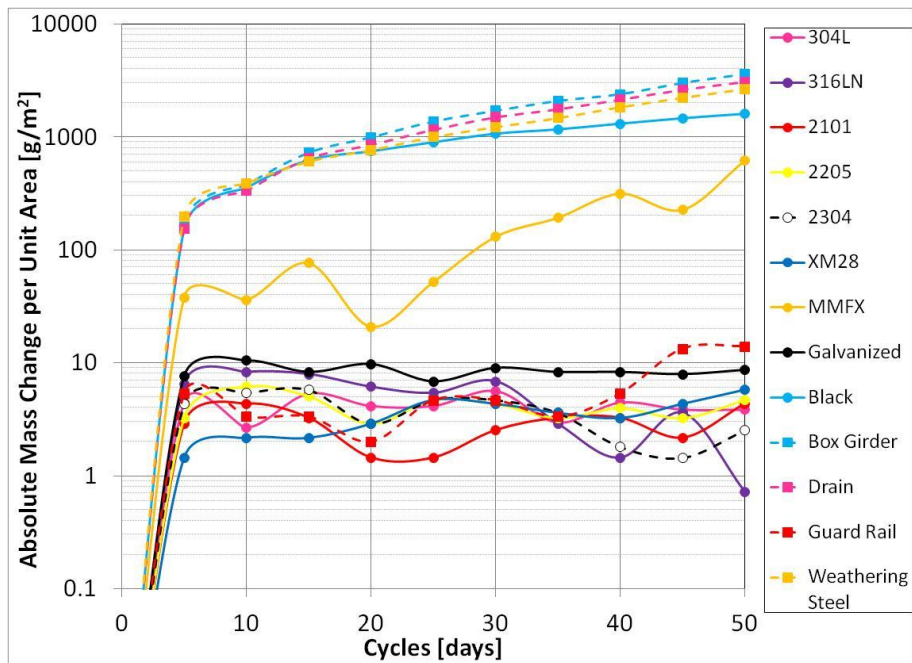


Figure 4-33: Average mass change per unit area vs. SAE J2234 cycles (in days) exposed to MgCl<sub>2</sub> anti-icing solution. Note: the ordinate axis is logarithmic.

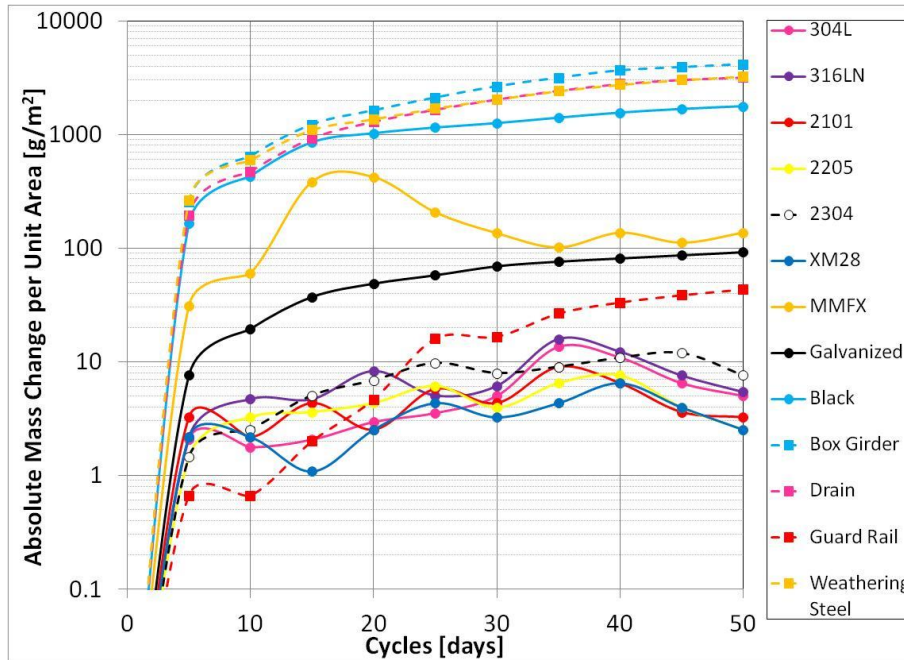


Figure 4-34: Average mass change per unit area vs. SAE J2334 cycles (in days) exposed to  $\text{CaCl}_2$  anti-icing solution. Note: the ordinate axis is logarithmic.

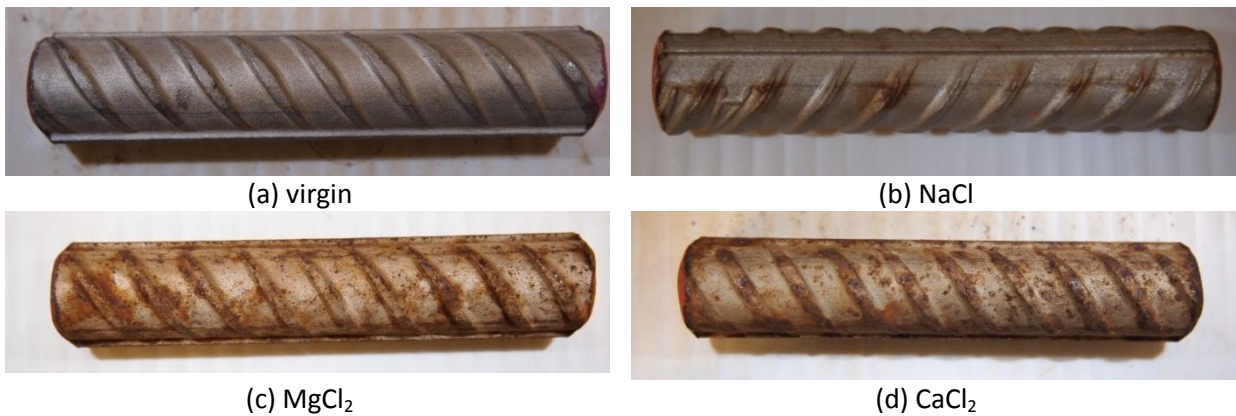
#### 4.5.2 Comparison between Anti-Icing Solution Type

Figure 4-35 through Figure 4-60 show “before and after” pictures of typical specimens of each steel exposed to each salt, as well as the plots of mass change per unit area against SAE J2334 cycles. Note that the scale for the ordinate axis of each material varies to show better detail of each specimen, due to the large range and scale between the steels (especially the stainless steels versus the plain carbon steels).

##### 4.5.2.1 Stainless Steels Exposed to Various Anti-Icing Solutions

The majority of stainless steel rebar grades showed corrosion that was only cosmetic in nature and in many cases consisted of corrosion products from the other steels that were floating around in the solution during immersion cycles. However, some steels did show signs of corrosion that appear to be of embedded carbon steel from processing (such as during rolling or contamination during subsequent handling). This was very prevalent in the XM28 rebar that was exposed to  $\text{NaCl}$  and can be seen in Figure 4-46 (a). The mass change per unit area was minor, in most cases less than  $10\text{g/m}^2$ . The highest measurement being  $15.92\text{ g/m}^2$ , was found in 316LN at 35 cycles exposed to  $\text{CaCl}_2$ . The resolution of the balance used to measure the mass change was nominally  $0.01\text{ g}$ ; however, differences of  $0.03\text{ g}$  are considered accurate. A change of  $0.02\text{ g}$  in the 20M and 15M bar respectively, would result in a

mass change per unit area of  $3.0 \text{ g/m}^2$  and  $3.6 \text{ g/m}^2$  and, assuming uniform corrosion, a depth loss of  $0.4 \text{ }\mu\text{m}$  and  $0.5 \text{ }\mu\text{m}$ . It is important to note that those numbers are conservative because they are calculated using the total mass change and do not correct for the mass of oxygen present in the corrosion products or the debris from the solution deposited on the bars. All stainless steels exposed to  $\text{CaCl}_2$  solution showed slightly higher mass changes per unit area than those exposed to the other solutions but this was only minor. The results of the various stainless steel grades exposed to anti-icing solutions are shown below in Figure 4-35 through Figure 4-45.



**Figure 4-35: 304L specimen (a) prior to testing and exposed to 50 cycles of (b) NaCl, (c)  $\text{MgCl}_2$  and (d)  $\text{CaCl}_2$**

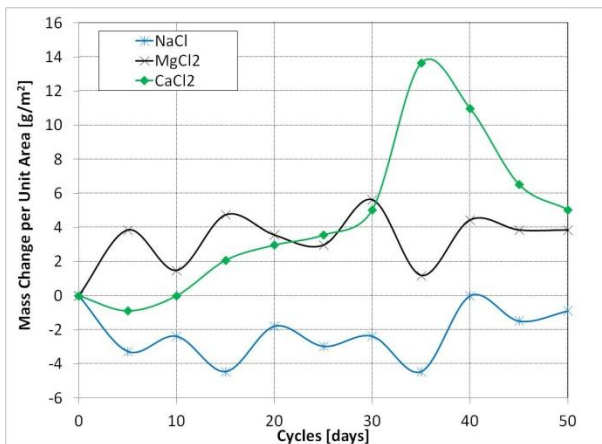


**Figure 4-36: 304L average mass change per unit area vs. SAE J2234 cycles (in days) exposed to various anti-icing solutions**

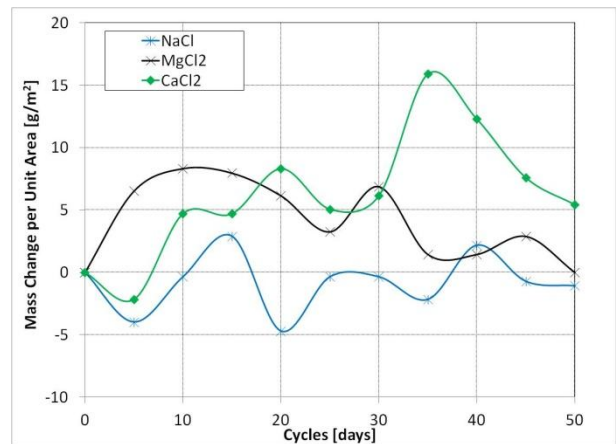


**Figure 4-37: 316LN average mass change per unit area vs. SAE J2234 cycles (in days) exposed to various anti-icing solutions**



Figure 4-38: 316LN specimen (a) prior to testing and exposed to 50 cycles of (b) NaCl, (c) MgCl<sub>2</sub> and (d) CaCl<sub>2</sub>



Figure 4-39: 2101 specimen (a) prior to testing and exposed to 50 cycles of (b) NaCl, (c) MgCl<sub>2</sub> and (d) CaCl<sub>2</sub>

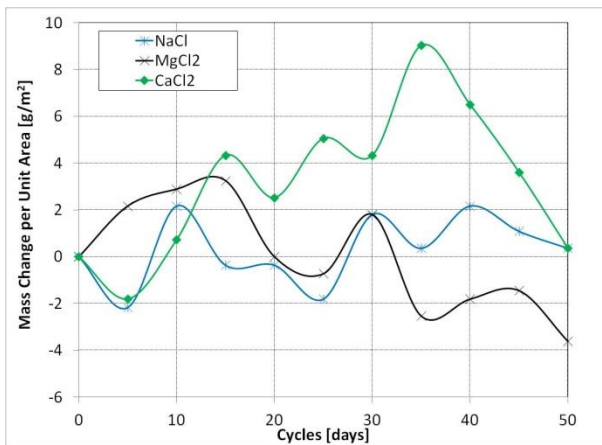


Figure 4-40: 2101 average mass change per unit area vs. SAE J2234 cycles (in days) exposed to various anti-icing solutions

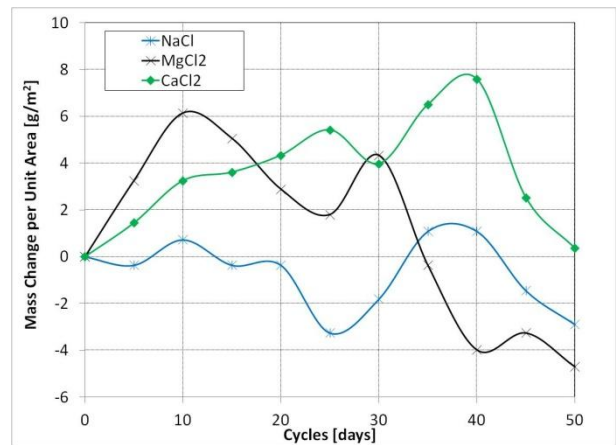


Figure 4-41: 2205 average mass change per unit area vs. SAE J2234 cycles (in days) exposed to various anti-icing solutions



Figure 4-42: 2205 specimen (a) prior to testing and exposed to 50 cycles of (b) NaCl, (c) MgCl<sub>2</sub> and (d) CaCl<sub>2</sub>



Figure 4-43: 2304 specimen (a) prior to testing and exposed to 50 cycles of (b) NaCl, (c) MgCl<sub>2</sub> and (d) CaCl<sub>2</sub>

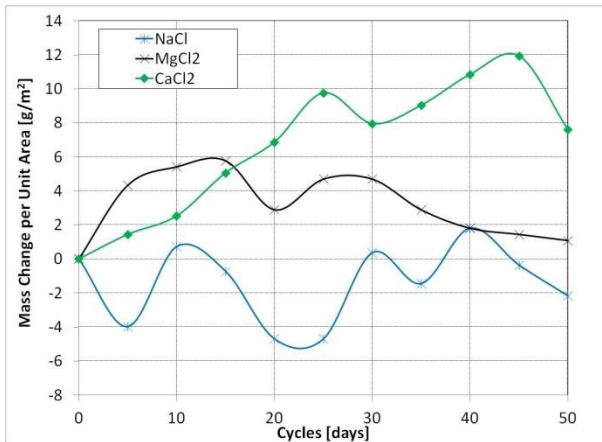


Figure 4-44: 2304 average mass change per unit area vs. SAE J2234 cycles (in days) exposed to various anti-icing solutions

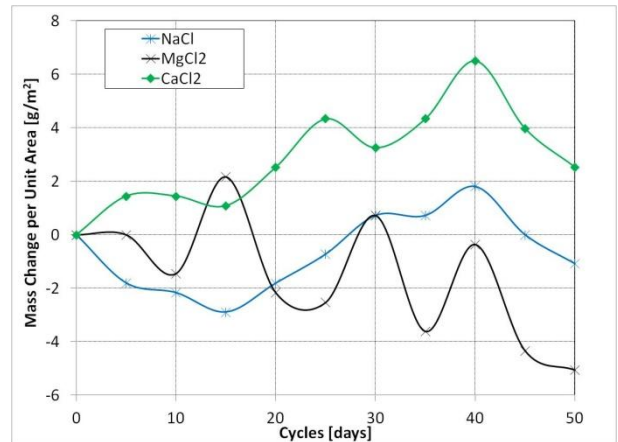


Figure 4-45: XM28 average mass change per unit area vs. SAE J2234 cycles (in days) exposed to various anti-icing solutions



**Figure 4-46: XM28 specimen (a) prior to testing and exposed to 50 cycles of (b) NaCl, (c) MgCl<sub>2</sub> and (d) CaCl<sub>2</sub>**

#### **4.5.2.2 Carbon Steels and Weathering Steel Exposed directly to Various Anti-Icing Solutions**

For the three plain carbon steels and the weathering steel, exposure to CaCl<sub>2</sub> solution caused the highest mass change per unit area. In fact, all the steels exposed to CaCl<sub>2</sub> had a mass change per unit area higher than steels exposed to MgCl<sub>2</sub> solution by 10%, 15%, 3% and 22% by wt. % of MgCl<sub>2</sub> for black steel rebar, the box girder steel, the drain steel and weathering steel, respectively. The NaCl solution caused the lowest amount of mass change per unit area.

In all cases, the corrosion products of the plate steel (box girder, drain, and weathering steel) delaminated and, in some cases, parts would fall off, as seen in the corner of the box girder and drain exposed to MgCl<sub>2</sub> shown in Figure 4-50 (c) and Figure 4-51 (c). This delamination of the corrosion products was visible in all plate steel specimens exposed to all salt solutions. The results of the various carbon steel specimens exposed to anti-icing solutions are shown below in Figure 4-47 through Figure 4-53.



**Figure 4-47: Black steel specimen (a) prior to testing and exposed to 50 cycles of (b) NaCl, (c) MgCl<sub>2</sub> and (d) CaCl<sub>2</sub>**

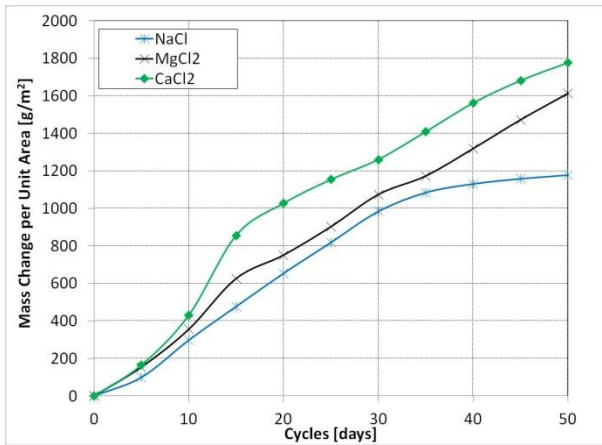


**Figure 4-48: Black steel average mass change per unit area vs. SAE J2234 cycles (in days) exposed to various anti-icing solutions**

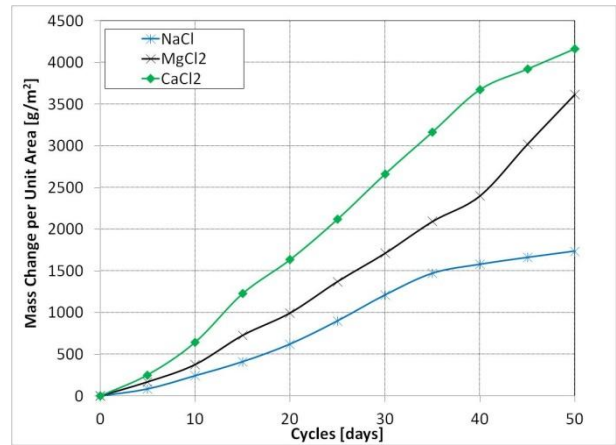


**Figure 4-49: Box girder average mass change per unit area vs. SAE J2234 cycles (in days) exposed to various anti-icing solutions**



(a) virgin



(b) NaCl



(c) MgCl<sub>2</sub>



(d) CaCl<sub>2</sub>

**Figure 4-50: Box girder specimen (a) prior to testing and exposed to 50 cycles of (b) NaCl, (c) MgCl<sub>2</sub> and (d) CaCl<sub>2</sub>**



(a) virgin



(b) NaCl



(c) MgCl<sub>2</sub>



(d) CaCl<sub>2</sub>

**Figure 4-51: Drain specimen (a) prior to testing and exposed to 50 cycles of (b) NaCl, (c) MgCl<sub>2</sub> and (d) CaCl<sub>2</sub>**

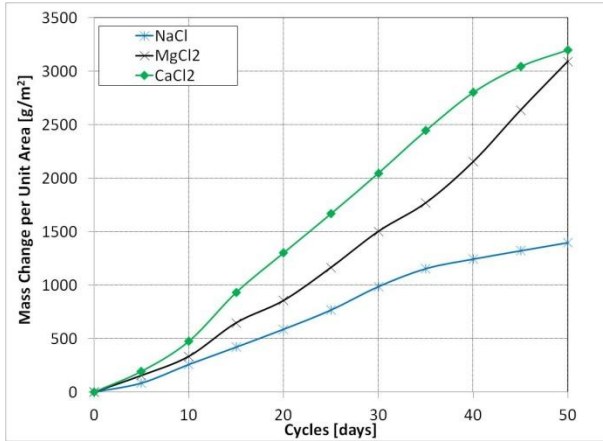


**Figure 4-52: Drain average mass change per unit area vs. SAE J2234 cycles (in days) exposed to various anti-icing solutions**

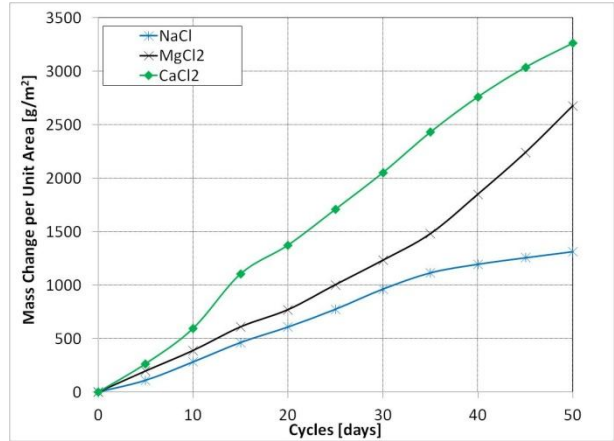


**Figure 4-53: Weathering steel average mass change per unit area vs. SAE J2234 cycles (in days) exposed to various anti-icing solutions**



(a) virgin



(b) NaCl



(c) MgCl<sub>2</sub>



(d) CaCl<sub>2</sub>

**Figure 4-54: Weathering steel specimen (a) prior to testing and exposed to 50 cycles of (b) NaCl, (c) MgCl<sub>2</sub> and (d) CaCl<sub>2</sub>**

#### 4.5.2.3 Galvanized Steels and MMFX Exposed to Various Anti-Icing Solutions

Surprisingly there was a significant difference between the performance of the galvanized rebar and the galvanized guard rail. This is attributed to the guard rail being a component taken from service in the field, where it would have had the opportunity to form a passive film of zinc hydroxide whereas

the virgin galvanized rebar would have had a surface layer of metallic zinc. In all cases, the guard rail showed a lower mass change per unit area than did the galvanized rebar. This may also be a result of the geometry of the galvanized rebar. With multiple curves from the dips and valleys created by the ribs, the zinc coating would be less uniform than the zinc coating of the guard rail. This may also add difficulties in forming uniform adhesion of any zinc hydroxide that may form.

The galvanized rebar performance was comparable to the stainless steel only when exposed to  $MgCl_2$ . When exposed to both  $CaCl_2$  and  $NaCl$  thick amounts of white corrosion products, probably zinc hydroxide, formed and adhered to the surface. Overall the mass change per unit area of the galvanized rebar when exposed to  $NaCl$  was the greater than that of bars exposed to  $MgCl_2$  or  $CaCl_2$ . This may be related to the reaction of  $NaCl$ , having sodium replace the zinc to form  $Na(OH)$  and the chloride replacing the hydroxide to form  $ZnCl_2$ , both of which have high solubility in water. The results of the two galvanized steels exposed to anti-icing solutions are shown below in Figure 4-55 through Figure 4-57.



**Figure 4-55: Galvanized rebar specimen (a) prior to testing and exposed to 50 cycles of (b) NaCl, (c)  $MgCl_2$  and (d)  $CaCl_2$**

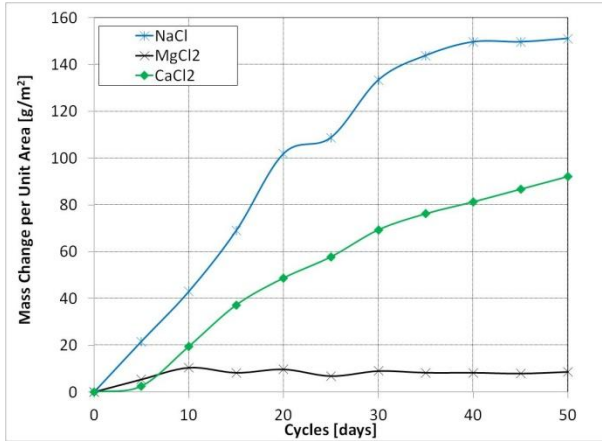


**Figure 4-56: Galvanized rebar average mass change per unit area vs. SAE J2234 cycles (in days) exposed to various anti-icing solutions**

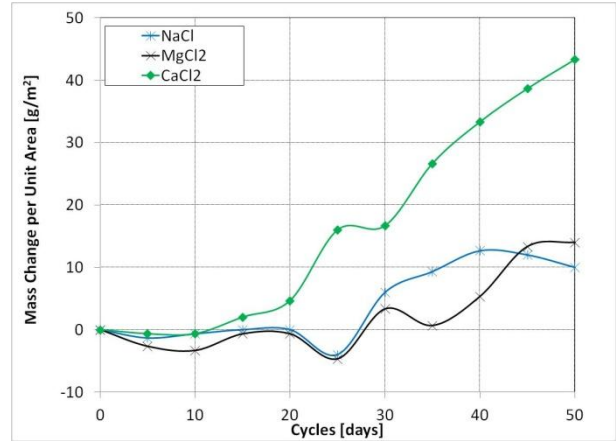


**Figure 4-57: Guard rail (galvanized plate) average mass change per unit area vs. SAE J2234 cycles (in days) exposed to various anti-icing solutions**

As mentioned, the guard rail outperformed the galvanized bar. Even when exposed to CaCl<sub>2</sub>, which was the most damaging solution, the guard rail showed mass changes less than half of that found with the galvanized rebar. When exposed to NaCl and MgCl<sub>2</sub>, the guard rail's mass change per unit area was only slightly higher (a few milligrams per meter squared) than that of the stainless steels. It is suspected that the CaCl<sub>2</sub> solution dissolved a sufficient amount of the zinc coating to begin attacking some of the steel, which is why there is a small stagnation period and a followed by a rapid increase in mass change per unit area. Also, in Figure 4-58 (c) the coating appears to have a slight reddish hue, which may be some of the steel beginning to form iron oxides.

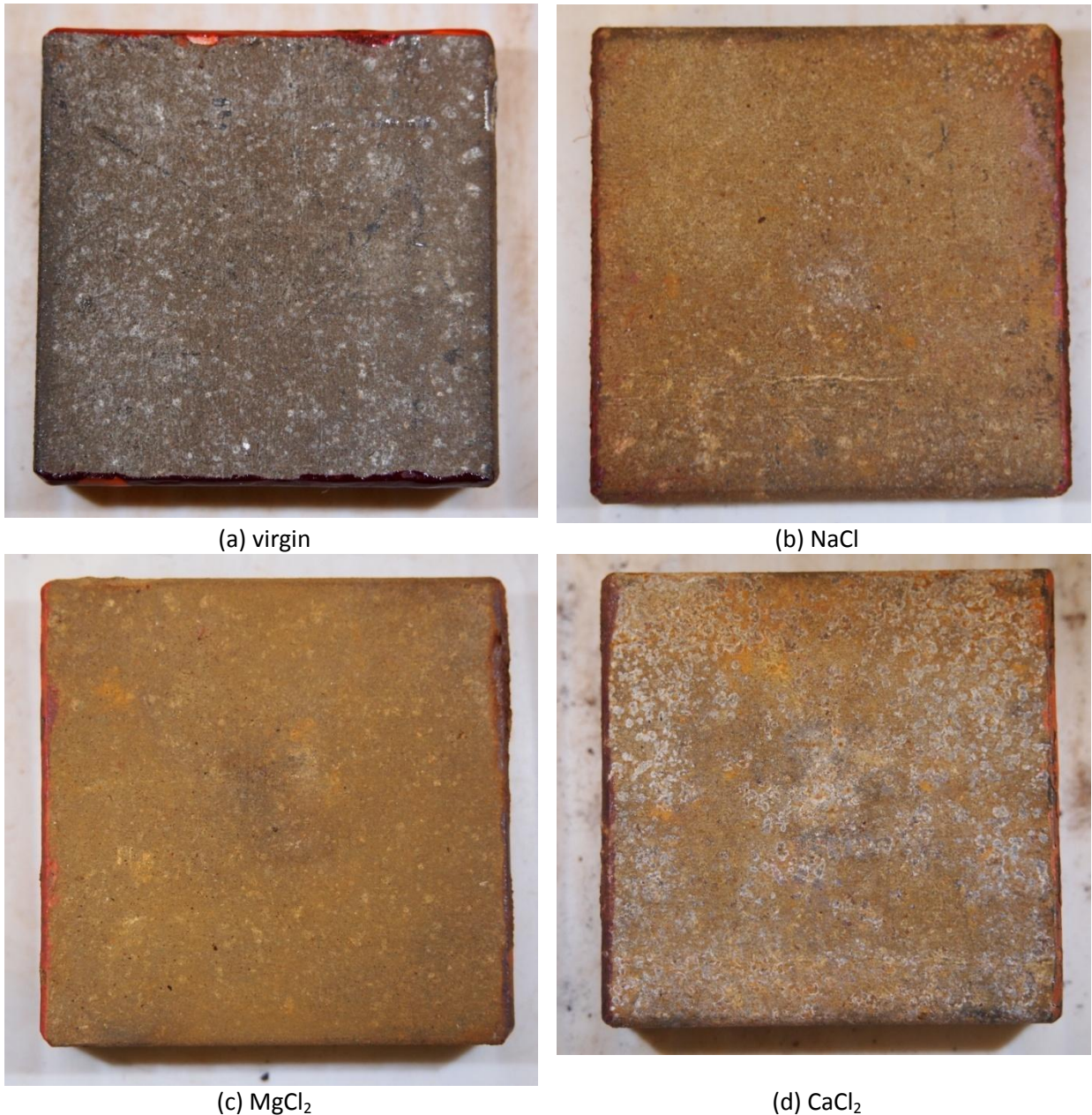


**Figure 4-58: Guard rail specimen (a) prior to testing and exposed to 50 cycles of (b) NaCl, (c) MgCl<sub>2</sub> and (d) CaCl<sub>2</sub>**

Unfortunately, the corrosion products formed on MMFX did not adhere to the surface, making it very difficult to compare mass changes to other steels and to the various solutions. The specimens exposed to NaCl showed the most variability, which is why the average value appears to show the least amount of mass change per unit area. On the other hand, most of the specimens exposed to MgCl<sub>2</sub> and CaCl<sub>2</sub> followed the trend displayed in the average in Figure 4-60. For the specimens exposed to MgCl<sub>2</sub> no

major mass changes were observed until 40 cycles, whereas specimens exposed to  $\text{CaCl}_2$  showed a significant mass change starting at 15-20 cycles. These results suggest exposure to  $\text{NaCl}$  is the worst, followed by  $\text{CaCl}_2$  and then  $\text{MgCl}_2$ , though this is speculative. It should be noted that MMFX was developed as a reinforcing bar alloy and was not intended to be exposed to neutral pH solutions. The results of the MMFX exposed to anti-icing solutions are shown below in Figure 4-60.



Figure 4-59: MMFX specimen (a) prior to testing and exposed to 50 cycles of (b)  $\text{NaCl}$ , (c)  $\text{MgCl}_2$  and (d)  $\text{CaCl}_2$

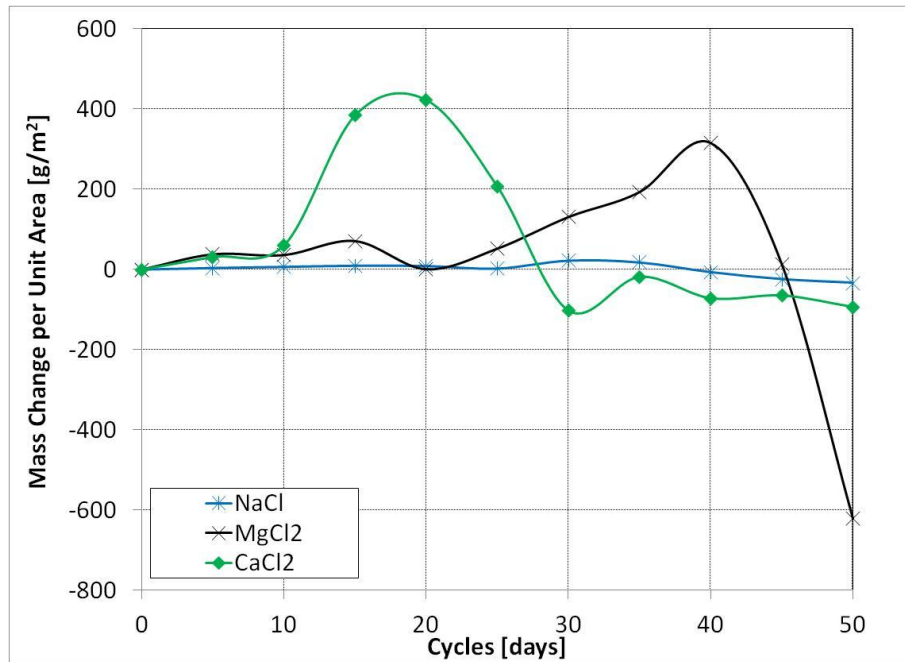


Figure 4-60: MMFX average mass change per unit area vs. SAE J2234 cycles (in days) exposed to various anti-icing solutions

## **Chapter 5 Summary and Conclusions**

This chapter summarizes and draws conclusions from the results obtained in Chapter 4. It is divided into sections based on the testing type they are: 5.1 Steel Embedded in Concrete, 5.2 Macro-cell Corrosion: ASTM G109, 5.3 Micro-cell Corrosion: Synthetic Pore Solution and 5.4 Cyclic Corrosion Chamber Tests.

### **5.1 Steel Embedded in Concrete**

None of the bars in concrete exhibited any signs of active corrosion. For the ASTM G109 samples this is shown in Figure 4-6 to Figure 4-8 for macro-cell corrosion and Figure 4-10 to Figure 4-11 for micro-cell corrosion. For the beams with ponding well, this is shown in Figure 4-15 to Figure 4-18 (micro-cell corrosion only). This is attributed to the quality and soundness of the concrete as established by the high resistance (Figure 4-9 and Figure 4-14) and the concrete was specified as a highway bridge deck quality concrete intended to survive  $\geq 75$  years. In addition, it was mixed, placed and cured in ideal laboratory conditions. This translates to significantly lower diffusion rates than would normally be expected from the concrete cast in the field and, thus, a much longer initiation period for active corrosion.

Knowing that, it may be expected that the results generated during testing yielded very little difference between the various solutions. The chlorides did not have sufficient time to diffuse to the bars in sufficient quantity to initiate active corrosion.

Furthermore, the time frame for many structures in the field to show signs of corrosion is still upwards of 20 years. It is safe to assume similar concrete in the lab would take significantly longer to show signs of corrosion. This makes it impractical to assume lab studies using similar mix designs, exposure to chloride conditions, etc. would provide reasonable results in the time frame of a graduate degree.

### **5.2 Macro-cell Corrosion: ASTM G109**

Outdoor specimens exhibit slightly higher corrosion rates and more variability in all corrosion related measurements (Figure 4-6 to Figure 4-8). This is a result of the varied temperature and humidity and it is speculated that the dilution due to precipitation would have hindered the crystallization of the salt, which blocks further ingress of the chlorides.

In all cases, micro-cell corrosion dominated macro-cell corrosion (Figure 4-12); however, these measurements all indicate that the steel was passive. From the results of Hansson et al. [24] and from the results of the ASTM G109 in this thesis it is apparent that the dominating form of corrosion is micro-cell corrosion. This is not to suggest that macro-cell corrosion cannot pose a significant threat to the corrosion of reinforcing steel, just that in most cases it is typically a few orders of magnitude lower than micro-cell corrosion.

### **5.3 Micro-cell Corrosion: Synthetic Pore Solution**

In cyclic polarization tests, steel exposed to NaCl had the most positive corrosion potential values and lowest corrosion current densities of the steels in four anti-icing solutions. On the reverse scan, the corrosion potential of this specimen is the most negative (Figure 4-25 and Figure 4-26). This suggests that the NaCl is more efficient at propagating corrosion once initiated and that the corrosion process is stable. This is generally regarded as a negative attribute. However, in nature the bars are not likely to polarize nearly as much as completed during cyclic polarization tests and the black steel rebar exposed to the other solutions showed signs of active corrosion prior to the steel exposed to NaCl.

MgCl<sub>2</sub> causes a significant drop in pH of the concrete by exchanging the Ca<sup>2+</sup> ions with Mg<sup>2+</sup> ions in the Ca(OH)<sub>2</sub>. This accompanied by the presence of Cl<sup>-</sup> ions results in the highest corrosion current rates of the steels in the four solutions tested. No signs of pitting were observed on both the autopsied specimens exposed to MgCl<sub>2</sub> (Figure 4-29 (b) and Figure 4-30 (b)) or the cyclically polarized specimens exposed to MgCl<sub>2</sub> (Figure 4-27 (b)). This indicates a completed breakdown of the passive film and mill scale. Therefore, the corrosion mechanism of the bars exposed to MgCl<sub>2</sub> is general corrosion at a lower pH.

Overall the MgCl<sub>2</sub> solution poses the largest threat to the concrete and to the reinforcing steel. The interaction between the Mg<sup>2+</sup> and the concrete, specifically the Ca(OH)<sub>2</sub> and C-S-H reported by a number of investigations, causes damage to the concrete and drastically decreases the pH (Figure 4-20). The drop in pH and presence of chlorides leaves the steel more susceptible to active corrosion than the other solutions (Figure 4-21 and Figure 4-23). The only initial benefit is that brucite may form and slow the initial ingress of more chlorides, but this would not be a dependable mechanism to protect the steel in the long-term, because with time MgCl<sub>2</sub> causes damage to the concrete, both gelatinizing and cracking the concrete, which would permit further ingress of MgCl<sub>2</sub> solution.

Black steel exposed to pore solution with NaCl, CaCl<sub>2</sub> and multi Cl<sup>-</sup> solutions performed similarly. The corrosion rates measured in all solutions were comparable (Figure 4-21 and Figure 4-23). The major difference between the specimens was that one of the bars exposed to CaCl<sub>2</sub> had a large spike in corrosion (Figure 4-24 and Figure D-9), after which the bar began to “self-heal” and return back to typical corrosion rates; the reason for this is, as yet, unclear. The black steel exposed to multi Cl<sup>-</sup> also showed one difference in that when undergoing CP testing, the maximum current density observed on the reverse scan was comparable to the bar exposed to MgCl<sub>2</sub> solution at approximately 100 A/m<sup>2</sup> (Figure 4-25). This is not likely to occur naturally because it is unlikely that steel will experience such high levels of polarization.

#### **5.4 Cyclic Corrosion Chamber Tests**

All stainless steel rebar grades exhibit similar behaviour when exposed to all forms of anti-icing solution using the SAE J2334 immersion test (Figure 4-32 to Figure 4-34). Embedded carbon steel particles (likely present from processing such as rolling and from packaging such as tie wires) will corrode rapidly on the surface of the stainless (an example of this is shown in Figure 4-46, particularly Figure 4-46 (b)); however, this is only cosmetic and the actual impact on mass change is negligible.

Galvanic coatings that have been exposed to the environment and are passivated are more protective in nature than fresh zinc coatings (Figure 4-56 and Figure 4-57) despite the zinc coating thickness on the “used” steel being 15% less than the zinc coating on the new steel (Table 4-7). This is likely a result of two phenomena: (i) the surface of the “used” steel contained the more corrosion resistant intermetallic ζ phase, where the surface of the “new” galvanized coating consisted of only the η phase (Table 4-9) and (ii) the “used” galvanized steel likely had the opportunity to form a stable passive film of zinc hydroxide.

When exposed to the MgCl<sub>2</sub> solution, the mass change of both new and used galvanized steel was comparable to the mass change found in the stainless steels (Figure 4-33); this was also true about the used galvanized steel when exposed to NaCl (Figure 4-32). In the new galvanic coating the NaCl solution caused the most mass change per unit area followed by the CaCl<sub>2</sub> solution (Figure 4-56). The CaCl<sub>2</sub> caused the most mass change per unit area in the used galvanized coating (Figure 4-57); this was still less severe than the new galvanized rebar.

All plain carbon steels and weathering steel performed poorly when exposed to all salt solutions (Figure 4-32 to Figure 4-34). In fact, weathering steel performed the poorest of these steels (with an average mass change per unit area of 1314, 2678 and 3264 g/m<sup>2</sup> in NaCl, MgCl<sub>2</sub> and CaCl<sub>2</sub>, respectively), while the weldable black steel rebar performed the best (with an average mass change per unit area of 1178, 1614 and 1778 g/m<sup>2</sup> in NaCl, MgCl<sub>2</sub> and CaCl<sub>2</sub>, respectively). This was a marginal difference and all steels should be considered highly susceptible to corrosion when exposed to any of these solutions.

## **Chapter 6 Recommendations**

This chapter provides recommendations for future testing and recommendations on what anti-icing solution and material the Ministry of Transportation should be use based solely on material performance from the results of Chapter 5. It is divided into sections based on the nature of the recommendations, they are: 6.1 Testing , 6.2 Anti-Icing Solutions and 6.3 Steel Selection When Exposed Directly to the Solution.

### **6.1 Testing**

The following recommendations are with respect to future testing and improvements to the test methods utilized in this thesis.

#### **6.1.1 Concrete**

The very high quality of the concrete mixture used prevented results being obtained in the permitted time of this project. It is, therefore, recommended that one (or multiple) of the following be altered: the mix design, the specimen design, and the exposure conditions. For example, the mix design could have a higher w/cm ratio, the reinforcing steel could have a lower concrete cover (though this would require a smaller maximum aggregate size), and the specimens could have exposure from multiple sides, cracks, etc. Any of these factors will help generate results for comparison studies within a reasonable time. If exact models are required to compare to real-life structures this would not be a reasonable experiment parameter.

Consequently, in the cases where actual life expectancy models are required, lab data would need to be correlated to structures with similar properties or testing of existing structures needs to be completed. Although this is not an exact science, it is unreasonable to expect concrete created in a laboratory to be similar to concrete cast in the field.

#### **6.1.2 ASTM G109**

Although the ASTM G109 is considered a landmark test in the field of corrosion, it is not by any means a rapid test. Furthermore, the quality of concrete has a significant impact on the ability of the salt solution to diffuse into the concrete. Therefore, for rapid testing of macro-cell tests when comparing attributes (such as steel grades, admixtures or anti-icing solutions) it is recommended the ASTM A955 Annex A.2 and A.3 be utilized. Despite the standard practice being specified for stainless steel rebar.

### ***6.1.3 Beams with Ponding Well***

Due to the reasons described above in Section 6.1.1, this test is not recommended for future testing. The time line is too short for the ions to properly diffuse through the sound concrete. Modifications to the concrete or the test may resolve this.

### ***6.1.4 Synthetic Pore Solution***

From the results, it is speculated that the mill scale of the bar acted as a protective physical barrier. The chlorides penetrated the mill scale and caused the underlying steel to actively corrode. This caused damaged to the mill scale, which eventually debonded from the underlying steel. For future testing, it is recommended that tests be performed comparing bars with and without the mill scale intact. The potentiostatic LPR tests generated from this research will be analyzed to determine the effects the four salt solutions have on the values of the double layer capacitor and, if possible, the Warburg diffusional element.

### ***6.1.5 Cyclic Corrosion Chamber***

More information is required to better compare the effects of used and new galvanic coatings and on more comparable specimens. In other words, specimens with the same geometry and, if possible, same zinc thickness should be used, with one set being used and another set being new. In order to better understand the commercially available stainless, stronger concentrations or longer times of exposure should be used. This would make it possible to compare the performance of each stainless. Lastly, this test is not suitable for materials like MMFX, as the only way to determine the consumed metal is to selectively pickle the steel. This would result in fresh metal exposed every time measurements were made.

To relate this information to a structural point of view, the mass loss of steel would be required. This could be accomplished in two ways (i) an approximate mass loss could be calculated based on the stoichiometric relation between the iron atoms and the surrounding oxygen and (ii) increasing the number of specimens and pickling a set number after each testing cycle. The former has a distinct disadvantage in that an assumption about the nature of the corrosion product(s) would need to be made. Assuming that the corrosion products are all  $\text{Fe}_2\text{O}_3$  may suffice for carbon steels but for stainless steels, MMFX, and other corrosion resistant steels this approach would not work. The later

would require additional specimens and an added pickling process to determine the mass loss but would be significantly more reliable than approximating mass loss using a stoichiometric ratio.

Using the current specimens that have been tested for 50 cycles, it would be possible to pickle them to determine the final mass loss. This would provide some of the required information, with the ultimate goal of determining the relationship of mass loss to exposure time.

Finally, to compare stainless steel grades, a significantly more aggressive environment would be required as the data from this test indicate that the current test regime has little impact on any of the stainless steel grades. By using a more aggressive environment the mass change would increase and the probability of a trend emerging would increase. This would help determine if the lower-cost stainless steel grades provide the required performance when compared with the more traditional stainless steel grades.

## **6.2 Anti-Icing Solutions**

At much colder temperatures, the coefficient of friction between car tires and ice is sufficient to ensure safe driving. If road salts were used to lower the melting temperature, and the melting temperature were not reached, the ice would remain solid; however, regelation between the tire and ice would occur at lower temperatures, thus destroying the higher coefficient of friction between the ice and tire at those colder temperatures. Due to this phenomenon, in these conditions it is not recommended to use anti-icing solutions, particularly  $\text{MgCl}_2$  and  $\text{CaCl}_2$ . Furthermore, in areas where  $\text{NaCl}$  was used and the temperature approaches or falls below the eutectic point of  $\text{NaCl}$  and water ( $-21.1^\circ\text{C}$ ), multi  $\text{Cl}^-$  should be applied to ensure that ice does not form and to minimize the roads exposure to the more deleterious  $\text{MgCl}_2$  and  $\text{CaCl}_2$ .

Overall it is recommended that  $\text{MgCl}_2$  not be used as an anti-icing agent. This is based on the fact that  $\text{MgCl}_2$  lowers the pH and attacks the concrete gelatinizing the paste component [29]. Once the pH has dropped, the amount of  $\text{Cl}^-$  required to initiate corrosion decreases as well as the steel's ability to repassivate once corrosion initiates. If the steels used in the area are galvanized, using  $\text{MgCl}_2$  may prove to cause less damage because zinc is passivated at low pH values. However, further tests are required to verify this is true for galvanized steel in concrete that is exposed to  $\text{MgCl}_2$

All of the solutions are known to damage reinforcing steel. From the pore solution testing, it was shown that NaCl, CaCl<sub>2</sub> and multi Cl<sup>-</sup> have comparable corrosion rates. However, CaCl<sub>2</sub> is also known to damage and crack the concrete [20] and showed potential for higher corrosion rates. Furthermore, when carbon steels and weathering steel were exposed directly to the various anti-icing solutions, CaCl<sub>2</sub> caused the most damage, followed closely by MgCl<sub>2</sub> and finally followed by NaCl, which, in some cases, showed mass changes per unit area less than 50% of those observed in specimens exposed to CaCl<sub>2</sub> solutions. It is, therefore, recommended that NaCl be used when possible, followed by multi Cl<sup>-</sup> and CaCl<sub>2</sub> as a final option. In particularly colder climates, the multi Cl<sup>-</sup> would provide the most suitable option as it would melt the ice with speed due to the presence of NaCl and provide adequate thawing at lower temperatures due to the presence of CaCl<sub>2</sub>.

### **6.3 Steel Selection When Exposed Directly to the Solution**

All stainless steels have significantly high resistance to chloride-induced corrosion when compared to carbon steel, by two to three orders of magnitude. From the cyclic corrosion chamber test, it is not possible to determine which grade of stainless steel provides the best resistance to chloride-induced corrosion. All forms of plain carbon steel and weathering steel corrode rapidly when exposed directly to all solutions and maintenance of these components will be inevitable. One plausible solution is using galvanic coatings on the exposed bar metal. This could be accomplished by using a flame-spray galvanic coating that could be applied as needed. Galvanic coatings provide significantly better protection than paint coatings which always have imperfections which can lead to accelerated corrosion in small specific areas. In contrast, damage to the zinc coating does not hinder the zinc's ability to act as a sacrificial anode, and corrode preferentially to the steel.

## References

- [1] M. S. Mirza and M. Haider, "The state of Infrastructure in Canada: Implications for the Infrastructure Planning and Policy," Montreal, 2003.
- [2] Environment Canada, "Code of Practice for the Environmental Management of Road Salts," Green Lane TM, 04 January 2007. [Online]. Available: [http://www.ec.gc.ca/nopp/roadsalt/cop/en/rs\\_main.htm](http://www.ec.gc.ca/nopp/roadsalt/cop/en/rs_main.htm). [Accessed 30 September 2010].
- [3] Ministry of Transportation Ontario, "Road Salt Management Keeping Ontario's Roads Safe in Winter," Government of Ontario, 10 June 2010. [Online]. Available: <http://www.mto.gov.on.ca/english/engineering/roadsalt.shtml>. [Accessed 30 September 2010].
- [4] P. K. Mehta, Concrete Structure, Properties, and Materials, W. J. Hall, Ed., Englewood Cliffs, New Jersey: Prentice-Hall, Inc., 1986, p. 1.
- [5] ASM International, "Concrete: The Advanced Industrial Material of the 21st Century," *ASM International*, vol. 26A, pp. 1325-1327, June 1995.
- [6] C. M. Hansson, A. Poursaei and S. J. Jaffer, "Corrosion of Reinforcing Bars in Concrete," Waterloo, 2007.
- [7] S. J. Jaffer and C. M. Hansson, "Chloride-Induced Corrosion Products of Steel in Cracked-Concrete Subjected to Different Loading Conditions," *Cement and Concrete Research*, vol. 39, pp. 116-125, 6 November 2009.
- [8] M. Warzecha and C. Drost, "Concrete Keeps Falling Off the Gardiner Expressway," *Toronto Life*, 11 May 2012. [Online]. Available: <http://www.torontolife.com/daily/informer/in-transit/2012/05/11/gardiner-expressway-falling-down/>. [Accessed 26 August 2012].
- [9] Activation Laboratories LTD., "A11-2513," Ancaster, 2011.
- [10] F. C. Campbell, Ed., Elements of Metallurgy and Engineering Alloys, Materials Park, Ohio: ASM International: The Materials Information Society, 2008, pp. 323, 372.
- [11] M. Pourbaix, Atlas of Electrochemical Equilibria in Aqueous Solutions, 2nd ed., Houston, Texas: National Association of Corrosion Engineers, 1974.
- [12] A. Nielsen, "Concrete Durability (in Danish)," *The Concrete Book (Beton Bogen)*, 1985.
- [13] M. Cremasco, "Analysis of the Effects of Anti-Icing Agents on the Mechanical Properties of

Concrete," University of Waterloo, Waterloo, 2013.

- [14] U.S. Department of Transportation - Federal Highway Administration, Manual of Practice for an Effective Anti-icing Program: A Guide For Highway Winter Maintenance Personnel, Maclean: Turner-Fairbank Highway Research Centre, 1996.
- [15] L. Fay, K. Volkening, C. Gallaway and X. Shi, "Performance and Impacts of Current Deicing and Anti-icing Products: User Perspective versus Experimental Data," in *87th Annual Meeting of the Transportation Research Board*, Washington, 2008.
- [16] T. D. Marcotte, "Characterization of Chloride-Induced Corrosion Products that Form in Steel-Reinforced Cementitious Materials," Waterloo, 2001.
- [17] B. P. Bergsma, "Effects of Surface Condition on the Corrosion Performance of Stainless Steel Rebar," Waterloo, 2009.
- [18] C. M. Hansson, T. Frølund and J. B. Markussen, "The Effect of Chloride Cation Type on the Corrosion of Steel in Concrete by Chloride Salts," *Cement and Concrete Research*, vol. 15, pp. 65-73, 1985.
- [19] D. B. McDonald and W. F. Perenchio, "Effects of Salt Type on Concrete Scaling," *Concrete international*, pp. 23-26, 1997.
- [20] A. Poursaee, A. Laurent and C. M. Hansson, "Corrosion of Steel Bars in OPC Mortar Exposed to NaCl, MgCl<sub>2</sub> and CaCl<sub>2</sub>: Macro- and Micro-cell Corrosion Perspective," *Cement and Concrete Research*, vol. 40, pp. 426-430, 30 September 2010.
- [21] H. Lee, R. D. Cody, A. M. Cody and P. G. Spry, "Effects of Various Deicing Chemicals on Pavement Concrete Deterioration," in *Mid-Continent Transportation Symposium Proceedings*, Iowa.
- [22] S. Chatterji, "Mechanism of the CaCl<sub>2</sub> Attack on Portland Cement Concrete," *Cement and Concrete Research*, vol. 8, pp. 461-468, 14 April 1978.
- [23] L. Sutter, T. Van Dam, R. K. Peterson and D. P. Johnston, "Long-Term Effects of Magnesium Chloride and Other Concentrated Salt Solutions on Pavement and Structural Portland Cement Concrete: Phase I Results," *Transportation Research Record: Journal of the Transportation Research Board*, vol. 1979, pp. 60-68, 2006.
- [24] C. M. Hansson, A. Poursaee and A. Laurent, "Macrocell and Microcell Corrosion of Steel in Ordinary Portland Cement and High Performance Concretes," *Cement and Concrete Research*, vol. 36, pp. 2098-2102, 2006.
- [25] D. Darwin, J. Browning, L. Gong and S. R. Hughes, "Effects of Deicers on Concrete Deterioration,"

*ACI Materials Journal*, pp. 622-627, December 2008.

- [26] B. T. Mussato, O. K. Gepraegs and G. Farnden, "Relative Effects of Sodium Chloride and Magnesium Chloride on Reinforced Concrete: State of the Art," *Transportation Research Record: Journal of the Transportation Research Board*, vol. 132, no. 12, pp. 59-66, 2006.
- [27] R. Kondo, M. Satake and H. Ushiyama, "Diffusion of Various ions into Hardened Portland Cement," in *28th General Assembly of the Cement Association of Japan*, Tokyo, Japan, 1974.
- [28] C. J. Newton and J. M. Sykes, "The Effect of Salt Additions on the Alkalinity of Ca(OH)<sub>2</sub> Solutions," *Cement and Concrete Research*, vol. 17, pp. 765-776, 1987.
- [29] D. R. M. Brew and F. P. Glasser, "Synthesis and Characterisation of Magnesium Silicate Hydrate Gels," *Cement and Concrete Research*, vol. 35, pp. 85-98, 2005.
- [30] M. Cohen and A. Bentur, "Durability of Portland Cement-Silica Fume Pastes in Magnesium Sulfate and Sodium Sulfate Solutions," *ACI Materials Journal*, pp. 148-157, May-June 1988.
- [31] J. Xn, L. Jiang, W. Wang and Y. Jiang, "Influence of CaCl<sub>2</sub> and NaCl from Different Sources on Chloride Threshold Value for the Corrosion of Steel Reinforcement in Concrete," *Construction and Building Materials*, vol. 25, pp. 663-669, 2011.
- [32] P. W. Brown and A. Doerr, "Chemical Changes in Concrete Due to the Ingress of Aggressive Species," *Cement and Concrete Research*, vol. 30, pp. 411-418, 17 December 1999.
- [33] C. M. Hansson, "The corrosion of Steel and Zirconium in Anaerobic Concrete," *Scientific Basis for Nuclear Waste Management*, vol. Vol. 50, pp. 475-482, 1986.
- [34] C. Andrade and C. Alonso, "Corrosion rate monitoring in the laboratory and on-site," *Construction and Building Materials*, vol. 10, pp. 315-328, 1996.
- [35] J. E. B. Randles, "Kinetics of Rapid Electrode Reactions," *Discussions of the Faraday Society*, vol. 1, pp. 11-19, 1947.
- [36] ASTM International, "G106 Standard Practice for Verification of Algorithm and Equipment for Electrochemical Impedance Measurements," ASTM International, West Conshohocken, 2012.
- [37] F. May, "Electrical Stimulation of the Brain," University of Nottingham, 2 December 2005. [Online]. Available: <http://www.felixmay.com/ESB/mechanisms.htm>. [Accessed 13 June 2011].
- [38] M. Stern and A. L. Geary, "Electrochemical Polarization: I. A Theoretical Analysis of the Shape of Polarization Curves," *Electrochemical Society*, vol. 104, no. 1, pp. 56-63, 1957.
- [39] C. Andrade and J. A. Gonzalez, "Quantitative Measurements of Corrosion Rate of Reinforcing

Steels Embedded in Concrete Using Polarization Resistance Measurements," *Werkstoffe und Korrosion*, vol. 29, pp. 515-519, 1978.

- [40] C. J. Newton and J. M. Sykes, "A Galvanostatic Pulse Technique for Investigation of Steel Corrosion in Concrete," *Corrosion Science*, vol. 28, no. 11, pp. 1051-1074, 1988.
- [41] D. W. Law, S. G. Millard and J. H. Bungey, "Galvanostatic Pulse Measurements of Passive and Active Reinforcing Steel in Concrete," *Corrosion Science*, vol. 56, no. 1, pp. 48-56, January 2000.
- [42] M. Otieno, H. Beushausen and M. Alexander, "Prediction of Corrosion Rate in Reinforced Concrete Structures - A Critical Review and Preliminary Results," *Materials and Corrosion*, vol. 9, no. 63, pp. 777-790, 2012.
- [43] K. C. Clear, "Transportation Research Board, Record No. 1211," Washington, 1992.
- [44] J. P. Broomfield, L. M. Rodriguez, L. M. Ortega and A. M. Garcia, "Proceedings of the International Symposium on Condition Assessment, Protection, Repair, and Rehabilitation of Concrete Bridges Exposed to Aggressive Environments," in *ACI Fall Convention*, Minneapolis, 1993.
- [45] A. Poursaei, "Potentiostatic Transient Technique, a Simple Approach to Estimate the Corrosion Current Density and Stern-Geary Constant of Reinforcing Steel in Concrete," *Cement and Concrete Research*, vol. 20, pp. 1451-1458, 2010.
- [46] K. Basham, "Choices in Corrosion-Resistant Rebar: A Comparison of the Features, Performance, and Costs of Five Rebar Options," *Concrete Construction*, 1 October 1999.
- [47] B. P. Bergsma and C. M. Hansson, "ACI SP-291-2 Formation and Stability of Protective Passive Films Formed on the New Generation of Stainless Steel Rebar Alloys," in *Corrosion of Reinforcing Steel in Concrete-Future Direction: Proceedings of the Hope & Schupack Corrosion Symposium*, Texas, 2013.
- [48] Canadian Standards Association, CSA S6-00 Canadian Highway Bridge Code, Rexdale, Ontario: Canadian Standards Association, 2000.
- [49] M. A. Islam, B. P. Bergsma and C. M. Hansson, "The Chloride-Induced Corrosion Behaviour of Stainless Steel and Carbon Steel Reinforcing Bars in Sound and Cracked Concrete," *Corrosion The Journal of Science and Engineering*, 17 October 2012.
- [50] A. Knudsen, F. M. Jensen, O. Klinghoffer and T. Skovsgaard, "Cost-Effective Enhancement of Durability of Concrete Structures by Intelligent Use of Stainless Steel Reinforcement," in *Proceedings of International Conference on Corrosion and Rehabilitation of Reinforced Concrete Structures*, Orlando, 1998.
- [51] S. R. Yeomans, Galvanized Steel in Concrete, in *Galvanized Steel Reinforcement in Concrete*, S. R.

Yeomans, Ed., Elsevier, 2004, p. 8.

- [52] C. Andrade and C. Alonso, Electrochemical Aspects of Galvanized Reinforcement Corrosion, in Galvanized Steel Reinforcement in Concrete, S. R. Yeomans, Ed., Oxford, 2004, pp. 111-144.
- [53] Z. Q. Tan and C. M. Hansson, "Effect of Surface Condition on the Initial Corrosion of Galvanized Steel Embedded in Concrete," *Corrosion Science*, vol. 59 (9), pp. 2512-2522, 2008.
- [54] A. P. Yadav, H. Katayama, K. Noda, H. Masuda, A. Nishikata and T. Tsuru, "Effect of Fe-Zn Alloy Layer on the Corrosion Resistance of Galvanized Steel in Chloride Containing Environments," *Corrosion Science*, vol. 49, no. 9, p. 3716, September 2007.
- [55] A. R. Marder, "The Metallurgy of Zinc-Coated Steel," *Progress in Materials Science*, vol. 45, pp. 191-271, 2000.
- [56] G. G. Clemena and Y. P. Virmani, "Comparison of the Corrosion Resistance of Selected Metallic Reinforcing Bars for Extension of Service Life of Future Concrete Bridges in Outdoor Concrete Blocks," *Corrosion*, 16-20 March 2003.
- [57] H. E. Townsend and J. C. Zoccola, "Eight-Year Atmospheric Corrosion Performance of Weathering Steel in Marine, Rural, and Industrial Environments," *ASTM Standard Technical Publication 767*, p. 45, 1982.
- [58] N. R. Damgaard, S. Walbridge, C. M. Hansson and J. Yeung, "Prediction and Prolongation of the Service Life of Weather Steel Highway Structures," *Journal of Constructional Steel Research*, vol. 66, no. 10, pp. 1174-1185, October 2010.
- [59] S. Kuroda, J. Kawakita and M. Takemoto, "An 18-Year Exposure Test of Thermal-Sprayed Zn, Al, and Zn-Al Coatings in Marine Environments," *Corrosion*, vol. 62, no. 7, November 2005.
- [60] D. A. Jones, Principles and Prevention of Corrosion, 2nd Edition ed., B. Stenquist, R. Kernan and P. Daly, Eds., Upper Saddle River, New Jersey: Prentice-Hall Inc., Toronto, 1996, pp. 81-84, 227, 404-405, 515.
- [61] C. P. Larrabee and S. K. Coburn, "First International Congress on Metallic Corrosion," *Journal of Colloid and Interface Science*, vol. 50, p. 276, 1962.
- [62] S. K. Coburn and Y. Kim, Metals Handbook, 9th Edition ed., vol. 13, Metals Park, Ohio: ASM International, 1987, p. 515.
- [63] W. P. Gallagher, "Conference Proceedings of 1970 National Association of Corrosion Engineers Spring Meeting," in *Corrosion*, Houston, 1970.
- [64] F. Deflorian and S. Rossi, "Premature Corrosion Failure of Structural Highway Components Made

- from Weathering Steel," *Engineering Failure Analysis*, vol. 9, pp. 541-551, 2002.
- [65] R. L. Brockenbraugh and R. J. Schmitt, Preprint C75 041-9, vol. 18, J. B. Varble, R. T. Jones and E. H. Phelps, Eds., New York, New York: IEEE, 1975, p. 39.
- [66] Frank Pianca, Ministry of Transportation Ontario, *Personal Communications About the Degradation of Weathering Steel in Infrastructure*, Waterloo, Ontario, 2008.
- [67] S. Hara, M. Miura, Y. Uchiumi, T. Fujiwara and M. Yamamoto, "Suppression of De-icing Salt Corrosion of Weathering Steel Bridges by Washing," *Corrosion Science*, vol. 47, pp. 2419-2430, 2005.
- [68] ASTM International, "G109 Standard Test Method for Determining Effects of Chemical Admixtures on Corrosion of Embedded Steel Reinforcement in Concrete Exposed to Chloride Environments," ASTM International, West Conshohocken, 2007.
- [69] F. J. Ansuini and J. R. Dimond, "Long-Term Field Tests of Reference Electrodes for Concrete - Ten Year Results," in *Corrosion 2001*, Houston, TX, 2001.
- [70] A. Poursaee, "Automatic System for Monitoring Corrosion of Steel in Concrete," *Advances in Engineering Software*, vol. 40, pp. 1179-1182, 2009.
- [71] ASTM International, "G1-03 Standard Practice for Preparing, Cleaning, and Evaluation of Corrosion Test Specimens," ASTM International, West Conshohocken, 2009.
- [72] Society of Automotive Engineers, SAE J2334, SAE Handbook 2003, 2002.
- [73] ASTM International, "C192/C192M Standard Practice for Making and Curing Concrete Test Specimens in the Laboratory," ASTM International, West Conshohocken, 2010.
- [74] ASTM International, "C873/C873M Standard Test Method for Compressive Strength of Concrete Cylinders Cast in Place in Cylindrical Molds," ASTM International, West Conshohocken, 2010.
- [75] ASTM International, "C39/ C39M Standard Test Method for Compressive Strength of Cylindrical Concrete Specimens," ASTM International, West Conshohocken, 2012.
- [76] B. Wolman, R. Dozzi, M. P. Collins, S. Costa, S. Dietrich, P. Girard, R. Griffith, D. P. Gustafson, A. Morin, J. R. Stacey, J. K. Whittaker and M. Tumkur, "G30.18-09 Carbon Steel Bars for Concrete Reinforcement," Canadian Standards Association, Mississauga, 2009.
- [77] ASTM International, "A242/A242M Standard Specification for High-Strength Low-Alloy Structural Steel," ASTM International, West Conshohocken, 2009.
- [78] ASTM International, "A588/A588M-05 Standard Specification for High-Strength Low-Alloy

Structural Steel, up to 50 ksi [345 MPa] Minimum Yield Point, with Atmospheric Corrosion Resistance," ASTM International, Conshohocken, 2005.

- [79] CSA, "CSA-G40.21-04: Structural Quality Steel," Canadian Standards Association, 2004.
- [80] M. Contractor, Interviewee, *Personal Communications Anti-icing Salt Supplier*. [Interview]. February 2013.
- [81] B. S. Phull and R. M. Kain, "Structural Practices: Corrosion and Protection of Structures in Marine Atmospheres," *Structural Magazine*, pp. 18-20, August 2004.
- [82] R. K. Nagle, E. B. Saff and A. D. Snider, *Fundamentals of Differential Equations and Boundary Value Problems*, 4th ed., K. Guardino, W. Hoffman and R. S. Reeve, Eds., Toronto, Ontario: Pearson Addison Wesley, 2004.
- [83] M. R. Spiegel and J. Liu, *Mathematical Handbook of Formulas and Tables*, 2nd ed., B. Gilson, Ed., Toronto, Ontario: McGraw-Hill, 1999, p. 136.
- [84] Canadian Standards Association, "CSA A23.1-09/A23.2-09 Concrete Materials and Methods of Concrete Construction/Test Methods and Standard Practices for Concrete," Canadian Standards Association, Mississauga, 2009.
- [85] Portland Cement Association, "Frequently Asked Questions Q: What is Meant by "Saturated Surface Dry Condition" of Aggregates," Portland Cement Association, 2013. [Online]. Available: [http://www.cement.org/tech/faq\\_saturated.asp](http://www.cement.org/tech/faq_saturated.asp). [Accessed 27 June 2013].
- [86] L. Butler, Interviewee, *Personal Communications*. [Interview]. January 2012.
- [87] ASTM International, "C143/C143M Standard Test Method for Slump of Hydraulic-Cement Concrete," ASTM International, West Conshohocken, 2003.
- [88] Hitachi High-Tech Science Corporation, "Description of ICP Optical Emission Spectrometry (ICP-OES)," Hitachi High-Tech Science Corporation, 2013. [Online]. Available: [http://www.hitachi-hitec-science.com/en/products/icp/tec\\_descriptions/descriptions1\\_e.html](http://www.hitachi-hitec-science.com/en/products/icp/tec_descriptions/descriptions1_e.html). [Accessed 13 May 2013].
- [89] A. Stefansson, I. Gunnarsson and N. Giroud, "New Methods for the Direct Determination of Dissolved Inorganic, Organic and Total Carbon in Natural Waters by Reagent-Free TM Ion Chromatography and Inductively Coupled Plasma Atomic Emission Spectrometry," *Analytica Chimica Acta*, vol. 582, no. 1, pp. 69-74, 16 January 2007.
- [90] J. Weiss, *Ion Chromatography*, 2nd ed., C. Dyllick and B. Böck, Eds., New York, New York: VCH Publishers Inc., 1995, pp. 1-13.

- [91] HORIBA, Ltd., "Home, Scientific, Products, X-Ray Fluorescence Analysis, Tutorial, Penetration Depths," HORIBA Scientific, 2013. [Online]. Available: <http://www.horiba.com/scientific/products/x-ray-fluorescence-analysis/tutorial/penetration-depths/>. [Accessed 24 May 2013].
- [92] R. Schlotz and S. Uhlig, Introduction to X-Ray Fluorescence (XRF), Madison, Wisconsin: Bruker AXS GmbH, Karlsruhe, West Germany, 2006, pp. 10-11.
- [93] Thermo Scientific, "Thermo Scientific Portable XRF Sample Analysis Techniques," Thermo Fisher Scientific Inc., 2013. [Online]. Available: <http://www.niton.com/en/portable-xrf-technology/how-xrf-works/portable-xrf-sample-analysis-techniques>. [Accessed 27 May 2013].
- [94] Thermo Scientific, "Sample Analysis Using Energy Dispersive X-ray Fluorescence (EDXRF)," Thermo Fisher Scientific Inc., 2013. [Online]. Available: [http://www.niton.com/en/portable-xrf-technology/how-xrf-works/x-ray-fluorescence-\(edxrf\)-overview](http://www.niton.com/en/portable-xrf-technology/how-xrf-works/x-ray-fluorescence-(edxrf)-overview). [Accessed 27 May 2013].

## Appendix A: Electrochemical Analysis

When analyzing the measurements acquired from a potentiostat, the Randles circuit [35] in Figure A-1 can be utilized and simplified based on the test being used.

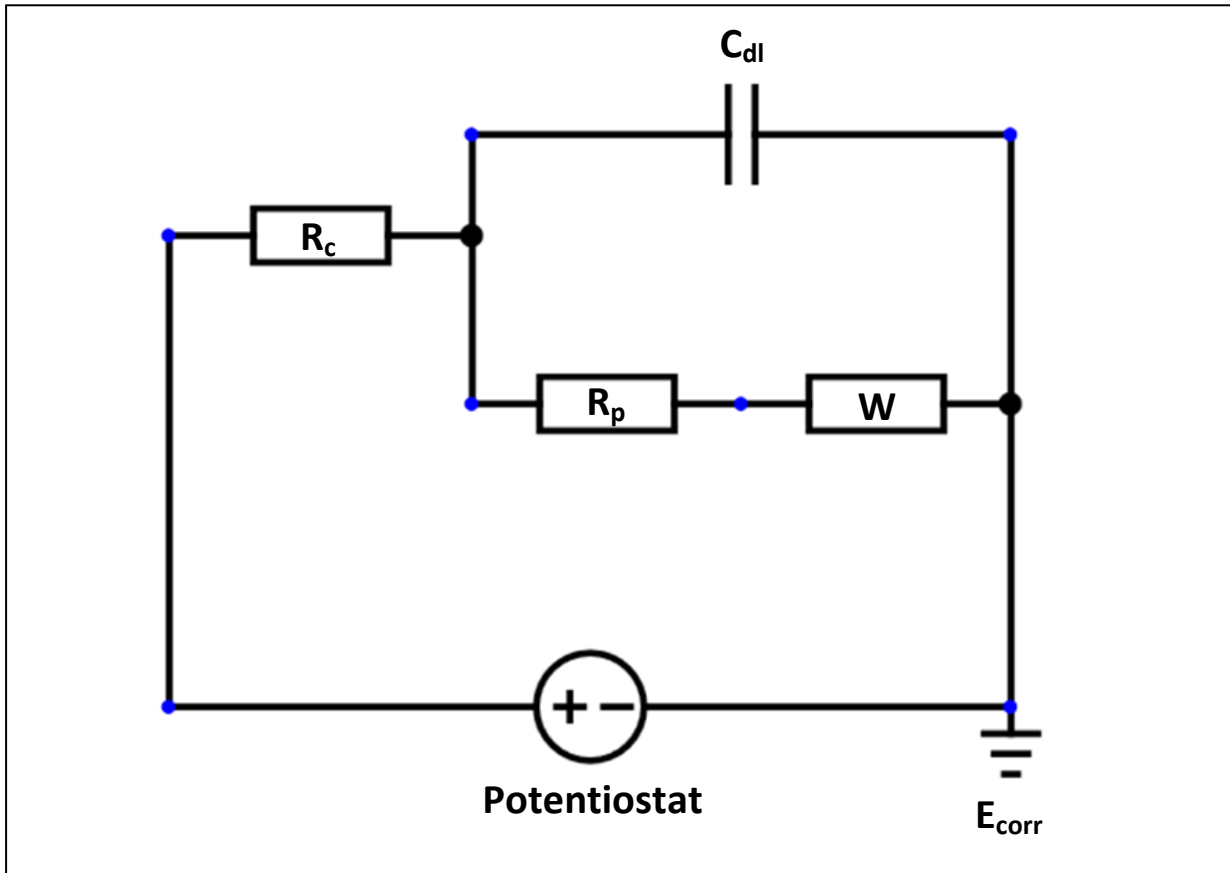


Figure A-1: Randles circuit

The various elements are as follows:

$R_c$  is the resistance of the medium the specimen resides in (this is typically concrete or synthetic pore solution).

$R_p$  is the polarization resistance (sometimes called the charge transfer resistance) this is the ease at which the specimen will relinquish electrons (i.e. corrode)

$C_{dl}$  is the double layer capacitor that is present at the surface due to the polarity of the specimen and the adsorbed surrounding water molecules.

W is the Warburg element. The Warburg element is a diffusion element that is represented by a straight line going up at a 45° angle on a Nyquist plot. Typically this element can be ignored for analysis. However, if the corrosion rate is limited, for example, by diffusion of oxygen through the concrete cover, it will be contributing to the circuit.

Some electrical signals used during testing can reach potentials where the surface conditions of the bar change, new species can develop and diffusion becomes the limiting factor. For this reason the application of this circuit for electrochemical analysis is only permissible in the linear region.

Testing carried out during through this dissertation remained primarily in the region where diffusional control was not issue and the Warburg element in Figure A-2 has been omitted. The potentiostat uses the reference electrode to determine the “ground” thus the potential used before a signal is applied by the potentiostat is measured at  $E_2$  and is the  $E_{corr}$  potential of the specimen.

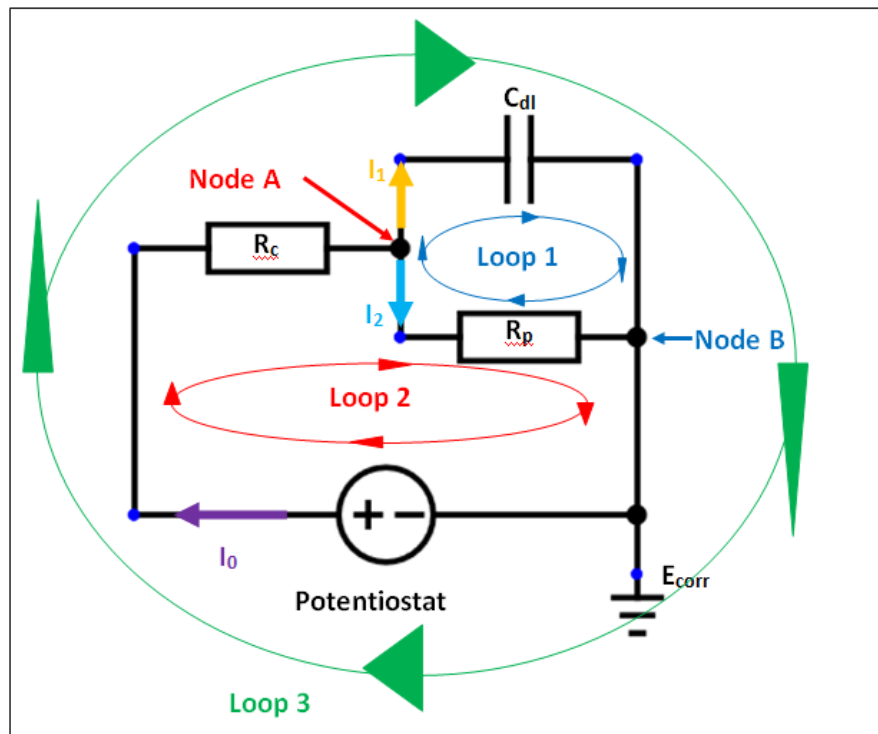


**Figure A-2: Randles circuit excluding the diffusional element, for analysis**

Applying Kirchhoff’s current law (KCL) and Kirchhoff’s voltage law (KVL) [82] to the circuit it is possible to determine the relationship for the current and the potential across the potentiostat: namely the applied current and the resulting potential for galvanostatic pulse (GP) techniques and the applied

potential and resulting current for the potentiostatic linear polarization to resistance (LPR) techniques. This is shown below and in equations A-1 through A-7.

	$I_2 R_p - \frac{1}{C_{dl}} q_1 = 0$	<b>A-1</b>
KVL loop1	$\frac{1}{C_{dl}} q_1 - R_p I_2 = 0$	
Differentiating with respect to time	$\frac{1}{C_{dl}} I_1 - R_p \frac{d(I_2)}{dt} = 0$	<b>A-2</b>
	$\Delta E - I_0 R_c - I_2 R_p = 0$	
KVL loop 2	$R_c I_0 + R_p I_2 = \Delta E$	<b>A-3</b>
KVL loop 3	$\Delta E - I_0 R_c - \frac{1}{C_{dl}} q_1 = 0$	
Note: this is a linear combination of equations A-1 and A-3	$R_c I_0 + \frac{1}{C_{dl}} q_1 = \Delta E$	<b>A-4</b>
	$I_0 = I_1 + I_2$	
KCL from nodes A and B	$I_0 - I_1 - I_2 = 0$	<b>A-5</b>

Where:

$I_0$  is the current passing through the potentiostat,

$I_1$  is the current passing through the double layer capacitor,

$I_2$  is the current passing through the polarization resistance,

$q_1$  is the charge held by the capacitor,

$\Delta E$  is the specimen's change in potential ( $E_{corr}$ ) measured at the potentiostat (it can be a function of time),

$R_c$  is the concrete resistance,

$R_p$  is the polarization resistance and

$C_{dl}$  is the double layer capacitor.

Note: for the following row reductions, "Rx" refers to row number x, example R1 is row number 1.

Substituting equations A-2, A-3 and A-5 into a matrix using the "D" operator for derivatives

$$\begin{bmatrix} 1 & -1 & -1 \\ 0 & \frac{1}{C_{dl}} & -R_p D \\ R_c & 0 & R_p \end{bmatrix} \begin{bmatrix} I_0 \\ I_1 \\ I_2 \end{bmatrix} = \begin{bmatrix} 0 \\ 0 \\ \Delta E \end{bmatrix}$$

A-6

$C_{dl} \times R2$   
 $R3 - R_c \times R1$

$$\begin{bmatrix} 1 & -1 & -1 \\ 0 & 1 & -C_{dl} R_p D \\ 0 & R_c & R_p + R_c \end{bmatrix} \begin{bmatrix} I_0 \\ I_1 \\ I_2 \end{bmatrix} = \begin{bmatrix} 0 \\ 0 \\ \Delta E \end{bmatrix}$$

$R1 + R2$   
 $R3 - R_c \times R2$

$$\begin{bmatrix} 1 & 0 & -1 - C_{dl} R_p D \\ 0 & 1 & -C_{dl} R_p D \\ 0 & 0 & R_p + R_c + C_{dl} R_p R_c D \end{bmatrix} \begin{bmatrix} I_0 \\ I_1 \\ I_2 \end{bmatrix} = \begin{bmatrix} 0 \\ 0 \\ \Delta E \end{bmatrix}$$

$R3 / (R_p + R_c + C_{dl} R_p R_c D)$

$$\begin{bmatrix} 1 & 0 & -1 - C_{dl} R_p D \\ 0 & 1 & -C_{dl} R_p D \\ 0 & 0 & 1 \end{bmatrix} \begin{bmatrix} I_0 \\ I_1 \\ I_2 \end{bmatrix} = \begin{bmatrix} 0 \\ 0 \\ \frac{\Delta E}{(R_p + R_c + C_{dl} R_p R_c D)} \end{bmatrix}$$

$R1 + (1 + C_{dl} R_p D) R3$

$$\begin{bmatrix} 1 & 0 & 0 \\ 0 & 1 & -C_{dl} R_p D \\ 0 & 0 & 1 \end{bmatrix} \begin{bmatrix} I_0 \\ I_1 \\ I_2 \end{bmatrix} = \begin{bmatrix} \frac{(1 + C_{dl} R_p D) \Delta E}{(R_p + R_c + C_{dl} R_p R_c D)} \\ 0 \\ \frac{\Delta E}{(R_p + R_c + C_{dl} R_p R_c D)} \end{bmatrix}$$

Going back to standard form to solve for  $I_0$

$$I_0 = \frac{(1 + C_{dl} R_p D) \Delta E}{(R_p + R_c + C_{dl} R_p R_c D)}$$

$$(R_p + R_c + C_{dl} R_p R_c D) I_0 = (1 + C_{dl} R_p D) \Delta E$$

$$(R_p + R_c) I_0 + (C_{dl} R_p R_c) \frac{d(I_0)}{dt} = \Delta E + (C_{dl} R_p) \frac{d(\Delta E)}{dt}$$

Governing equation for potential and current relationship across the potentiostat

$$\left( \frac{R_p + R_c}{C_{dl} R_p} \right) I_0 + (R_c) \frac{d(I_0)}{dt} = \left( \frac{1}{C_{dl} R_p} \right) \Delta E + \frac{d(\Delta E)}{dt}$$

A-7

Defining and substituting the appropriate current or potential signals with the corresponding initial conditions to equation A-7 will result in the governing equations for the system.

## A-1 Galvanostatic Pulse Technique

With the GP technique, a constant current is applied, therefore  $I_0$  and its derivatives are known. The initial condition is a circuit with only the concrete resistance. This is due to the fact that the double layer capacitor has not yet had the opportunity to charge and acts as a closed circuit. As the current is applied the capacitor builds charge and acts as an open circuit.

$$I_0 = I_{applied} = constant$$

Defining the input signal

$$\frac{d(I_0)}{dt} = 0$$

**A-8**

Defining the initial condition

$$\Delta E(t = 0) = I_{applied} R_c$$

**A-9**

Where:

$I_{applied}$  is the input current defined by the test

Substituting the input signal (equation A-8) into the governing equation for the system (equation A-7)

$$\frac{d(\Delta E)}{dt} + \left( \frac{1}{C_{dl} R_p} \right) \Delta E = \left( \frac{R_p + R_c}{C_{dl} R_p} \right) I_{applied}$$

**A-10**

Using method of undetermined coefficients to find the complimentary solution [82]

$$\Delta E_c = C e^{\tau t}$$

**A-11**

$$\tau = \frac{-1}{C_{dl} R_p}$$

Where:

$\Delta E_c$  is the complimentary solution,  $\tau$  is the time constant and  $C$  is a constant of integration.

$$\Delta E_p = A$$

Assumed form of a particular solution

$$\frac{d(\Delta E_p)}{dt} = 0$$

**A-12**

Where:

$\Delta E_p$  is a particular solution and

$A$  is a constant, the assumed form of a particular solution.

Solving for the constant "A" of a particular solution from A-12

$$0 + \left( \frac{1}{C_{dl} R_p} \right) A = \left( \frac{R_p + R_c}{C_{dl} R_p} \right) I_{applied}$$

**A-13**

$$A = (R_p + R_c)I_{applied}$$

$$\Delta E = \Delta E_p + \Delta E_c$$

Substituting the complimentary and particular solutions to solve for the general solution

$$\Delta E = A + Ce^{\tau t}$$

**A-14**

$$\Delta E = (R_p + R_c)I_{applied} + Ce^{\left(\frac{-t}{C_{dl}R_p}\right)}$$

Substitute the initial conditions from A-9 into A-14 to determine the constant

$$\Delta E(t = 0) = I_{applied}R_c = (R_p + R_c)I_{applied} + Ce^{\left(\frac{-(0)}{C_{dl}R_p}\right)}$$

**A-15**

$$I_{applied}R_c = (R_p + R_c)I_{applied} + C$$

$$C = -I_{applied}R_p$$

**A-16**

$$\Delta E = (R_p + R_c)I_{applied} - I_{applied}R_p e^{\left(\frac{-t}{C_{dl}R_p}\right)}$$

Final equation for the system undergoing a GP test

$$\frac{\Delta E}{I_{applied}} = R_c + R_p \left(1 - e^{\left(\frac{-t}{C_{dl}R_p}\right)}\right)$$

**A-17**

## A-2 Potentiostatic Technique

With LPR technique, a constant potential difference is applied, therefore  $\Delta E$  and its derivatives are known. The initial condition is a circuit with only the concrete resistance. This is due to the fact that the double layer capacitor has not yet had the opportunity to charge and acts as a closed circuit. As the potential difference is applied the capacitor builds charge and acts as an open circuit.

$$\Delta E = \Delta E_{applied} = constant$$

Defining the input signal

$$\frac{d(\Delta E)}{dt} = 0$$

**A-18**

Defining the initial condition

$$I_0(t = 0) = \frac{\Delta E_{applied}}{R_c}$$

**A-19**

Substituting the input signal (equation A-8) into the governing equation for the system (equation A-7)

$$(R_c) \frac{d(I_0)}{dt} + \left( \frac{R_p + R_c}{C_{dl} R_p} \right) I_0 = \left( \frac{1}{C_{dl} R_p} \right) \Delta E_{applied} \quad \text{A-20}$$

Using method of undetermined coefficients to find the complimentary solution

$$I_{0c} = C e^{\tau t} \quad \text{A-21}$$

$$\tau = \frac{-(R_p + R_c)}{C_{dl} R_p R_c}$$

Where:  
 $I_{0c}$  is the complimentary solution.

$$I_{0p} = A$$

Assumed form of a particular solution

$$\frac{d(I_{0p})}{dt} = 0 \quad \text{A-22}$$

Where:  
 $I_{0p}$  is a particular solution and

$$0 + \left( \frac{R_p + R_c}{C_{dl} R_p} \right) A = \left( \frac{1}{C_{dl} R_p} \right) \Delta E_{applied}$$

Solving for the constant "A" of a particular solution from A-12

$$A = \frac{\Delta E_{applied}}{(R_p + R_c)} \quad \text{A-23}$$

$$I_0 = I_{0p} + I_{0c}$$

Substituting the complimentary and particular solutions to solve for the general solution

$$I_0 = A + C e^{\tau t}$$

$$I_0 = \frac{\Delta E_{applied}}{(R_p + R_c)} + C e^{\left( \frac{-(R_p + R_c)t}{C_{dl} R_p R_c} \right)} \quad \text{A-24}$$

Substitute the initial conditions from A-9 into A-14 to determine the constant

$$I_0(t = 0) = \frac{\Delta E_{applied}}{R_c} = \frac{\Delta E_{applied}}{(R_p + R_c)} + C e^{\left( \frac{-(R_p + R_c)(0)}{C_{dl} R_p R_c} \right)} \quad \text{A-25}$$

$$\frac{\Delta E_{applied}}{R_c} = \frac{\Delta E_{applied}}{(R_p + R_c)} + C$$

$$C = \frac{\Delta E_{applied}}{R_c} - \frac{\Delta E_{applied}}{(R_p + R_c)} \quad \text{A-26}$$

Final equation for the system undergoing a LPR test

$$I_0 = \frac{\Delta E_{applied}}{(R_p + R_c)} + \left( \frac{\Delta E_{applied}}{R_c} - \frac{\Delta E_{applied}}{(R_p + R_c)} \right) e^{\left( \frac{-(R_p + R_c)t}{C_{dl} R_p R_c} \right)} \quad \text{A-27}$$

$$\frac{I_0}{\Delta E_{applied}} = \frac{1}{(R_p + R_c)} + \left( \frac{R_p}{R_c(R_p + R_c)} \right) e^{\left( \frac{-(R_p + R_c)t}{C_{dl} R_p R_c} \right)} \quad \text{A-28}$$

Comparing equation A-17 to A-27 it is easy to see that A-27 is more complex, specifically the time constant is more complex making curve fitting more difficult. However, with both GP and LPR methods the initial spike and steady state response are comparable as shown below in section A-3.

### A-3 Steady State Testing

Looking at the steady state results of direct current testing such as potential static and potential dynamic tests, the circuit can be reduced further to Figure A-3.

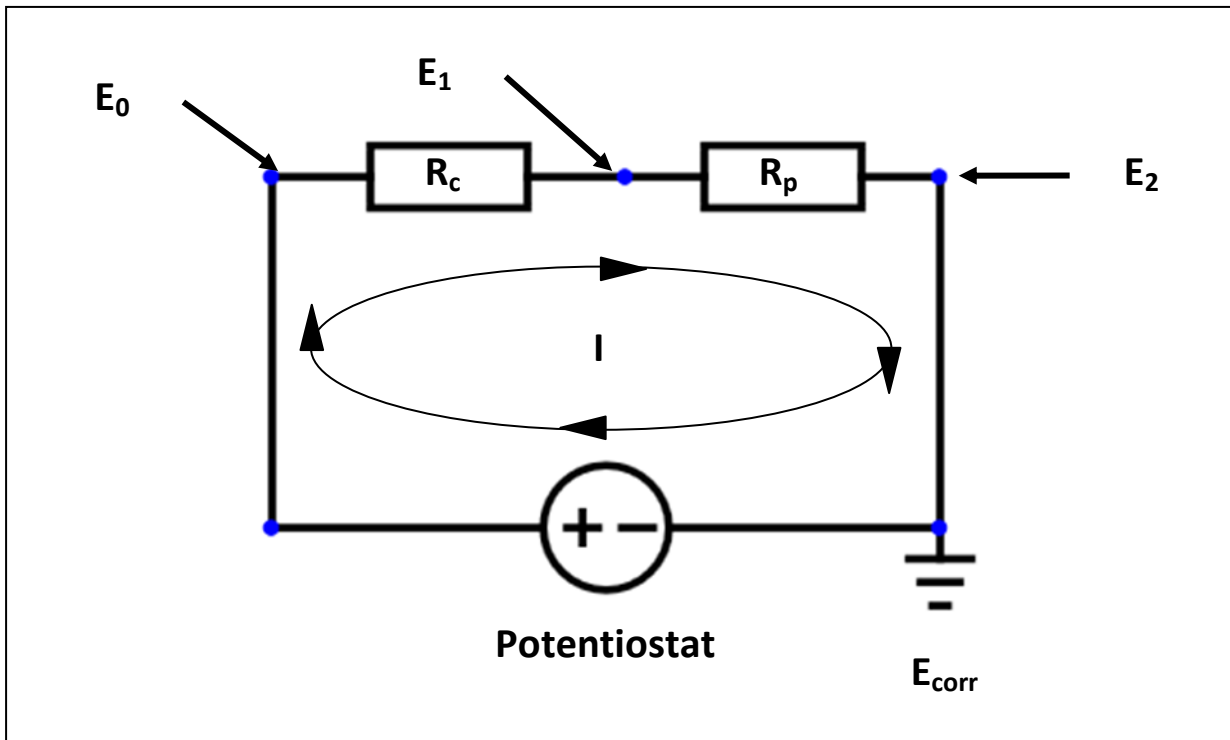


Figure A-3: Simplified Randles circuit at steady-state

Anodic LPR

$$\Delta E_A = (E_0 - E_2)_A = 20mV$$

Cathodic LPR

$$\Delta E_C = (E_0 - E_2)_C = -20mV$$

KVL

$$E_{Rc} + E_{Rp} - E_p = 0$$

Substituting elements

$$IR_c + IR_p = (E_0 - E_2)$$

$$R_p = \frac{(E_0 - E_2)}{I} - R_c$$

$$R_{p,A} = \frac{\Delta E_A}{I_A} - R_c$$

$$R_{p,C} = \frac{\Delta E_C}{I_C} - R_c$$

Assuming linear anodic and  
Cathodic regions

$$R_p = \frac{R_{p,A} + R_{p,C}}{2}$$

Substituting for  $R_{p,A}$  and  $R_{p,C}$

$$R_p = \left[ \frac{\Delta E_A - I_A R_c}{I_A} + \frac{\Delta E_C - I_C R_c}{I_C} \right] / 2$$

$$R_p = \frac{I_C \Delta E_A - I_C I_A R_c + I_A \Delta E_C - I_A I_C R_c}{2 I_A I_C}$$

$$R_p = \frac{I_C \Delta E_A + I_A \Delta E_C - 2 I_A I_C R_c}{2 I_A I_C}$$

$$R_p = \frac{I_C \Delta E_A + I_A \Delta E_C}{2 I_A I_C} - R_c$$

Assuming

$$I_A = -I_C = I$$

$$R_p = \frac{-I \Delta E_A + I \Delta E_C}{-2 I^2} - R_c$$

$$R_p = \frac{\Delta E_A - \Delta E_C}{2 I} - R_c$$

Let

$$\Delta I = I_A - I_C = I - (-I) = 2I$$

$$R_p = \frac{\Delta E_A - \Delta E_C}{\Delta I} - R_c \quad \text{A-29}$$

Similarly it can be shown that the steady state for GP is just a re-arrangement of equation A-29

$$\Delta I = \frac{\Delta E_A - \Delta E_C}{R_c + R_p} \quad \text{A-30}$$

## A-4 Cyclic Polarization

Cyclic Polarization scans can range from a few millivolts to several hundred volts. As such, the scans will typically pass through linear, log-linear and a variety of other points of interest. This section deals with the derivation of the linear and log-linear portion of a CP curve.

### A-4.1 Linear Region ( $\sim \pm 20$ mV)

Cyclic Polarization scans typically go well beyond the linear region. This limits the usefulness of this derivation to only within the  $\sim \pm 20$  mV range. Furthermore, it will be shown that the slope of this line is the total resistance of the system.

$$\Delta E = t \Delta \dot{E}_{applied}$$

Defining the input signal

$$\frac{d(\Delta E)}{dt} = \Delta \dot{E}_{applied} \quad \text{A-31}$$

Where

$\Delta \dot{E}_{applied}$  is the rate of change of the potential difference defined by the LPR test.

Defining the initial condition

$$\lim_{t \rightarrow 0} I_0(t) = \frac{t \Delta \dot{E}_{applied}}{R_c} \rightarrow 0 \quad \text{A-32}$$

Substituting the input signal (equation A-8) into the governing equation for the system (equation A-7)

$$(R_c) \frac{d(I_0)}{dt} + \left( \frac{R_p + R_c}{C_{dl} R_p} \right) I_0 = \left( \frac{1}{C_{dl} R_p} \right) t \Delta \dot{E}_{applied} + \Delta \dot{E}_{applied} \quad \text{A-33}$$

Using method of undetermined

$$I_{0c} = C e^{\tau t} \quad \text{A-34}$$

coefficients to find the complimentary solution, this is the same as equation A-21

$$\tau = \frac{-(R_p + R_c)}{C_{dl}R_pR_c}$$

$$I_{0p} = Bt + A$$

Assumed form of a particular solution

$$\frac{d(I_{0p})}{dt} = B$$

**A-35**

Where:

B is a constant, from the assumed form of a particular solution.

Solving for the constants "A" and "B" of a particular solution from A-35

$$(R_c)B + \left(\frac{R_p + R_c}{C_{dl}R_p}\right)(Bt + A) = \left(\frac{1}{C_{dl}R_p}\right)t\Delta\dot{E}_{applied} + \Delta\dot{E}_{applied}$$

$$\begin{aligned} (R_c)B + \left(\frac{R_p + R_c}{C_{dl}R_p}\right)A + \left(\frac{R_p + R_c}{C_{dl}R_p}\right)Bt \\ = \left(\frac{1}{C_{dl}R_p}\right)t\Delta\dot{E}_{applied} + \Delta\dot{E}_{applied} \end{aligned}$$

$$\left(\frac{R_p + R_c}{C_{dl}R_p}\right)Bt = \left(\frac{1}{C_{dl}R_p}\right)t\Delta\dot{E}_{applied}$$

$$B = \frac{\Delta\dot{E}_{applied}}{(R_p + R_c)}$$

**A-36**

$$(R_c)B + \left(\frac{R_p + R_c}{C_{dl}R_p}\right)A = \Delta\dot{E}_{applied}$$

$$\frac{R_c\Delta\dot{E}_{applied}}{(R_p + R_c)} + \left(\frac{R_p + R_c}{C_{dl}R_p}\right)A = \Delta\dot{E}_{applied}$$

$$A = \left(\Delta\dot{E}_{applied} - \frac{R_c\Delta\dot{E}_{applied}}{(R_p + R_c)}\right)\left(\frac{C_{dl}R_p}{(R_p + R_c)}\right)$$

$$A = \left(\frac{\Delta\dot{E}_{applied}(R_p + R_c) - R_c\Delta\dot{E}_{applied}}{(R_p + R_c)}\right)\left(\frac{C_{dl}R_p}{(R_p + R_c)}\right)$$

$$A = \left( \frac{R_p \Delta \dot{E}_{applied}}{(R_p + R_c)} \right) \left( \frac{C_{dl} R_p}{(R_p + R_c)} \right) = \frac{R_p^2 C_{dl} \Delta \dot{E}_{applied}}{(R_p + R_c)^2} \quad \text{A-37}$$

Substituting the complimentary and particular solutions to solve for the general solution

$$I_0 = I_{0p} + I_{0c}$$

A-38

Substitute the initial conditions from A-9 into A-14 to determine the constant

$$I_0 = A + Bt + Ce^{\tau t}$$

$$I_0(t = 0) =$$

A-39

$$0 = A + B(0) + Ce^{\tau(0)}$$

$$0 = A + C$$

$$C = -A = \frac{-R_p^2 C_{dl} \Delta \dot{E}_{applied}}{(R_p + R_c)^2} \quad \text{A-40}$$

$$I_0 = Bt + A(1 - e^{\tau t})$$

Final equation for the system undergoing a LPR test

$$I_0 = \frac{\Delta \dot{E}_{applied}}{(R_p + R_c)} t + \frac{R_p^2 C_{dl} \Delta \dot{E}_{applied}}{(R_p + R_c)^2} \left( 1 - e^{\left( \frac{-(R_p + R_c)}{C_{dl} R_p R_c} t \right)} \right) \quad \text{A-41}$$

Rearranging equation A-31 to solve for t and substituting into equation A-41 which gives the relationship between I and E

$$I_0 = \frac{\Delta \dot{E}_{applied}}{(R_p + R_c)} \left( \frac{\Delta E}{\Delta \dot{E}_{applied}} \right) + \frac{R_p^2 C_{dl} \Delta \dot{E}_{applied}}{(R_p + R_c)^2} \left( 1 - e^{\left( \frac{-(R_p + R_c)}{C_{dl} R_p R_c} \left( \frac{\Delta E}{\Delta \dot{E}_{applied}} \right) \right)} \right)$$

$$I_0 = \frac{\Delta E}{(R_p + R_c)} + \frac{R_p^2 C_{dl} \Delta \dot{E}_{applied}}{(R_p + R_c)^2} \left( 1 - e^{\left( \frac{-(R_p + R_c) \Delta E}{C_{dl} R_p R_c \Delta \dot{E}_{applied}} \right)} \right) \quad \text{A-42}$$

Equation A-42 provides the relationship for cyclic polarization. As mentioned this is only applicable in the linear region where the Randle's circuit applies. As the name implies, the relationship in this area is linear. The first term,  $\frac{\Delta E}{(R_p + R_c)}$  dominates. As the value for the double layer capacitor is small, scan

rates for CP tests are typically low (less than 1[mV/s]), and the value of  $\frac{R_p^2}{(R_p+R_c)^2}$  is always less than one.

#### **A-4.2 Log-Linear Region ( $\sim\pm 200$ mV)**

When at equilibrium the rate of the forward reaction is the same as the rate of the reverse reaction. For example, the rate of hydrogen gas evolution is the same as the rate of hydrogen decomposition. That is to say equation A-43 occurs at the same rate as equation A-44.



This phenomenon results because a buildup of charge (unbound excess electrons) cannot exist. This also means that it is not possible to measure the equilibrium current density. In order to determine the equilibrium current the system must be pushed from equilibrium either by means of a potential source or a current source. The resulting current (or applied current depending on the test) is the difference between the anodic curve and the cathodic curve. The relationship between current and electric potential of a given system is log linear [60] as shown below in Figure A-4.

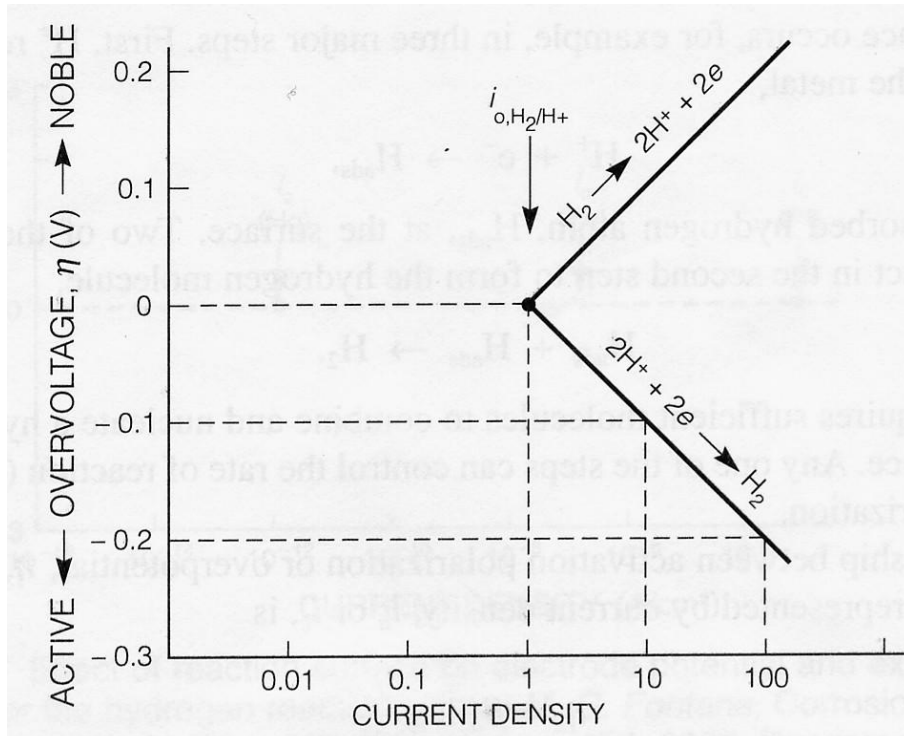


**Figure A-4: Example relationship between current and potential. The anodic curve shows the decomposition (oxidation) of hydrogen gas and the formation (reduction) of hydrogen ions to hydrogen gas [60]**

The derivation of this relationship is shown below beginning with the rates of the forward and reverse reaction.

Equations for the forward and reverse reactions for a single species

$$r_f = K_f e^{\left(-\frac{\Delta G_f^*}{RT}\right)} \quad r_r = K_r e^{\left(-\frac{\Delta G_r^*}{RT}\right)} \quad \text{A-45 [60]}$$

At equilibrium the forward and reverse reaction are equal (which is why  $i_o$  cannot be measured directly).

$$r_f(i = i_o) = r_r(i = i_o) = \frac{i_o a}{nF} \quad \text{A-46 [60]}$$

Equation A-46 can be rearranged to produce equation A-47

$$i_o = K'_f e^{\left(-\frac{\Delta G_f^*}{RT}\right)} = K'_r e^{\left(-\frac{\Delta G_r^*}{RT}\right)} \quad \text{A-47 [60]}$$

$$\text{Where } K'_f = \frac{nFK_f}{a} \text{ and } K'_r = \frac{nFK_r}{a}$$

Where:

$r_f$  and  $r_r$  are the rates of the forward and reverse reactions,  
 $K_f$  and  $K_r$  are the rate constants of the forward and reverse reactions,  
 $\Delta G^*_f$  and  $\Delta G^*_r$  are the change in Gibbs free energy of the forward and reverse reactions,  
 $R$  is the ideal gas constant,  
 $T$  is the absolute temperature,  
 $i_0$  is the exchange current density,  
 $a$  is the atomic weight,  
 $n$  is the number of equivalents exchanged (i.e. number of electrons) and  
 $F$  is Faraday's constant.

When an over potential is applied the discharge reaction rate is reduced by  $\alpha n F \eta_c$  and that of the ionization is increased by  $(1-\alpha)n F \eta_c$ .

$$\begin{aligned} \eta_c &= E_c - e \\ \eta_a &= E_a - e \\ i_c &= K'_f e^{\left(\frac{-(\Delta G^*_f - \alpha n F \eta_c)}{RT}\right)} \text{ and } i_a = K'_r e^{\left(\frac{-(\Delta G^*_r + (1-\alpha)n F \eta_a)}{RT}\right)} \end{aligned} \quad \text{A-48 [60]}$$

Where:

$\eta_a$  and  $\eta_c$  is the anodic and cathodic potential change from the half-cell electrode potential,  
 $E_a$  and  $E_c$  are the potential change from the half-cell electrode potential,  
 $e$  is the half-cell electrode potential (in the case of hydrogen  $e=0$  V) and  
 $i_a$  and  $i_c$  is the anodic and cathodic current density.

Defining the net current when applying a cathodic over potential

$$i_{app,c} = i_c - i_a = K'_f e^{\left(\frac{-(\Delta G^*_f - \alpha n F \eta_c)}{RT}\right)} - K'_r e^{\left(\frac{-(\Delta G^*_r + (1-\alpha)n F \eta_c)}{RT}\right)} \quad \text{A-49}$$

Where:

$i_{app,c}$  and  $i_{app,a}$  are the cathodic and anodic net applied currents.

Substituting  $i_0$  from equation A-47 into equation A-49

$$i_{app,c} = i_0 \left( e^{\left(\frac{\alpha n F \eta_c}{RT}\right)} - e^{\left(\frac{-(1-\alpha)n F \eta_c}{RT}\right)} \right) \quad \text{A-50}$$

Similarly it can be shown that an anodic over potential results in equation A-51.

$$i_{app,a} = i_a - i_c = i_0 \left( e^{\left(\frac{\alpha n F \eta_a}{RT}\right)} - e^{\left(\frac{-(1-\alpha)n F \eta_a}{RT}\right)} \right) \quad \text{A-51}$$

If  $\eta$  is sufficiently high than the right term disappears in equations A-50 and A-51, simplifying to A-52 and expressed as A-53

$$\begin{aligned} i_{app,c} &= i_0 e^{\left(\frac{\alpha n F \eta_c}{RT}\right)} \\ i_{app,a} &= i_0 e^{\left(\frac{\alpha n F \eta_a}{RT}\right)} \end{aligned} \quad \text{A-52}$$

As stated by Jones the relationship between over potential and the rate of reaction shown in equation A-52 can be simplified to equation A-53 [60]

$$\eta_c = \beta_c \log \frac{i_c}{i_o}$$

$$\eta_a = \beta_a \log \frac{i_a}{i_o}$$

A-53  
[60]

$$\text{Where } \beta = \frac{RT \ln 10}{anF} = \frac{RT2.3}{anF}$$

Where:

$\beta_a$  and  $\beta_c$  is the anodic and cathodic Tafel slope.

Typically these reactions are not spontaneously happening alone, usually there are two or more species reacting with one another to create the driving force for the system. For example, zinc can dissolve in an aside and be reduced (the anodic reaction). At the surface of the zinc, the excess electrons can oxidize the available hydrogen ions to produce hydrogen gas (the cathodic reaction). The potentials of both species with shift to a new intermediate potential  $E_{corr}$ , and the speed of the reaction will be  $i_{corr}$  this is shown below in Figure A-5.

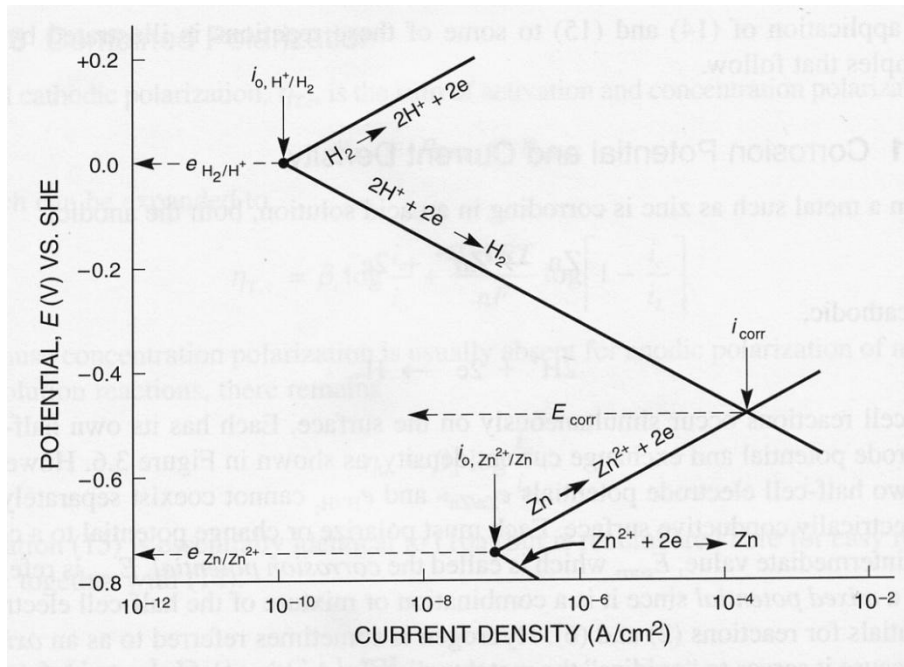
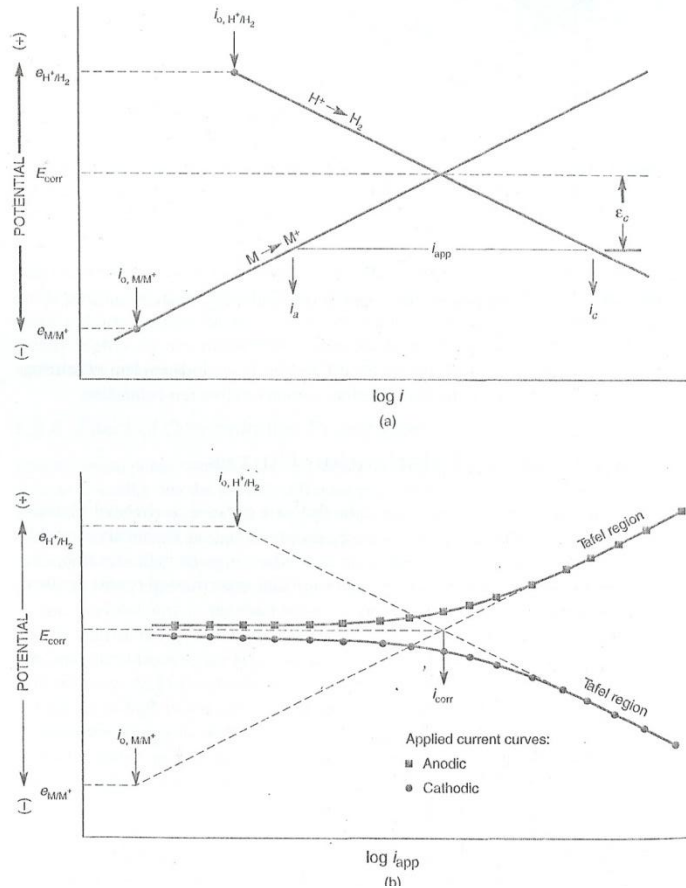


Figure A-5: Mixed potential of zinc dissolving in an acid [60].

Once again, at equilibrium,  $E_{corr}$ ,  $i_{corr}$  cannot be measured directly. To determine  $i_{corr}$  the potential must be shifted by means of a potential source or current source as shown in Figure A-6. Once this shift is

made the data can be extrapolated linearly back to determine the intersection of the anodic and cathodic slopes to determine  $i_{corr}$ .



**Figure A-6: (a) The theoretic cathodic and anodic curves of a metal dissolving reducing hydrogen ions to hydrogen gas and (b) showing the resulting measured potential from the theoretic curves [60]**

The log-linear region of a CP scan is where the Tafel slopes can be found. These values can be used to determine the Stern-Geary constant. The relationship between the Stern-Geary constant and the Tafel slopes are shown below.

$$\epsilon_c = E_c - E_{corr}$$

$$\epsilon_a = E_a - E_{corr}$$

**A-54**

Where:

$E_a$  and  $E_c$  are the applied anodic and cathodic potentials and  
 $\varepsilon_a$  and  $\varepsilon_c$  is the anodic and cathodic over potential difference from  $E_{corr}$ .

$$\varepsilon_c = \beta_c \log \frac{i_c}{i_{corr}}$$

Similar to equation A-53,  
the over potential and  $i_{corr}$   
values can be used.

**A-55 [60]**

$$\varepsilon_a = \beta_a \log \frac{i_a}{i_{corr}}$$

$$AR_p = \lim_{\varepsilon \rightarrow 0} \frac{d\varepsilon}{di_{app}} \cong \lim_{\varepsilon \rightarrow 0} \frac{\Delta\varepsilon}{\Delta i_{app}}$$

**A-56 [60]**

Where:

A is the surface area.

Substituting equation A-53  
and A-54 and A-55 into  
A-56

$$AR_p = \frac{\varepsilon_c}{i_{app,c}} = \frac{\varepsilon_c}{i_c - i_a}$$

**A-57**

Rearranging and  
substituting A-55 into A-57

$$AR_p = \frac{\varepsilon_c}{i_{corr} 10^{\frac{\varepsilon_c}{\beta_c}} - i_{corr} 10^{\frac{\varepsilon_c}{\beta_a}}}$$

**A-58**

$$\begin{aligned} a^x &= e^{x \ln a} = \sum_{i=0}^n \frac{(x \ln a)^i}{i!} \\ &= 1 + x \ln a + \frac{(x \ln a)^2}{2!} + \frac{(x \ln a)^3}{3!} + \dots \end{aligned}$$

**A-59[83]**

Using the first two terms  
of a Taylor series  
expansion equation A-58  
to simplify the exponential  
term in equation A-58

$$AR_p = \frac{\varepsilon_c}{i_{corr} \left[ 1 + \frac{\varepsilon_c}{\beta_c} \ln 10 - \left( 1 + \frac{\varepsilon_c}{\beta_a} \ln 10 \right) \right]}$$

$$AR_p = \frac{\varepsilon_c}{i_{corr} \ln 10 \left( \frac{\varepsilon_c}{\beta_c} - \frac{\varepsilon_c}{\beta_a} \right)}$$

$$AR_p = \frac{\varepsilon_c}{i_{corr} \varepsilon_c \ln 10 \left( \frac{\beta_a - \beta_c}{\beta_a \beta_c} \right)}$$

$$AR_p = \frac{\beta_a \beta_c}{i_{corr} \ln 10 (\beta_a - \beta_c)}$$

$$i_{corr} = \frac{1}{AR_p} \left[ \frac{\beta_a \beta_c}{\ln 10 (\beta_a - \beta_c)} \right] = \frac{B}{AR_p} \quad \text{A-60}$$

Similarly for an anodic over potential,  $\epsilon_a$

$$i_{corr} = \frac{1}{AR_p} \left[ \frac{\beta_a \beta_c}{\ln 10 (\beta_c - \beta_a)} \right] = \frac{-B}{AR_p}$$

It is important to note that  $\beta_c$  is a negative value and depending on the current convention chosen, the measured or applied current could also be negative or positive (though on logarithmic curves these are all represented as positive values to avoid log of a negative number). For this reason the more conventional way of expressing B is shown below in equation A-61 and A-62.

$$B = \frac{\beta_a \beta_c}{\ln 10 (\beta_a + \beta_c)} = \frac{\beta_a \beta_c}{2.3(\beta_a + \beta_c)} \quad \text{A-61}$$

$$i_{corr} = \frac{B}{AR_p} \quad \text{A-62}$$

## **Appendix B: Casting and Concrete**

The concrete being tested was intended to replicate structurally reinforced concrete exposed to chlorides with freezing and thawing conditions. According to CSA A23.1-09 table 4 this would be considered class C-1 concrete [84]. The requirements for this concrete are shown below in Table B-1

**Table B-1: Requirements for C, F, N A, and S classes of exposure [84]**

Class of exposure*	Maximum water-to-cementing materials ratio†	Minimum specified compressive strength (MPa) and age (d) at test‡	Air content category as per Table 4	Curing type (see Table 20)			Chloride ion penetrability requirements and age at test‡
				Normal concrete	HVSCM 1	HVSCM 2	
C-XL	0.40	50 within 56 d	1 or 2§	3	3	3	< 1000 coulombs within 56 d
C-1 or A-1	0.40	35 at 28 d	1 or 2§	2	3	2	< 1500 coulombs within 56 d
C-2 or A-2	0.45	32 at 28 d	1	2	2	2	—
C-3 or A-3	0.50	30 at 28 d	2	1	2	2	—
C-4** or A-4	0.55	25 at 28 d	2	1	2	2	—
F-1	0.50	30 at 28 d	1	2	3	2	—
F-2	0.55	25 at 28 d	2††	1	2	2	—
N‡‡	As per the mix design for the strength required	For structural design	None	1	2	2	—
S-1	0.40	35 at 56 d	2	2	3	2	—
S-2	0.45	32 at 56 d	2	2	3	2	—
S-3	0.50	30 at 56 d	2	1	2	2	—

\*See Table 1 for a description of classes of exposure.

†The minimum specified compressive strength may be adjusted to reflect proven relationships between strength and the water-to-cementing materials ratio. The water-to-cementing materials ratio shall not be exceeded for a given class of exposure.

‡In accordance with ASTM C 1202, an age different from that indicated may be specified by the owner. Where calcium nitrite corrosion inhibitor is to be used, the same concrete mixture, without calcium nitrite, shall be prequalified to meet the requirements for the permeability index in this Table. For field testing, the owner shall specify the type of specimen and location from which it is taken. If cores are required, the concrete cores shall be taken in accordance with Clause 6.1.2.3.3 of CSA S413.

§Use air content category 1 for concrete exposed to freezing and thawing. Use air content category 2 for concrete not exposed to freezing and thawing.

\*\*For class of exposure C-4, the requirement for air-entrainment should be waived when a steel trowelled finish is required. The addition of supplementary cementing materials may be used to provide reduced permeability in the long term, if required.

††Interior ice rink slabs and freezer slabs with a steel trowelled finish have been found to perform satisfactorily without entrained air.

‡‡See Clause 8.12 for concrete mixes for concrete floors.

## B-1 Determining Saturated Surface Dry Conditions

The amount of water in a mix design is determined by the water to cement ratio, which is used to ensure that the cement has enough water to properly undergo hydration as well as ensuring that there is not an excess of water, which could result in weaker cement. Unfortunately, the aggregates used in concrete can contain water and can disrupt this ratio. If the aggregates contain too much water then the actual w/cm ratio will be higher than specified by the mix. Likewise if the aggregates have too little or even no water, they will absorb water from the mix causing the w/cm ratio to drop. Aggregates can be described in four states which are shown below in Figure B-1.

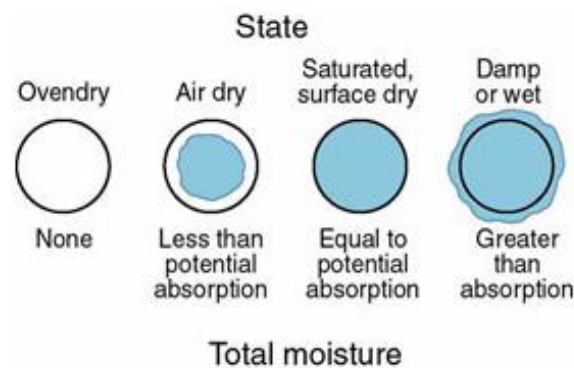


**Figure B-1: Various states of aggregates used in concrete [85]**

For this reason, aggregates should be saturated surface dry (SSD). When aggregates are SSD they will not supply water or absorb more water. The following shows how to determine the SSD conditions as a percent of the aggregate mass.

$$m_{a,SSD} = m_{a,d} + m_{w,SSD} \quad \text{B-1}$$

$$m_{w,SSD} = m_{a,d}A_{SSD} \quad \text{B-2}$$

$$A_{SSD} = \frac{m_{a,SSD} - m_{a,d}}{m_{a,d}} \quad \text{B-3}$$

$$m_{a,SSD} = m_{a,d} + m_{a,d}A_{SSD} \quad \text{B-4}$$

$$m_{a,SSD} = m_{a,d}(1 + A_{SSD})$$

$$m_{a,d} = \frac{m_{a,SSD}}{(1 + A_{SSD})} \quad \text{B-5}$$

Where:

$m_{a,SSD}$  is the mass of SSD aggregate, this is what a mix design calls for,

$m_{a,d}$  is the mass of completely dry aggregate,

$m_{w,SSD}$  is the mass of water required to achieve SSD conditions for a given mass of dry aggregate and

$A_{SSD}$  is the amount of absorbed water, as a fraction of the aggregate required to achieve SSD conditions (a property of the aggregate)

Similarly the amount of water in the aggregate can be defined as follows

$$m_a = m_{a,d} + m_{w,a} \quad \text{B-6}$$

$$m_{w,a} = m_{a,d}A_w \quad \text{B-7}$$

$$A_w = \frac{m_a - m_{a,d}}{m_{a,d}} \quad \text{B-8}$$

$$m_a = m_{a,d} + m_{a,d}A_w \quad \text{B-9}$$

$$m_a = m_{a,d}(1 + A_w) \quad \text{B-10}$$

Where:

$m_a$  is the mass of the aggregate including any water present, what would be measured from a hopper etc.,

$m_{w,a}$  is the mass of the water found in a mass of aggregate,

$A_w$  is the absorbed water currently in the aggregate expressed as a fraction of the aggregate.

B-4 + B-7 - B-7, this

$$m_{a,SSD} = m_{a,d} + m_{a,d}A_{SSD} + m_{w,a} - m_{w,a}$$

represents the mass of the aggregate dry, the water in the aggregate, removing the water from the aggregate and adding enough water to reach SSD conditions

Substitute in B-7 for  $m_{w,a}$

$$m_{a,SSD} = m_{a,d} + m_{a,d}A_{SSD} + m_{a,d}A_w - m_{a,d}A_w$$

$$m_{a,SSD} = m_{a,d} + m_{a,d}A_w + m_{a,d}(A_{SSD} - A_w) \quad \text{B-11}$$

Substitute B-9 into B-11

$$m_{a,SSD} = m_a + m_{a,d}(A_{SSD} - A_w)$$

Substitute B-5 for  $m_{a,d}$

$$m_{a,SSD} = m_a + \frac{m_{a,SSD}}{(1 + A_{SSD})} (A_{SSD} - A_w)$$

$$m_a = m_{a,SSD} - m_{a,SSD} \left[ \frac{(A_{SSD} - A_w)}{(1 + A_{SSD})} \right]$$

$$m_a = m_{a,SSD} \left\{ 1 - \left[ \frac{(A_{SSD} - A_w)}{(1 + A_{SSD})} \right] \right\} \quad \mathbf{B-12}$$

Equation B-12 shows the relation between the amount of aggregate required, compensating for the difference between the actual amounts of water in the aggregate and the amount of water needed for SSD conditions. This process must be completed for each aggregate used as all can and likely will vary. The mix design used during testing contained two aggregates, 12.7 mm (0.5 in) crushed stone and sand. The amount of water in the coarse aggregate was found using the following procedure:

1. Weigh a sample of the aggregate (this is the mass of the dry aggregate and the absorbed water in the aggregate,  $m_a$ )
2. Heat the stone in an oven at 100°C for 2 hours
3. Weight the sample
4. Repeat steps 2 and 3 until no change in mass is noted (this is the mass of the dry aggregate,  $m_{a,d}$ )
5. Soak the aggregate in water for 24 hours
6. Remove the aggregate from the water onto a cloth and pat dry (do not allow the aggregate to dry beyond SSD)
7. Weight the sample (this is the mass of the dry aggregate plus the mass of the absorbed water to make the aggregate SSD,  $m_{a,SSD}$ )

Using equations B-3 and B-8,  $A_{SSD}$  and  $A_w$  can be determined and plugged into equation B-12 to determine the amount of aggregates required. Using this procedure it was found that the coarse aggregates used for casting had 1.81% and 2.05% for the amount of absorbed water and absorbed water to reach SSD conditions respectively. The procedure for determining  $A_{SSD}$  and  $A_w$  is different from that of the course aggregate and was found to be unreliable during the first cast (micro-cell beams). As a result, the sand was dried for the remaining casts and a value of 1.61% was used for  $A_{SSD}$ , which was determined experimentally by Liam Butler, a Ph.D. Candidate [86].

Finally, the amount of water added during mixing must be corrected to reflect the extra water the aggregate brings with it or the water that the aggregate will be absorbing. This is shown below in the following equations.

$$m_{w,r} = m_w + m_{w,SSD} - m_{w,a} \quad \text{B-13}$$

Where:

$m_{w,r}$  is the mass of the water required for casting and

$m_w$  is the mass of the water specified by the mix design (assuming aggregates are SSD).

Substitute B-2 and B-7

$$m_{w,r} = m_w + m_{a,d}A_{SSD} - m_{a,d}A_w$$

$$m_{w,r} = m_w + m_{a,d}(A_{SSD} - A_w)$$

Substitute B-5

$$m_{w,r} = m_w + \frac{m_{a,SSD}}{(1 + A_{SSD})}(A_{SSD} - A_w)$$

$$m_{w,r} = m_w + m_{a,SSD} \left[ \frac{(A_{SSD} - A_w)}{(1 + A_{SSD})} \right] \quad \text{B-14}$$

$$m_{w,r} = m_w + \sum_{i=1}^n m_{a,SSD_i} \left[ \frac{(A_{SSD_i} - A_{w_i})}{(1 + A_{SSD_i})} \right] \quad \text{B-15}$$

Using equation B-14 or using a similar method for multiple aggregates equation B-15 can be utilized to adjust the amount of water added to the mix to obtain the appropriate proportions of water to maintain the correct w/cm ratio.

## B-2 Casts

To determine the amount of concrete required and to determine the size and shape of the specimens the ponding well and length of the bars were chosen to mimic the ASTM G109 standard as this would reduce prep time for the bars, as well as make the comparison of macro-cell to micro-cell corrosion easier. Finally, alterations to the thickness of the G109's were made, increasing the thickness from 115mm to 155mm. This was due to a consolidation issue with the cast-in ponding well. The values used are shown below in Table B-2. Note that the G109 cast of 20 specimens was broken up into two casts due to the limitations of the mixer size- this resulted in one fewer compression testing cylinders for one of the casts.

**Table B-2: Specimen size calculations**

Symbol	Name	Calculation	Value	Unit	Alt. Value	Alt. Unit	Comment(s)
∅.r	diameter of rebar	ASTM G109	0.010	m	0.394	in	
L.r	length of rebar	ASTM G109	0.360	m	14	in	
∅.e	diameter of reference electrode	measured	0.015	m	1	in	
∅.ca	diameter of coarse aggregate	ASTM G109	0.014	m	9/16	in	
r.c	radius of compression testing cylinder	ASTM C39	0.051	m	2	in	
L.c	length of compression testing cylinder	ASTM C39	0.203	m	8	in	
V.c	volume of compression testing cylinder	=L.c*π*r.c <sup>2</sup>	0.002	m <sup>3</sup>	0.058	ft <sup>3</sup>	
N.c	number of compression testing cylinders per cast		4				
L.G	length of G109	ASTM G109	0.280	m	11	in	
W.G	width of G109	ASTM G109	0.155	m	6	in	increase from 115mm to 155mm for consolidation reasons
H.G	height of G109	ASTM G109	0.225	m	8.9	in	
L.Gp	length of G109 ponding well	ASTM G109	0.150	m	5.9	in	
W.Gp	width of G109 ponding well	ASTM G109	0.075	m	3	in	
H.Gp	height of G109 ponding well	ASTM G109	0.075	m	3	in	
V.G	volume of G109	=L.G*W.G*H.G-(L.Gp*W.Gp*H.Gp)	0.009	m <sup>3</sup>	0.315	ft <sup>3</sup>	neglects rebar volume
N.G1	number of G109 cast 1 & 2		20				4 salts, 4 samples, indoor use, +1ref/mistake
N.G2	number of G109 cast 3		15				4 salts, 3 samples, outdoor use, +1ref/mistake

Table B-2: Specimen size calculations continued

Symbol	Name	Calculation	Value	Unit	Alt. Value	Alt. Unit	Comment(s)
t.cv	vertical cover thickness of rebar		0.040	m	1.6	in	
t.ch	horizontal cover thickness of rebar		0.070	m	2.8	in	
S.r	spacing between rebar	CSA S6-06 Section 8.14.2.1.1 $=\text{Max}(1.5*\phi.r, 1.5*\text{Agg.c}, 0.040)$	0.040	m	1.6	in	
n.r	number of rebar per slab		6		6		
n.e	number of electrodes per slab		1		1		
L.s	length of slab	$=2*t.ch+N.r*\phi.r+N.e*\phi.e+(N.r+N.e-1)*S.r$	0.455	m	17.9	in	
W.s	width of slab	used ASTM G109	0.280	m	11	in	
H.s	height of slab	$=H.sp+2*t.cv+\phi.r$	0.165	m	6.5	in	
L.sp	length of slab ponding well	$=L.s-(W.s-W.sp)$	0.325	m	12.8	in	this was done to achieve uniform wall thickness
W.sp	width of slab ponding well	used ASTM G109	0.150	m	5.9	in	
H.sp	height of slab ponding well	used ASTM G109	0.075	m	3	in	
V.s	volume of slab	$=L.s*W.s*H.s-(L.sp*W.sp*H.sp)$	0.017	m <sup>3</sup>	0.613	ft <sup>3</sup>	neglects rebar volume
N.s	number of slabs		5				4 salts +1 ref/mistake
V.at	volume of air test		0.017	m <sup>3</sup>	0.600	ft <sup>3</sup>	
S.F.	safety factor for casting		1.10				10% additional material
V.st	volume of slabs total inc. air test & comp. test	$=(V.s*N.s+V.at+N.c*V.c)*S.F.$	0.121	m <sup>3</sup>	4.289	ft <sup>3</sup>	

Table B-2: Specimen size calculations continued

Symbol	Name	Calculation	Value	Unit	Alt. Value	Alt. Unit	Comment(s)
V.Gt1	volume of G109 total 1 inc. air test & comp. test	$= (V.G * N.G1 + V.at + N.c * V.c) * S.F.$	0.222	m <sup>3</sup>	7.847	ft <sup>3</sup>	
V.Gt2	volume of G109 total 2 inc. air test & comp. test	$= (V.G * N.G2 + V.at + N.c * V.c) * S.F.$	0.173	m <sup>3</sup>	6.114	ft <sup>3</sup>	

The following tables (Table B-3 through Table B-6) outline the constituents for the various batches. The primary difference between the batches is the first cast (the micro-cell beam cast) used aggregates directly from the hopper. The aggregates in the hopper contain variable amounts of moisture; this was particularly true with regards to the sand. This made it exceptionally difficult to properly adjust the constituents to ensure the w/cm ratio was maintained. As a result, the remaining casts had the sand spread out across the floor with a fan blowing across the surface to achieve “bone” dry conditions, making it significantly easier to compensate for the required amounts of aggregates and water.

Table B-3: Cast 1 constituents for micro-cell beams

Constituent	Value	Unit	Alt. Value	Alt. Unit
mass of coarse aggregate	126.9	kg	279.8	lbm
mass of coarse aggregate compensated	126.6	kg	279.1	lbm
mass of fine aggregate	85.6	kg	188.8	lbm
mass of fine aggregate compensated	84.3	kg	185.8	lbm
mass of TYP10 GU cement	36.1	kg	79.5	lbm
mass of slag	11.9	kg	26.2	lbm
volume of Euclid Air Extra	28.8	ml	0.973	oz
volume of Euclid Water Reducer	97.2	ml	3.285	oz
volume of superplasticizer used	100	ml	3.381	oz
volume of water	18.824	kg	41.500	lbm
volume of compensated water	20.495	kg	45.184	lbm

\*Note the aggregates were not properly dried; as a result 18.8l of water was used.

**Table B-4: Cast 2 constituents for 15 G109s**

<b>Constituent</b>	<b>Value</b>	<b>Unit</b>	<b>Alt. Value</b>	<b>Alt. Unit</b>
mass of coarse aggregate	180.9	kg	398.9	lbm
mass of coarse aggregate compensated	180.5	kg	397.9	lbm
mass of fine aggregate	122.1	kg	269.1	lbm
mass of fine aggregate compensated	120.1	kg	264.8	lbm
mass of TYP10 GU cement	51.4	kg	113.4	lbm
mass of slag	17.0	kg	37.4	lbm
volume of Euclid Air Extra	41.0	ml	1.387	oz
volume of Euclid Water Reducer	138.5	ml	4.683	oz
volume of superplasticizer used	400	ml	13.523	oz
volume of water	26.837	kg	59.165	lbm
volume of compensated water	29.219	kg	64.416	lbm

**Table B-5: Cast 3 constituents for 10 G109s**

<b>Constituent</b>	<b>Value</b>	<b>Unit</b>	<b>Alt. Value</b>	<b>Alt. Unit</b>
mass of coarse aggregate	116.1	kg	256.0	lbm
mass of coarse aggregate compensated	115.8	kg	255.3	lbm
mass of fine aggregate	78.3	kg	172.7	lbm
mass of fine aggregate compensated	77.1	kg	169.9	lbm
mass of TYP10 GU cement	33.0	kg	72.7	lbm
mass of slag	10.9	kg	24.0	lbm
volume of Euclid Air Extra	26.3	ml	0.890	oz
volume of Euclid Water Reducer	88.9	ml	3.005	oz
volume of superplasticizer used	170	ml	5.747	oz
volume of water	17.2	kg	37.966	lbm
volume of compensated water	18.7	kg	41.336	lbm

**Table B-6: Cast 3 constituents for 10 G109s**

<b>Constituent</b>	<b>Value</b>	<b>Unit</b>	<b>Alt. Value</b>	<b>Alt. Unit</b>
mass of coarse aggregate	116.1	kg	256.0	lbm
mass of coarse aggregate compensated	115.8	kg	255.3	lbm
mass of fine aggregate	78.3	kg	172.7	lbm
mass of fine aggregate compensated	77.1	kg	169.9	lbm
mass of TYP10 GU cement	33.0	kg	72.7	lbm
mass of slag	10.9	kg	24.0	lbm
volume of Euclid Air Extra	26.3	ml	0.890	oz
volume of Euclid Water Reducer	88.9	ml	3.005	oz
volume of superplasticizer used	150	ml	5.071	oz
volume of water	17.2	kg	37.966	lbm
volume of compensated water	18.7	kg	41.336	lbm

The procedure for mixing the concrete was as follows

1. The mixer is cleaned and “pat” dry to remove possible contaminants and to minimize the amount of water absorbed by the metal mixer
2. The fine aggregate, coarse aggregate, slag, and cement are mixed together in the mixer
3. The air entraining agent and water reducer are added to the mixing water and thoroughly stirred
4. The majority of the water and admixture solution is slowly added to the concrete
5. The remaining water is added mixed with small amounts of super plasticizer and added to the mix until proper casting consistency is achieved. Once achieved the remaining water is added and allowed to mix in with the concrete.
6. The concrete is then placed into the moulds in thirds.
7. Between each third, the moulds are vibrated on a vibration table until no more air bubbles are observed at the surface.
8. Curing
  - a. The freshly poured concrete molds are placed under wet burlap and covered with vapor barrier
  - b. Between 48 and 72 hours the concrete is removed from the molds and allowed to cure in a humidity chamber (100% relative humidity) for 28 days from the time of casting.

### B-3 Concrete Properties

The following tables describe air, slump and strength of the various batches of concrete. The test method for slump followed ASTM C 143/C 143M – 03 Standard Test Method for Slump of Hydraulic-Cement Concrete [87]. The air content according to CSA A23.1/A23.2 is between 5-8% [84], and recommended with the given slump that the concrete be rodded. This was not followed as the small crevices and complexity of the formwork geometry, plus the limit of available labour made it more practical to use the vibrating table for the specimens.

**Table B-7: Air content and slump**

Cast	Air	Slump	
		mm	in
1	8.2%	80	3 ¼
2	3.5%*	70	2 ¾
3	5.5%	170	6 ¾
4	5.0%	170	6 ¾

\* Below specified air content

**Table B-8: Twenty eight day concrete strength**

Batch	Sample	Diameter		Cross-sectional area		Maximum Load		Strength		Type of Fracture
		mm	in	mm <sup>2</sup>	in <sup>2</sup>	kN	lbf	MPa	psi	
1 Beams	1	102	4	8107	13	342	76928	42.2	6120	Shear (d)
	2	102	4	8107	13	361	81111	44.5	6450	Shear (d)
	3	102	4	8107	13	351	78824	43.2	6270	Shear (d)
2 15 G109s	1	102	4	8107	13	433	97302	53.4	7740	Cone (a)
	2	102	4	8107	13	486	109350	60.0	8700	Shear (d)
	3	102	4	8107	13	487	109497	60.1	8710	Columnar (e)
3 10 G109s	1	102	4	8107	13	426	95769	52.5	7620	Cone (a)
	2	102	4	8107	13	446	100176	55.0	7970	Cone (a)
4 10 G109s	1	102	4	8107	13	412	92670	50.8	7370	Cone (a)
	2	102	4	8107	13	415	93235	51.2	7420	Cone (a)
	3	102	4	8107	13	423	95009	52.1	7560	Columnar (e)

## **Appendix C: Experimental Methods**

This section briefly describe how some of the techniques used in this dissertation for material identification function. Specifically this section reviews: inductively coupled plasma optical emission spectroscopy (ICP-OES), ion beam chromatography (IC) and X-ray fluorescence (XRF).

### **C-1 Inductively Coupled Plasma Optical Emission Spectroscopy and Ion Beam Chromatography: Tests Used to Determine Anti-Icing Solution Composition**

ICP-OES uses a working coil with high powered radio frequencies to create plasma (typically Argon gas is used for this) which in turn bombards the specimen. The specimen is introduced into the plasma as a spray. The high energy plasma's ions and electrons react with the specimen; the specimen is in turn broken down into charged ions. This reaction emits radiation at specific wavelengths which can be compared to known concentrations of specific elements and interpolated to determine the composition of the unknown specimen [88], [89].

IC utilizes coulomb's law. The specimen is carried through a loop with a buffer material that has the same charge and pH. At this point the analyte ions "bump" out or exchange with the stationary phase of the same charge. Next the buffer solution previously carrying the specimen is changed. This is typically done by the addition of  $\text{Na}^+$  or  $\text{Cl}^-$  ions, depending on whether a cation analysis or anion analysis is being completed respectively. The addition of these molecules will debond the analyte molecules. Molecules are debonded depending upon their number of charged groups on their surface. The debonded analytes must then be detected using a various compositional analysis techniques [90].

### **C-2 X-Ray Fluorescence**

XRF was used to determine the composition of the various steels and their coatings. The equipment used was Thermo Fisher Scientific Inc.'s Niton™ which tested three different areas of each specimen and averaged. It is important to note that the results of XRF will penetrate the surface. The depth of detection is based on the depth to which the bombarding X-rays penetrate the material and the detectability of the returning X-rays, this results in a detection depth of anywhere between a few micrometers and a few millimeters [91] this can depend on the material type as heavier metals are

more easily measured at greater depths, whereas lighter elements such as liquids or plastics the X-rays can easily pass through, and thickness of up to 10cm are possible[92].

X-ray fluorescence uses the principals of quantum to determine the elemental composition of a sample. The samples are exposed to a variety of wavelengths of X-rays which bombard the surface of the specimen. Some of the X-rays will come into contact with electrons contained in the inner shell of an atom. The excited electron will be displaced and a void will be left in its place leaving the atom unstable. One of the electrons from an outer shell (which is at a higher energy level) will then drop down to fill the newly created void. This process results in a reduction of energy and as a result the electron moving from the outer shell to the inner shell will emit an X-ray this is shown schematically in Figure C-1. X-rays emitted in this fashion are unique to the elements that they came from. This allows a detector and analyzer to determine what this element is and upon multiple iterations, can determine the composition of the specimen.

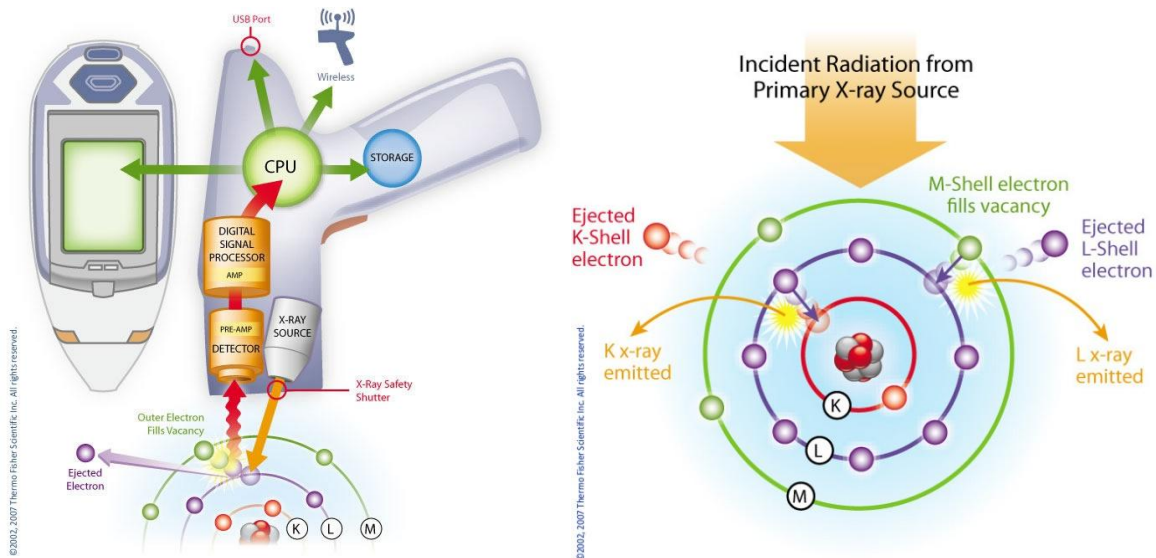


**Figure C-1: Schematic diagram showing the internal components of a hand-held XRF[93] (left) and the principles of XRF [94] (right)**

## Appendix D: Experimental Results

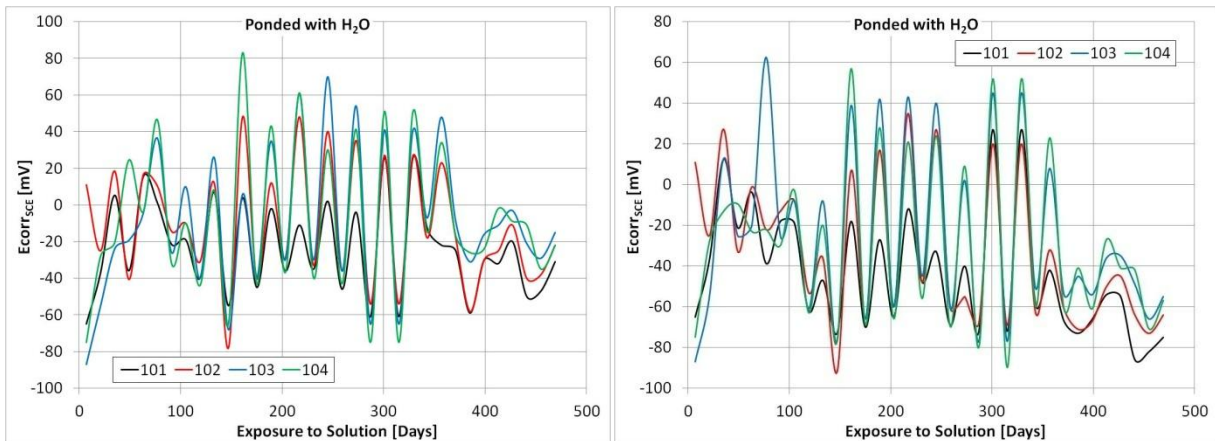
The following section contains all of the individual measurements of each specimen. The scale of the ordinate axis in all cases reflects the scale of the measurements and therefore varies for plots even of the same type of measurement.

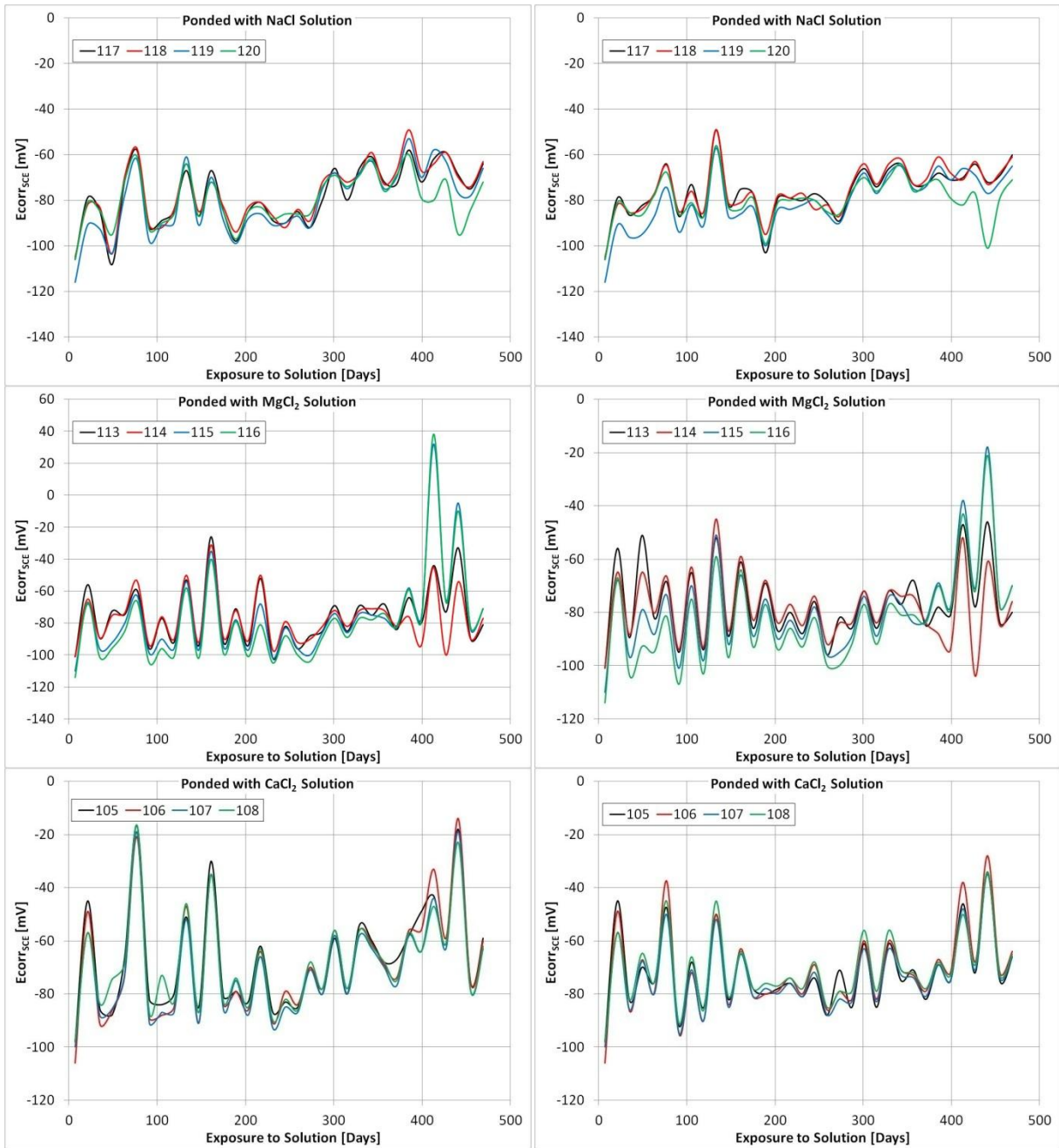
### D-1 Macro-cell Results: ASTM G109

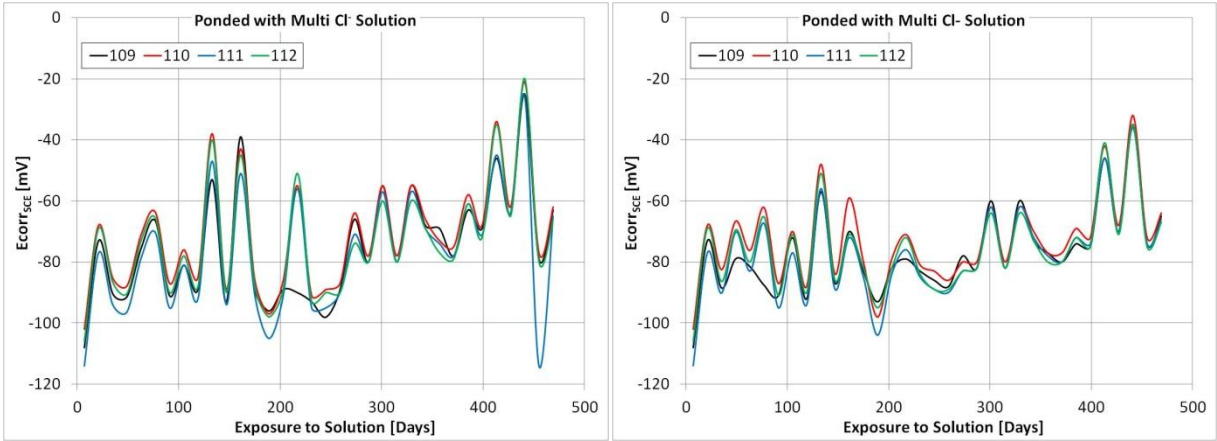
All measurements of the same type and with the same environmental exposures show similar trends with respect to time with little variability. All the measurements suggest that the black steel is still passive.

#### D-1.1 Corrosion Potential Measurements

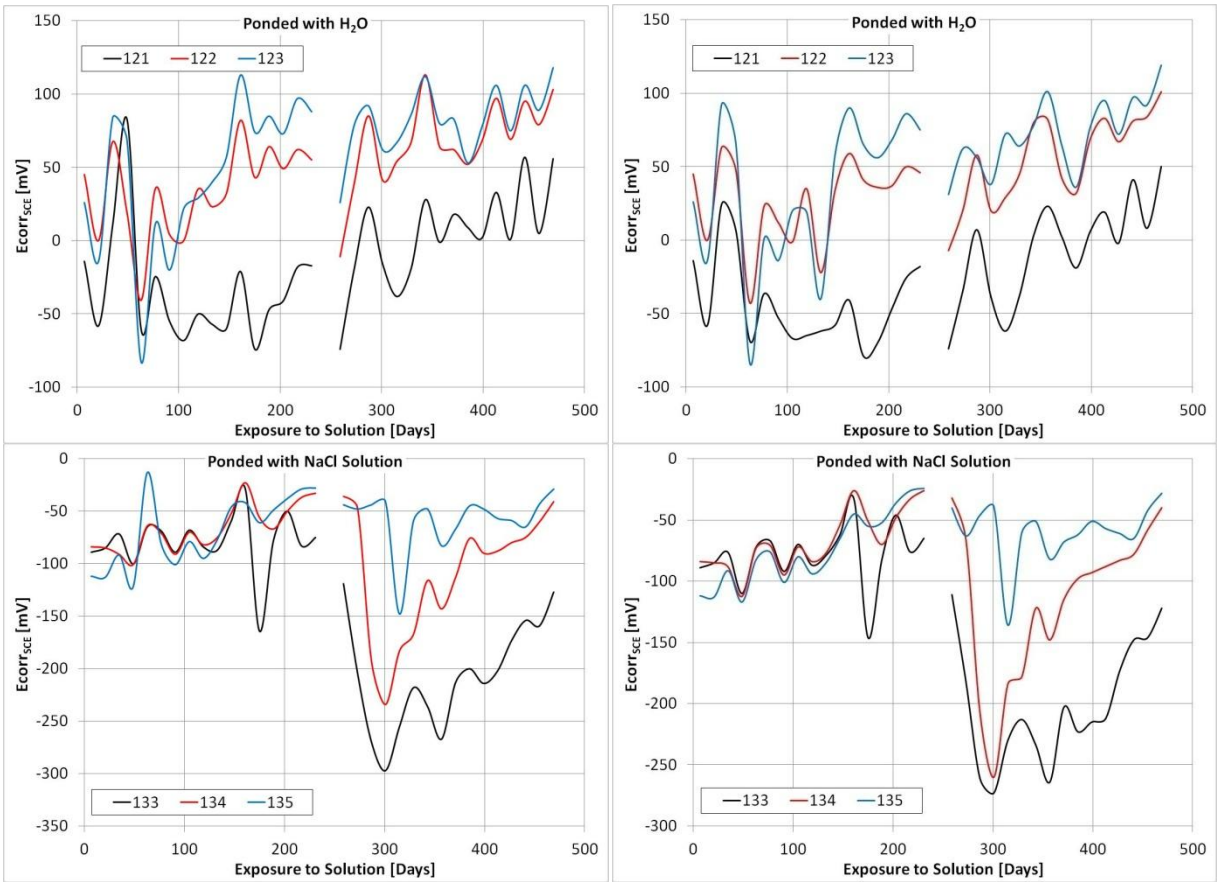
The following is a series of plots displaying corrosion potential measurements made with respect to time, using a SCE and a multi-meter. Measurements were taken bi-weekly (i.e. every two weeks). Figure D-1 and Figure D-2 show the corrosion potential measurements of all the indoor and outdoor specimens respectively.







**Figure D-1: Individual corrosion potential measurements of indoor specimens exposed to various ant-icing solution mixed potentials (left) and anodic potentials (right)**



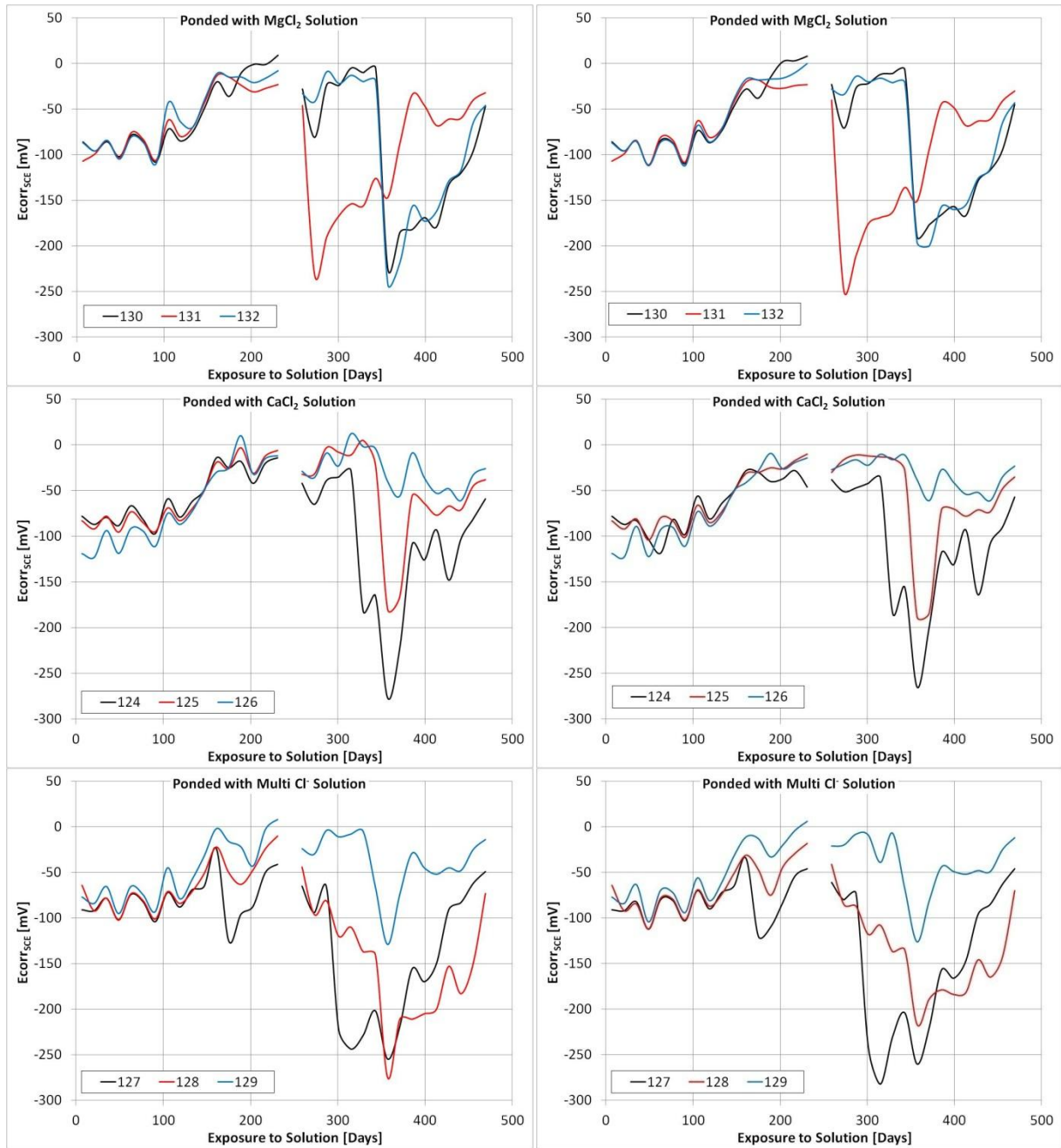


**Figure D-2: Individual corrosion potential measurements of outdoor specimens exposed to various ant-icing solution mixed potentials (left) and anodic potentials (right)**

### ***D-1.2 Galvanic Corrosion Current Density***

The following is a series of plots displaying macro-cell corrosion current density measurements made with respect to time. Potential measurements were made across each 100  $\Omega$  resistor which could then be converted to macro-cell corrosion current density rates. Measurements were taken using a

Keithley™ Model 2700 DMM, Data Acquisition, Data logging System in conjunction with ExceLINX™, a Microsoft™ Excel add-on. Measurements were taken weekly. Figure D-3 and Figure D-4 show the corrosion current density measurements of all the indoor and outdoor specimens respectively.

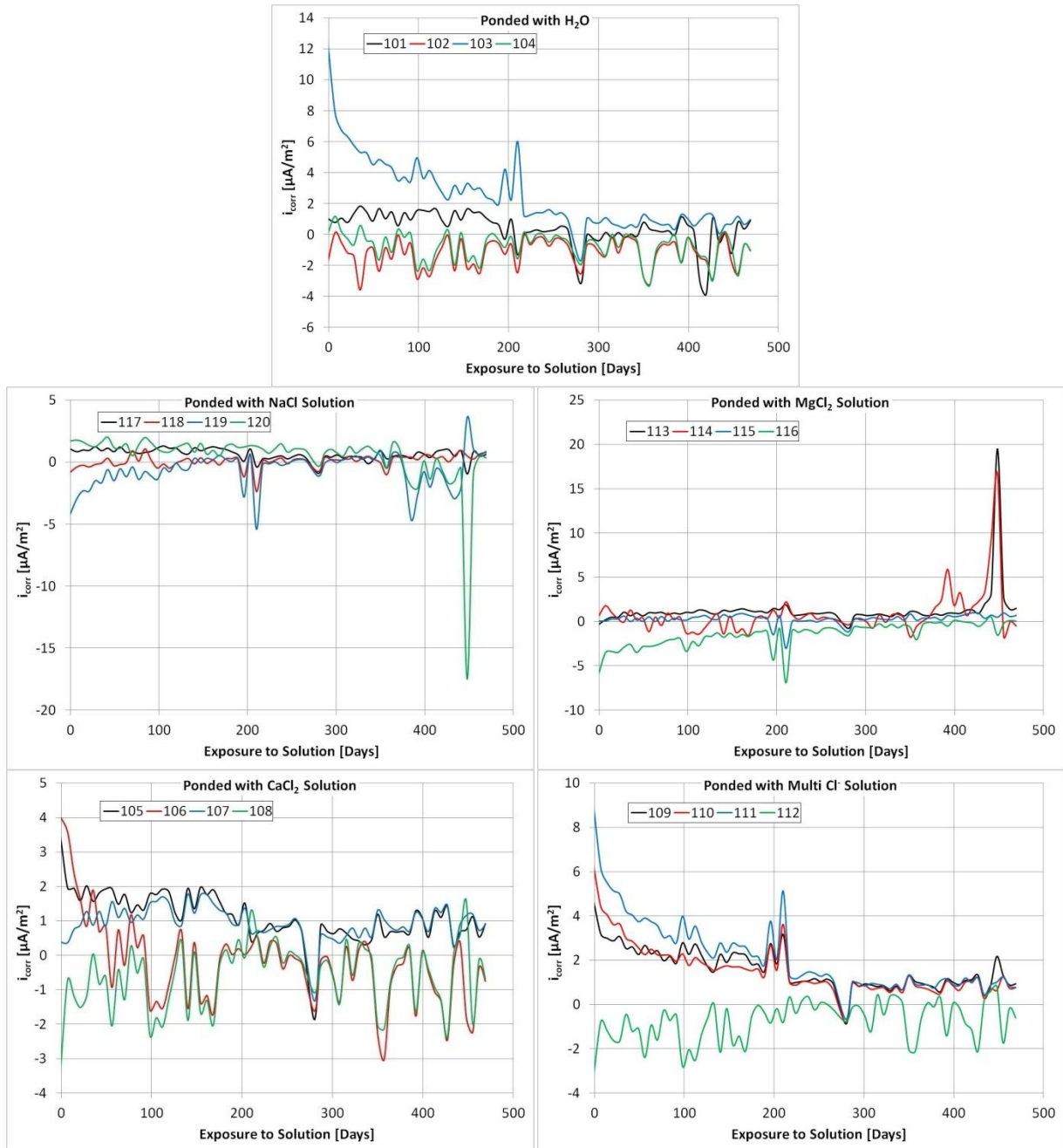


**Figure D-3: Individual corrosion current density measurements of indoor specimens exposed to various ant-icing solution**

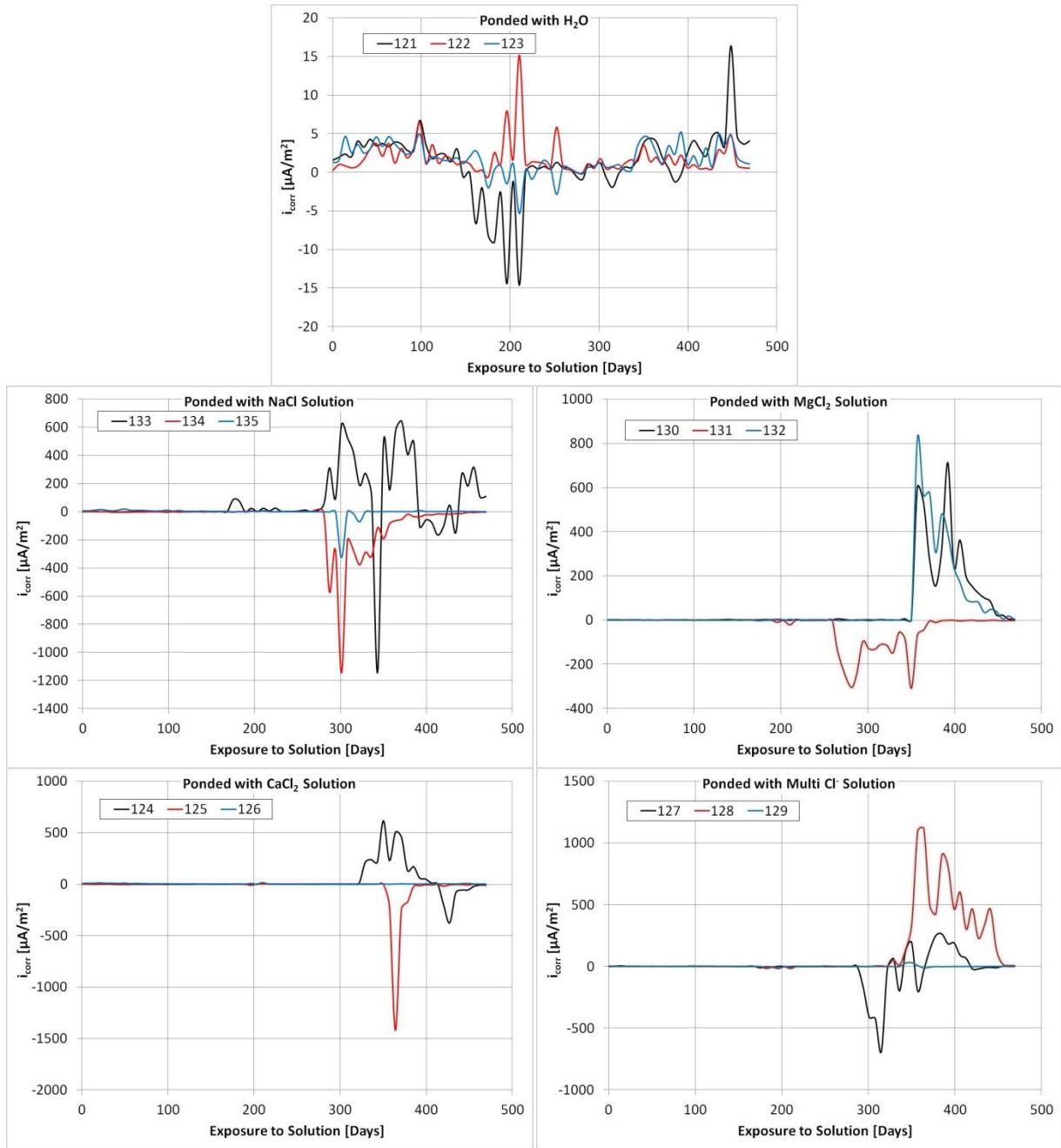
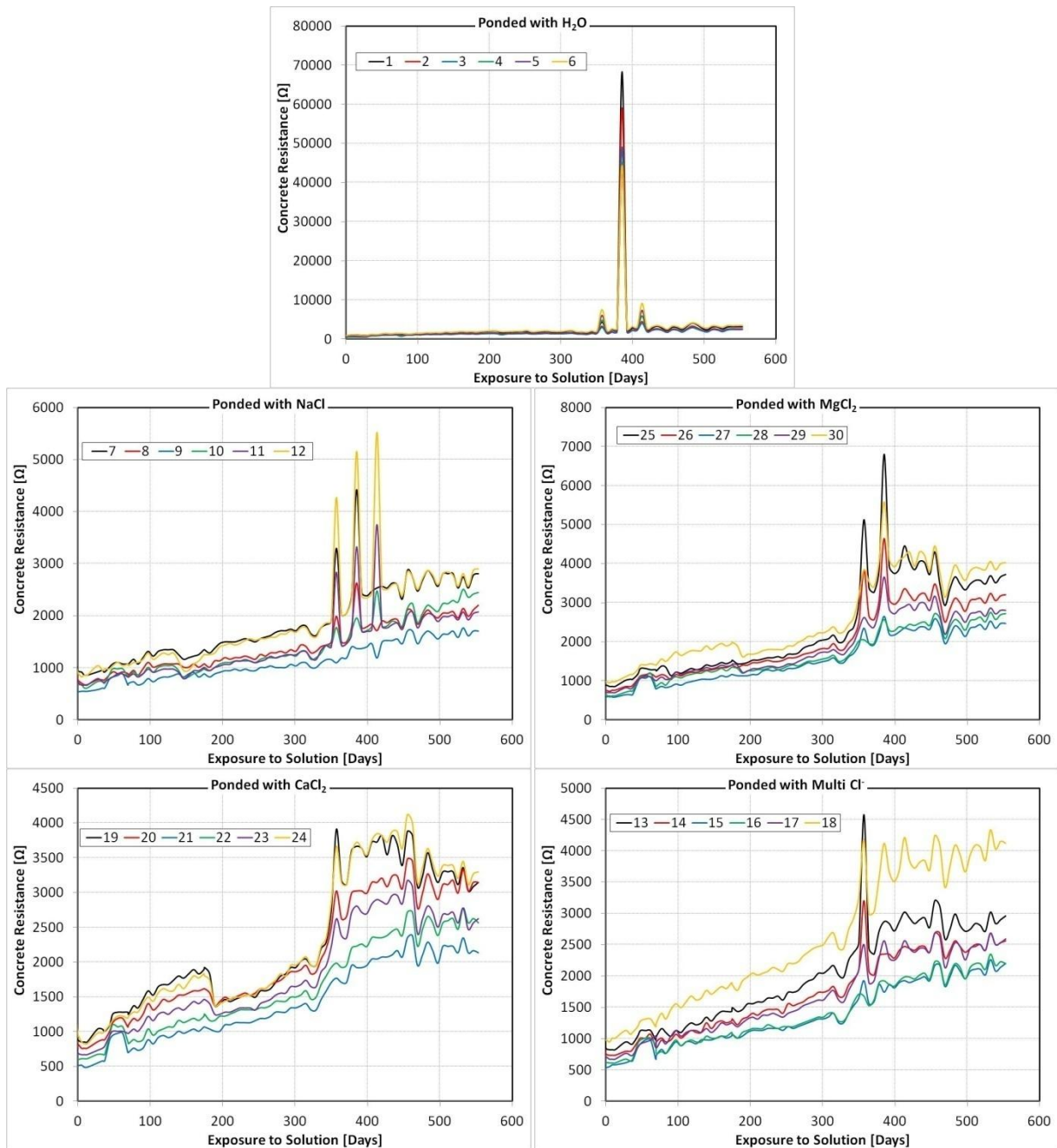


**Figure D-4: Individual corrosion current density measurements of outdoor specimens exposed to various ant-icing solution**

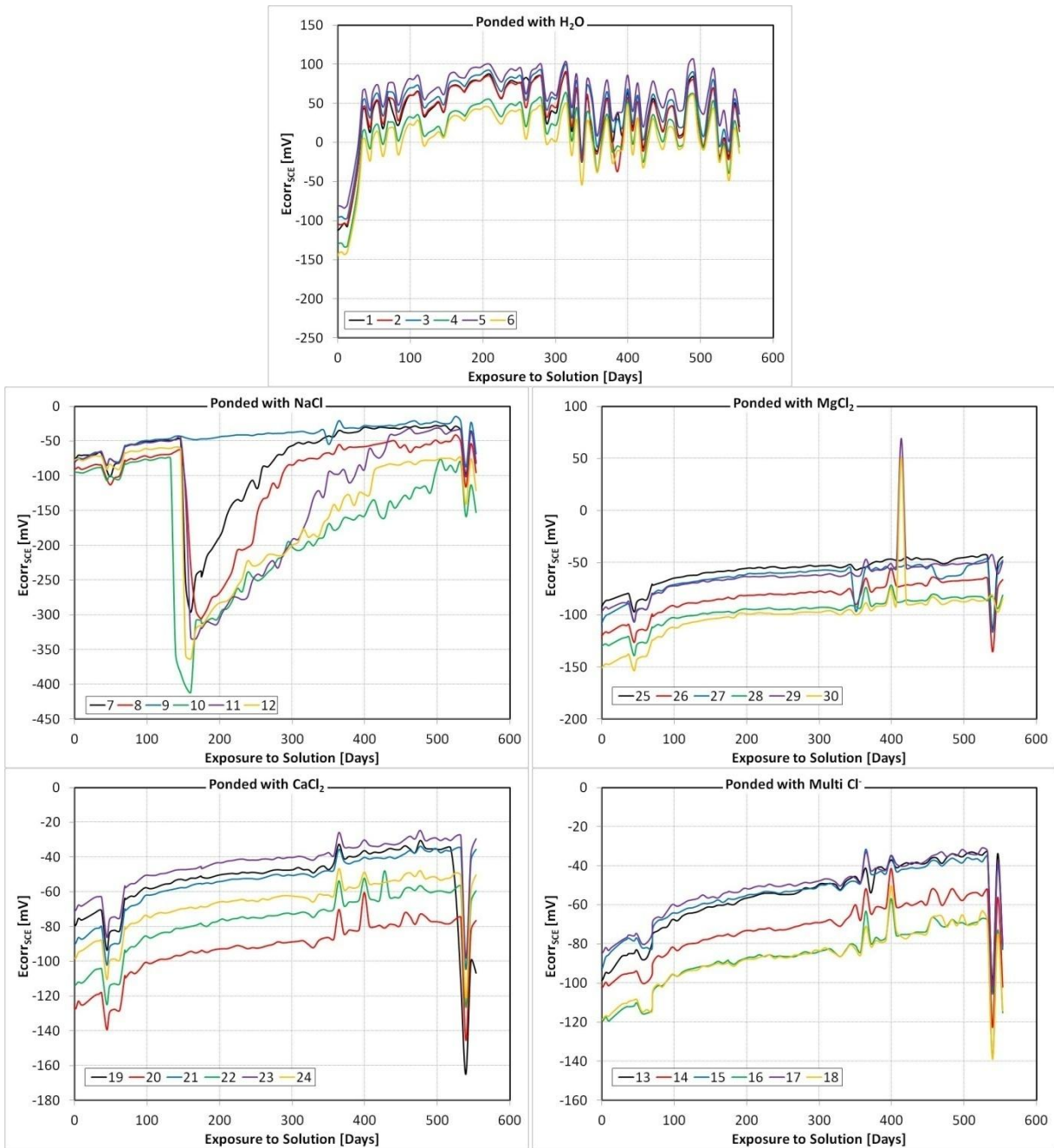
## D-2 Micro-cell Results: Beams with Ponding Well

Figure D-5, Figure D-6 and Figure D-7 show the individual measurements of the concrete resistance, corrosion potential and corrosion current density respectively of the beams with a cast-in ponding

well. Each plot shows the individual data for six black steel bars in each beam. The ordinate axis for each plot will vary even between measurements of the same type.



**Figure D-5: Concrete resistance measurements of concrete between individual bars and Ti mesh counter electrode in the ponding well of concrete exposed to various anti-icing solutions against time**



**Figure D-6: Corrosion potential measurements of individual bars in concrete exposed to various anti-icing solutions against time**

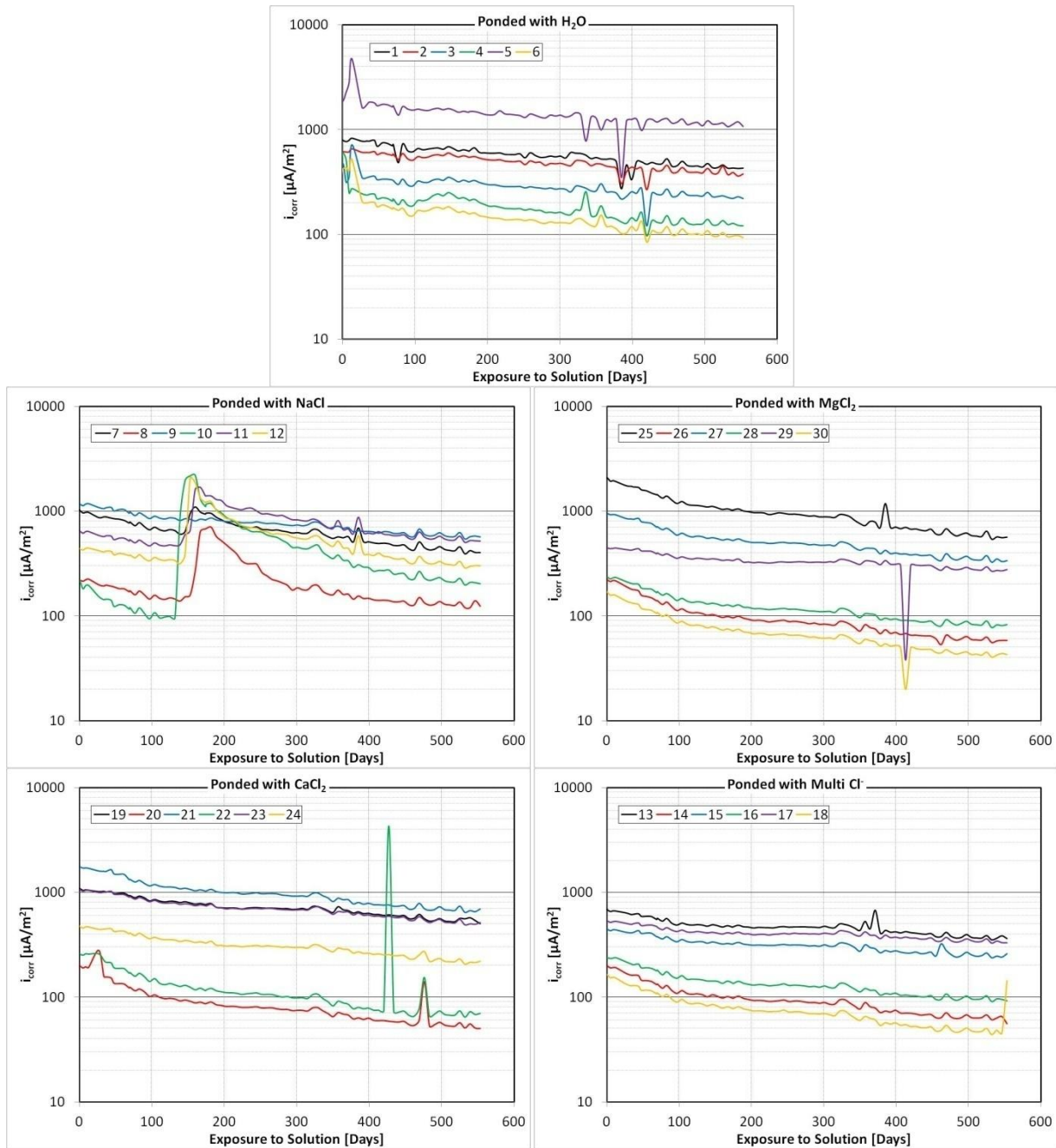
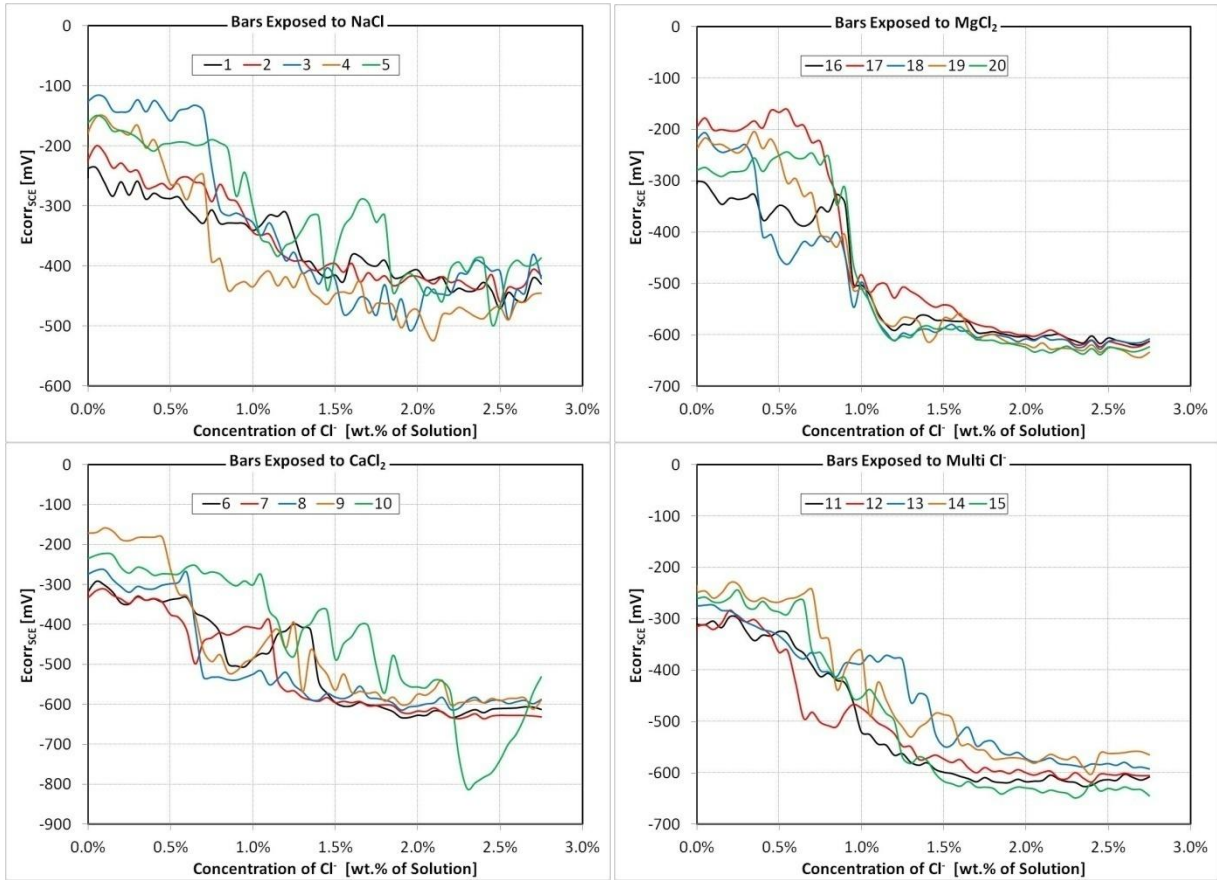


Figure D-7: Corrosion current density measurements of individual bars in concrete exposed to various anti-icing solutions against time, note that the ordinate axis is logarithmic

### D-3 Micro-cell Results: Synthetic Pore Solution

The following in Figure D-8 shows the individual  $E_{corr}$  measurements of each bar. There is a significant amount of scatter due to the sensitivity of  $E_{corr}$  measurements to the environment such as temperature, electrical noise etc. Regardless of the scatter the general trends can be observed

between all the black steel exposed to the same anti-icing solutions; this is particularly true for the bars exposed to the  $MgCl_2$  solution when they transfer from passive to active corrosion.



**Figure D-8: Corrosion potential measurements of individual bars in pore solution exposed to varying concentrations of anti-icing solution. Note that the ordinate axis scale varies for each solution.**

The following in Figure D-9 shows the individual  $i_{corr}$  measurements of each bar. Similar to the  $E_{corr}$  measurements there is a significant amount of scatter and the bars exposed to the  $MgCl_2$  solution show the highest level of consistency when transferring from passive to active corrosion.

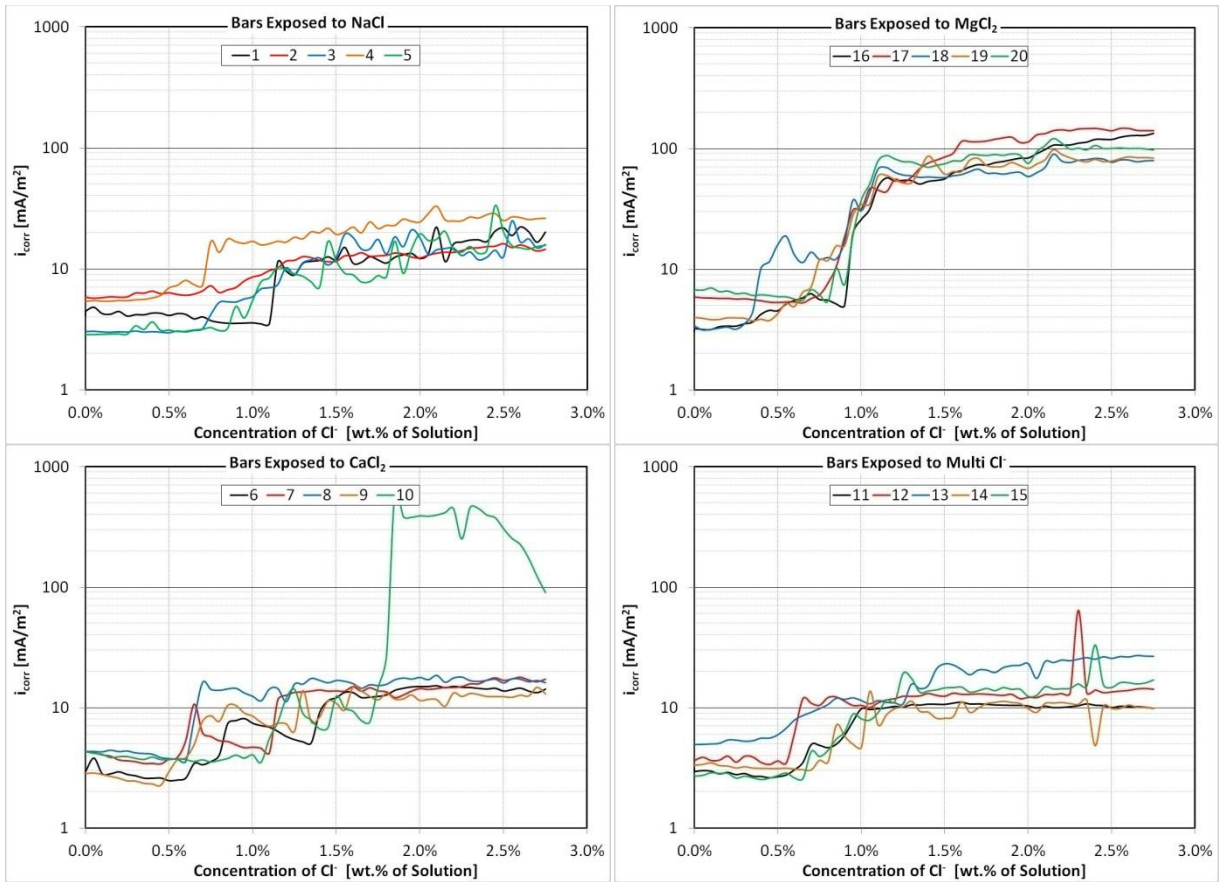
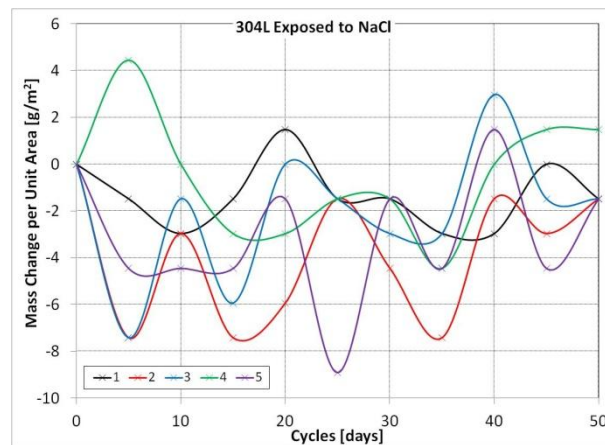
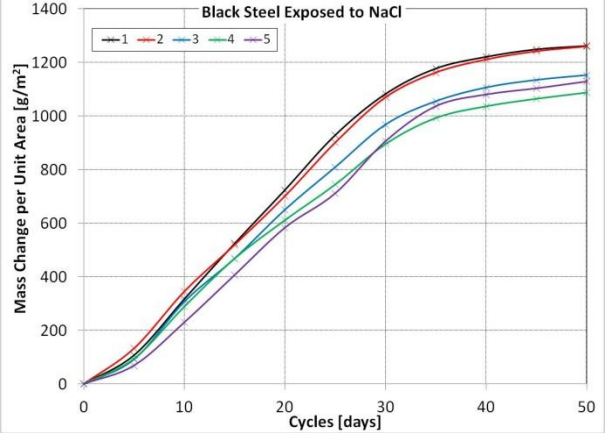
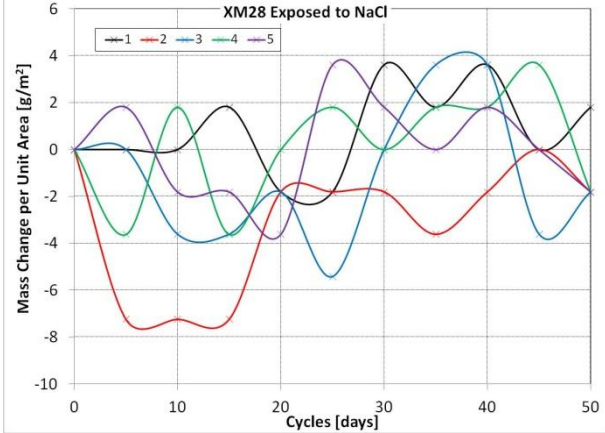
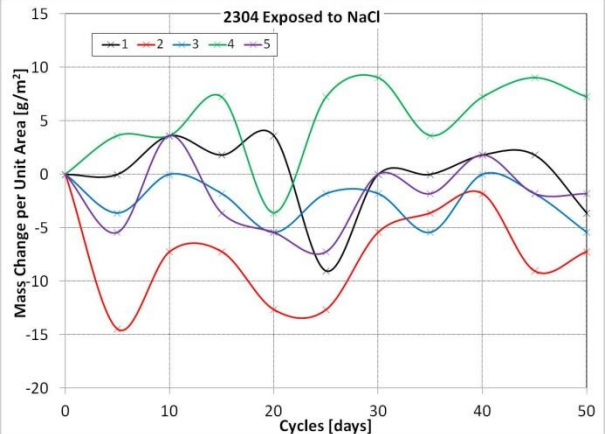
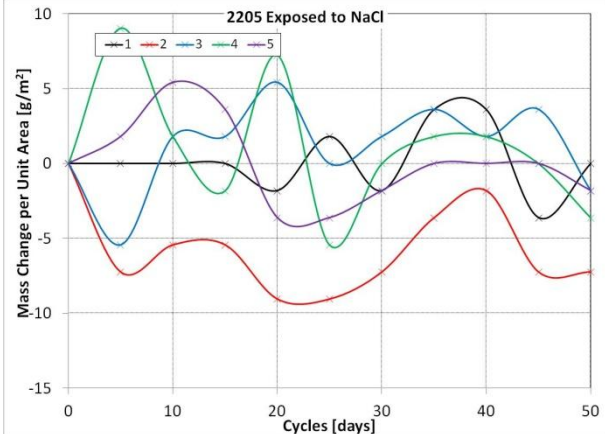
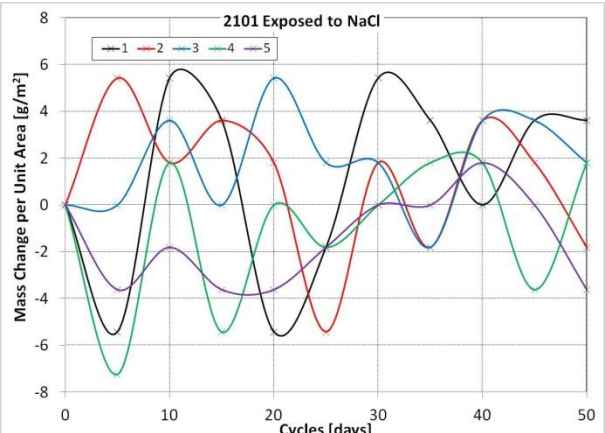
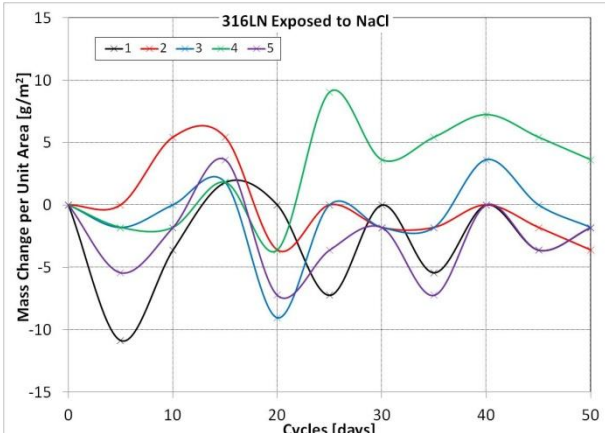


Figure D-9: Corrosion current density measurements of individual bars in pore solution exposed to varying concentrations of anti-icing solution. Note that the ordinate axis scale is logarithmic.

#### D-4 Cyclic Corrosion Chamber Testing: SAE J2334-Immersion Testing

The following plots Figure D-10, Figure D-11 and Figure D-12 show the mass change per unit area of the individual steel specimens exposed to NaCl,  $\text{MgCl}_2$ ,  $\text{CaCl}_2$ , respectively.





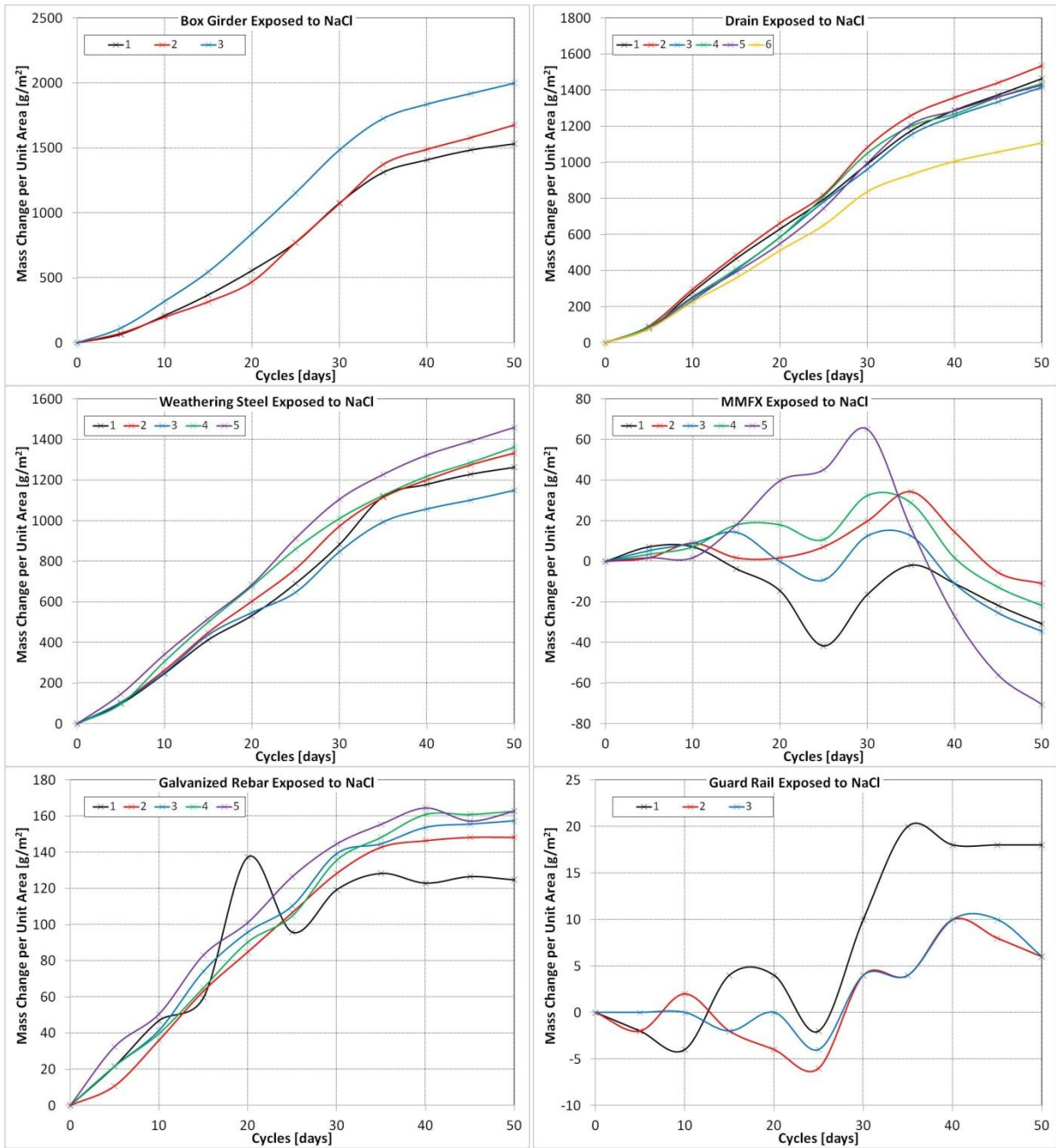
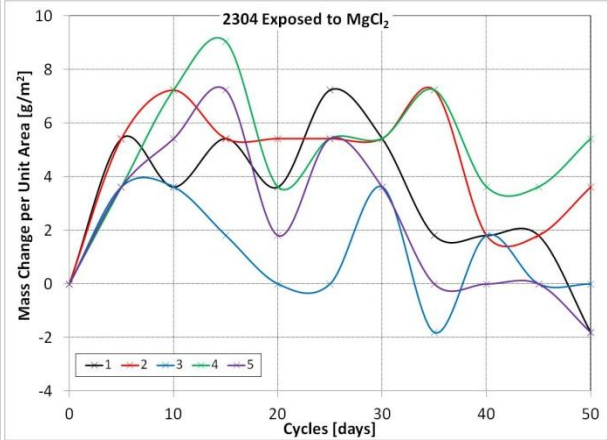
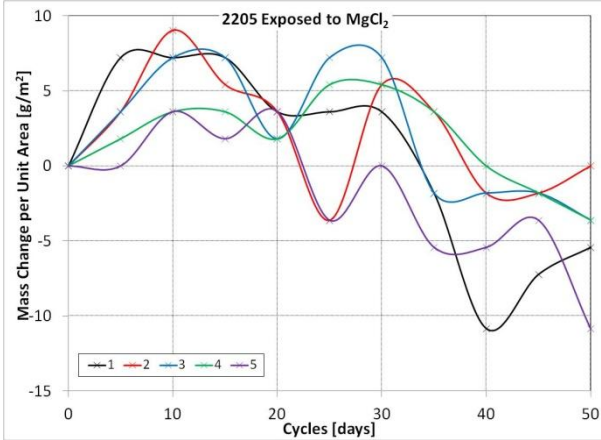
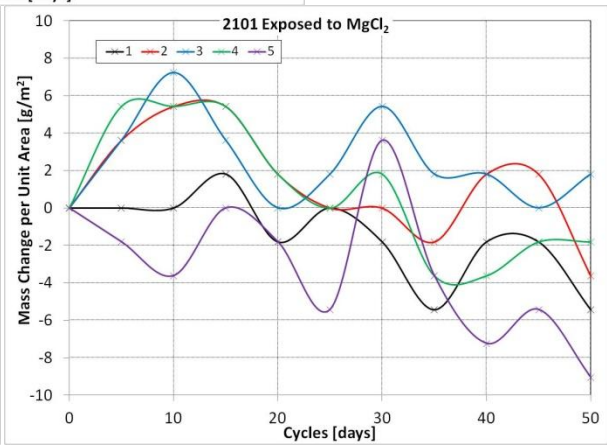
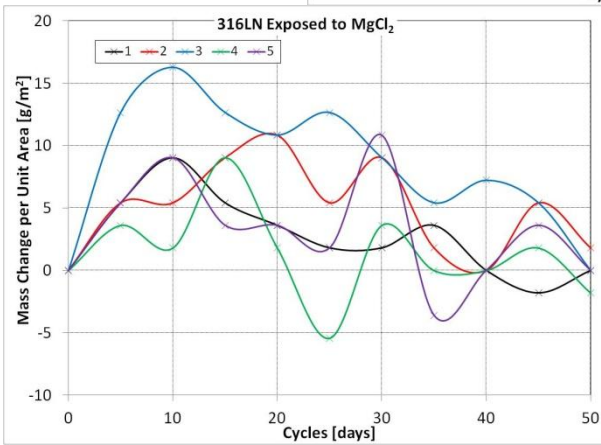
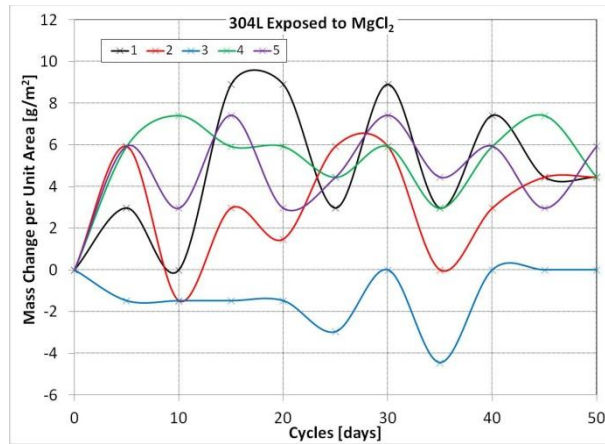
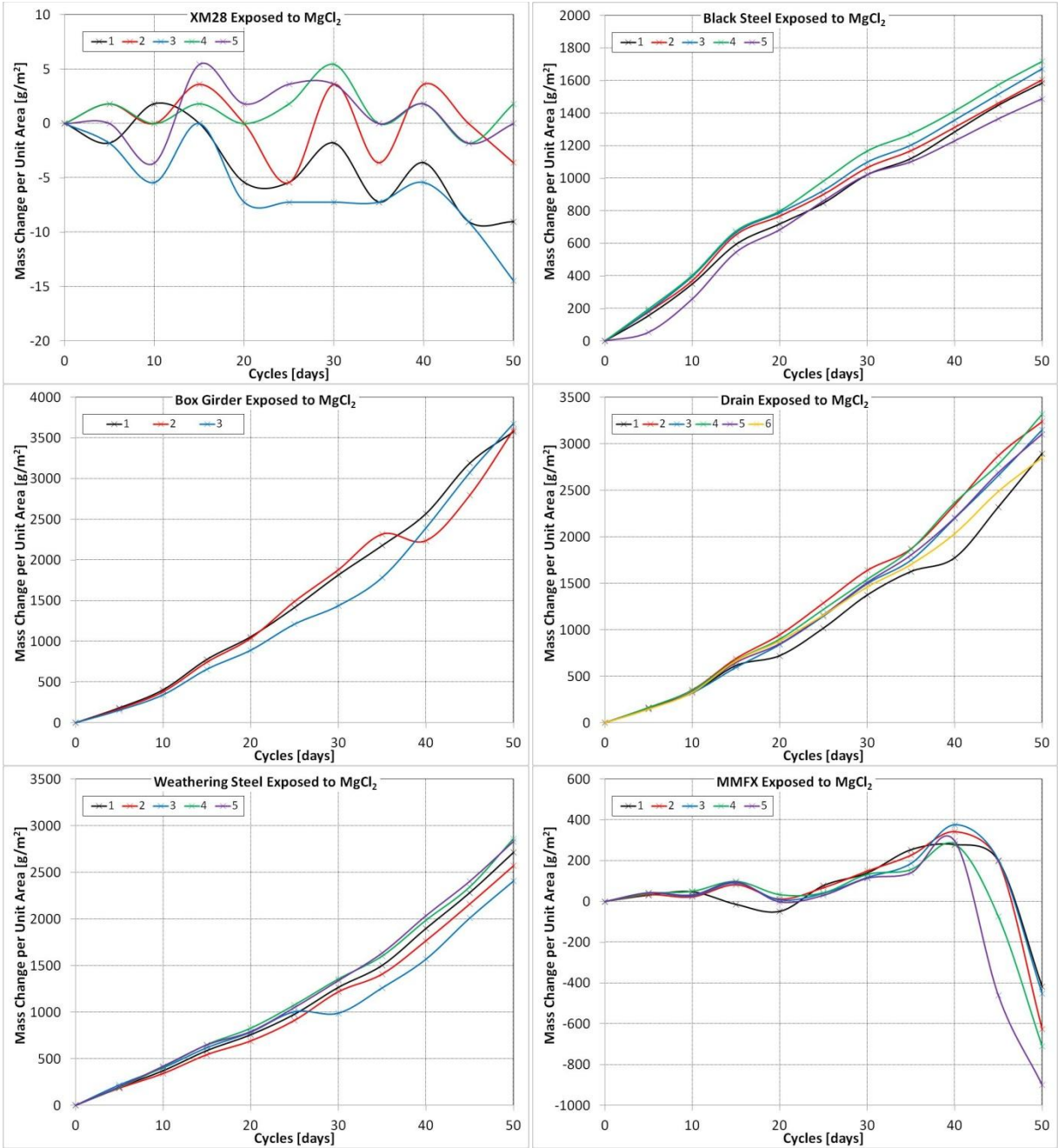
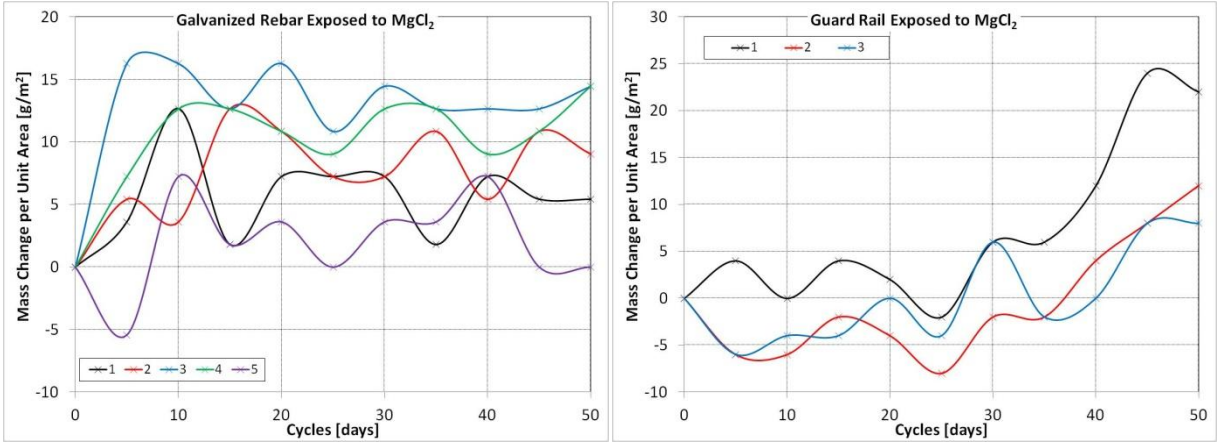


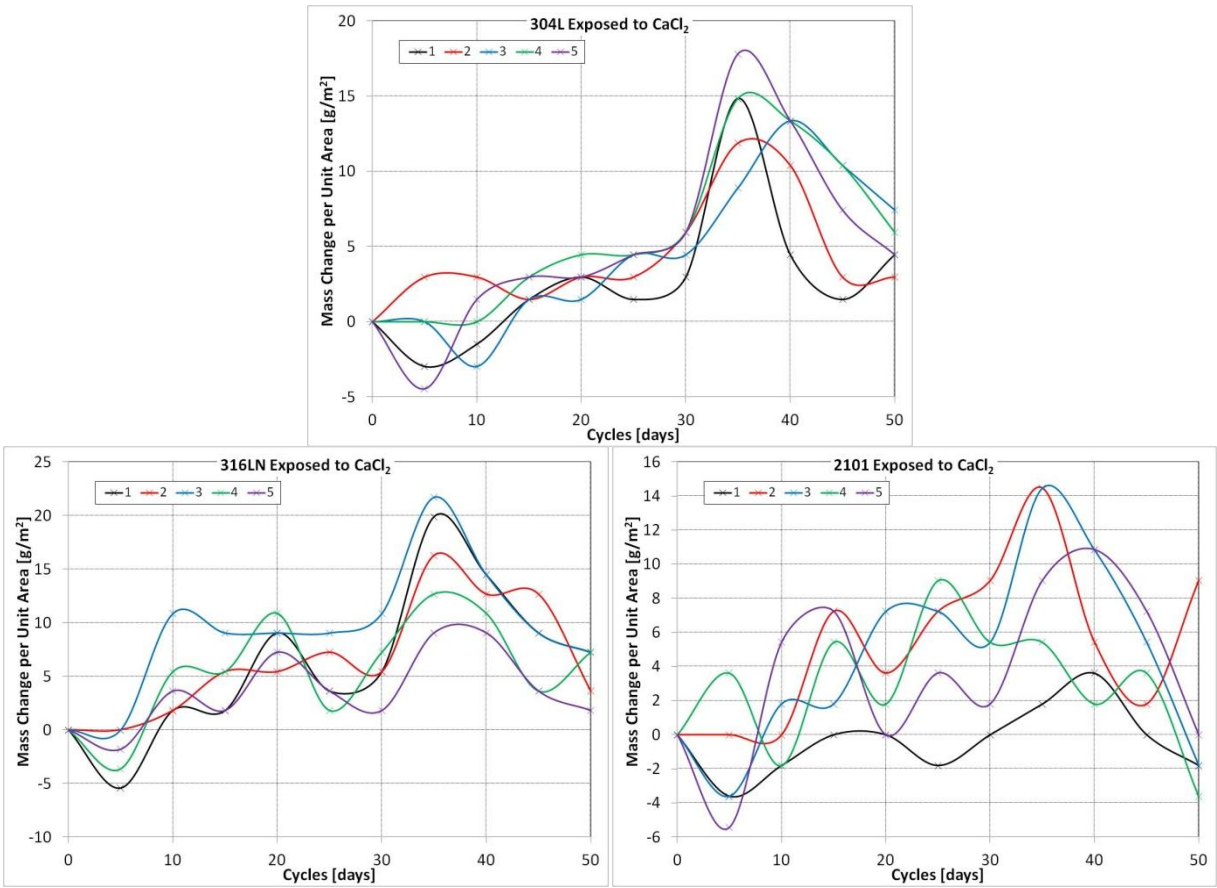
Figure D-10: Individual specimens exposed to NaCl solution vs. SAE J2334 cycles. Note that the ordinate axis for each plot varies in order to show the detail of the individual specimens.

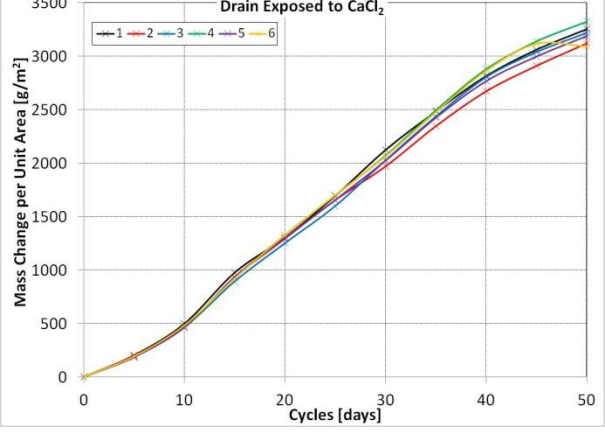
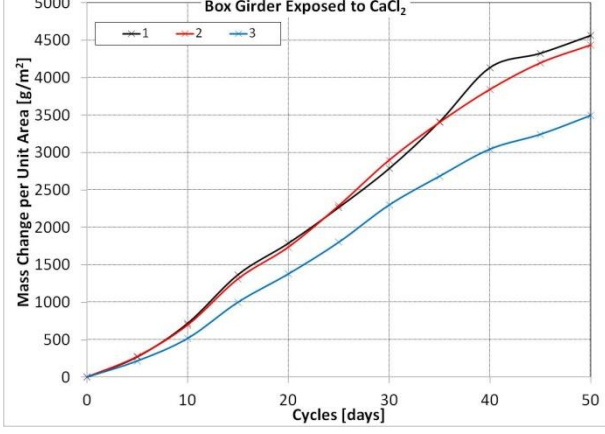
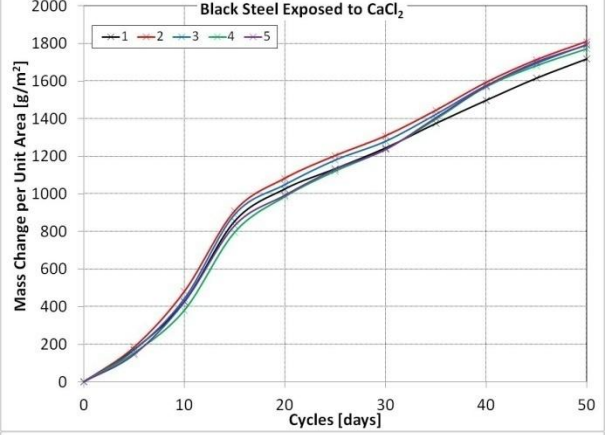
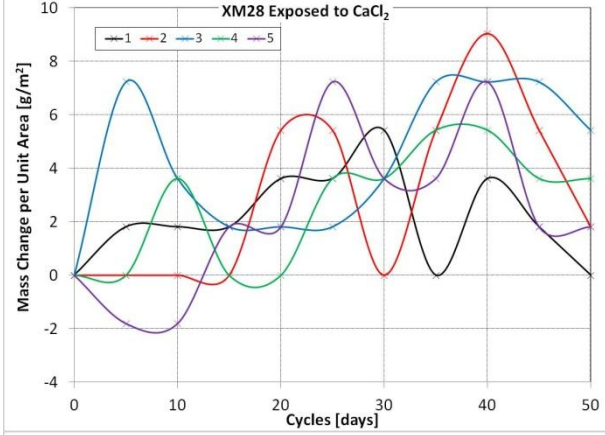
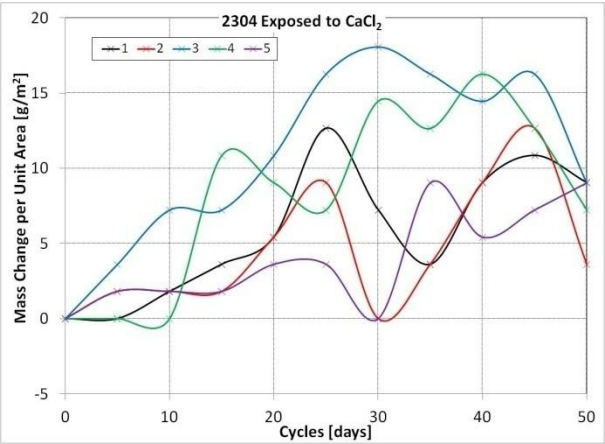
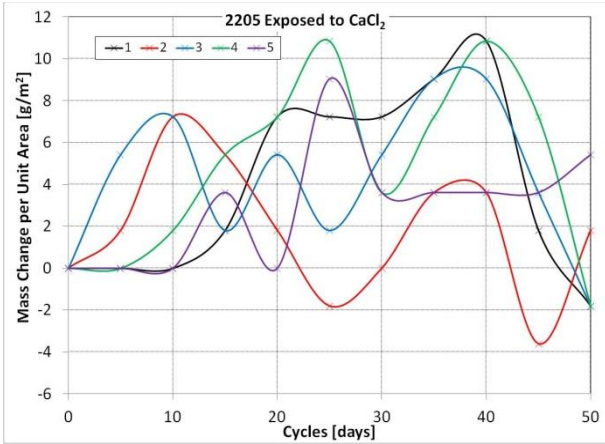






**Figure D-11: Individual specimens exposed to MgCl<sub>2</sub> solution vs. SAE J2334 cycles. Note that the ordinate axis for each plot varies in order to show the detail of the individual specimens.**





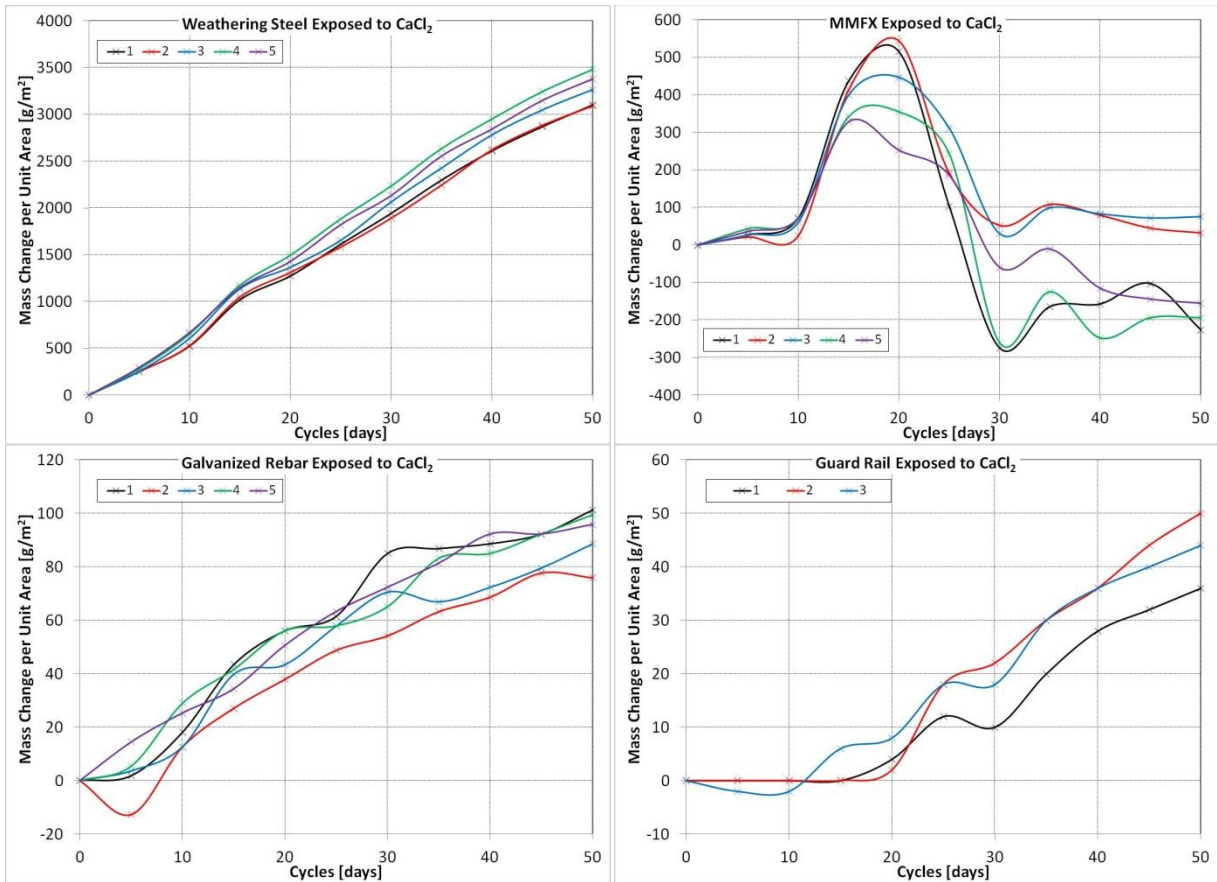


**Figure D-12: Individual specimens exposed to  $\text{CaCl}_2$  solution vs. SAE J2334 cycles. Note that the ordinate axis for each plot varies in order to show the detail of the individual specimens.**